MAGNETISATION REVERSAL BEHAVIOUR IN ADVANCED MAGNETIC FILMS

by Chee Kheng Lim

UNIVERSITY
of
GLASGOW

Submitted for the degree of Ph.D. at the Department of Physics and Astronomy, University of Glasgow

October 2002

To my beloved Da-Eun

" You are the answer to every question and the solution to every problem.
Your love is the greatest blessing god could ever give me."

SUMMARY

Multilayer magnetic thin films have attracted much attention both in the scientific community and the magnetic recording industry due to their commercial value. The work presented in this thesis is mainly a study of the magnetisation reversal mechanism of the free layer of the spin-valve. A spin-valve is a metallic multilayered structure that exhibits giant magnetoresistance. It consists of two soft ferromagnetic layers separated by a thin nonmagnetic layer. The magnetisation of one of the ferromagnetic layers is fixed by an adjacent antiferromagnetic layer by exchange bias coupling. The magnetisation direction of the other ferromagnetic layer can be rotated by applying a small external field. Hence, it is called the free layer.

This thesis begins in Chapter 1 with an introduction to the basic concept of ferromagnetism, including various magnetic energies. The origin of giant magnetoresistance and spin-dependent scattering phenomena are also discussed. Various spin-valve structures are described such as the top and bottom spin-valves and spin-valves with a synthetic antiferromagnet. The modified Stoner-Wohlfarth model is also discussed in Chapter 1. This model is used throughout the thesis to analyse the experimental observation. Various reversal modes are derived from the model, for instance coherent rotation, discontinuous jumps and symmetrically split rotation.

Chapter 2 is devoted to a discussion of the instrumentation and experimental techniques employed. Some magnetic thin film characterisation techniques such as vibrating sample magnetometry, B-H looper and magnetostriction tester, are described briefly. This is followed by an introduction to transmission electron microscopy. Magnetic imaging techniques using the transmission electron microscope are presented. An overview of Fresnel imaging, Low Angle Diffraction and Differential Phase Contrast is given. Fresnel imaging is used extensively in this thesis. A brief introduction to magnetic force microscopy is included.

Electron beam lithography, which is used to fabricate small structures, is explained in Chapter 2. This includes fabrication processes like spin-coating, exposure, developing and deposition.

The free layer magnetisation reversal process for a range of spin-valves is presented in Chapter 3. The spin-valves discussed in this chapter have different magnetostriction coefficients, magnetocrystalline anisotropies and coercivities. Some are top spin-valves and some are bottom spin-valves. They also have different exchange biasing structures, which are the antiferromagnet and the synthetic antiferromagnet.

Marked differences in free layer reversal mode are apparent for these spin-valves. Reversal could be by simple magnetisation rotation or by rotation combined with complex domain processes. However, experimental results showed that a simple reversal process was often associated with films with low magnetostriction and magnetocrystalline anisotropy. The texture of the film was found to have no significant effect on the observed free layer reversal mechanism.

The effect on the free layer reversal process of replacing the antiferromagnet with a synthetic antiferromagnet is discussed in Chapter 4. Three bottom spin-valves with different synthetic antiferromagnetic structures were studied. The experimental results showed no significant difference in free layer reversal process in these spin-valves.

Domain structures were studied for a series of bottom spin-valves annealed in different magnetic fields. Magnetic imaging showed a significant improvement in films annealed at 20 000 Oe. No difference in magnetic domain structures for films annealed in 250 Oe and 10 000 Oe was evident.

Asymmetric magnetisation reversals processes were seen on occasion. Insight into why the reversal mode varied in the way it did was obtained using a modified Stoner-Wohlfarth model. The model provided a good description of the various modes and there was reasonable agreement between predicted and observed fields at which key stages of the reversals took place. Even though a single variable parameter model of the kind used cannot describe a multi-domain state, its use in inferring the nature of domain configurations that arise is discussed as are its other strengths and weaknesses.

The effect of temperature on free layer reversal process is discussed in Chapter 5. It was found that the spin-valve with the thinner synthetic antiferromagnetic layer was more susceptible to temperature changes. A change in the reversal process was observed between room temperature and 200°C. The process changed from a simple coherent rotation to an asymmetrical reversal process. No such changes were observed for the spin-valve with the thicker synthetic antiferromagnetic layer.

The studies of magnetisation reversal of magnetic thin films were extended to patterned magnetic elements in Chapter 6. The design and construction of a new in-situ magnetising rod is described in Chapter 6. The rod allows a pulsed field to be applied to the specimen. My work involves mainly the characterisation of the rod.

The rod was used to study the angular dependence of switching field for a rounded ends $Ni_{80}Fe_{20}$ element. The experimental results showed a slight increase in the switching field with field orientation relative to the long axis of the element for most of

the elements. The data was analysed using the Stoner-Wohlfarth and Kondorsky models. The overall results indicate that the angular dependence of switching field shows a Kondorsky-type behaviour at small field orientation tending toward Stoner-Wohlfarth-type behaviour at large field orientation.

The final experimental chapter discusses the fabrication work on a micro-electromagnet. The aim of fabricating a micro-electromagnet was to serve as an alternative magnetising method to study patterned magnetic elements. The micro-electromagnet acts as a source of local field, which allows magnetising of a few elements in an array. A fabrication technique was developed and the completed device was shown to be able to generate magnetic field. However, the strength of the field has yet to be calibrated.

This thesis ends with general conclusions and discussion on further future work in Chapter 8.

ACKNOWLEDGEMENTS

I want to thank all the many people who helped make my three years research period a joyful experience. This thesis would not have been possible without the help from everyone throughout the course of this work. Most valuable was the excellent supervision and help from Prof. John. N. Chapman and Dr. Mahfuzur Rahman. I am truly indebted to their endless patience and encouragement.

This thesis was enabled by the sponsorship from Seagate Technology and supplemented by the Overseas Research Student Award Scheme, whose support I acknowledge. Special thanks to Dr. Alan B. Johnston, Mr. Denis O. O'Donnell and Mr. Patrick J. N. Doherty from Seagate Technology at Londonderry who not only supplied the samples but also contributed to helpful advice and comment. Special thanks are extended to all the colleagues at Seagate technology at Londonderry who helped make my summer internship an invaluable experience.

I would like to express my appreciation to Dr. Sam McFadyen, Dr. Pat Nicholson, Dr. Peter Aitchison and Dr. Stephen McVitie for teaching me about various microscopes in the Solid State Physics group. Especially for Dr. Sam McFadyen who worked overtime to keep the microscopes in working order. I am also thankful to Dr. Jamie Scott and Ms. Agne Kundrotaite for their help on the magnetic force microscope. Dr. Jamie Scott also played an important role in the provision of computer network within the group.

I would like to acknowledge the help from the group secretary, Ms. Lucy Murray for arranging all the flights and accommodation for conferences. Thanks also to Mr. Colin How, Mr. Brian Miller and Mr. William Smith for maintaining the Jeol microscopes and provision of photographic film.

I particularly appreciate the support and friendship of Gary Yi, Mhairi Crawford, Yi Fang Chen, Damien McGrout and Derek McQuade. Thanks for their willingness to listen and talk during my difficult time. Thanks also to Prof. A. Long and Prof. A. Craven for useful discussion and suggestion.

Finally it remains for me to thank my family and friends in Malaysia for their continual support. Special thanks to David Lim for being a great friend. And, to my beloved Da-Eun and her family, whose everlasting love and care see me though my darkest hours. Their unequalled kindness and generosity I shall forever cherish.

DECLARATION

This thesis is a record of the work carried out by me in the Department of Physics and Astronomy at the University of Glasgow during 1999-2002. The described herein is my own, apart from some preparation of samples which were prepared by Mr. D. O. O'Donnell and Mr. P. J. N. Doherty from Seagate technology. Some of the work given in this thesis can be found in the following papers:

[1] Lorentz microscopy investigation of the free layer reversal in CoFe and Co top spin-valves
C. K. Lim, J. N. Chapman, M. Rahman, A. B. Johnston, K. O'Donnell, J. Magn. Magn. Mater. **238** 301 (2002),

[2] Asymmetric magnetisation reversal of the free layer of a spin-valve
C. K. Lim, J. N. Chapman, M. Rahman, A. B. Johnston, K. O'Donnell, J. Phys. D: Appl. Phys. **35** 2344 (2002),

[3] TEM studies of the variation with temperature and processing conditions of free layer reversal mechanisms in spin-valves
C. K. Lim, J. N. Chapman, M. Rahman, A. B. Johnston, K. O'Donnell,
(To be published)

[4] A new design of specimen stage for in-situ magnetising experiments in the transmission electron microscope
G. Yi, W. A. P. Nicholson, J. N. Chapman, C. D. W. Wilkinson, S. McVitie, C. K. Lim
(To be published)

This thesis has not previously been submitted for a higher degree.

CHAPTER 1: FERROMAGNETISM AND PROPERTIES OF MULTILAYER THIN FILMS

Introduction

Ferromagnetism arises when there are net atomic magnetic moments which line up in such a way that magnetisation persists after the removal of the applied field. This magnetisation is known as the spontaneous magnetisation. Magnetic moments are produced by the orbital motion and spin of the electrons around the atoms. These motions are equivalent to tiny current loops and hence individual atoms create magnetic fields around them as the result of the orbital and spin angular momentum.

Because of energy considerations, the spontaneous magnetisation breaks up into uniformly magnetised regions called magnetic domains. Within each domain the individual atomic spins interact with each other, each of them trying to align others in its own direction by the exchange interaction, which originates from quantum mechanical properties of spins. However, the direction of alignment varies from domain to domain. If we represent the material as being composed of a large number n, of magnetic moments per unit volume, each with magnetisation equivalent to m, and variable orientation, the macroscopic magnetisation M then has modulus $|M| \leq M \equiv nm$. The total magnetic moment of a sample of the substance is the vector sum of the magnetic moments of the component domains. Sometimes certain crystallographic axes are preferred by the magnetic moments. In the absence of an external magnetic field the magnetic moments will align along one of these equivalent "magnetic easy axes". This phenomenon is known as magnetic anisotropy [1-4].

An important parameter in ferromagnetism is the Curie temperature, T_C. It is defined as the critical temperature above which the ferromagnetic material becomes paramagnetic. Therefore, there is no spontaneous magnetisation above T_C. Below T_C, an increasing magnetic field applied to a ferromagnetic substance will cause an increase in the net magnetisation in the direction of the applied field. This will happen either by coherent magnetisation rotation (reversible) within domains or by domain wall motion (often irreversible but can be reversible) where domains that are aligned with the field increase in size. Materials such as iron (Fe), Nickel (Ni), Cobalt (Co) and many alloys of these three elements are ferromagnetic.

1.1: Ferromagnetism of thin films

Thin film ferromagnetism has attracted much attention in both the scientific community and magnetic recording industries [5,6]. There are two aspects of a thin film ferromagnetism important for the recording industries. These are the domain structure and response to a magnetic field. The properties of a thin film ferromagnetic material depend strongly on these two factors.

1.1.1: Magnetic energy

Ferromagnetic thin films generally comprise many domains due to minimisation of the free energy. In general, various types of energy are considered in the domain theory, which are the Zeeman energy (E_z), exchange energy (E_e), magnetostatic energy (E_m), uniaxial anisotropy energy (E_k), magnetostriction energy E_λ and magnetic domain wall energy E_w [1-4]. These will be discussed in turn.

1.1.1a: Zeeman energy, E_z

The direction of the magnetic moments can be changed from one direction to another by the application of an external magnetic field. The Zeeman energy in the specimen due to the external magnetic field is given by

$$E_z = -\mu_o \int_V M \,.\, H \, dV$$

where H is the applied field and V is the sample volume. The applied field will tend to align the magnetic moments in the field direction and Zeeman energy is minimum when the magnetic moments are parallel to the field direction.

1.1.1b: Exchange energy, E_{ex}

The most important interaction between the atomic magnetic moments is the exchange interaction [7]. This energy depends only on the angle between neighbouring atomic moments, independent of their orientation relative to their bond direction. Hence, it is isotropic. The exchange forces responsible for producing ferromagnetic order are considered to be short range forces and in many cases only interactions with the nearest neighbours are significant.

The potential energy between two magnetic moments due to unpaired electron spins S_i and spin S_j is proportional to $S_i \,.\, S_j$ and can be expressed as

$W_{ij} = -2 J_{ij} S_i \,.\, S_j$

where J_{ij} is called the exchange integral. It is positive by definition for ferromagnetism. Hence parallel spins have lower energy than antiparallel ones for the case of ferromagnetism, figure 1.1(a). Therefore, the exchange energy is given by

$$E_{ex} = -2\Sigma_{ij} J_{ij} S_i . S_j$$

where the summation is taken over nearest neighbour pairs only. Since $|S|$ can be taken as constant, we may write

$$E_{ex} = -2 J_{ij} S^2 \Sigma_{ij} \cos \varphi_{ij}$$

where φ_i is the angle between S_i and S_j. This shows that E_{ex} is minimum when the magnetic moments between nearest neighbours are parallel to each other, $\varphi_{ij} = 0$. Therefore, the exchange energy does not predict or encourage the formation of domains.

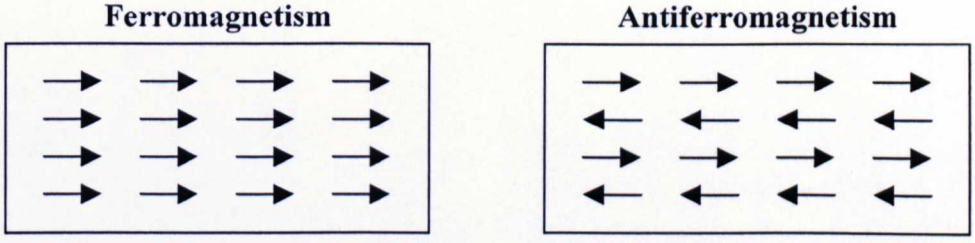

Figure 1.1: (a) *When $J_{ij} > 0$, all magnetic moments prefer to align parallel to each other and* (b) *when $J_{ij} < 0$, antiparallel alignment is preferred.*

It was mentioned earlier that J_{ij} is positive by definition but it is not necessarily so in all materials. J_{ij} may be negative. When the exchange integral between nearest neighbours is negative, it tends to align the neighbouring spins antiparallel to each other below a certain temperature known as the Neel temperature, T_N. These materials are called antiferromagnets, figure 1.1(b).

1.1.1c: Magnetostatic energy, E_m

The subdivision of ferromagnetic thin films into domains is due to the magnetostatic energy, which arises from the long range magnetostatic interactions between the magnetic dipoles present in the specimen. These free poles give rise to both an external stray field and internal field. This internal field is called the demagnetising field, H_d. The total of the external and internal field can be expressed by

$$\boldsymbol{H}_m = \frac{1}{4\pi}\int_V \frac{-\nabla \cdot \boldsymbol{M}}{R^2} dV + \frac{1}{4\pi}\int_S \frac{\boldsymbol{M} \cdot \boldsymbol{n}}{R^2} dS$$

where R is the position vector for the point in space where the field from the charge is evaluated and n is the outward pointing unit vector, normal to the surface. The term $\nabla \cdot M$ is equivalent to the magnetic volume charge and $M \cdot n$ is the magnetic surface charge.

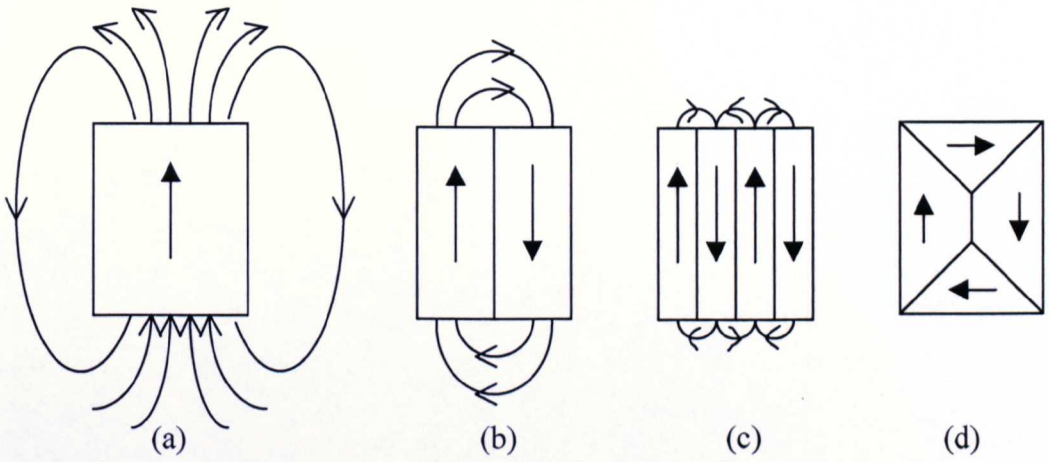

Figure 1.2: Formation of domains due to magnetostatic energy minimisation. E_m is highest in (a) and reduces to (c). A flux-closure structure has no stray field, (d).

The magnetostatic energy contribution takes the form,

$$E_m = \frac{\mu_o}{2} \int \boldsymbol{H}^2 dV$$

where μ_o is the permeability of free space and integration is taken over all space. It can be seen from the equation that E_m is reduced when the volume occupied by the stray field decreases, figure 1.2. Therefore, magnetostatic energy prefers a multi-domain state. However, domain formation leads to a higher exchange energy due to the large angle φ between spins in the wall and hence competition between different magnetisation states. A flux-closure structure is the most preferable state when there is little or no Zeeman and anisotropy energy. In this configuration, the stray field or magnetostatic energy is minimal.

1.1.1d: Anisotropy energy, E_K

Anisotropy is an important property of ferromagnetic materials. Magnetic moments prefer to align along certain favoured directions. There are a few different anisotropies in ferromagnets, but uniaxial anisotropy is the dominant one [7,8].

For a single cubic crystal, the anisotropy energy is described by the first two terms of a series expansion,

$$E_K = \int_V [K_1(\alpha^2\beta^2 + \beta^2\gamma^2 + \gamma^2\alpha^2) + K_2\alpha^2\beta^2\gamma^2)]dV$$

where α, β and γ are the direction cosines and K_1 and K_2 are the first and second order anisotropy constants of the materials. The integration is performed over the volume V of the material.

For hexagonal crystalline structures or uniaxial crystals, the anisotropy energy is described by

$$E_K = \int_V [K_1(1-\gamma^2) + K_2(1-\gamma^2)^2]dV$$

where γ is the direction cosine measured from the uniaxial axis. In uniaxial anisotropy, the magnetic moments preferred directions point either parallel or antiparallel to the uniaxial anisotropy axis or easy axis. This means that both the parallel and antiparallel alignment of magnetic moments with the easy axis will have the same uniaxial anisotropy energy. For instance, if we take the vertical axis in figure 1.2 as the uniaxial anisotropy axis, then it does not matter whether the magnetic moments are pointing upward or downward, the uniaxial anisotropy energy is the same in both cases. Configuration in figure.1.2(a) favours the exchange interaction while the magnetostatic energy is lower in figure1.2(c).

In micro-polycrystalline materials, the magnetocrystalline anisotropy varies locally from one crystal to another. This local fluctuation in anisotropy leads to magnetisation ripple [9].

1.1.1e: Magnetostriction energy, E_λ

For magnetostrictive materials [10], the magnetic hysteresis is controlled also by mechanical stresses and mechanical deformations in an external magnetic field. Magnetostriction originates in the interaction between the atomic magnetic moments, as in magnetic anisotropy. The separation of these atomic magnetic moments, r, due to magnetostriction changes with increasing magnetic field. The saturation value, λ, is defined as $\frac{\partial l}{l}$ the fractional change in length.

In general, for materials with positive magnetostriction coefficient, the magnetisation is increased by tension and the material expands when magnetised. Hence, the spontaneous magnetisation in a certain direction causes strain. Strain makes the crystal cease to be cubic. The dependence of magnetisation on stress may also be

described in terms of the energy associated with the stress and the direction of spontaneous magnetisation M_s in the domain,

$$E_\lambda = \frac{3}{2}\lambda_s \sigma \sin^2 \alpha$$

where λ_s is the magnetostriction coefficient of expansion at saturation and α is the angle between the saturation magnetisation M_s and the tension σ [11–13]. This energy term is similar to the uniaxial anisotropy energy term described in the previous section.

1.1.1f: Magnetic domain wall energy, E_w

Domain walls divide regions of magnetisation into individual domains. The magnetisation rotates coherently across the transition region. There are various types of domain wall. When the magnetisation of the wall is normal to the plane of the surface, the wall is called a Bloch-type wall [14-16], figure 1.3a. The magnetostatic energy of the free poles appearing at the surface of the film increases with a decrease in thickness of the film.

When the thickness of the film decreases below a certain critical thickness, the Neel-type wall is energetically favoured, figure 1.3b. In a Neel-type wall, the plane of spin rotation inside the wall changes from being normal to the film surface to being parallel to the film surface due to the magnetostatic interaction. This means that the walls possess free poles on both sides of the wall surface and the corresponding magnetostatic energy is reduced with a decrease of the film thickness since the number of free poles decreases as the wall area decreases. As a consequence of the free poles on the wall surfaces, Neel-type walls tend to be attracted to each other and form double walls. The width of a Neel wall also tends to be greater than the Bloch wall due to the charged nature of the wall. Another type of domain wall is the cross-tie wall, which contains both Neel-like and Bloch-like regions, shown in figure 1.3c. The cross-tie wall is formed when the film thickness is too large for a Neel wall to form and too small for Bloch wall formation [14-16].

Another important magnetic domain wall which is often observed in magnetic thin films is the 360° wall. The magnetisation on both sides of the wall is identical, shown in figure 1.3(d).

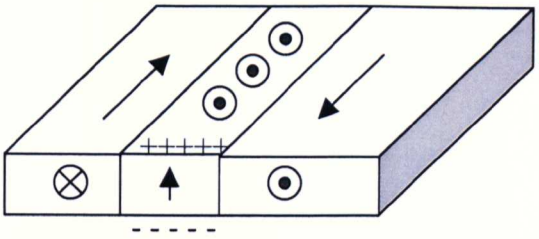

(a) Bloch-type wall

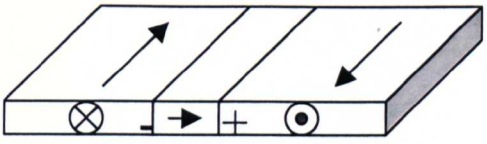

(b) Neel-type wall

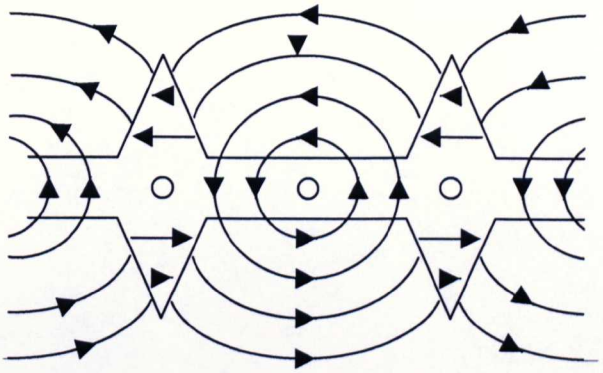

(c) Planar view of cross-tie wall

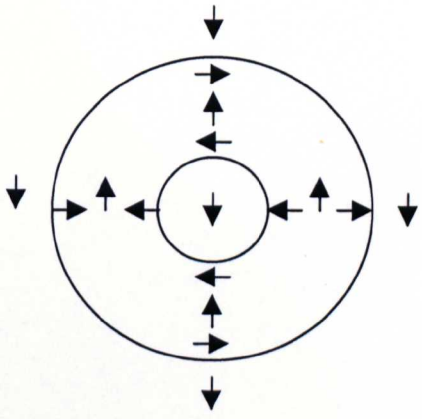

(d) Planar view of 360°

Figure 1.3: Illustration of (a) Bloch-type, (b) Neel-type walls, (c) cross-tie wall and (d) 360° wall.

The domain wall energy is found by considering the changes in energy of moments in domain walls caused by the exchange interaction and anisotropy. Anisotropy will tend to decrease the wall thickness since anisotropy prefers to have all the magnetic moments aligned along the anisotropy axis, either parallel or antiparallel to it. At the same time, the exchange interaction tries to make the wall thicker since the exchange energy is minimum when neighbouring magnetic moments are aligned in parallel.

1.1.1g: Total energy

The magnetisation reversal behaviour is determined by the total magnetic energy in the system, which is the summation of all the energy contributions,

$$E_{total} = E_z + E_{ex} + E_K + E_\lambda + E_w$$

Any observed magnetic configuration at any stage corresponds to a minimum in E_{total}. However, it is very likely for magnetic moments to get trapped in a local energy minimum. Hence, the response to field is also dependent on the history of the specimen causing hysteresis. Hysteresis occurs due to discontinuous jumps or irreversible rotation, leading to a kind of switching action. In anisotropic ferromagnetic materials, the magnetic moments prefer to lie along the anisotropy axes leading to a lower energy

state as noted [17]. When an external magnetic field is applied, this can dislodge the direction of the magnetic moments and cause a jump to the next available local energy minimum which is closer to the field direction and hence lower in energy. This behaviour of the rotation is irreversible and hence hysteretic. Two important properties obtained from hysteresis behaviour are the remanence which indicates the value of magnetic flux density B_r, remaining after the applied field has been reduced to zero and the value of magnetic field strength required to reduced the remaining flux density to zero, called coercivity, H_c.

1.2: Hysteresis loop

The net magnetic moment of a ferromagnetic material is frequently equal to zero initially until H is applied to it. Then, B increases with H until saturation is reached, figure 1.4a. When H decreases to zero, B is not zero but equal to B_r. As H is increased in the opposite direction B goes to zero when $H = H_c$, hence coercivity [18].

For the case of a spin-valve structure, the loop is not centred at the origin. The offset of the loop from origin by H_i is due to the present of unidirectional anisotropy in some materials. H_i is therefore also called the offset field.

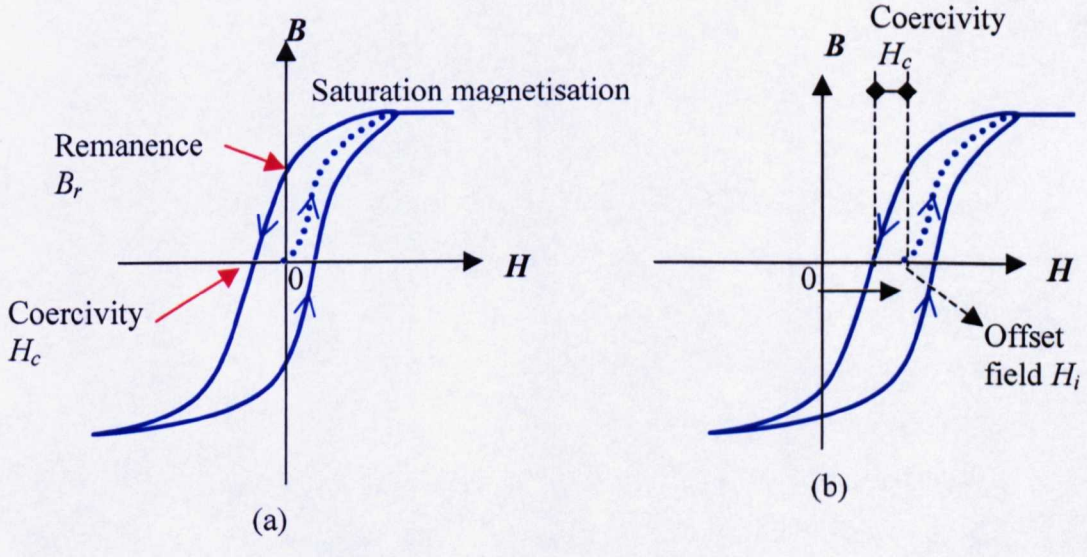

Figure 1.4: (a) A typical ferromagnet hysteresis loop, and (b) an offset of the loop due to the unidirectional anisotropy.

1.3: Giant magnetoresistance

1.3.1: Spin dependent scattering

The underlying mechanism of giant magnetoresistance is a coherent interplay of spin-dependent scattering of conduction electrons occurring at the interfaces or in the bulk and the reflection from spin-dependent potential barriers between the magnetic (ferromagnetic) and non-magnetic (spacer) layers [19-21].

When an electrical field is applied, the spin-oriented conduction electrons are accelerated until they hit a scattering centre. For an electron moving through a magnetic layer with the same spin as the magnetisation in that layer, nearly all available quantum states are full (known as the majority state). Conversely, for an electron of the opposite spin moving through the same layer, the states available to it are partially filled (minority state). Scattering is dependent on the availability of states into which an electron can scatter. So, an electron in the minority state scatters more.

The average distance the conduction electrons accelerate is called the electron mean free path and is of the order of nanometers in the metallic layers [22]. Hence, the thickness of the magnetic and non-magnetic layer have to be less than the electron mean free path in order for the conduction electrons to travel from one layer to the other.

Intrinsic structural defects such as vacancies, stacking faults, lattice distortions and grain boundaries that are produced during the deposition process make their own contribution to the scattering potentials. However, these scattering potentials are spin-independent. The spin dependence of the conductivity comes from the electronic band structure, which is not the same for the majority and minority-spin electrons. Due to this spin-polarised band structure, both the Fermi velocities and Fermi surfaces become spin-dependent. Together with the spin asymmetry of the density of electron states at the Fermi level, this leads to the spin-dependent scattering probabilities. Since the conductivity is proportional to the mean free path of the electrons which is in turn proportional to the electron velocity at the Fermi level and inversely proportional to the average density of states, the conductivity is spin-dependent [23-27].

When both ferromagnetic layers are parallel to each other, spin up electrons are weakly scattered in all layers therefore carrying a large part of the electric current, figure 1.5. However, spin down electrons are strongly scattered, hence participate little in the conduction current. By taking ρ_u and ρ_d to be the resistivity of the spin up and the spin down electrons respectively, the resistivity of the multilayer in this configuration, ρ_p (resistivity in the parallel configuration), is

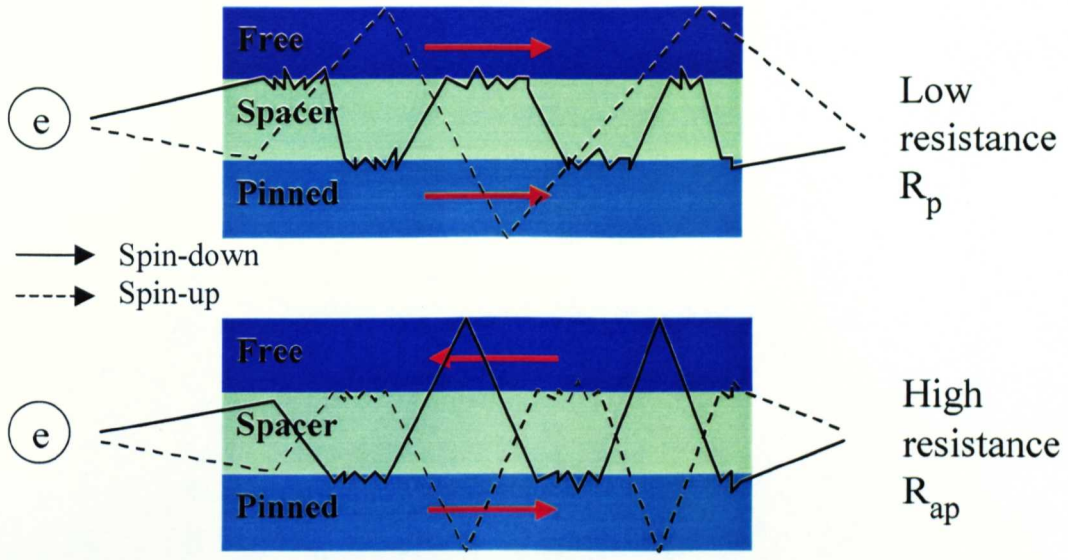

Figure 1.5: Electron spin-dependent scattering at interfaces.

$$\rho_p = \frac{\rho_u \rho_d}{(\rho_u + \rho_d)}$$

When the ferromagnetic layers are antiparallel to each other, both spin up and spin down electrons are alternately strongly and weakly scattered as they travel through the successive ferromagnetic layers, figure 1.5. The resistivity in this configuration, ρ_{ap} is

$$\rho_{ap} = \frac{(\rho_u + \rho_d)}{4}$$

The GMR ratio which is defined as the relative change in resistivity from highest resistivity (antiparallel) to lowest resistivity (parallel). A GMR curve is shown in figure 1.6.

$$GMR = \frac{\left|\rho_p - \rho_{ap}\right|}{\rho_p} \times 100\%$$

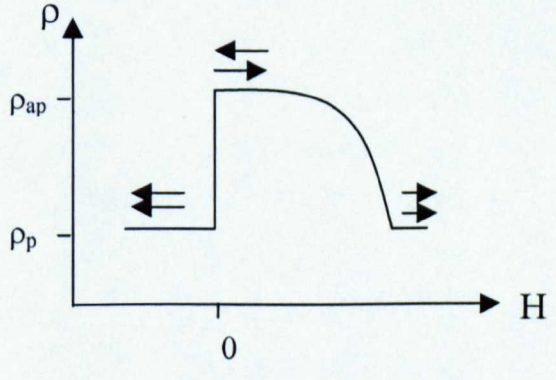

Figure 1.6: A GMR curve.

1.3.2: Interfacial and bulk scattering

Both interfacial and bulk scattering can contribute to the spin-dependent scattering. Their relative role depends on such factors as quality of interfaces, amount of bulk scattering centres, composition of multilayers and thickness of layers. It is still an open issue which one is the dominant mechanism. However, it is generally thought that interfacial roughness between the ferromagnet and spacer layers plays an important role in spin-dependent scattering. When the interface is too rough, the mean free path of the conduction electrons becomes too small compared to the thickness of the ferromagnetic layer. This will prevent the spin-dependent scattering mechanism from occurring [22-27].

Other important aspects of the interfacial properties like chemical impurities, variation in thickness and geometrical roughness can also influence the spin-dependent scattering of the conduction electrons. Bulk scattering comes from the scattering centres produced by the imperfections and impurities in the ferromagnetic and spacer layer. In general, in order to improve the GMR performance, it is essential to maximise the spin-asymmetry of the scattering due to both bulk and interfacial spin-dependent scattering. Minimising the spin-independent scattering by matching the conduction band between the non-magnetic layer and the spin-up channel of the ferromagnetic layer, for instance matching Fe Ni or Co with Cu will also enhance GMR [22].

1.4: Spin-valve

A spin-valve (SV) is a metallic multilayered structure that exhibits giant magnetoresistance [22]. The layer structure is shown in figure 1.7. It consists of two soft ferromagnetic (FM) layers separated by a thin nonmagnetic layer (spacer layer). The magnetisation direction of one FM layer is fixed by an adjacent antiferromagnetic (AFM) layer (pinning layer) by exchange bias coupling. The magnetisation direction of the second FM layer (free layer) can be rotated by applying a small external magnetic field of a few Oe. The two FM layers tend to be weakly coupled ferromagnetically so that in zero field the free layer is uniformly magnetised parallel to the pinning layer.

In general, the net thickness of all the layers is smaller than, or of the order of, the mean free path of the conduction electrons. The seed layer enhances growth in a certain desired crystallographic orientation and hence reduces the magnetocrystalline anisotropy. The cap layer protects the structure against corrosion from the atmosphere.

1.4.1: Top and bottom spin-valve

A TSV is so-called because the free layer is grown first with all other layers on top of it while the AFM layer is grown first in a bottom spin valve (BSV), as shown is figure 1.7.

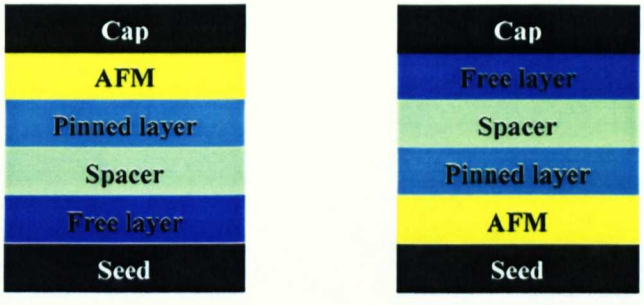

a: Top spin-valve b: Bottom spin-valve

Figure 1.7: Diagram showing (a) the top spin-valve, and (b) bottom spin-valve structure.

1.4.2: Exchange bias

In AFM materials, the number of magnetic moments pointing in one direction is equal to the number of moments pointing in the opposite direction in an alternating fashion, resulting in zero net moment. However, at the interface with the FM layer, there can be unequal numbers of parallel and antiparallel magnetic moments at the surface due to grain orientation, size, shape or roughness. Since the FM is ordered at its Curie temperature (T_c) which is greater than the Neel temperature (T_N) of the AFM, a field applied to coupled FM-AFM systems at $T_c > T > T_N$ will align the FM magnetisation in the field orientation, whilst the AFM will remain paramagnetic. As the temperature is lowered through T_N, the localised AFM moments at the interface will couple to the aligned FM moments, sharing the same magnetisation direction. The strong exchange interaction between moments in the AFM will keep them from rotating out of their alignment direction at a temperature below T_N. The coupling between the AFM and FM layers is known as the exchange bias coupling H_{ex} [28-29], shown in figure 1.8. The blocking temperature is the temperature when the exchange bias coupling vanish.

1.4.3: Interlayer coupling

The spacer layer can be as thin as possible provided that a sufficient decoupling of the two FM layers still exists, so that the magnetisation of the free layer is still free to rotate. There are two important couplings between the two ferromagnetic layers, which

are the "orange-peel" coupling and the indirect exchange Ruderman-Kittel-Kasuya-Yosida (RKKY) coupling [30].

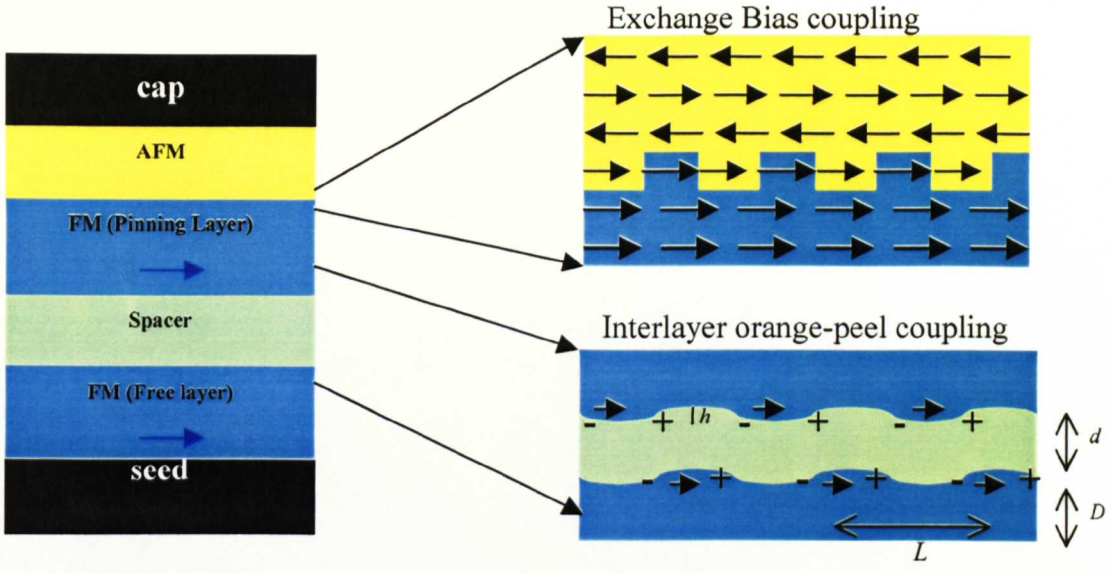

Figure 1.8: Basic composition of a spin-valve structure with the exchange bias coupling and interlayer coupling mechanism.

1.4.3a: "Orange-peel" interaction

The interlayer 'orange-peel' coupling comes from the magnetostatic interaction due to the correlated waviness of the ferromagnetic layers in non-ideal films, figure 1.8. The roughness at the interfaces is correlated because of the propagation of roughness profile from layer to layer during the deposition process. This magnetostatic interaction would like to keep the magnetic moments at each sides of the interface (FM/NM/FM) align in the parallel configuration and hence, ferromagnetic coupling occurs. The coupling can be approximated by

$$H_{magnetostatic} = \left(\frac{\pi^2 h^2 M_s}{\sqrt{2}LD}\right)\exp\left(-\frac{2^{3/2}\pi d}{L}\right)$$

where h and L are the amplitude and period of the waviness at the interface. D and d are the thickness of the free and spacer layer respectively. M_s is the saturation magnetisation of the free layer [31-33].

1.4.3b: RKKY interaction

The indirect exchange RKKY coupling arises from the oscillatory character of spin-polarised conduction electrons [34-37]. These conduction electrons scatter from the interface and impurities in the spacer layer. As a result, interference between the

incoming and scattered electron waves is generated giving rise to oscillatory probability densities. Since spin-up and spin-down electrons have different scattering probabilities at the interfaces and impurities, this leads to a oscillatory spin density. However, all these oscillations cancel out for electrons below the Fermi energy level because of completely filled energy states. Spin density oscillations only occur at the Fermi energy level, the oscillations being a function of the spacer layer thickness. Depending on the thickness of the spacer layer, the RKKY interaction can favour either a ferromagnetic or an antiferromagnetic configuration.

The observed magnitude of the coupling is the result of the competition between exchange and magnetostatic interactions. Indirect exchange is dominant when the average interfacial roughness is lower than 4 Å. Magnetostatic coupling is dominant when roughness reaches values higher than 7 Å [34-37].

1.4.4: Synthetic antiferromagnetic spin-valves

There are two main problems with antiferromagnetic pinning. Firstly, the magnitude of the exchange field proves itself to be unable to completely pin the magnetisation of the pinned layer and partial loss of the pinning direction occurs when the height of the sensor gets into the submicrometer range due to the presence of the self-demagnetising field. Secondly, the blocking temperature of the antiferromagnet is too low, between 200°C and 400°C. These difficulties can be partially overcome by synthetic antiferromagnetic pinning (SAF) [38-42].

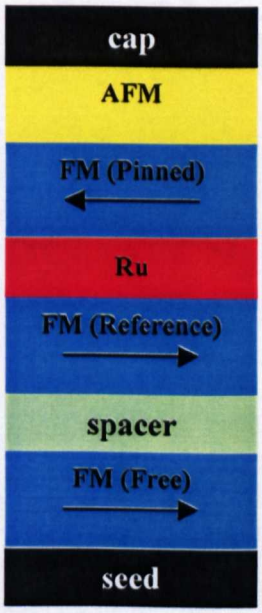

The pinning action using the synthetic antiferromagnetic structure is enhanced by the strong RKKY coupling between the reference and pinned layer via the Ruthenium (Ru) spacer. The Ru thickness in the SAF is a very sensitive parameter due to the oscillatory behaviour of the coupling and is chosen to lie in the range, 3-9 Å, where antiferromagnetic coupling is favoured. H_{ex} for the SAF is significantly higher than the conventional value, >3000Oe. The field required to align the two strongly antiferromagnetically coupled pinned and reference layers is > 10 000 Oe.

1.5: The modified Stoner-Wohlfarth model

The Stoner-Wohlfarth model is developed based on the assumptions that no domains are involved in the reversal process [43-46]. The model states that due to the anisotropy energy, moment rotation under applied field variations consists of reversible and irreversible portions. Hence, two energy terms are included in the model, which are the uniaxial anisotropy energy and Zeeman energy.

For the case of a spin-valve structure, the model is modified to include the unidirectional anisotropy energy term. It assumes that the unidirectional interlayer coupling between the pinned and free layer is homogeneous and can be represented by a global offset field [44].

The modified model takes an (reduced) energy function of the form:

$$\Gamma = H_K \sin^2(\varepsilon - \phi) - [2H\cos(\theta - \phi) + 2H_i \cos\phi)]$$

where H_K, H, and H_i are the uniaxial field, in-plane external field and offset field (unidirectional or pinning). H_K is equal to $2K_u/\mu_o M_s$ where μ_o and M_s are the permeability of free space and the saturation magnetisation respectively. The relationship between ε, ϕ and θ relative to the unidirectional direction is shown in figure 1.9. The energy function is solved for the energy minimum which requires $\frac{\partial \Gamma}{\partial \phi} = 0$ and $\frac{\partial^2 \Gamma}{\partial \phi^2} > 0$. The model is used extensively in this thesis for analysing the free layer magnetisation reversal in spin-valves. It is worth pointing out that the contribution from the magnetostriction and magnetocystalline effects are taken into account in terms of the uniaxial anisotropy in this simple model.

The model is used in the following way. Plots of Γ against ϕ are studied for various values of H. The locus of the minimum value of Γ then indicates how the orientation of the magnetisation should vary with H. Figure 1.10 shows an example of an energy contour plot. The energy curves are plotted as Γ against ϕ at various H. They show all the energy maxima and minima position along ϕ from -180° to 360°. The bold number beside the curve marks the field magnitude in Oersted units. The solid dots on the curves mark the positions of global energy minima. The level of the energy minima on each curve is different. This is due to the interplay between various energy terms in the energy function. When there is a dominating energy term, the energy curve will have a deep minimum. However, when all the energy terms almost counter balance each other, the energy minima become very shallow and broad.

There are various magnetisation reversal mechanisms that can be deduced from the model such as coherent rotation, discontinuous jumps and symmetrical splitting. These mechanisms are derived by following the energy minima path on the energy contours throughout a field cycle.

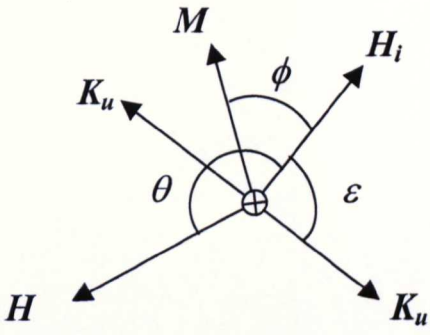

Figure 1.9: Schematic showing key angular relationships.

1.5.1: Coherent rotation

Figure 1.10 shows an example of a coherent rotation process in the energy contours. The negative and positive fields represent fields applied parallel and antiparallel to the pinned direction respectively. When the positive applied field is increased to 30 Oe, there is only one energy minimum path available, shown by the blue dotted line. The energy minima shifts smoothly in a regular intervals from 0° to 180° with positive increasing field. Therefore, the magnetisation undergoes a coherent rotation in this case. The rotation is in the anticlockwise sense. The reversal process is shown in the diagram drawn on the bottom right hand corner of figure 1.10.

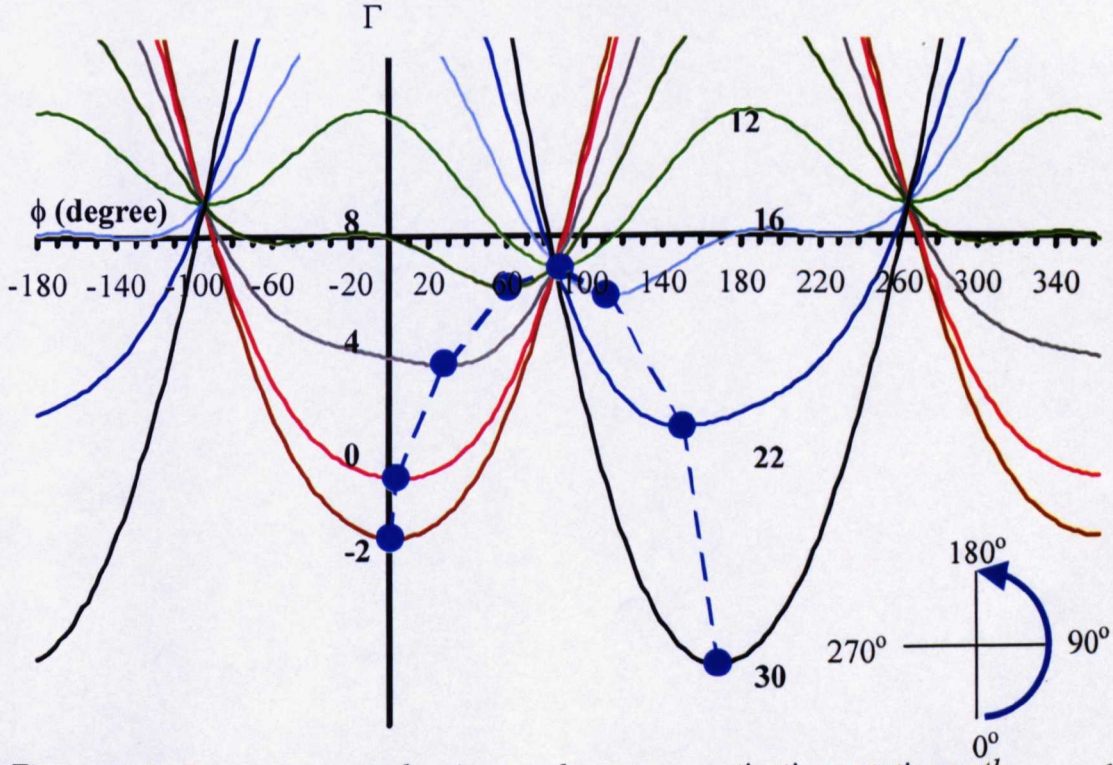

Figure 1.10: Energy contour showing a coherent magnetisation rotation path.

1.5.2: Discontinuous jump

The second reversal mechanism that can be predicted by the model involves a discontinuous jump. A discontinuous magnetisation jump is shown in the energy contours in figure 1.11. When the field is increased from negative to positive, the energy minima path shows a smooth rotation towards 180° in the anticlockwise sense. However, at H = 16 Oe, the relevant local minimum is at $\phi \approx 130°$, whilst the next (and only) energy minimum is at about 220° when H is increased to 18 Oe. The huge angular gap in between energy minima leads to a discontinuous jump of $\approx 90°$. The discontinuous jump leads to an over shoot of the magnetisation past the field direction. Therefore, the magnetisation will follow a coherent rotation path in the clockwise sense back to the field direction after the jump has occurred. This discontinuous jump in magnetisation often results in domain formation. The reversal process is shown in the diagram at the bottom right hand corner of the energy contours.

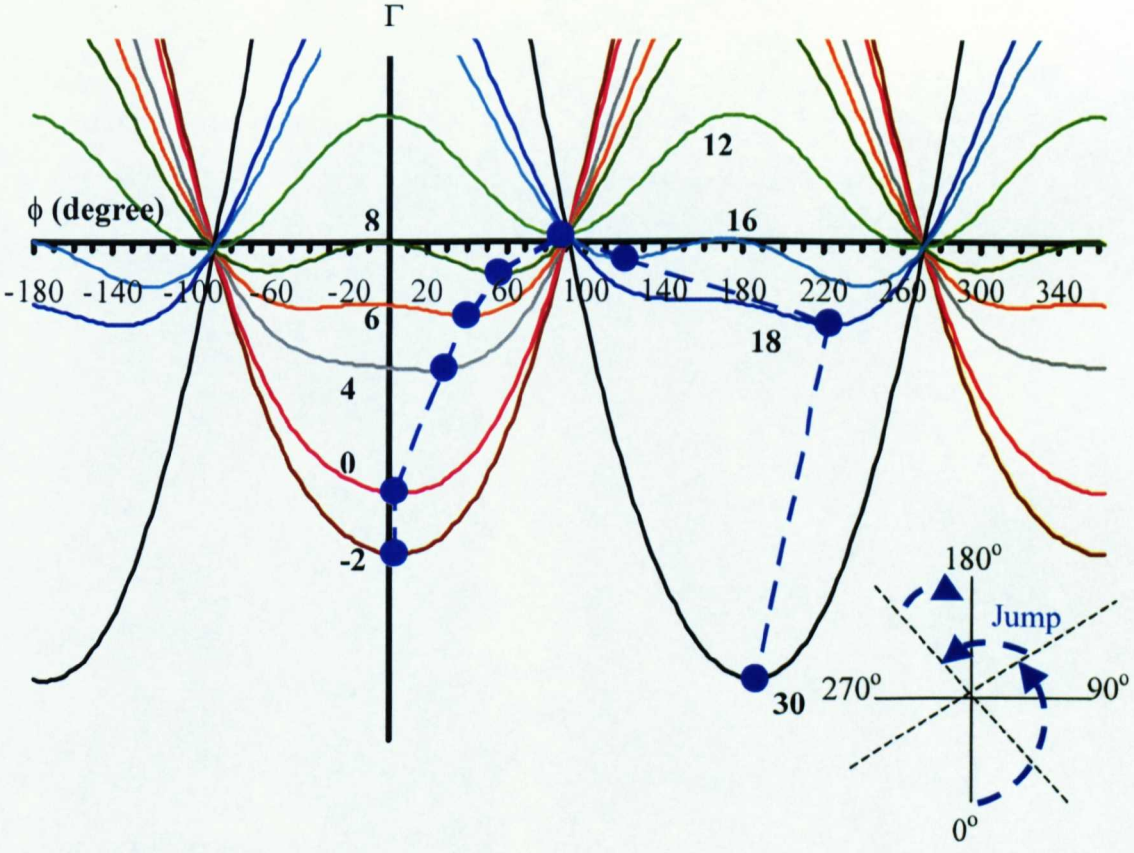

Figure 1.11: Energy contours showing a discontinuous magnetisation jump path.

1.5.3: Symmetrically split rotation

Another important reversal mechanism deduced from the model is the symmetrical split in rotation. Symmetrically split rotation will occur when there are two equivalent energy minima paths available as shown in figure 1.12.

In the energy contours, when H is increased in the positive direction the energy minima broaden as at $H = 4$ Oe. Further increase in H to 8 Oe creates two equivalent energy minima, at $\approx -60^{\circ}$ and $\approx 60^{\circ}$. Since there is no favourable path between these two energy minima, magnetisation splits symmetrically. As a result, domains are created where the magnetisation in each domain rotates in opposite directions. These domains are often observed when H is applied close to the unidirectional anisotropy axis. The domain walls generated by this symmetrical splitting lie orthogonal to the field direction. Hence, they also have a very low mobility.

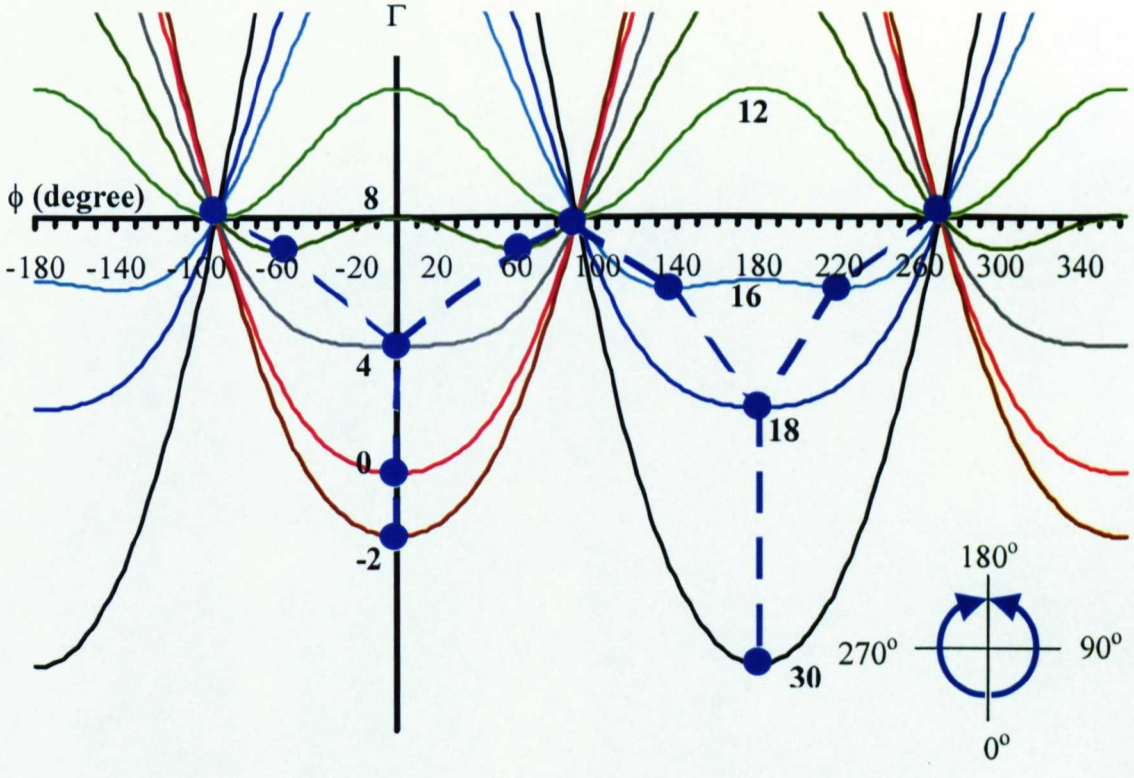

Figure 1.12: Energy contours showing a symmetrical magnetisation splitting path.

1.6: Magnetic Recording

Magnetic recording systems which utilize magnetic disks constitute the main form of data storage and retrieval in present-day computer and data processing systems. In the recording process, information is written and stored as magnetisation patterns on the magnetic recording medium based on CoCrPt alloys. When a command is made to

store some data on a disk, the data flows into a cache where it is encoded using special mathematically derived formulae. Then, free sectors on the disk will be selected and the actuator moves the write head, which is basically an electromagnet, over those sectors just prior to writing and the time it takes the actuator to move to the selected data track is called the "seek" time. A pattern of electrical pulses representing the data pass through the coils in the writing head, producing a related pattern of magnetic fields at a gap in the head. These magnetic fields alter the magnetic orientations of bit regions on the disk itself, so now the bits represent the data, figure 1.13(a).

In the read back process, the actuator moves the reading head over the track where the chosen data is stored by consulting the table of stored data locations in the drive. When the correct sectors pass beneath the reading head, the magnetic flux from the magnetisation patterns on the recording medium intercepts the reading head. This induces resistivity changes in the sensitive GMR materials located in the read element within the reading head, figure 1.13(b). The electrical signals are then decoded to reveal the data that had been stored on the disk. A very important performance criterion for a disk recording system is the amount of information it can store per unit area. Since information is typically stored as abrupt magnetisation changes, designated as transitions, along a track on the disk, the areal density is the product of the linear bit density and the track density. Linear density is defined to be the density with the magnetic transitions can be packed along a track and the track density is the density with which these tracks can in turn be packed together in a radial direction.

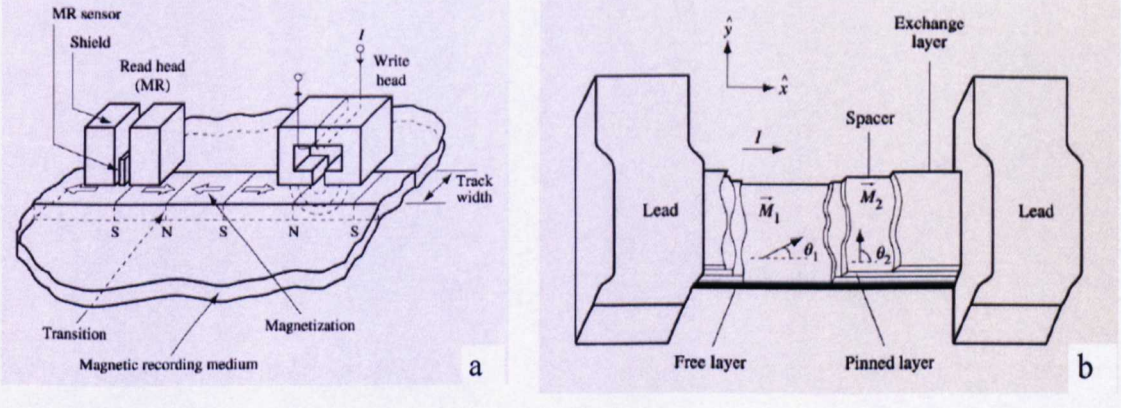

Figure 1.13: (a) Magnetic recording process, (b) the spin-valve structure as the reading element.

In the next chapter, a detailed description of all experimental techniques and instrumentation used to perform experiments involved in this thesis is given. This is followed by the experimental results on continuous spin-valve films in chapter 3, 4 and

5. Studies on free layer magnetisation reversal behaviour in a range of spin-valve films are presented in chapter 3. The reversal process was studied as a function of applied field orientations. These spin-valve films also have different magnetostriction coefficients and magnetocrystalline anisotropy. In chapter 4, the experimental results of the effect of a synthetic antiferromagnet and the annealing conditions on the free layer reversal process is discussed. The effect of temperature on the free layer reversal process is discussed in chapter 5. An in-situ TEM annealing experiment was also carried out to study the reversal process before and after anneal. This is described in chapter 5.

Chapter 6 describes my work on characterising the new in-situ magnetising TEM rod. Experiments on patterned magnetic elements were also carried out using the new rod and this is discussed in chapter 6. Chapter 7 presents the work on fabricating a micro-electromagnet. The micro-electromagnet was designed to generate a local magnetic field for studying interaction between magnetic elements in an array.

Finally, a general conclusion is given in chapter 8. A discussion on further future work is also included in the final chapter.

References:

[1] Chikazumi, S. Physics of Magnetism, John Wiley and Sons Inc. New York (1966),

[2] D. Jiles, Introduction to magnetism and magnetic materials, Chapman & Hall (1998),

[3] A. Aharoni, Introduction to the theory of ferromagnetism, Oxford (1996),

[4] A. Hubert and R. Schafer, Magnetic domains: the analysis of magnetic microstructures, Springer (1998),

[5] J. M. Daughton, J. Magn. Magn. Mater. 192 334 (1999),

[6] D. E. Speliotis, J. Magn. Magn. Mater. 193 29 (1999),

[7] J. H. Van Vleck, J. Phys. Rev. 52 1178 (1937),

[8] Harvey Brooks, Phys. Rev. 58 909 (1940),

[9] H. Hoffmann, IEEE Trans. Magn. 4 32 (1968),

[10] E. Quandt, A. Ludwig, J. Appl. Phys. 85 6232 (1999),

[11] Henryk Szymczak, J Magn. Magn. Mater. 200 425 (1999),

[12] N. Buiron, L. Hirsinger, and R. Billardon, J. Magn. Magn. Mater. 196 868 (1999),

[13] F. Liorzou, Y. Yu, and D. C. Atherton, J. Appl. Phys. 83 7106 (1998),

[14] J. N. Chapman, K. J. Kirk, Magnetic Hysteresis in Novel Magnetic Materials 207 (1997),

[15] E. E. Huber, D. O. Smith, and J. B. Goodenough, J. Appl. Phys. 29 294 (1958),

[16] A. E. Labonte, J. Appl. Phys. 40 2450 (1969),

[17] Z. Wang, Y. Nakamura, J. Magn. Magn. Mater. 155 187 (1996),

[18] T. Leineweber, H. Kronmuller, J. Physical B 275 5 (2000),

[19] C. Prados, D. V. Dimitrov, G. C. Hadjipanayis, J. Magn. Magn. Mater. 192 19 (1999),

[20] E. Yu. Tsymbal and D. G. Pettifor, J. Magn. Magn. Mater. 202 163 (1999),

[21] R. E. Camley, J. Barnas, J. Phys. Rev. Lett. 63 664 (1989),

[22] B. Dieny, J. Magn. Magn. Mater. 136 335 (1994),

[23] R. Q. Hood, L. M. Falicov, D. R. Penn, Phys. Rev. B 49 368 (1994),

[24] A. Vedyayev, M. Chshiev, B. Dieny, J. Magn. Magn. Mater. 184 145 (1998),

[25] E. Yu. Tsymbal, D. G. Pettifor, J. Appl. Phys. 81 4579 (1997),

[26] E. Yu. Tsymbal, D. G. Pettifor, Phys. Rev. B 54 15314 (1996),

[27] E. Yu. Tsymbal, D. G. Pettifor, J. Phys. Condens. Matter 8 L569 (1996),

[28] A. E. Berkowitz, Kentaro Takano, J. Magn. Magn. Mater. 200 552 (1999),

[29] J. C. S. Kools, IEEE Trans. Magn. 32 3165 (1996),

[30] J. L. Leal, M. H. Kryder, IEEE Trans. Magn. 32 4642 (1996),

[31] D. Wei and H. Neal Bertram, IEEE Trans. Magn. 32 3434 (1996),

[32] L. Neel, C. R. Acad. Sci. (France) 225 1545 (1962),

[33] J. C. S. Kools, Th. G. S. M. Rijks, A. E. M. De Veirman and R. Coehoorn, IEEE Trans. Magn. 31 3918 (1995),

[34] P. Bruno, J. Appl. Phys. 76 6972 (1994),

[35] M. D. Stiles, Phys. Rev. B 39 7238 (1993),

[36] M. D. Stiles, J. Appl. Phys. 79 5805 (1995),

[37] M. D. Stiles, J. Magn. Magn. Mater. 200 322 (1999),

[38] D. V. Dimitrov, J. Van Ek, Y. F. Li, J. Q. Xiao, J. Magn. Magn. Mater 218 273 (2000),

[39] L. Thomas, A. J. Kellock, S. S. P. Parkin, J. Appl. Phys. 87 5061 (2000),

[40] J. L. Leal, M. H. Kryder, J. Appl. Phys. 83 3720 (1998),

[41] G. W. Anderson, Y. Huai, and M. Pakala, J. Appl. Phys. 87 5728 (2000).

[42] Y. Huai, J. Zhang, G. W. Anderson, P. Rana, S. Funada, C. Y. Hung, M. Zhao, and S. Tran, J. Appl. Phys. 85 5528 (1999),

[43] E. C. Stoner and E. P. Wohlfarth, IEEE Trans. Magn. 27 3475 (1948),

[44] M. Labrune, J. C. S. Kools, A. Thiaville, J. Magn. Magn. Mater. 171 1 (1997),

[45] J. P. King, J. N. Chapman, J. C. S. Kools, M. F. Gillies, J. Phys. D: Appl. Phys. 32 1087 (1999),

[46] M. F. Gillies, J. N. Chapman, IEEE Trans. Magn. 24 1778 (1995),

CHAPTER 2: EXPERIMENTAL TECHNIQUES AND INSTRUMENTATION

Introduction

The purpose of this chapter is to describe the various experimental techniques and instrumentation involved in my research. This includes the preparation and characterisation of magnetic thin films in section 2.1. The general principle of transmission electron microscopy is discussed in section 2.2. This is followed in section 2.3 by various imaging modes and more specifically magnetic imaging in section 2.4. Another type of magnetic imaging, magnetic force microscopy is described in section 2.5. The last section in this chapter, section 2.6 is about fabrication using electron beam lithography.

2.1: Magnetic thin film deposition and characterisation

2.1.1: Sputter deposition technology

Sputter deposition, also known as physical vapour deposition, or PVD, is one of the most widely used techniques for the fabrication of thin-film structures on semiconductor wafers. Sputter deposition is usually carried out in diode plasma systems known as magnetrons. The negative plate, also known as the cathode, is bombarded by ions by the plasma. Cathode atoms are dislodged from the metal surface. The plasma is created when electrons ejected from the surface of the cathode ionise the argon. The atoms that are released may then deposit on other surfaces inside the vacuum system, forming thin films, figure 2.1. The thickness of the deposited film is determined by the distance between the target and the substrate and the duration of exposure to the target. The substrate remains stationary throughout the deposition process.

The principal type of system currently used for high-rate deposition of metals, alloys and compounds is known as the magnetron cathode system. This type of tool uses magnetic confinement of electrons in the plasma. By containing the plasma closer to the cathode, therefore trapping electrons near the surface of the target, higher ionisation rates may be achieved. This results in a higher plasma density.

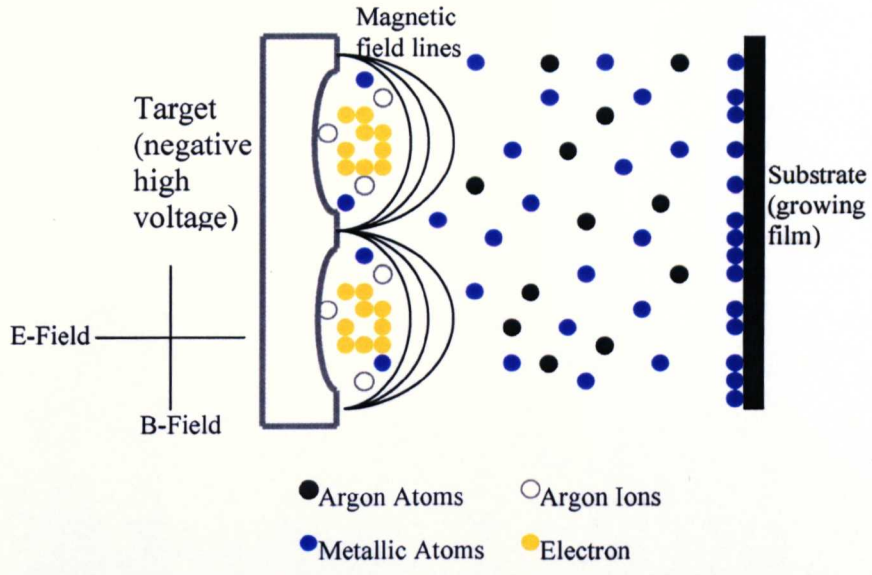

Figure 2.1: Illustration of sputter deposition.

In many magnetron deposition configurations, it is acceptable to physically move the sample during deposition to effectively average out the nonuniform deposition flux and create a uniform film. This leads to the planetary deposition technique [1]. In contrast to static deposition, the substrate is swung and rotated in a planetary motion. The substrate is held on a stage on the robot arm, and the stage is rotated at a rate of 300rpm for the Veeco planetary multitarget cluster that I used to prepare some of my specimens. This rotating stage is swung under the target at a desired rate. The thickness of the film is determined by the rate of swing and the number of times it swings under the target. This technique is able to produce a high quality thin film with extremely good thickness uniformity.

2.1.2: Vibrating Sample Magnetometer (VSM)

A vibrating sample magnetometer operates on Faraday's law of induction, which tells us that a changing magnetic field will produce an electric field. This electric field can be measured and can give information about the changing magnetic field. The output voltage is proportional to the rate of change of B in the coil.

$$V_{pickup} = -N_{pickup}(d\Phi / dt) = -N_{pickup}S(dB / dt)$$

Here, Φ is the magnetic flux density and S is the cross-sectioned area of the pick up coil.

In a VSM, the sample to be measured is placed in the sample holder rod, which is attached to the vibration exciter. The end of the rod hangs down between the pole pieces of an electromagnet, which generate the external applied field. The exciter vibrates the sample at a set frequency, typically 85 Hz for the DMS model VSM.

If the sample is magnetic, the applied magnetic field magnetises the sample. The stronger the applied field, the larger the magnetic moment is. The magnetic dipole moment of the sample creates a magnetic field around the sample, known as the magnetic stray field. As the sample is set to vibrate, this magnetic stray field changes as a function of time, which is sensed by a set of pick-up coils.

The alternating magnetic field causes an electric field in the pick-up coils according to Faraday's law of induction. Therefore, the VSM may be used to measure the basic BH loop.

2.1.3: B-H Looper

The B-H Looper description in this section is specifically for the Looper SHB109. The B-H Looper is a non-destructive magnetic metrology instrument to precisely characterise the magnetic properties of a magnetic film across a whole wafer. There are two principle parts: one part for applying a magnetic field to the magnetic wafer and the other for monitoring the magnetisation of the wafer in the magnetic field.

The first part is composed of two pairs of Helmholz coils generating orthogonal fields in the plane of the specimen. By suitably exciting the pairs of coils a resulting field can be generated in any in-plane direction.

Detection involves a pair of extremely sensitive pickup coils, a normal pickup coil and a transverse pickup coil. The normal pickup coil is more sensitive than the transverse one.

On the Looper SHB109, there are two coil assemblies, one large and one small. The large coil assembly can output a maximum field of 75 Oe and it is used with a pickup capable of measuring up to 6'' wafers. The small coil can output up to 200 Oe plus a DC offset of 20 Oe. The small coils are used for measuring 3'' diameter silicon samples.

The Looper SHB109 may also be used to measure the magnetoresistance value. This is done by first measuring the DC resistance of the material. A fixture containing 4 small probes is lowered onto the surface of the film at the centre of the wafer. These 4 probes are used to make what is known as a 4 terminal measurement of the resistance, which is an extremely accurate method of measuring low impedances. Two of the probes are used to supply an electrical current to the sample. The other two probes are used to measure the voltage across the region of film being measured. As the voltmeter has extremely high internal impedance (typically 500 MΩ) no current is drawn through

it and in this way any error which would normally result from the contact resistance of these probes is eliminated.

Once the DC resistance measurement has been made, a magnetic field is applied. The change in the resistance resulting from the applied field is often expressed as a percentage of the original DC resistance measured with no field applied.

2.1.4: Magnetostriction tester

The magnetostriction coefficient of the thin film in this thesis is measured using the LAFOUDA magnetostriction tester. The magnetostriction tester includes a special acoustic enclosure that protects the delicate measurement from the elevated sound level typically found in clean rooms. Inside the enclosure, the cantilever beam technique is used to achieve a state-of-the-art sensitivity of 10^{-8} of $\frac{dl}{l}$ on films as thin as 50 Angstroms.

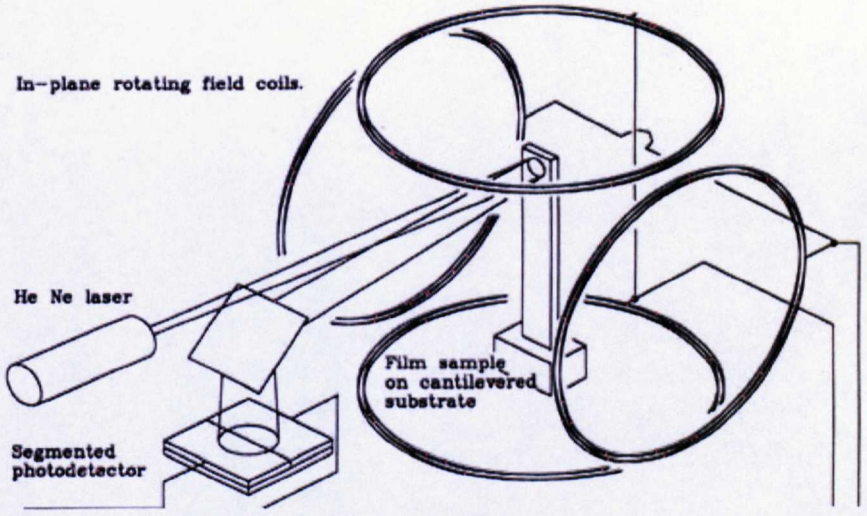

Figure 2.2: Schematic showing a magnetostriction tester.

The test sample size is typically 38mm long by 6mm wide on a 500 μm thick wafer, as shown in figure 2.2. When a magnetic field is applied, the dimensions of the sample will change due to the strain in the sample. This minute change in dimension is detected using a laser reflected from the sample surface. The tester will produce a graph of sample strain (proportional to the magnetostriction) as a function of applied field magnitude, in any range within the 1 to 50 Oe interval. Therefore, the sample magnetostriction coefficient can be deduced only if 50 Oe is sufficient to saturate the sample. This is usually enough for the case of the free layer of the spin-valve films.

Other means of magnetostriction coefficient measurement techniques are reported in [2-4].

2.2: Transmission electron microscopy (TEM)

Since the first commercial TEM was built in 1936, it has been developed into a highly efficient and versatile tool for the characterisation of materials in today's world. It is used extensively throughout my studies on spin-valves for magnetic imaging. Electron microscopy can be used to observe the magnetic domain structure in magnetic specimens. The magnetic contrast arises because of the small deflections that the electrons experience as they pass though the magnetic specimen [5,6].

The resolution of the microscope depends on the wavelength of the electrons. The full relativistic expression for the wavelength λ is

$$\lambda = \frac{hc}{\sqrt{eV(eV + 2m_0c^2)}}$$

where c is the speed of light, V is the acceleration voltage and m_0 is the rest mass of the electron. It is possible to accelerate the electrons, from a few eV to MeV and to control the beam current. Hence, it is potentially possible to achieve extremely high spatial resolution. In the case of magnetic imaging, a resolution of 2-20nm is feasible. The main limitation on the resolution of the electron microscope are the aberrations in the magnetic lenses.

The instrument used for the work presented here is a Philips CM20 (S)TEM operating at 200 keV that has been modified to permit imaging of magnetic materials. The general layout of this TEM is shown in figure 2.3a.

2.2.1: Electron source

The electron source can be a piece of tungsten, usually a wire bent into a hairpin, that acts as the cathode. The filament is heated by the passage of a current to about 2500-3000 K while being held at a high negative potential with respect to the anode and the rest of the microscope. Electrons thermionically emitted from the filament are accelerated rapidly towards the anode and a beam of high energy electrons are emitted through a circular aperture at its centre into the microscope column.

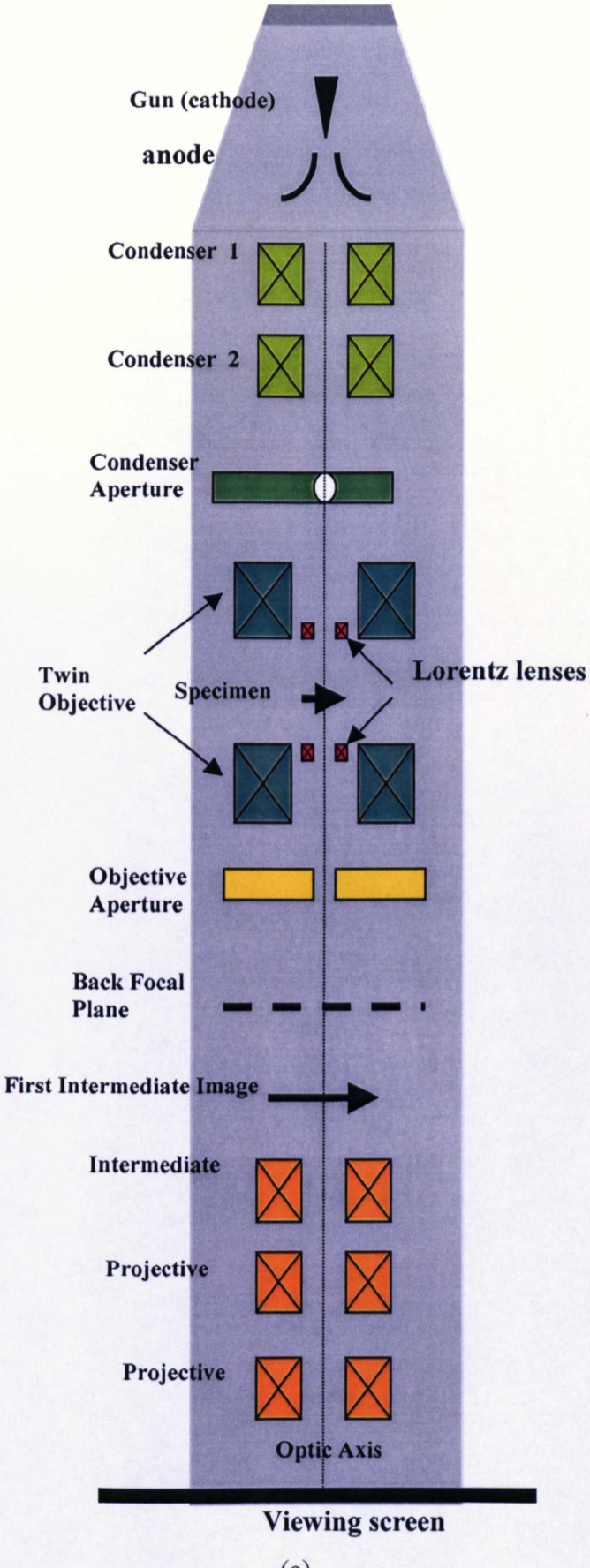

(a)

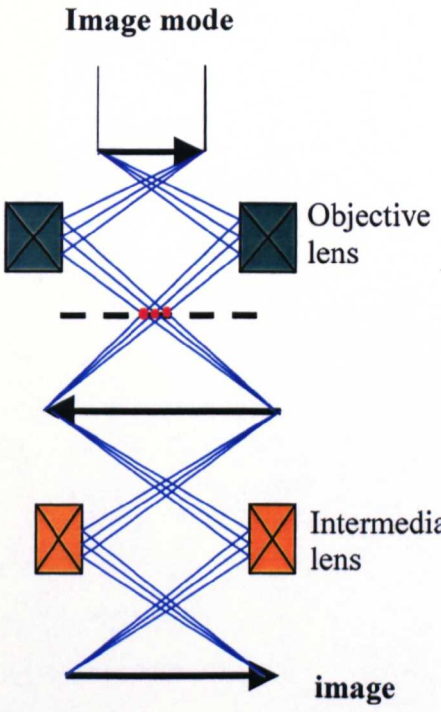

(b)

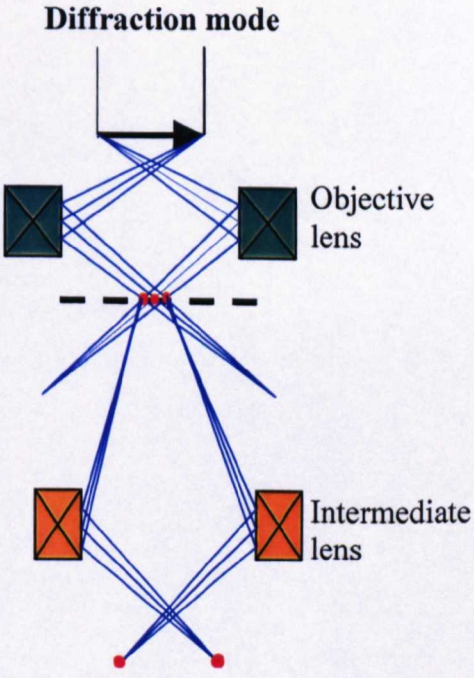

(c)

Figure 2.3: (a) The general layout of the modified TEM column with the Lorentz lens located just above and below the objective lens, (b) Imaging mode, and (c) Diffraction mode.

The brightness is a measure of how many electrons per second per unit solid angle can be directed at a given area of the specimen. For a thermionic gun, the brightness B is given by

$$B = 2\times10^5 TV\exp(-\frac{\phi}{kT}) \qquad \mathrm{Am^{-2}Sr^{-1}}$$

where T is the temperature of the filament in Kelvin and ϕ is the thermionic work function of the filament material in eV. It is best to use a material with high melting point and low work function. For instance, the melting point of tungsten is 3653 K and its work function is 3.0 eV.

The brightness can be improved by using a field emission gun. When a metal surface is subjected to an extremely high electric field ($>10^9$ $\mathrm{Vm^{-1}}$), electrons can leave the surface, without requiring to overcome the metal work function, by the quantum tunnelling effect. As a consequence, the brightness can be increased by a factor of a thousand or more. The field emission current density is expressed by the Fowler-Nordheim equation [7],

$$j = 6.2\times10^{-6}\frac{(\frac{E_f}{\phi})^{1/2}F^2}{(E_f+\phi)}\exp(\frac{-6.8\times10^9\phi^{3/2}}{F}) \qquad \mathrm{Am^{-2}}$$

where E_f is the Fermi energy and F is the applied electric field. For the case of tungsten E_f = 5 eV. The Fowler-Nordheim equation shows that the field emission current depends on the work function and on E_f. Both quantities vary during the operation of the gun. The work function changes due to diffusion of impurities from within the filament material or to surface interactions or the absorption of gases. Therefore, an ultrahigh vacuum of $\leq 5\times10^{-8}$ Pa must be achieved and maintained in the field-emission system.

2.2.2: Detectors: Slow scan CCD camera

A CCD camera is mounted on the 35mm port above the microscope viewing chamber. The conversion of an electron image into a light image is done by using a thin scintillator. The light image is then transferred to the surface of the CCD by a fiber optic plate. The CCD consists of an array of light-sensitive elements (pixels) which detect and store the light produced by the electron beam at each point on the scintillator. An image is exposed by turning the beam on and off for a specified amount of time. After exposure, control electronics supervise the readout of the image data and its digitisation and transfer to a computer for immediate processing and analysis.

2.2.3: Magnetic lenses

The beam of electrons in the microscope column is focused by the magnetic fields from a series of electromagnetic lenses. A magnetic lens consists of a cylindrical wire winding surrounded by a magnetic yoke, shown in figure 2.4. In the centre of the lens is a pole piece. This pole piece is responsible for shaping the magnetic flux generated by the current in the winding into a correct form in the lens gap. Most lenses in the microscope are weak lenses with large gaps. These lenses either act to demagnify the electron beam onto the specimen, or to magnify the image or the diffraction pattern and project it onto the viewing screen. The general imaging system of a TEM consists of at least three types of lenses: condenser lens, objective lens and the intermediate lens. The Lorentz force experienced by a moving electron with velocity v in a magnetic strength B, can be expressed as

$$\boldsymbol{F} = e(\boldsymbol{B} \times \boldsymbol{v})$$

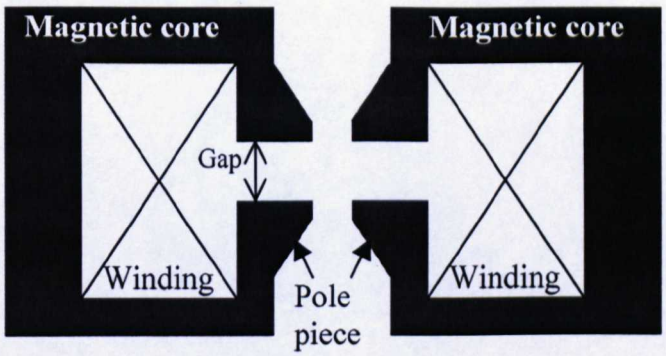

Figure 2.4: Electromagnetic lens in the TEM.

Condenser lenses

The functions of the condenser lenses are to demagnify the beam emitted by the electron gun (spot size) and to control the beam diameter and convergence angle as the beam hits the specimen. Below the condenser lenses is a series of apertures ranging from 200 μm to 20 μm diameter, called the condenser apertures. A smaller aperture produces an electron beam with a higher coherence and smaller convergence angle.

Objective and intermediate lenses

The objective lens is the strongest lens. The role of the objective lens is to form the first intermediate image and diffraction pattern. It is also the main imaging lens and thus it determines the resolution and performance of the microscope. The image produced by the objective usually has a magnification of 50-100 times. The image is

further magnified by a series of intermediate and projector lenses. Each lens provides a magnification of up to 20 times.

The first intermediate lens has two settings, image mode and diffraction mode, shown in figures 2.3b and c. In the image mode, the intermediate lens is focused on the image plane of the objective. In the diffraction mode, the intermediate lens is focused on the back focal plane of the objective lens and the diffraction pattern is projected onto the viewing screen. The magnification of the diffraction pattern is described by the camera length of the system.

In a conventional TEM, the specimen is immersed in the high magnetic field (0.5-1.0 T) of the objective lens. Therefore, the magnetic structures of the specimen are severely distorted or damaged. To overcome this problem, the Philips CM20 electron microscope is fitted with a pair of minicondenser lenses also known as the Lorentz lenses situated above and below the specimen [8]. The role of the minicondenser lenses are to replace the main objective lens as the imaging lens. Hence, this enables the specimen to be imaged in a nearly field free space. However, the resolution using the Lorentz lens is not as high as the objective lens. During magnetic imaging in this condition, the objective lens can either remain switched off or be weakly excited at the control of the operator. This allows controllable amounts of magnetic field to be induced in the plane of the magnetic sample by simply tilting the specimen rod. Therefore, magnetisation experiments become possible in-situ [9,10]. The range of field that can be applied is limited to 6300 Oe, which is the maximum field that can be applied by the objective lenses. A resolution of down to 2 nm may be achieved in field free magnetic imaging.

2.3: Imaging modes

A series of interchangeable objective apertures varying in size from 50 μm to 200 μm are placed close to the back focal plane of the objective lens. These apertures play an important role when imaging structural contrast. When the aperture is centred about the optical axis, this is known as bright field imaging. The contrast in bright field imaging is produced by differences in the intensities of electrons scattered coherently from various part of the specimen. If the aperture is displaced to intercept the desired beam, it can be used to select a particular diffracted beam. This imaging mode is known as dark field imaging.

2.4: Magnetic imaging

Magnetic imaging in the TEM is also known as Lorentz microscopy since the image contrast is generated as a result of the deflection experienced by electrons as they pass through the magnetic specimen. The deflection angle in the x-direction due to the interaction between the incident electron beam along z-axis and the magnetic induction in the film along y-axis is called the Lorentz angle β_L, shown in figure 2.5. This is given by

$$\beta_L(x) = \frac{e\lambda}{h}\int_{-\infty}^{\infty} B_y(x,z)dz$$

where $B_y(x,z)$ is the y-component of the magnetic induction at the point (x,z) and λ is the electron wavelength, h is Planck's constant and e is the electronic charge. For a uniform film with in-plane magnetisation and of thickness t,

$$\beta_L = \frac{eB_o\lambda t}{h}$$

where B_o is the saturation induction ($B_o = \mu_o M_s$).

β_L seldom exceeds 100 μrad and can be less than 1μrad in the case of some magnetic multilayers or films with low values of saturation magnetisation.

The deflection of the electron beam by the transverse magnetic induction in the specimen can also be expressed in terms of the phase shift caused by the magnetic vector potential φ_m. The phase shift between two points x_1, x_2 along the x-axis is given by

$$\Delta\varphi(x) = \frac{2\pi et}{h}\int_{x_1}^{x_2} B_y(x)dx$$

2.4.1: Fresnel mode

In the Fresnel mode, the intensity distribution of electrons at a distance Δz below or above the specimen is imaged by under or overfocusing of the imaging lens [11]. For illustration, figure 2.5, consider a magnetic specimen comprising three domains separated by two 180° domain walls. The electron trajectories either converge or diverge at a distance Δz below the specimen. Therefore, domain walls appear as bright and dark bands. For micropolycrystalline specimens magnetisation ripple is frequently seen in the domains themselves [12]. Such ripple is a consequence of a modest degree of dispersion in the film, arising from the different preferred magnetisation orientation of individual crystallites. As the ripple direction is known to be orthogonal to the mean

direction of magnetisation within a domain the latter quantity can be identified with ease.

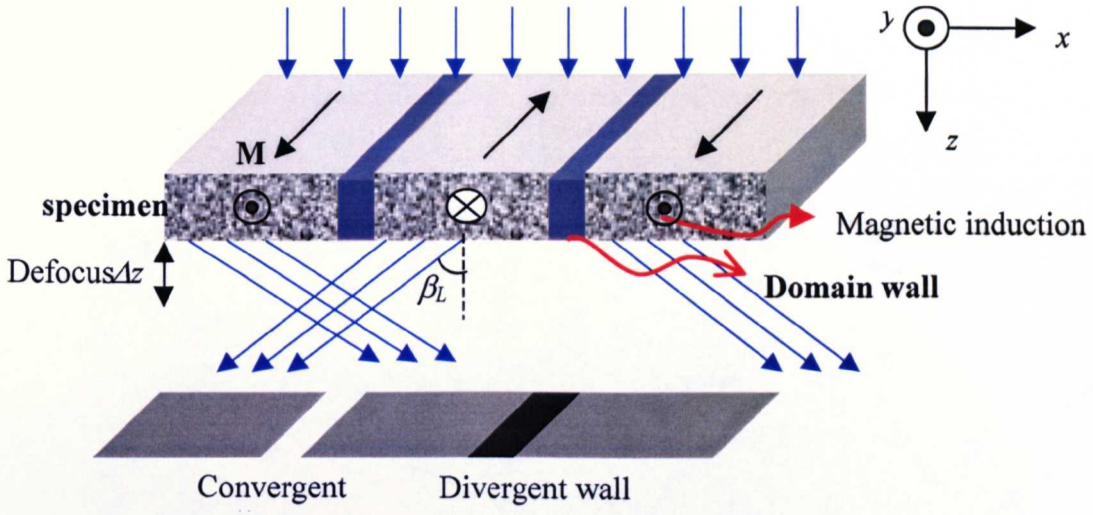

Figure 2.5: Deflection of electrons reveal magnetic domain walls as bright (convergent) and dark (divergent) bands in Fresnel imaging.

Fresnel imaging can be implemented readily and good contrast magnetic images can be generated fairly quickly. However, the fact that the image is defocused results in poor resolution. Hence, it is more suitable for imaging continuous magnetic films.

2.4.2: Low angle diffraction

In low angle diffraction, the diffraction pattern is recorded with large camera length. Camera length is defined as the ratio of the displacement of the beam in the observation plane to the deflection angle itself. The magnification of the intermediate and projector lenses of the microscope must be sufficient to render the small Lorentz deflection visible. For the case of the three domains example, the primary beam splits into two spots with an angular separation $2\beta_L$. The intensity of the individual spots is indicative of the relative fraction of the illuminated area of sample with given magnetisation orientation. In a polycrystalline film with no preferred direction of magnetisation, the splitting of the primary beam results in a circular diffraction pattern.

2.4.3: Differential Phase Contrast

Differential phase contrast (DPC) imaging is a type of scanning transmission electron microscopy (STEM) [13,14]. A general review on DPC imaging is given by Chapman in [15]. In DPC, magnetic information is obtained by scanning the electron probe in a regular raster fashion across the specimen. The signal from the deflected

probe is picked up by a segmented detector sited in the far field, figure 2.6. Due to the Lorentz deflections, the probe is not centred on the detector but deflected by the angle β_L. This causes different signal intensities to fall on the four segments of a quadrant detector. Direct comparison of signals from opposite segments of the quadrant detector provides a direct measure of the two components of β_L. Hence the magnetic structure of the magnetic film can be deduced. The Lorentz deflection angle β_L is proportional to the in-plane component of the magnetic induction integrated along the electron trajectory.

The resolution of DPC imaging is approximately equal to the electron probe size. In turn, the probe size is determined by the spot size selected on the microscope and the size of the condenser aperture. In the Philips CM20 electron microscope with FEG, a probe size of <10nm can be achieved with the specimen located in the field free space.

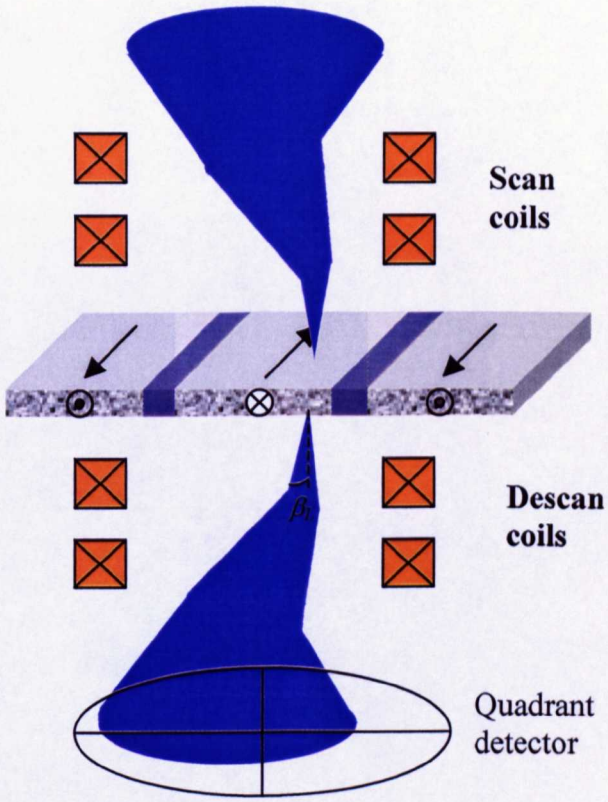

Figure 2.6: Principle of DPC imaging.

2.5: Magnetic force microscopy

Magnetic force microscopy (MFM) is a type of scanning probe microscopy (SPM). The basic setup of the microscope is shown in figure 2.7.

The most fundamental component of the SPM is the scanner. The scanner scans the probe over a sample in a raster pattern. The precision of scanning is controlled by a

piezoelectric tube, which is able to provide sub-angstrom movement increments. The second most important component is the probe or tip. The tips are secured on the end of cantilevers. The cantilevers have spring constants which are less than interatomic bond strengths (about 1 N/m) and allow topographical imaging of surface atomic structure. Interactions between the tip and sample deflect the cantilever. This deflection is monitored by reflecting a laser beam off the cantilever into a segmented photodiode detector. It has a resolution of approximately 20nm for magnetic imaging. An image is formed by mapping this laser-detected deflection while scanning.

To obtain magnetic information from a magnetic sample, the tip used in MFM is coated with a magnetised material (CoCr or NiFe) [16,17]. MFM scanning usually consists of two passes over the sample. The first pass is a standard atomic force microscopy trace that maps out the surface topography by gently tapping along the surface (tapping mode). A second pass then samples the magnetic stray field by scanning at constant height (lift scan height) typically 50-100 nm above the surface. At this distance, the short range Van der Waals and electrostatic forces are negligible. The cantilever responds to the magnetic force gradient acting on the magnetised tip [18].

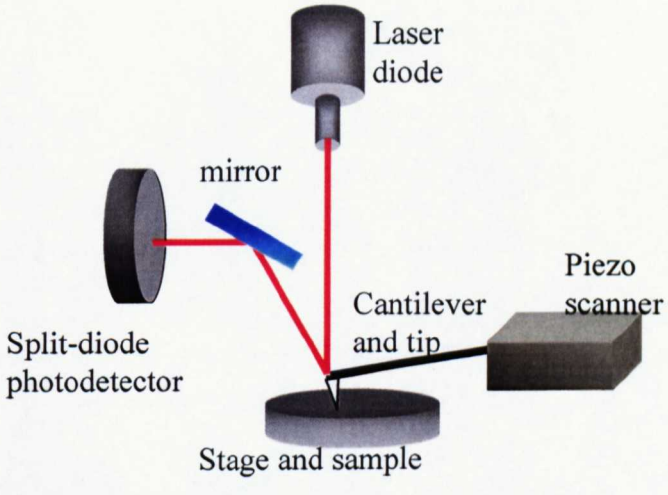

Figure 2.7: A magnetic force microscope setup.

2.5.1: Magnetic forces on the tip

A magnetised tip brought into the stray field of a magnetic sample will have the magnetic potential energy E [19, 20],

$$E = -\mu_o \int \boldsymbol{M}_{tip} \cdot \boldsymbol{H}_{sample} dV_{tip}$$

where M_{tip} is the magnetisation of the tip and H_{sample} is the magnetic field from the sample. And the equation is integrated over the whole volume of the tip. Therefore, the force acting on the MFM tip can be calculated,

$$\boldsymbol{F} = -\nabla E = \mu_o \int \nabla(\boldsymbol{M}_{tip} \cdot \boldsymbol{H}_{sample}) dV_{tip}$$

During the scanning, the cantilever is oscillated at or close to its resonant frequency. Therefore, it is reasonable to treat the cantilever as a harmonic oscillator having resonant frequency f, given by

$$f = \frac{1}{2\pi}\sqrt{\frac{C_{eff}}{m}} \quad \text{(Hz)}$$

where m is the effective mass of the tip and cantilever and C_{eff} is the effective cantilever constant which in turn consist of two components,

$$C_{eff} = C - \frac{\partial F}{\partial z} \quad \text{(N/m)}$$

where C is the cantilever constant. In the close proximity of the sample the force acting on the magnetic tip changes when the distance between the tip and sample is changed, described as the force derivative $\partial F/\partial z$. The force derivative on the tip acts on the cantilever just like an additional cantilever constant and hence

$$f = \frac{1}{2\pi}\sqrt{\frac{C - \partial F/\partial z}{m}} \quad \text{(Hz)}$$

Therefore, the force derivative from the stray field of a magnetic sample changes the cantilever resonant frequency to

$$f = f_o\sqrt{1 - \frac{\partial F/\partial z}{C}} \quad \text{(Hz)}$$

where f_o is the free resonant frequency of the cantilever in the case of no tip sample interaction. When the resonant frequency changes, this results in a change in cantilever oscillation amplitude which is detected by the tip motion sensor. The shift in resonant frequency tends to be very small, typically in the range 1-50 Hz for a cantilever having a resonant frequency $f_o \sim 100$ kHz.

2.6: Electron beam lithography

Electron beam lithography is a very powerful method for defining very small structures [21] where dimensions are an order of magnitude smaller than those achievable with photolithography. All the electron beam lithography work in this thesis was done using a Leica-Cambridge EBPG 5 HR 100. This e-beam writer can be run at

20, 50 and 100 kV and is capable of writing high resolution patterns with feature sizes as small as 20nm over areas as large as 5x5 inches [22]. The machine is situated in a class 10 clean room.

The electron beam writer is almost identical to an electron microscope where the electrons emerging from the heated tungsten filament are directed and focused into a spot at the bottom of the column by a series of magnetic lenses. The sample sits on a motor-driven stage at the bottom of the column under computer control. The electron beam spot is scanned over an area of the sample by a computer-controlled system. The scanning pattern is pre-designed by computer software. A complete lithographic process includes spin-coating resists and baking, e-beam exposure, post-exposure development, metallisation, lift-off or etching, to be discussed in the next few sections.

2.6.1: Electron-solid interactions

Although the electron beam writer is capable of forming extremely fine probes, things become more complex when the electrons hit the substrate. As the electrons penetrate the resist, they experience small angle scattering events (forward scattering), which tend to broaden the initial beam diameter. As the electrons penetrate through the resist into the substrate, they occasionally undergo large angle scattering events (backscattering).

Forward scattering results in a slightly broader beam profile at the bottom of the resist than at the top. The increase in effective beam diameter in nanometers due to forward scattering is given by

$$d_f = 0.9(\frac{R_t}{V_b})^{1.5} \text{ (nm)}$$

where R_t is the resist thickness in nanometers and V_b is the beam voltage in kV. Therefore, to minimise forward scattering when patterning very fine structures, it is important to use the thinnest possible resist and the highest available accelerating voltage of the beam writer, figure 2.8e-f.

2.6.2: Resist coating, e-beam exposure and developing

In order for the designed pattern to be written on the sample by the electron beam, a recording medium responsive to the electron beam, known as resist is coated on the sample prior to exposure. The coating is done using a spin coater. There are two categories of resist, positive and negative. Depending on the type of resist, electrons interacting with it will either break its constituent long-chain molecules leaving

fragments of lower molecular weight (positive resist) or induce cross-linking between them (negative resist) [23]. In positive resist, post exposure developing in a suitable solvent removes the "broken" molecules and the pattern left in the developed resist is the pattern exposed to the e-beam, shown in figure 2.8a-b. Polymethyl methacrylate (PMMA) was one of the first materials developed for e-beam lithography. It is a standard positive e-beam resist and remains as one of the highest resolution resists available [24].

The ultimate resolution of the e-beam writer with PMMA is limited by the degree to which primary and secondary electrons are scattered in the resist. Post exposure developing of PMMA is done by using a developer called methyl-isobutyl ketone (MIBK). MIBK alone is too strong a developer and removes some of the unexposed resist. Therefore, the developer is diluted by mixing in a weaker developer such as isopropyl alcohol (IPA). A mixture of 1 part MIBK to 3 parts IPA produces very high contrast but very low sensitivity. By making the developer stronger, 1:1 MIBK:IPA, the sensitivity is improved significantly with only a small loss of contrast. In the case of negative resist, post exposure developing will remove the unexposed regions.

Resists are coated on the sample using a spin-coater. The thickness of the resist depends on the spin speed and the viscosity of the resist solution. In turn, the viscosity depends on the amount of resist dissolved in an appropriate solvent. For the case of PMMA, the solvent is either chlorobenzene (for thicker layers) or o-xylene (for thinner layers). After spinning, the resist is baked in an oven for a certain period of time at a particular temperature to induce intermolecular cross-linking in the resist. The usual baking time for PMMA is 30-60 minutes at a temperature of 180°C.

2.6.3: Metallisation and lift-off

Properly exposed resist has an overhang profile as shown in figure 2.8b. An overhang is very important for a successful lift-off process by providing a clean separation of the metal, figure 2.8c. Thicker resist has a better overhang profile than the thinner resists. However, an overhang can be created for thinner resist by using a bilayer resist system. The sensitivity of the resist is defined as the point at which all of the resist film is removed. Ideally, the film thickness would drop abruptly to zero at the critical dose. In practice, the thickness drops with a finite slope. If D_1 is the largest dose at which no film is lost and D_2 is the dose at which all of the film is lost, the sensitivity of the resist is defined as

$$\log(\frac{D_2}{D_1})^{-1}$$

A higher molecular weight resist will give smaller line widths for a given dosage as compared to lower molecular weight resists. Hence, by coating a higher molecular weight resist on top of a lower molecular weight resist, the overhang profile can be produced. Metallisation can be carried out after resist developing followed by lift-off. When metal is evaporated onto the sample from directly below, it deposits on the sample surface and on the resist surface. The PMMA resist can be dissolved away by acetone. The metal that was previously on the resist is "lifted-off" and only the pattern on the sample remains, figure 2.8d.

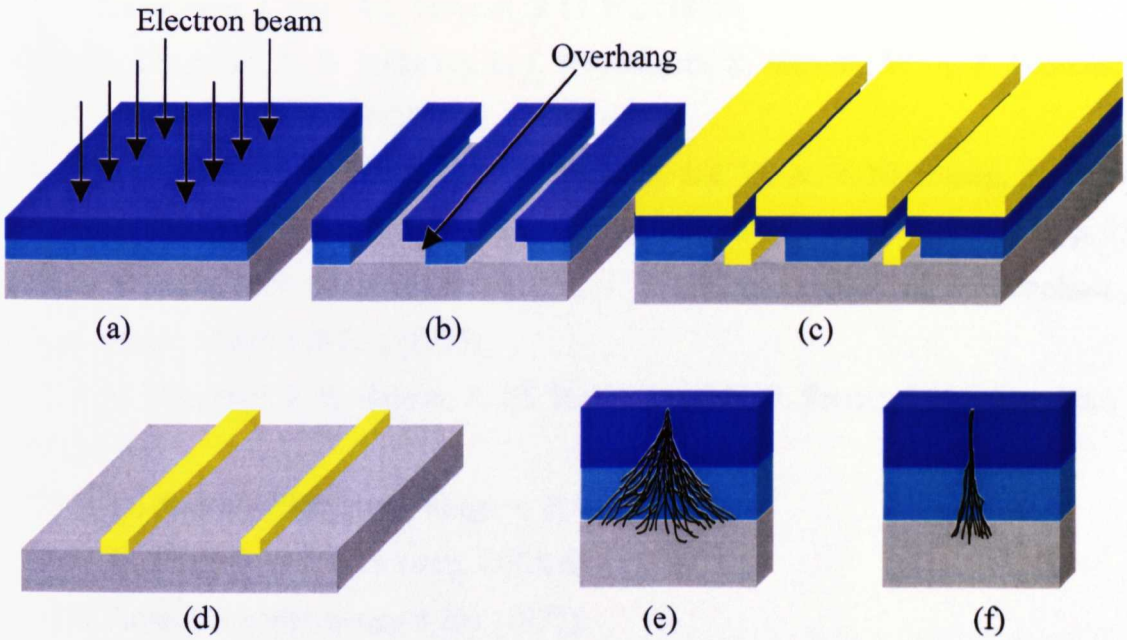

Figure 2.8: (a) Bilayer positive resist system with higher molecular weight top layer and lower molecular weight bottom layer, (b) Overhang profile created by the bilayer resist, (c) metallisation, (d) after lift-off; electron forward scattering profile in resist for (e) low accelerating voltage and (f) high accelerating voltage.

2.6.4: Etching

Etching is a method used to remove surface layers of the sample. There are two basic methods of etching, wet and dry etching. Wet etching involves removal of material via a chain reaction in a chemical solution. In dry etching, the sample is bombarded by a flux of ions. There is a big difference between the outcome of typical wet and dry etching processes. Since the wet etching process is isotropic, etching occurs in the lateral as well as the vertical direction causing an undercut profile. On the other

hand, dry etching is anisotropic and occurs predominantly vertically. Therefore, a better etch profile can be produced. In both dry and wet etching, a mask is required to protect regions that are to remain unetched. The mask can either be the resist or metal. Fabrication of NiFe thin film elements using the dry etching method was developed and has been reported by Khamsehpour in [25].

References:

[1] Y. Feng, M. Pakala, Y. Huai, G. Anderson, K. Rook and S. Gupta, J. Appl. Phys. **87** 6612 (2000),

[2] X. Jin, C. O. Kim, Y. P. Lee and Y. Zhou, J. Vac. Sci. Technol A: Vacuum, Surfaces and Films, **20** 612 (2002),

[3] T. J. Gafron, S. E. Russek, S. L. Burkett, J. Vac. Sci. Technol A: Vacuum, Surfaces and Films, **19** 1195 (2001),

[4] J. H. Claassen, M. A. Willard and V. G. Harris, Rev. Sci. Instruments. **73** 3265 (2002),

[5] J. N. Chapman, M. R. Scheinfein, J. Magn. Magn. Mater. **200** 729 (1999),

[6] J. N. Chapman and K. J. Kirk, Magnetic Hysteresis in Novel Magnetic Materials **195** (1997),

[7] D. Nicolaescu, J. Vac. Sci. Technol. B **11** 392 (1993),

[8] J. N. Chapman, A. B. Johnston, L. J. Heyderman, S. Mcvitie, W. A. P. Nicholson, IEEE Trans. Magn. **30** 4479 (1994),

[9] J. N. Chapman, L. J. Heyderman, S. McVitie, and W. A. P. Nicholson, Advanced Materials '95, Proc. 2nd NIRIM International Symposium on Advanced Materials, p. 23,

[10] S. McVitie, J. N. Chapman, L. Zhou, L. J. Heyderman and W. A. P. Nicholson, J. Magn. Magn. Mater. **148** 232 (1995),

[11] J. N. Chapman, P. E. Batson, E. M. Woddell and R. P. Ferrier, Ultramicroscopy **3** 203 (1978),

[12] H. Hoffmann, IEEE Trans. Magn. **4** 32 (1968),

[13] N. H. Dekkers and H. de Lang, Optik **41** 452 (1974),

[14] H. Rose, Ultramicroscopy **2** 251 (1977),

[15] J. N. Chapman, J. Phys. D: Appl. Phys. **17** 623 (1984),

[16] H. N. Lin, Y. H. Chiou, B. M. Chen, H. P. D. Shieh, C. R. Chang, J. Appl. Phys. **83** 4997 (1998),

[17] D. L. Bradbury, L. Folks, R. Street, J. Magn. Magn. Mater. **177-181** 980 (1998),

[18] P. Grutter, D. Ruger, H. J. Mamin, G. Castillo, C. J. Lin, I. R. McFadyen, J. Appl. Phys. **69** 5883 (1991),

[19] R. D. Gomez, E. R. Burke, I. D. Mayergoyz, J. Appl. Phys. **78** 6441 (1996),

[20] D. Rugar, H. J. Mamin, P. Guethner, S. E. Lambert, J. E. Stern, I. McFadyen and T. Yogi, J. Appl. Phys. **68** 1169 (1990),

[21] T. Matsuzaka, Y. Soda, Hitachi Review **48** 340 (1999),

[22] R. R. S. Cumming, S. Thomas, S. P. Beaumont and J. M. R. Weaver, Appl. Phys. Lett. **68** 322 (1996),

[23] J. M. Shaw, J. D. Gelorme, N. C. LaBianca, W. E. Conley and S. J. Holmes, IBM Journal of Research and Development **41** (1997),

[24] Y. Hsu, T. E. F. M. Standaert, G. S. Oehrlein, T. S. Kuan, E. Sayre, K. Rose, K. Y. Lee, S. M. Rossnagel, J. Vac. Sci. Technol. B **16** 3344 (1998),

[25] B. Khamsehpour, C. D. W. Wilkinson, J. N. Chapman, Appl. Phys. Lett. **67** 3194 (1995).

CHAPTER 3: STUDIES OF MAGNETISATION REVERSAL BEHAVIOUR IN A RANGE OF SPIN-VALVES

Introduction

In this chapter, experimental results on the free layer reversal of a number of different spin-valve (SV) structures are presented. The magnetostriction coefficient (λ_s) was measured in each case and was found to vary from positive to negative values. The magnetisation reversal process of two top spin-valves (TSV) with a combination of free layers is studied in section 3.1. The magnetisation reversal process was observed using the Fresnel imaging mode. Low angle diffraction (LAD) has also been used to provide a more quantitative description of the level of dispersion present during the reversal. The formation of complex domain structures during a magnetisation cycle is discussed, in particular the formation of asymmetrical domains between outward and return paths during the magnetisation process. The reversal process was also investigated as a function of the applied field orientations. The purpose of the experiments was to understand in detail the reversal mechanisms that can occur in the free layer of spin-valves. This is very important from the point of view of performance and noise characteristics when the spin-valve is used as the magnetic read-back sensor [1-3].

The effect of the exchange bias layer on free layer reversal was investigated by using conventional antiferromagnet (AFM) and synthetic antiferromagnet (SAF) top spin-valves. Both these had a large magnetostriction coefficient, section 3.2. The difference between top and bottom spin-valves films is discussed in section 3.3. In bottom spin-valves, the free layer is grown at the top of the multilayer. Thus, it may have a rougher interface with the spacer layer due to the roughness accumulated from all the layers underneath. This may lead to higher Neel coupling between the pinned and free layer. However, the free layer in the bottom spin-valve is also grown in the part of the multilayer where the grains are much more developed. Thus, it is important to understand the effect that all these factors have on the free layer reversal process. This will help to improve the performance of bottom spin-valves, widely used to replace top spin-valves as the read back sensor in computer hard disk drives. This is due to the higher sensitivity achieved by using bottom spin-valves [4].

A modified Stoner-Wohlfarth model was used to analyse the reversal process observed experimentally [5]. Agreement was found between the model and experiments for cases where coherent rotation was the dominant process. The model fails to show

the cause for the asymmetrical domain wall orientations, which were observed in some of the films. This analysis is presented in section 3.4 and 3.5. Finally, the role of film texture is studied in section 3.6.

All the SV films will be denoted in the form - Free layer, Exchange bias layer (AFM or SAF), Type of SV (TSV or BSV). For instance, NiFe/CoFe AFM TSV represents a NiFe/CoFe combined free layer with a conventional type antiferromagnetic exchange bias layer and it is a top spin-valve. The same naming convention is used throughout this thesis. All films were grown on TEM membranes at Seagate Technology at Londonderry.

3.1: Free layer magnetisation reversal process of NiFe/CoFe AFM TSV and NiFe/Co AFM TSV

Spin-valve films were deposited by DC magnetron sputtering in a vacuum of better than 5 x 10^{-8} Torr. The SV films studied in this section were two top spin-valves (TSVs) with crossed anisotropy, the stack sequence being seed/NiFe25/CoFe16/Cu25/CoFe27/PtMn200/cap. The second TSV has the same stack sequence but the CoFe layers were replaced by Co layers. The number indicates the thickness of each layer in units of Angstroms. The TSV films are referred to as NiFe/CoFe AFM TSV and NiFe/Co AFM TSV. The exact composition of Co_xFe_{1-x} is not known due to industrial confidentiality.

The direction of the offset field in a SV with crossed anisotropy is orthogonal to the uniaxial easy axis. SVs with crossed anisotropy are favourable for sensor applications because they exhibit a high sensitivity combined with a low coercivity compared with parallel anisotropy [5]. The films have a free bilayer structure (NiFe/CoFe or NiFe/Co). The presence of a Co alloy adjacent to the non-magnetic Cu spacer leads to an enhanced GMR (higher spin-dependent scattering), measured to be 12.5% and 13.2% respectively using the conventional four-point probe technique. However, Co has a much higher magnetostriction coefficient than CoFe, measured at $7.5x10^{-6}$ for NiFe/Co and $0.4x10^{-6}$ for NiFe/CoFe. NiFe has a lower coercivity (magnetically softer) and hence requires a lower field to switch than the CoFe or Co layer alone. Hence, in this configuration, the effective free layers are NiFe/CoFe and NiFe/Co composite layers.

For the NiFe/CoFe AFM TSV, in-situ magnetising experiments were carried out for five different values of θ. Please refer to Chapter 1 figure 1.9 for the definition of θ and all the key parameters involved in all the experiments. Extensive Fresnel image

sequences were obtained in each case and, depending on θ, magnetisation reversal was found to proceed by rotation or through domain processes or both. However, for this sample, domain processes were relatively uncommon and most of the images showed only magnetisation ripple of varying strength and orientation. All images were acquired with largest imaging defocus current in order to maximise magnetic contrast. Same imaging condition were used for all the experiments discussed hereafter.

Figure 3.1 shows an instance where domain processes were involved as the magnetisation reversed under decreasing positive field. Positive numbers denote an applied field in the opposite direction to the preferred orientation of the free layer. In a typical cycle the field in the plane of the specimen varied from +25 Oe to -25 Oe and back again. These fields correspond to $+30^{\circ}$ to -30° tilt with objective current set at 50mA. Images shown here illustrate the most important stages of the reversal process. Red arrows denote the mean direction of magnetisation, deduced in all cases from the magnetisation ripple, whilst the number at the top right corner of each image denotes the field magnitude in Oe.

On the outward path in this sequence the magnetisation ripple intensified, figure 3.1b, without significant change of direction, as the field was reduced below a value where the magnetisation lay essentially parallel to H, figure 3.1a. As H was further reduced, low angle walls formed and, whilst the walls themselves were not particularly mobile, the magnetisation within the domains underwent substantial changes in orientation over a small field range, figures 3.1d-f. Reversal was essentially completed for fields <10 Oe except for small area chain domains, which collapsed into 360° walls, figures 3.1f-g. Walls such as these were difficult to eliminate and persisted up to much larger values of field.

Increasing positive field on the return path leads to ripple rotation in the anticlockwise sense. Ripple rotation soon turns into low angle domains upon further increasing field, figure 3.1h. Most of the low angle domains vanish quickly and the magnetisation continues to rotate in the anticlockwise sense. The remaining domain persists and collapses into a 360° wall when the reversal nears completion, figure 3.1j-k.

The outward reversal process closely resembled that reported by Murdoch et al. [7] where the generation of walls is a direct consequence of local areas of film relaxing towards each of the two easy directions of magnetisation as H decreased. The domain walls observed on the return path were not aligned along the uniaxial axis. Therefore, they were not formed as a result of the symmetrical split of rotation in the opposite direction. The possible causes of the domain walls are discussed in section 3.4.

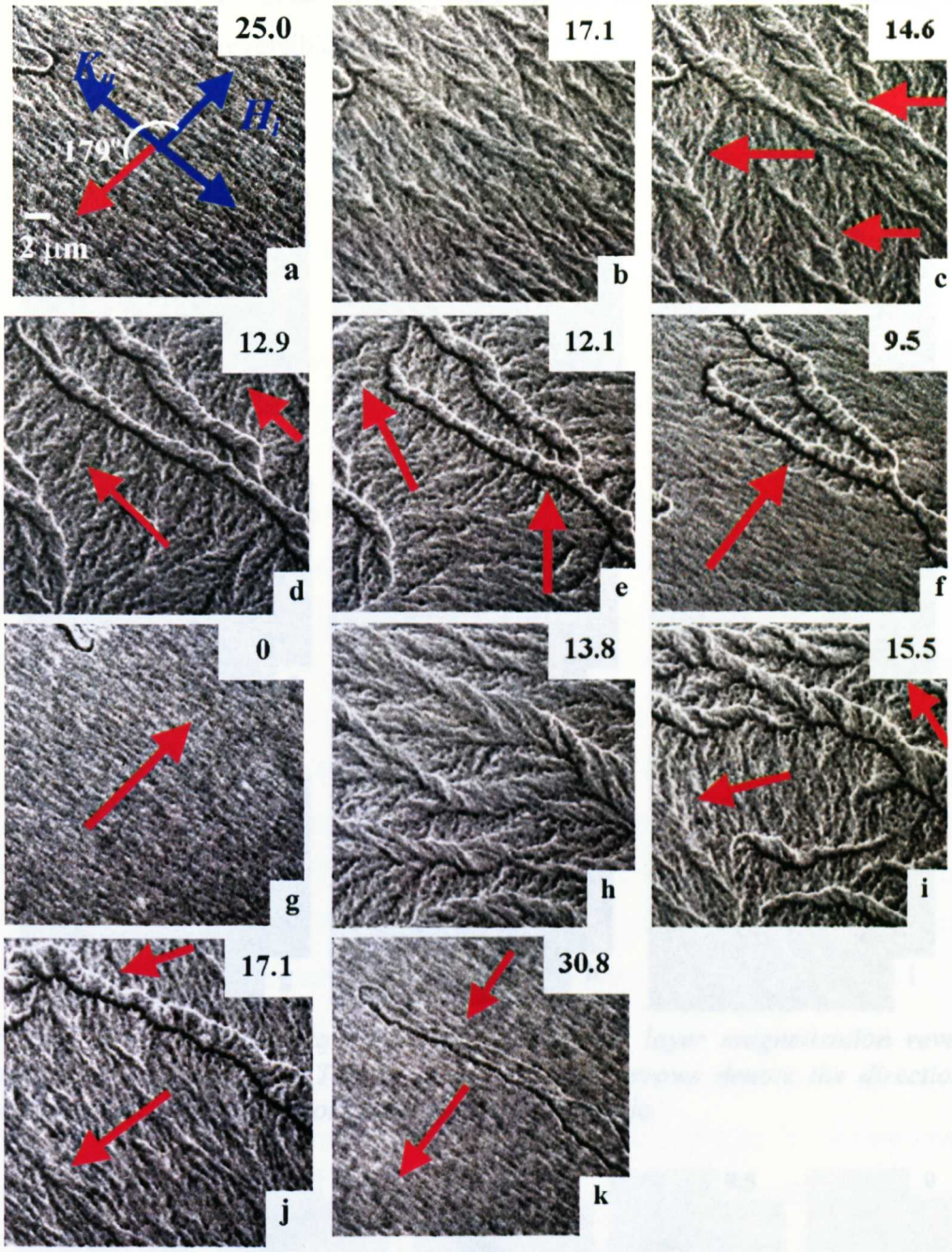

Figure 3.1: Fresnel image sequence showing the free layer magnetisation reversal process for NiFe/CoFe AFM TSV at $\theta = 179^{o}$. Red arrows denote the direction of magnetisation as determined from the magnetisation ripple.

Figure 3.2 shows the Fresnel image sequence when the external field was applied at 170° to the offset field direction. For this applied field orientation, no walls were observed and reversal was predominantly by magnetisation rotation. Magnetisation rotated in the clockwise sense on the outward path, figure 3.2a-f and in the anticlockwise sense on the return path, figure 3.2g-i. Low angle diffraction (LAD) images in figure 3.3 show the rotation of the diffraction spot. In this configuration symmetry was broken where one of the easy directions is always more favourably

oriented so that the magnetisation as a whole simply rotated towards it leading to an altogether simpler and reversible process.

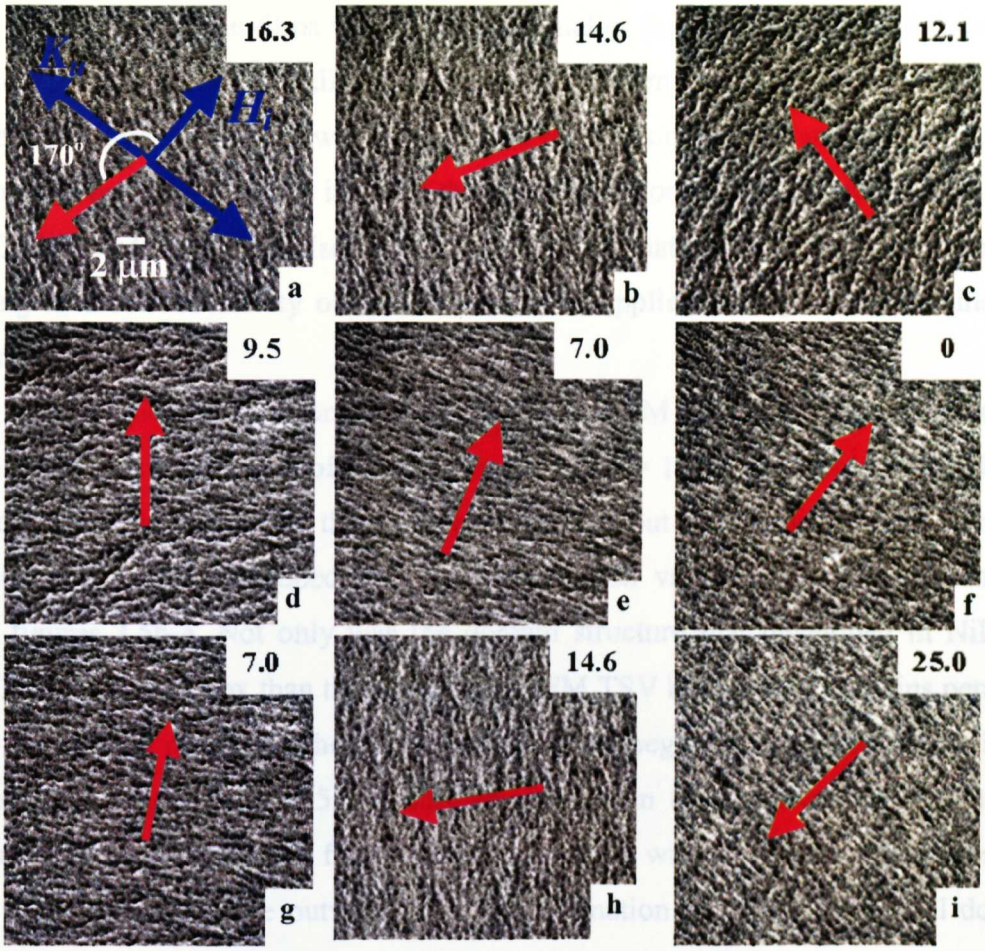

Figure 3.2: Fresnel image sequence showing the free layer magnetisation reversal process for NiFe/CoFe AFM TSV at θ = 170°. Red arrows denote the direction of magnetisation as determined from the magnetisation ripple.

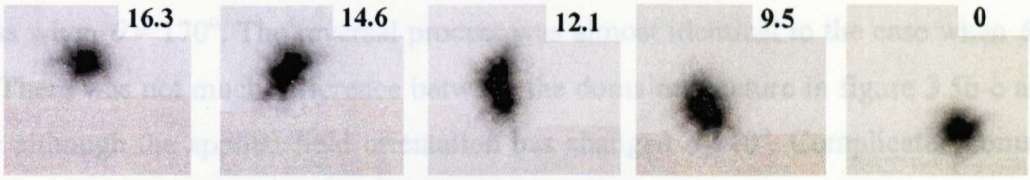

Figure 3.3: Low Angle Diffraction image sequence of NiFe/CoFe AFM TSV at θ = 170° showing the rotation.

Given that, with a few exceptions, simple reversal processes were involved, the net moment of the imaged area could be deduced from each Fresnel image and these plotted to yield *M-H* curves as shown in figure 3.4a. The corresponding *MR* curves, figure 3.4b, were then plotted assuming that $MR \propto \frac{1}{2}(1-\cos\phi)$. Examination of the family of curves shows that the offset field was ≈14 Oe. Furthermore, all the *M-H*

curves were very narrow indicative of low coercivity <1 Oe and a high degree of reversibility. Note that the *M-H* curve for $\theta = 90^{o}$ did not represent a complete 180° rotation because the field applied was not sufficiently strong.

In polycrystalline films with grain size smaller than the domain wall thickness, the effect of the magnetocrystalline anisotropy on the film anisotropy tends to disappear by averaging over grains. However, the local fluctuations of the anisotropy decrease domain wall mobility and thus increase the coercivity. For a (111) textures film such as NiFe/CoFe AFM TSV, the anisotropy is strongly dominated by the induced anisotropy resulting in a low coercivity observed when H is applied orthogonal to the induced anisotropy axis.

The magnetisation reversal for the NiFe/Co AFM TSV was more complicated. Figure 3.5 shows a sequence of Fresnel images for $\theta = 179^{o}$. The ripple intensified as the field was reduced from the positive direction but this time a more complex distribution of walls developed with wall orientation varying over a wider angular range, figures 3.5b-e. Not only was the domain structure that developed in NiFe/Co AFM TSV more complex than the NiFe/CoFe AFM TSV but also the domains persisted over a wider field range. On the return path, reversal began with ripple rotation in the anticlockwise sense, figure 3.5g. A further increase in the positive field resulted in domain formation as shown in figure 3.5h. The domain wall orientation was almost 90° to the walls formed on the outward path. The formation of the asymmetrical domain walls is discussed in section 3.4.

For applied fields at smaller θ the process changed little but with complex domain structures forming even for values as low as 135°. Figure 3.6 shows reversal process when $\theta = 170^{o}$. The reversal process was almost identical to the case when $\theta = 179^{o}$. There was not much difference between the domain structure in figure 3.5b-c and 3.6b-c although the applied field orientation has changed by 10°. Complicated domain formation still occurred over a large field range.

The dispersion in magnetisation is shown in LAD images in figure 3.7, where the diffraction spot in LAD was very diffused. The highly diffused diffraction spot formed an almost complete circle, figure 3.7c-d. This suggests a widely dispersed magnetisation in the free layer. With such complex magnetisation distributions, analysis was impractical and *M-H* loops and the corresponding *MR* behaviour cannot be derived, unlike the case for the NiFe/CoFe AFM TSVs. However, examination of complete image sequences show that the NiFe/Co AFM TSV has a much larger hysteresis than

the NiFe/CoFe AFM TSV. The best estimate of the coercivity and offset field were 8.5 Oe and 6.5 Oe respectively.

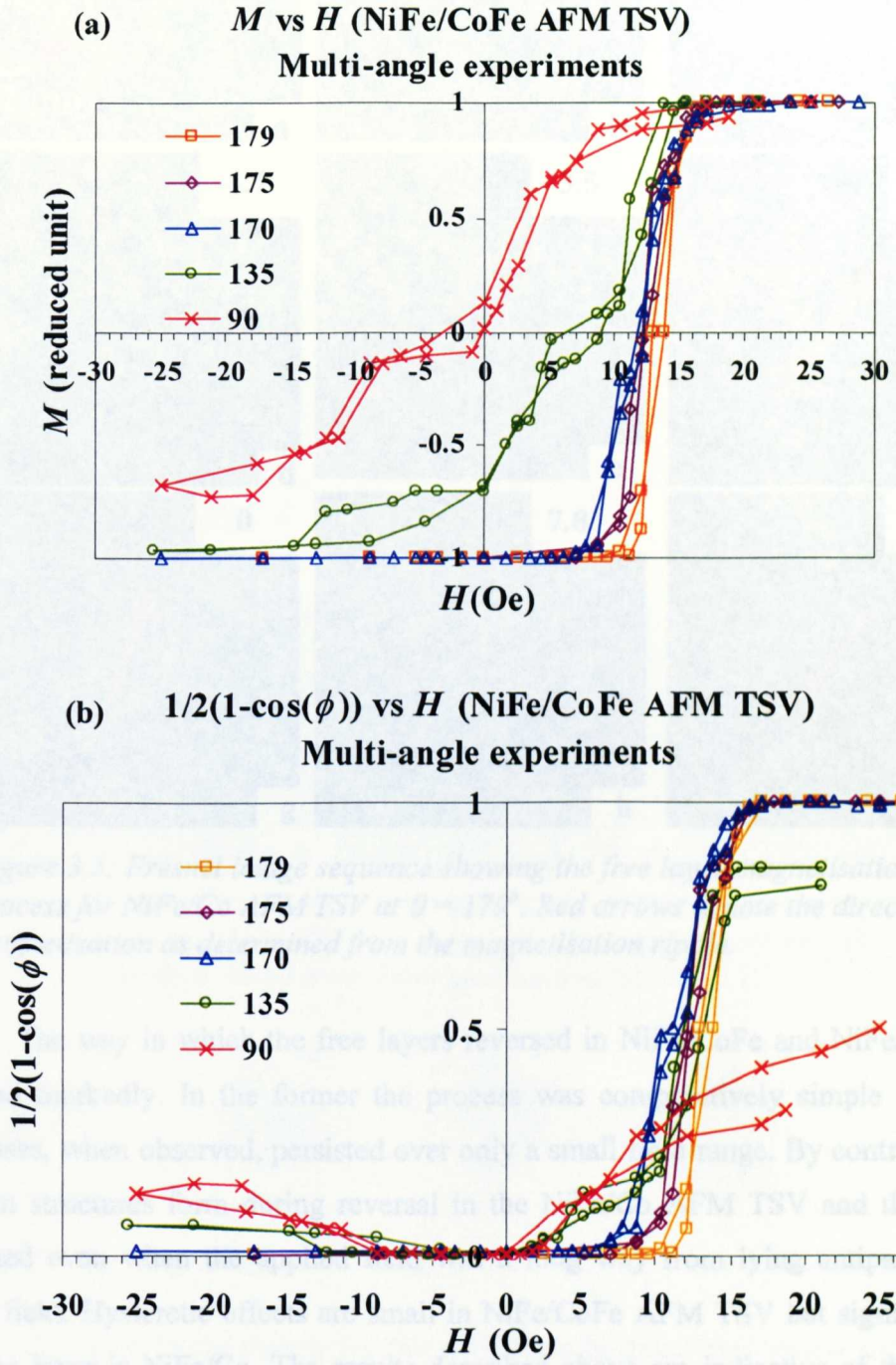

Figure 3.4: (a) M vs H curves for NiFe/CoFe AFM TSV at θ = 179°, 175°, 170°, 135° and 90° and (b) the corresponding MR curves.

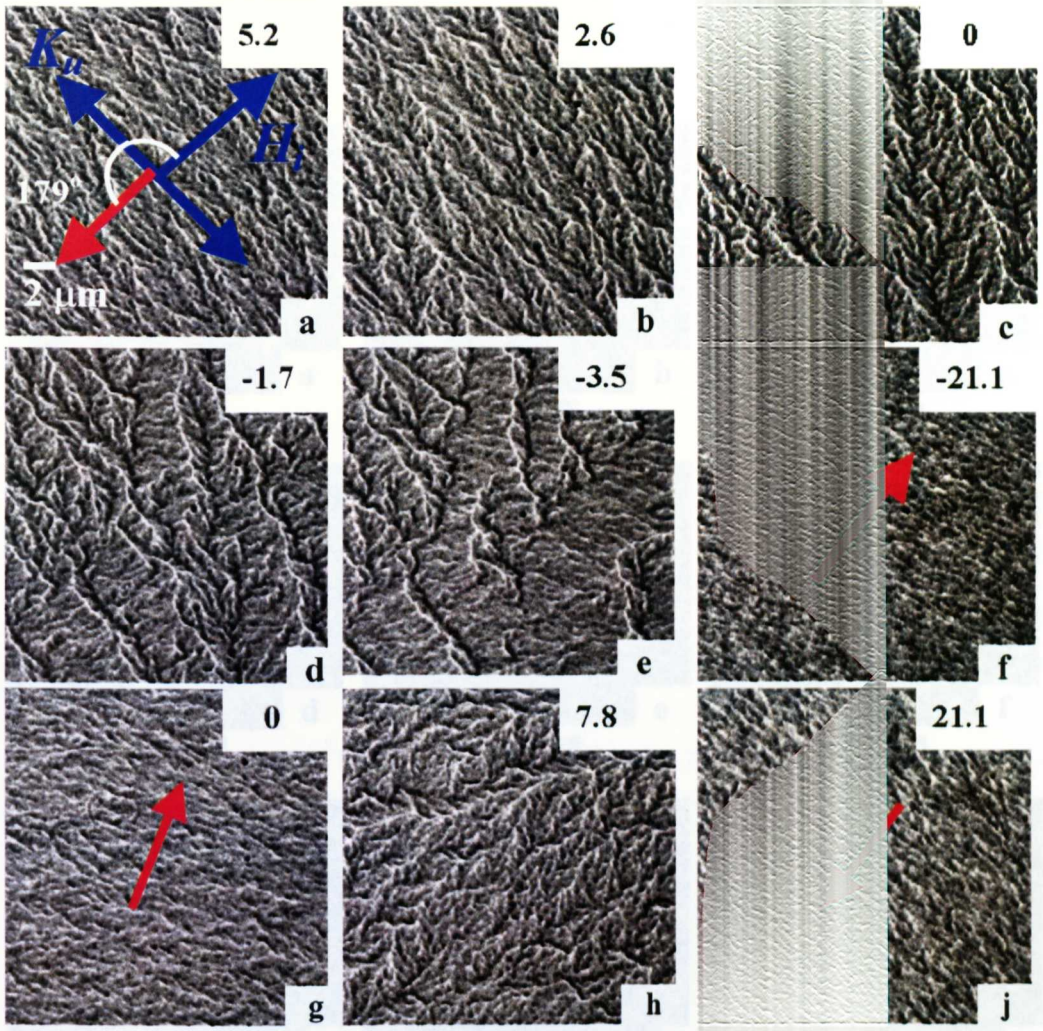

Figure 3.5: Fresnel image sequence showing the free layer magnetisation reversal process for NiFe/Co AFM TSV at $\theta = 179^{o}$. Red arrows denote the direction of magnetisation as determined from the magnetisation ripple.

The way in which the free layers reversed in NiFe/CoFe and NiFe/Co bilayers differed markedly. In the former the process was comparatively simple and domain processes, when observed, persisted over only a small field range. By contrast complex domain structures form during reversal in the NiFe/Co AFM TSV and these usually persisted even when the applied field was a long way from lying antiparallel to the offset field. Hysteretic effects are small in NiFe/CoFe AFM TSV but significant when the free layer is NiFe/Co. The results described above are indicative of there being a well defined preferred direction of magnetisation when the free layer is of NiFe/CoFe AFM TSV and that variations about this mean direction are small leading to reversal by rotation other than in high symmetry orientations. For NiFe/Co AFM TSV, by contrast, the local variations about any mean direction are substantial making the latter an ill-defined quantity. Thus adjacent small areas can behave quite differently leading to the formation of complex tangled domain structures.

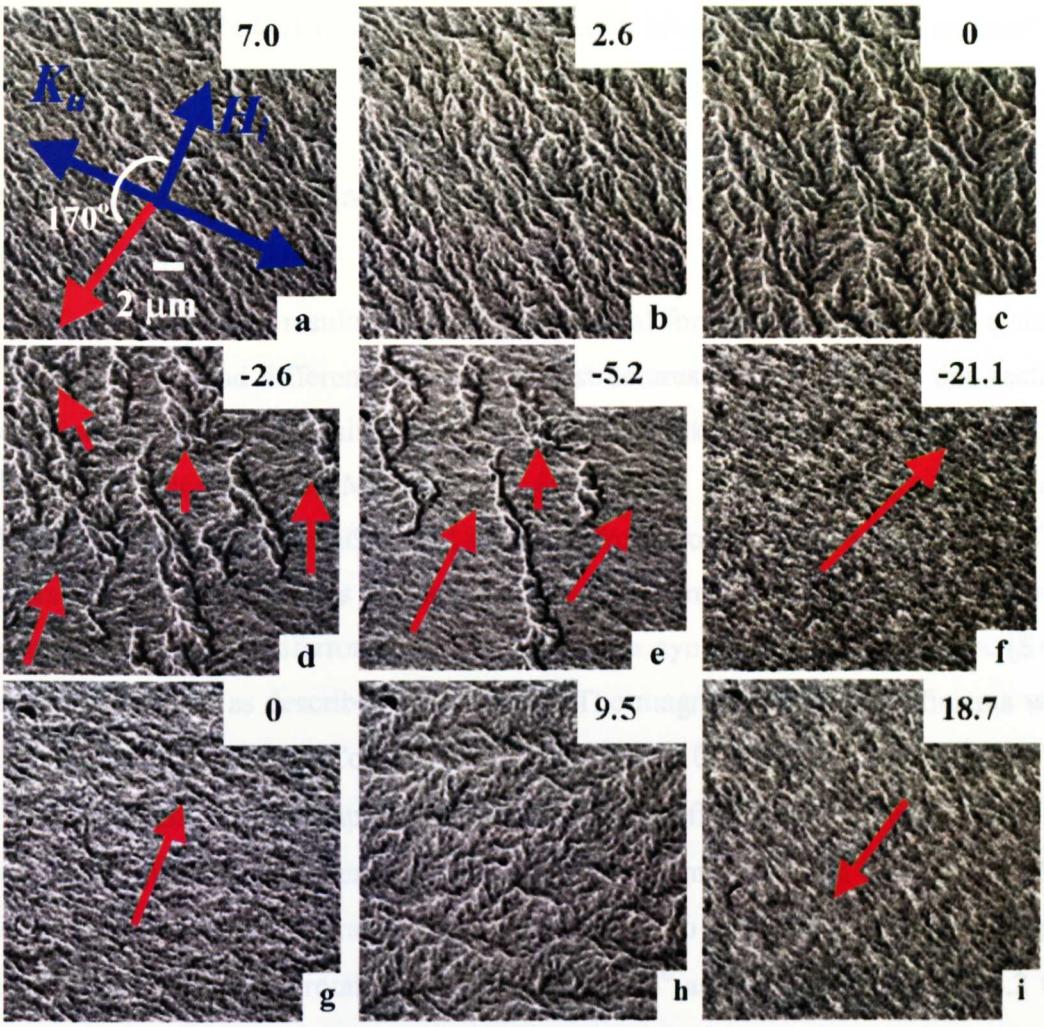

Figure 3.6: Fresnel image sequence showing the free layer magnetisation reversal process for NiFe/Co AFM TSV at $\theta = 170^{o}$. Red arrows denote the direction of magnetisation as determined from the magnetisation ripple.

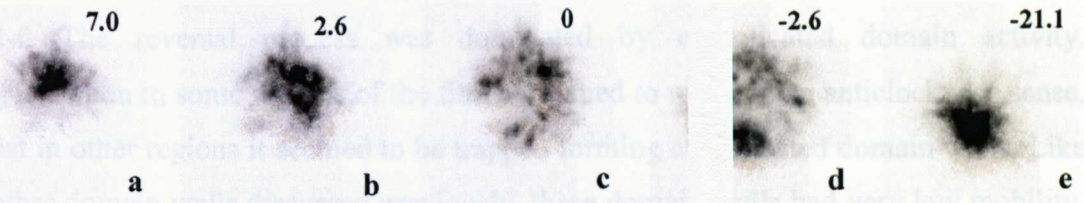

Figure 3.7: Low Angle Diffraction image sequence of NiFe/Co AFM TSV at $\theta = 170^{o}$.

The most likely reason for this difference in behaviour would seem to be the much higher magnetostriction of NiFe/Co AFM TSV compared with NiFe/CoFe AFM TSV, a factor of approximately 20 [8]. The magnetocrystalline anisotropy of Co is also comparatively higher than CoFe. This would lead to significant spatial fluctuations of local anisotropy in what are almost certainly highly stressed films [9]. Stronger local anisotropy fluctuation results in the low wall mobility observed in NiFe/Co AFM TSV and hence higher coercivity. Certainly the irregular and irreversible processes observed

in the NiFe/Co AFM TSV provide a very likely reason for the poorer signal-to-noise ratio obtained when NiFe/Co rather than NiFe/CoFe bilayer is used as the material for the free layer.

3.2: Free layer magnetisation reversal process of CoFe AFM TSV and CoFe SAF TSV

The experimental results on free layer reversal for top spin-valves with a single free layer of CoFe and different exchange bias structures are presented in this section. These were also crossed anisotropy TSVs with stack compositions of the form seed/CoFe30/Cu26/CoFe27/PtMn150/cap for the CoFe AFM TSV and seed/CoFe30/Cu26/CoFe27/Ru9/CoFe18/PtMn150/cap for the CoFe SAF TSV. The numbers indicate the thickness of each layer in Angstroms. The pinning was achieved using a conventional antiferromagnet (AFM) and a synthetic antiferromagnet (SAF) respectively [10,11], as described in chapter 2. The magnetostriction coefficients were measured to be 6.6 x 10^{-6} for CoFe AFM TSV and 7.6 x 10^{-6} for CoFe SAF TSV.

An external field was applied at $\theta = 180^{\circ}$ to the offset field direction. Figure 3.8 shows the Fresnel image sequence for the free layer magnetisation in CoFe AFM TSV. As H was reduced from saturation, the ripples began to intensify as shown in figure 3.8a-b. The magnetisation rotated through about $\approx 45^{\circ}$ as H was reduced to 24.2 Oe, figure 3.8c. The magnetisation at this stage was very dispersed and there were signs of low angle domain wall formation. These soon developed into a more complex domain structure with wall orientation varying over a wide angular range as shown in figure 3.8d-f. The reversal process was dominated by complicated domain activity. Magnetisation in some regions of the film continued to rotate in an anticlockwise sense, whilst in other regions it seemed to be trapped forming complicated domain walls. Like all other domain walls discussed previously, these domain walls had very low mobility, some domains still remained even when $H = 0$ Oe, figure 3.8g. Regions characterised by magnetisation rotation had almost completed the reversal process at this field, as shown in the upper half of figure 3.8g. Some domains collapsed into a 360° wall, figure 3.8h.

Upon increasing field in the positive direction on the return path, no significant ripple rotation was observed for figures 3.8h-i. However, the ripple intensified and developed into domains with walls lying almost along the uniaxial axis, figure 3.8j. The presence of these domains was due to the split magnetisation rotation in opposite directions to each other. Further increases in positive field resulted in the growth in size of the domains with magnetisation rotating in the clockwise sense, figure 3.8k. The

remaining domains collapsed into 360° loops when the reversal neared completion, figure 3.8l.

Figures 3.8m-q show the corresponding LAD images sequence for the outward reversal process. It shows that as the field was decreased in the positive direction, the diffraction spot stretched over a semi-circle, figure 3.8m-q. The dispersed magnetisation rotation was shown by the rotation of the stretched diffraction spot.

The most peculiar behaviour observed in the reversal of CoFe AFM TSV was once again the asymmetrical domain wall orientation between the outward and return path. The domains in this specimen were formed after a rotation of $\approx 45°$ in the outward path. This characteristic was similar to those observed in NiFe/CoFe AFM TSV and NiFe/Co AFM TSV. It was not entirely clear what mechanism has stopped the rotation and triggered the formation of these domains. Further discussion is given in sections 3.4 and 3.5.

The free layer reversal in CoFe SAF TSV was quite similar to CoFe AFM TSV in terms of complex domain formation, as shown in figure 3.9. Low angle domain walls began to form at H = -12.2 Oe, figure 3.9c. The size of the chain-like domain formed was about the same as those observed in CoFe AFM TSV. The domain wall orientation was also rather irregular. These domains eventually collapsed into 360° loops at high positive field. Dispersion during reversal is also shown in figure 3.9j-k as LAD image.

The return path is shown in figure 3.9f-i. Increasing field in the positive direction leads to increased ripple intensity and domain formation, figure 3.9g-h. These domains lie almost along the uniaxial axis. Further increases in field caused the domains to collapse into 360° loops, figure 3.9i.

In both CoFe AFM TSV and CoFe SAF TSV, it was not feasible to deduce the M vs H plot from the images due to the presence of complex domains. The best estimated offset field and coercivity are $\approx$ 20 Oe, $\approx$ 6 Oe for CoFe AFM TSV, and $\approx$ 2 Oe, $\approx$ 14 Oe for the CoFe SAF TSV. The most apparent differences between CoFe AFM TSV and CoFe SAF TSV were the orientation of the domain walls, offset field and coercivity. It seems that replacing the AFM with SAF has a noticeable effect on the offset field and coercivity of the TSV. However, despite of all these differences, the magnetisation reversal process behaviour as a whole is quite similar in term of domain complexity and 360° loops. It was also noticed that domain walls on both the outward and return paths lay almost parallel to the uniaxial axis in CoFe SAF TSV. This is different from the other SV films studied so far for which asymmetrical domain wall orientation between the outward and return paths were often observed.

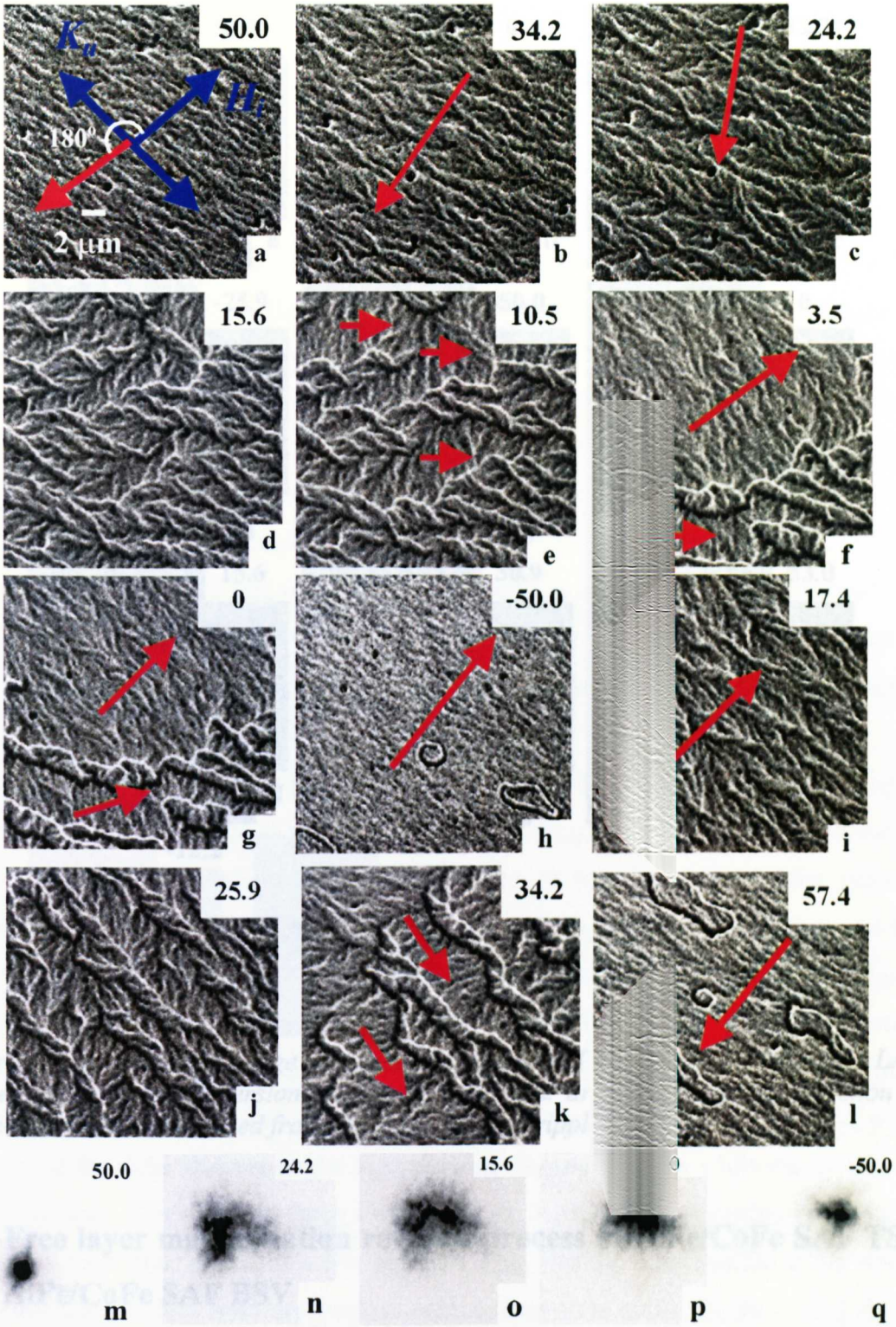

Figure 3.8: (a-l) Fresnel image sequence showing the free layer magnetisation reversal process for CoFe AFM TSV at $\theta = 180^{o}$, (m-q) LAD image sequence for the outward path.

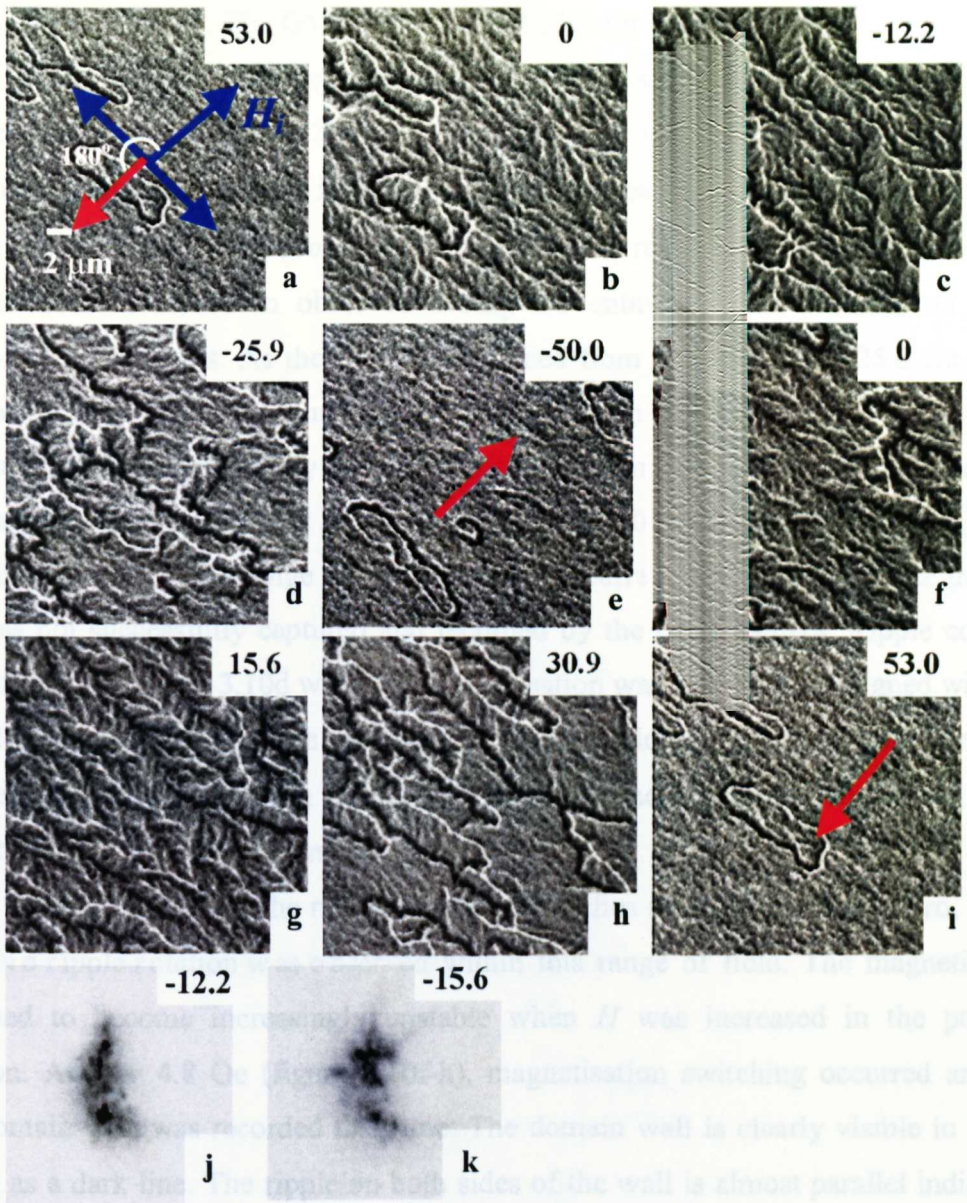

Figure 3.9: (a-i) Fresnel image sequence of CoFe SAF TSV at $\theta = 180^{o}$ and (j-k) LAD images showing the dispersion during reversal. Red arrows denote the direction of magnetisation as determined from the magnetisation ripple.

3.3: Free layer magnetisation reversal process of NiFe/CoFe SAF TSV and NiFe/CoFe SAF BSV

The investigation of free layer reversal was extended to top and bottom spin-valve film with a synthetic antiferromagnetic layer. The stack compositions are seed50/NiFe25/CoFe16/Cu26/CoFe27/Ru9/CoFe18/PtMn150/cap50 for the TSV and seed60/PtMn185/CoFe20/Ru9/CoFe23/Cu23/CoFe13/NiFe25/cap50 for the BSV. The number indicates thickness of each layer in Angstroms. These films will be referred to as NiFe/CoFe SAF TSV and NiFe/CoFe SAF BSV hereafter. Both the NiFe/CoFe SAF

TSV and BSV have a negative magnetostriction coefficient measured at -2.0 x 10^{-6} and -2.3 x 10^{-6} respectively. The GMR ratio is about 13% for both films.

In-situ Fresnel imaging experiments were done and the image sequences recorded are shown in figure 3.10. The external field was applied antiparallel to the offset field direction at θ = 180°. The free layer reversal was remarkably simple compare to all the reversal processes showed in the previous sections. There was no complex domain formation observed during the entire reversal process, on either outward or return paths. As the field was reduced from saturation H = 25.0 Oe to 2.6 Oe, figures 3.10a-b, there was no magnetisation rotation observed. However, the ripple contrast has intensified slightly indicating that the magnetisation has become unstable. The magnetisation switched at H = 0.9 Oe (figure 3.10c) with a rapid sweeping of a 180° domain wall. The change in magnetisation occurred at such a rapid rate that the wall was not successfully captured and recorded by the CCD camera. Ripple contrast had weakened in figure 3.10d when the magnetisation was increasingly aligned with the applied field. Further increase of the applied field along the offset field direction saturated the film. It is worth noting that there was no significant change in ripple orientation throughout the reversal process.

On the return path, the ripple contrast intensifies as H is reduced to zero, figure 3.10e. No ripple rotation was observed within this range of field. The magnetisation continued to become increasingly unstable when H was increased in the positive direction. At H = 4.8 Oe (figure 3.10f-h), magnetisation switching occurred and the 180° domain wall was recorded this time. The domain wall is clearly visible in figure 3.10f-g as a dark line. The ripple on both sides of the wall is almost parallel indicating an antiparallel magnetisation direction separated by a 180° wall. The wall swept across the film at a very high speed. The domain with magnetisation pointing in the same direction as the field (domain on the right ride) rapidly grew in size while the domain on the left shrank. Note that all three images, figure 3.10f-h were recorded at the same field but over a time period of a few seconds. This was the only sample so far where time dependent effects were apparent on such a short time scale. Figure 3.10i-j shows the LAD images during the rapid reversal. A faint trace of switching is visible in figure 3.10j.

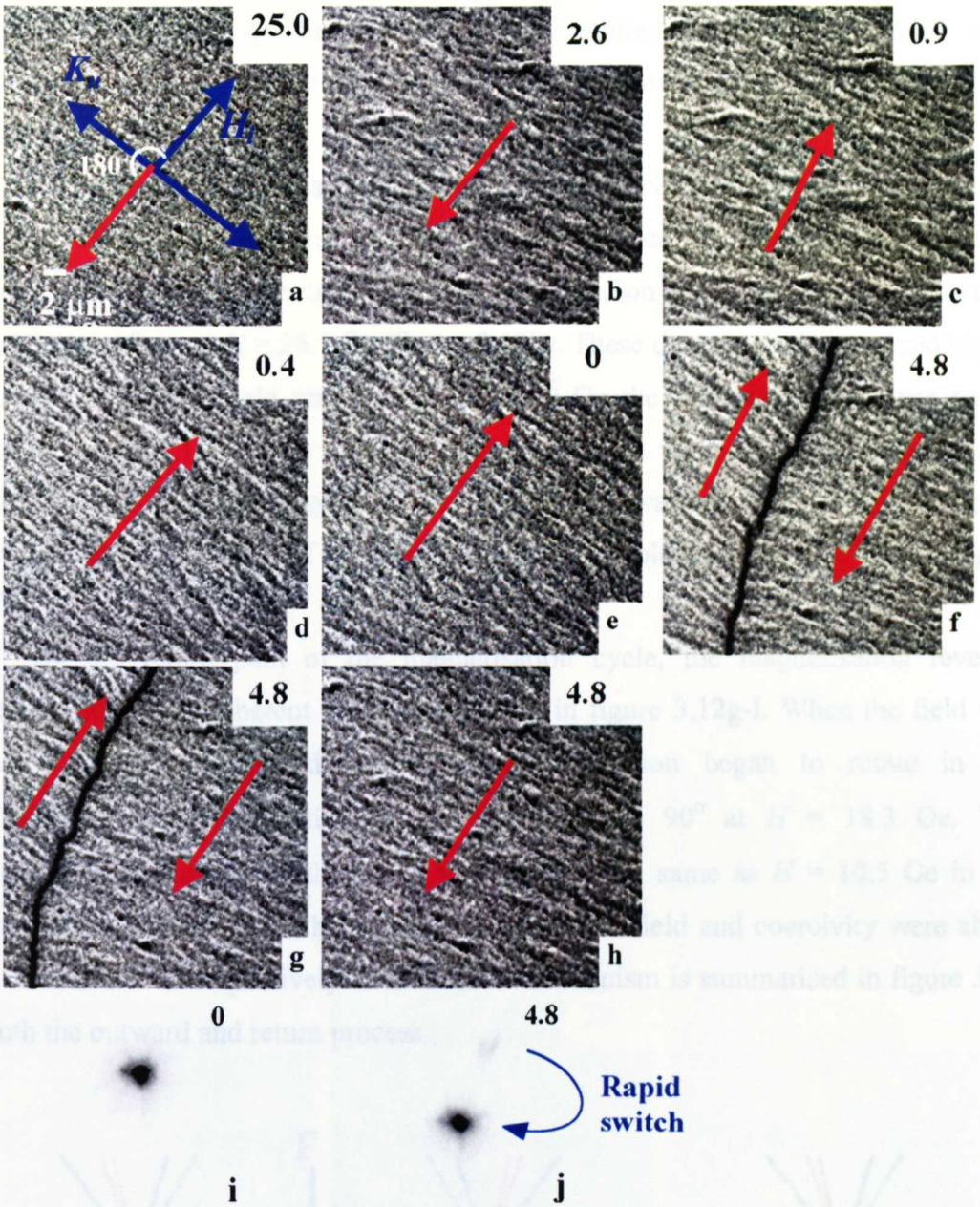

Figure 3.10: (a-h) Fresnel image sequence showing the free layer magnetisation reversal process for NiFe/CoFe SAF TSV and (i-j) LAD image at switching. Red arrows denote the direction of magnetisation as determined from the magnetisation ripple.

The value of offset field and coercivity can be estimated to be 3 Oe and 2 Oe respectively.

The reversal process was correctly predicted by the modified Stoner-Wohlfarth model. The model has been used in similar circumstances previously [12]. Using the value of H_K = 0.1 Oe, H_i = 2.9 Oe, θ = 180° and ε = 90°, the model predicted a 180° switch at 2 and 3 Oe. The deduced energy contour is shown in figure 3.11. The model shows no magnetisation rotation on either reversal path, consistent with experimental observation. The reversal process is completely symmetrical. The high mobility of the

domain wall observed in the experiment also implies there are only weak local anisotropy fluctuations in the film [13]. This is consistent with the small H_K value predicted by the model.

The free layer magnetisation reversal process for NiFe/CoFe SAF BSV is shown in figure 3.12. On the outward path the reversal process was dominated by domain formation due to the symmetrical split in magnetisation rotation. Low angle domain walls began to form at $H = 26.1$ Oe (figure 3.12b). These domain walls remained highly stationary for a wide field range until at $H = 0$ Oe the reversal process was nearly complete, figure 3.12b-f. The orientation of the domain walls along the uniaxial axis and the low wall mobility suggest that the applied field was very well aligned along the offset field direction. Some of the domains eventually collapsed into 360° loops, figure 3.12f.

On the return path of the magnetisation cycle, the magnetisation reversal proceeded purely by coherent rotation as shown in figure 3.12g-l. When the field was increased in the positive direction, the magnetisation began to rotate in the anticlockwise sense. Magnetisation has rotated by ≈ 90° at $H = 18.3$ Oe. The magnetisation orientation at this point was roughly the same as $H = 10.5$ Oe in the outward path, figure 3.12d. This means that the offset field and coercivity were about 14.4 Oe and 3.9 Oe respectively. The reversal mechanism is summarised in figure 3.13 for both the outward and return process.

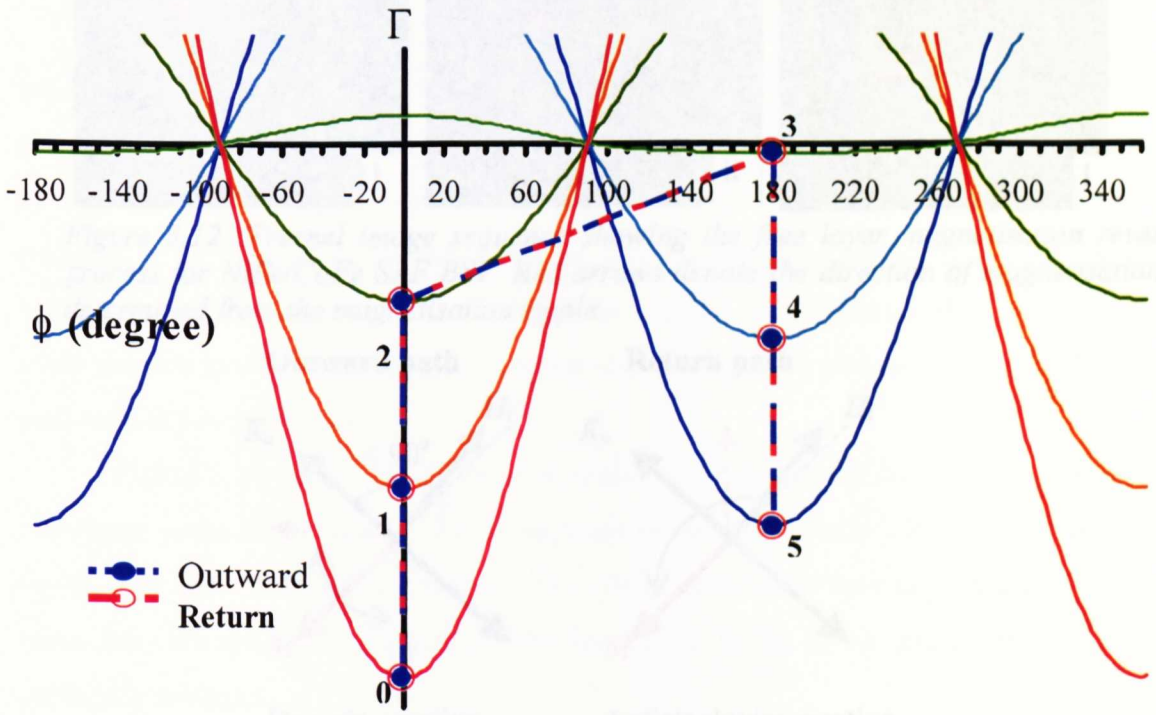

Figure 3.11: Energy contour deduced from modified Stoner-Wohlfarth model with $H_K = 0.1$ Oe, $H_i = 2.9$ Oe, $\varepsilon = 90^o$ and $\theta = 180^o$ for the NiFe/CoFe SAF TSV.

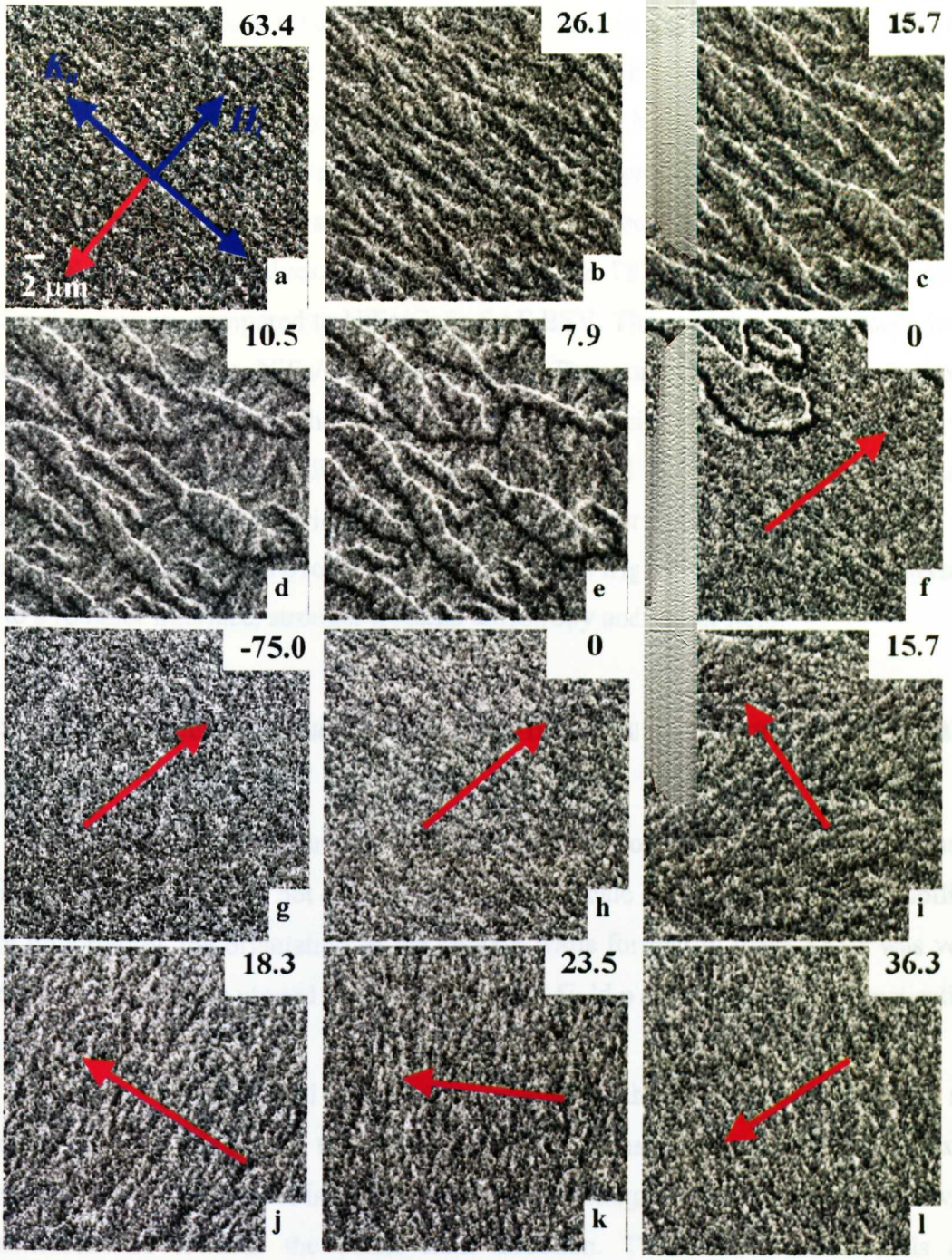

Figure 3.12: Fresnel image sequence showing the free layer magnetisation reversal process for NiFe/CoFe SAF BSV. Red arrows denote the direction of magnetisation as determined from the magnetisation ripple.

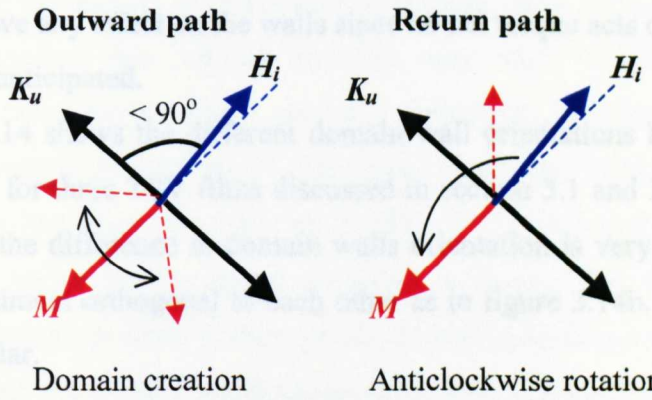

Figure 3.13: Outward and return magnetisation reversal mechanism for NiFe/CoFe SAF BSV.

The asymmetrical reversal process with domain formation on one path and coherent rotation on the other is most probably caused by the offset of unidirectional anisotropy from being orthogonal to the uniaxial axis. More detailed analysis of the origin of this asymmetrical reversal is presented in Chapter 4, section 4.4 and 4.5.

The experiments have shown the difference in free layer magnetisation reversal of top and bottom spin-valves. The NiFe/CoFe SAF TSV has a relatively low offset field and coercivity compared to NiFe/CoFe SAF BSV. The model also suggests a weak uniaxial anisotropy for NiFe/CoFe SAF TSV. The combination of weak uniaxial anisotropy, offset field and the magnetostriction coefficient results in a very simple reversal process. Since the NiFe/CoFe SAF TSV and BSV have almost identical stack composition and magnetostriction coefficient, the formation of domains in the NiFe/CoFe SAF BSV was probably attributed to the higher magnetisation dispersion due to a rougher interface, stronger uniaxial anisotropy and offset field.

3.4: Asymmetrical domain wall orientation on outward and return path

The complexity of domains observed in some of the TSVs studied in both sections 3.1 and 3.2 relates not only to small domain scale but also to low wall mobility. More importantly, the orientation of the domain walls formed in these TSVs was very different between the outward and return applied field path during the magnetisation cycle.

When an external field is applied orthogonal to the uniaxial axis, domains are expected to form parallel to the uniaxial axis for films with a significant uniaxial anisotropy. This is because it is equally likely for the magnetisation to rotate clockwise as anticlockwise towards the offset field direction. Therefore, domain walls are expected to lie parallel to the uniaxial axis and orthogonal to the applied field due to symmetrical split magnetisation rotation. The applied field orthogonal to the domain walls will not have any effect on the walls since no net torque acts on it. As a result, low wall mobility is anticipated.

Figure 3.14 shows the different domain wall orientations between the outward and return paths for three TSV films discussed in section 3.1 and 3.2. It can be seen in figure 3.14 that the difference in domain walls orientation is very significant. In some cases, they are almost orthogonal to each other as in figure 3.14b. But in general, they are highly irregular.

The diagonal domain walls in NiFe/CoFe AFM TSV, at field 12.9 Oe are simpler and less in density than those in the other two TSVs. As mentioned in section 3.1, the magnetisation reversal in this TSV proceeded mainly by rotation. The formation of the diagonally orientated domain walls across the image was expected. On the return path, domain walls formed after some degree of rotation of magnetisation. This type of behaviour was also observed on the return path of NiFe/Co AFM TSV and on the outward path of CoFe AFM TSV. At this point, part of the magnetisation continued to rotate, whilst some seemed to be trapped and creating domains. As mentioned in section 3.2, the exact mechanism responsible for stopping the rotation is not fully understood. Asymmetrical magnetisation reversal with coherent rotation on one path of the reversal process and by domain wall activity on the other has been observed previously, for example in exchange biased bilayers [14,15]. These films were quite different from those on which I am reporting here.

One possible explanation is that apart from the unidirectional 'orange-peel' interlayer coupling through the Cu spacer and the uniaxial anisotropy, other couplings may be present. The presence of the extra couplings break the symmetrical configuration, hence creating the asymmetrical domains due to asymmetrical reversal. It is hard to know which type of coupling may be present but one possibility is biquadratic coupling through the Cu spacer. The biquadratic coupling is the second order coupling of the exchange bias and it favours an orthogonal orientation to the pinned direction [16,20]. However, attempts so far to include the biquadratic term in the model to explain the asymmetry have not been successful. Observation of the biquadratic coupling effect in spin-valves with a synthetic antiferromagnet is also reported Zhang et al [21].

Dispersion in the pinned layer may also be the source of the asymmetry. It is possible that the magnetisation in the pinned layer is not uniform but some degree of dispersion is present [22]. If this is the case, then the pinned axis is no longer a well-defined axis. The net pinning direction may be orthogonal to the uniaxial axis. But, as a small field is applied, this pinning direction may begin to disperse a little. This dispersion may cause asymmetrical geometry. Moreover, interlayer coupling through the Cu spacer depends strongly on the interfacial roughness. Inhomogeneous switching behaviour of the free layer was reported in [23]. It was reported that inhomogeneous switching could occur for Cu spacer thickness $\approx$ 2 nm. This is due to the lateral variation of the coupling strength through the spacer layer. Since the coupling strength from 'orange-peel' and pinhole mechanisms are related to imperfections at the interface,

the coupling strength may display spatial fluctuation. Thus, different rates of rotation and switching experienced by different parts of the free layer cause domains to form in a very irregular way. The Cu spacer thickness in all the TSVs discussed in this chapter is ≈ 2.5 nm. This is very close to the thickness reported in [23].

Intermixing at the interface during deposition and post-deposition anneal may also influence the magnetic moment and hence the induced uniaxial anisotropy near the interface [24,25].

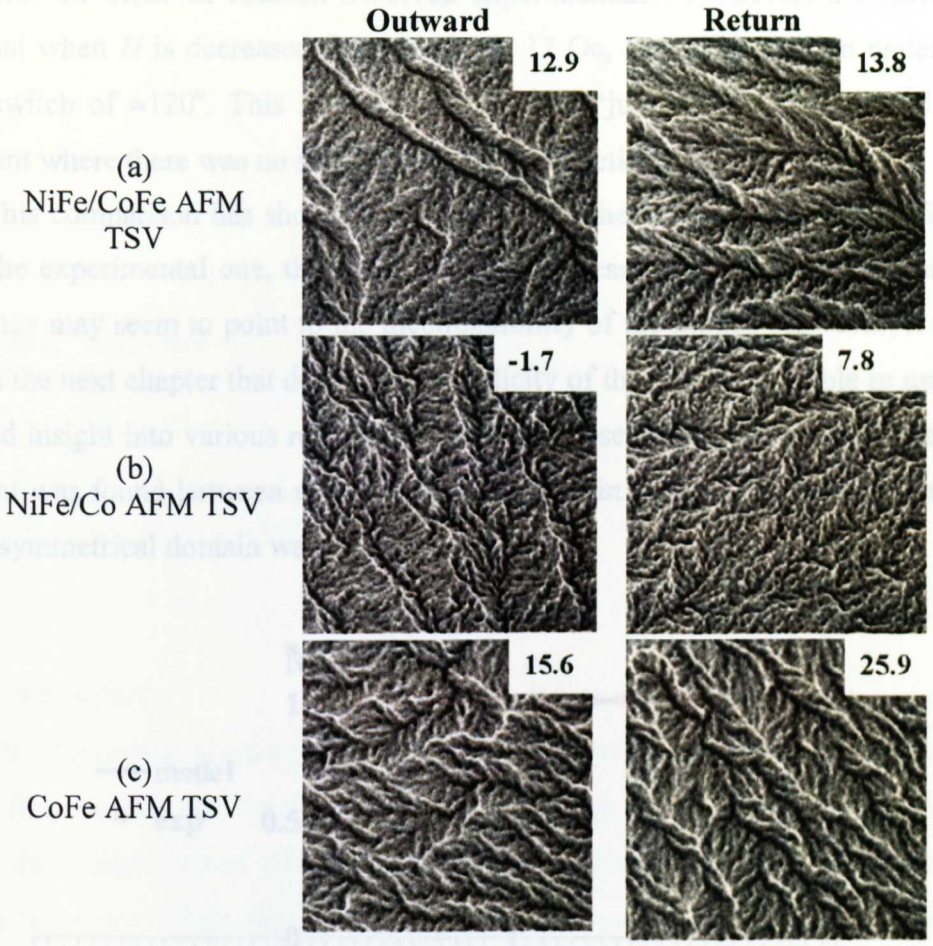

Figure 3.14: Fresnel images showing the asymmetrical domain wall orientation between the onward and return path.

3.5: Analysis of asymmetrical domain using a modified Stoner-Wohlfarth model

The modified Stoner-Wohlfarth model was used successfully to provide some insight into the reversal process for NiFe/CoFe SAF TSV in section 3.3. To try to understand the formation of asymmetrical domain wall orientation reported in section 3.2, the model is used again here to compare with the reversal process of NiFe/CoFe AFM TSV.

Figure 3.15 shows the fit of M vs H loop between the model and experiment. The loop was derived from the model by using the parameters $H_K = 0.7$ Oe, $H_i = 13$ Oe, $\varepsilon = 90^\circ$ and $\theta = 179^\circ$ while the experimental data is taken from figure 3.4a for the series $\theta = 179^\circ$. The experimental M vs H loop agrees very well with the modelled loop. The corresponding energy contour is also shown in figure 3.16. The model predicts a symmetrical magnetisation rotation for both the outward and return paths. The sense of rotation, which is clockwise on the outward path and anticlockwise on the return path, agrees with the sense of rotation observed experimentally. However, the model also shows that when H is decreased from 14 Oe to 12 Oe, the magnetisation undergoes a sudden switch of $\approx 120^\circ$. This sudden magnetisation 'jump' was not observed in the experiment where there was no sudden 'jump' in magnetisation.

This comparison has shown that although the theoretical M vs H loop fits very well to the experimental one, the actual reversal process itself is rather different. This discrepancy may seem to point to the incompatibility of the model. However, it will be shown in the next chapter that despite the simplicity of the model, it is able to provide a very good insight into various reversal mechanisms observed in the experiments. Good agreement was found between model and experiment in many cases but not yet in the case of asymmetrical domain wall orientations.

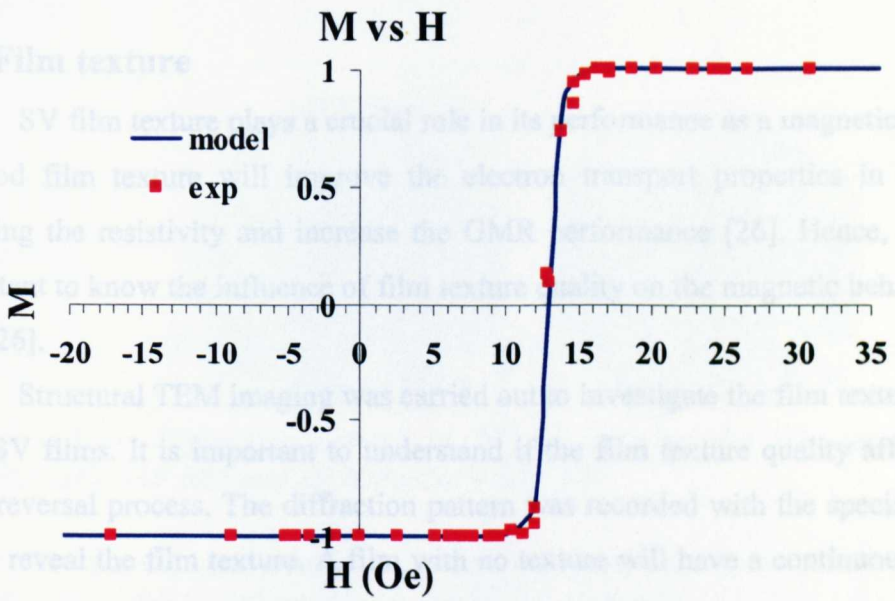

Figure 3.15: Comparison of both experimental and theoretical M vs H loop for NiFe/CoFe AFM TSV for $\theta = 179^\circ$.

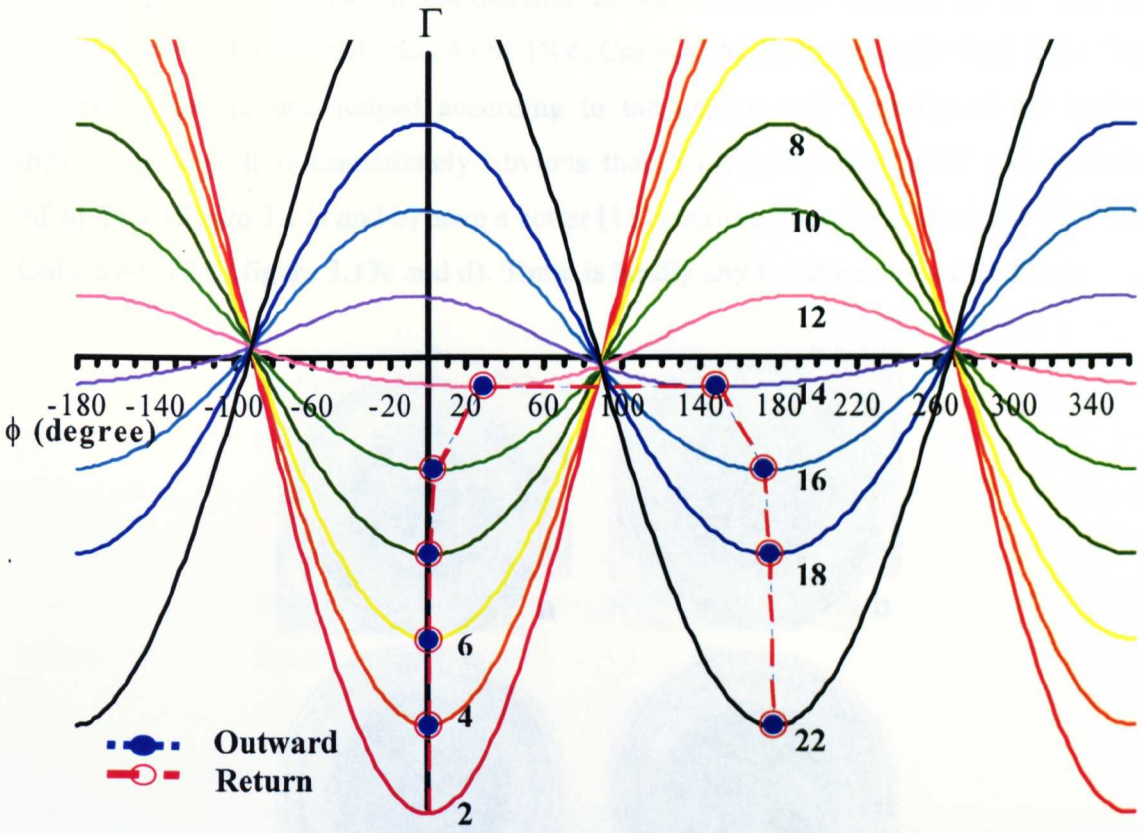

Figure 3.16: Energy contours deduced from modified Stoner-Wohlfarth model with $H_K = 0.7$ Oe, $H_i = 13$ Oe, $\varepsilon = 90^o$ and $\theta = 179^o$.

3.6: Film texture

SV film texture plays a crucial role in its performance as a magnetic sensor [26]. A good film texture will improve the electron transport properties in the film by reducing the resistivity and increase the GMR performance [26]. Hence, it is equally important to know the influence of film texture quality on the magnetic behaviour of the film [26].

Structural TEM imaging was carried out to investigate the film texture quality of the TSV films. It is important to understand if the film texture quality affects the free layer reversal process. The diffraction pattern was recorded with the specimen tilted at 20^o to reveal the film texture. A film with no texture will have a continuous diffraction ring since the diffraction of electrons is isotropic. When texture is present, electron diffraction along certain crystallographic axes is stronger than along other axes. Hence, tilting the specimen through a certain angle will reveal the diffraction rings missing when the specimen is not tilted. The intensity of the broken rings depends on the quality of the texture [27].

Figure 3.17 shows a comparison of the diffraction pattern at 20° tilt for NiFe/CoFe AFM TSV, NiFe/Co AFM TSV, CoFe AFM TSV and CoFe SAF TSV. The quality of texture was judged according to the degree and intensity of the broken diffraction ring. It is immediately obvious that NiFe/CoFe AFM TSV and NiFe/Co AFM TSV (figure 3.17a and b) have a better [111] texture than the CoFe AFM TSV and CoFe SAF TSV (figure 3.17c and d). There is hardly any texture in the latter films.

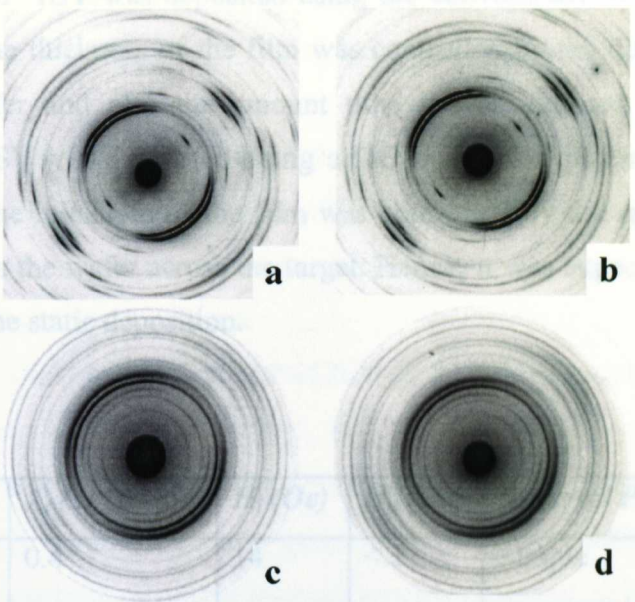

Figure 3.17: Diffraction pattern at 20° tilt showing the texture of the TSV films. (a) NiFe/CoFe AFM TSV, (b) NiFe/Co AFM TSV, (c) CoFe AFM TSV, and (d) CoFe SAF TSV.

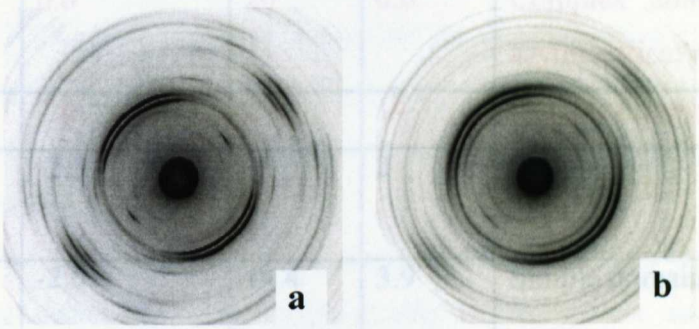

Figure 3.18: Diffraction pattern at 20° tilt showing the film texture quality (a) NiFe/CoFe SAF BSV and (b) NiFe/CoFe SAF TSV.

The experimental results show that complex and asymmetrical domain wall orientation appears in NiFe/CoFe AFM TSV, NiFe/Co AFM TSV and CoFe AFM TSV. This seems to suggest that film texture was not the cause of asymmetrical domain walls formation.

The same structural experiments were also done for the NiFe/CoFe SAF TSV and NiFe/CoFe SAF BSV film. Figure 3.18a-b shows the corresponding diffraction

pattern. It can be seen that the NiFe/CoFe SAF BSV (figure 3.18a) has a better texture quality than the NiFe/CoFe SAF TSV film (figure 3.18b). Despite this, NiFe/CoFe SAF TSV still had the simplest free layer reversal process compared to all other SV films investigated so far. This seems to imply once again that film texture does not play a major role in determining the free layer reversal process. The slightly better texture in NiFe/CoFe SAF BSV could be due to the difference in the film deposition technique. The NiFe/CoFe SAF TSV was deposited using the conventional DC magnetron static deposition where the thickness of the film was controlled by the distance between the target and the wafer and also the amount time it was exposed to the target; the NiFe/CoFe SAF BSV was deposited using a DC magnetron planetary cluster. In the planetary system, the thickness of the film was controlled by the rate of swing of the robot arm that holds the wafer across the target. Hence, it was expected to have a more uniform film than the static deposition.

3.7: Discussion

	λ_s (x 10^{-6})	H_i (Oe)	H_c (Oe)	*Reversal Process*	Texture
NiFe/CoFe AFM TSV	0.4	14	< 1	Simple domains, asymmetrical walls	Strong
NiFe/Co AFM TSV	7.5	6.5	8.5	Complex domains, asymmetrical walls	Strong
CoFe AFM TSV	6.6	20	6.0	Complex domains, asymmetrical walls	Weak
CoFe SAF TSV	7.6	2	14	Complex domains	Weak
NiFe/CoFe SAF TSV	-2.3	3	2	Simple	Moderate
NiFe/CoFe SAF BSV	-2.0	14.4	3.9	Simple domains	Strong

The table above summaries λ_s, H_i, H_c, the reversal process and texture of all the SV samples discussed in this chapter. We should also recall that the magnetocrystalline anisotropy increase going from NiFe to CoFe to Co.

The results show that the NiFe/CoFe AFM TSV, NiFe/CoFe SAF TSV and NiFe/CoFe SAF BSV (highlighted in blue) have a relatively simple reversal process compared to the NiFe/Co AFM TSV, CoFe AFM TSV and CoFe SAF TSV (highlighted in red). The simple reversal process is associated with those samples with low

magnetostriction coefficient, low magnetocrystalline anisotropy and low coercivity. This seems to suggest that low magnetostriction and magnetocrystalline anisotropy, which result in low magnetisation dispersion, lead overall to a simpler magnetisation reversal process. As a result, the free layer reversal was mainly by coherent rotation with minimal domain formation when an external field was applied along the offset field direction. Lower localised anisotropy fluctuations also lead to higher domain wall mobility. Conversely, strong localised anisotropy fluctuations, inevitable in polycrystalline films with high anisotropy in the grains lead to complex domains, hence higher coercivity.

The CoFe AFM TSV and CoFe SAF TSV showed complex domain formation during free layer reversal similar to that in NiFe/Co AFM TSV. Replacing the AFM by the SAF in the SV leads to an increase in coercivity and decrease in offset field. The reason for these changes is not obvious.

The asymmetrical reversal of NiFe/CoFe SAF BSV is probably due to a small offset whereby the uniaxial anisotropy axis is not exactly orthogonal to the unidirectional anisotropy. Evidence for this is presented in the next chapter. The combination of weak magnetostriction, coercivity and offset field in the NiFe/CoFe SAF TSV sample leads to the simplest reversal process observed so far.

In general varying the orientation of the applied field from antiparallel to the offset direction led to simplification of the reversal process. Domain formation did not occur and reversal was primarily by magnetisation rotation. The exception was the NiFe/Co AFM TSV and here it seems likely that the magnetisation dispersion is the greatest. Thus whilst for most films, breaking the symmetry by making $\theta \neq 180^{\circ}$ meant it was favourable for all local moment to rotate in the same sense, it appears this was not the case if the dispersion is high.

The structural experiments studying the texture of the films have shown that there is no apparent correlation between the quality of film texture and asymmetrical complex domain formation.

In summary, the experimental results presented in this chapter suggest that magnetostriction effects and magnetocrystalline anisotropy in polycrystalline SV films influence the magnetisation reversal mechanism very strongly.

References:

[1] Henryk Szymczak, J. Magn. Magn. Mater. **200** 425 (1999),

[2] P. A. Voltairas, D. I. Fotiadis, C. V. Massalas, J. Magn. Magn. Mater. **213** 43 (2000),

[3] L. Baril, B. Gurney, D. Wilhoit, V. Speriosu, J. Appl. Phys. **85** 5139 (1999),

[4] H. Kanai, K. Noma, J. Hong, Fujitsu Sci. Tech. J. **37** 174 (2001),

[5] M. Labrune, J. C. Kools, A. Thiaville, J. Magn. Magn. Mater. **171** 1 (1997),

[6] R. Coehoorn, J. C. S. Kools, Th. G. S. M. Rijks and K. M. H. Lensen, J. Philips Res. **51** 93 (1998),

[7] S. J. T. Murdoch, J. N. Chapman, T. G. Pokhil, J. Appl. Phys. **87** 4945 (2000),

[8] P. A. Voltairas, D. I. Fotiadis, C. V. Massalas, J. Magn. Magn. Mater. **213** 43 (2000),

[9] De-Hua Han, Jian-Gang Zhu, Jack H. Judy, and John M. Sivertsen, J. Appl. Phys. **81** 4519 (1997),

[10] M. Saito, N. Hasegawa, F. Koike, H. Seki, and T. Kuriyama, J. Appl. Phys. **85** 4928 (1999),

[11] D. V. Dimitrov, J. van Ek, Y. F. Li and J. Q. Xiao, J. Appl. Phys. **87** 6427 (2000),

[12] J. P. King, J. N. Chapman, J. C. S. Kools, M. F. Gillies, J. Phys. D: Appl. Phys. **32** 1087 (1999),

[13] C. Appino, M. Valsania, V. Basso, J. Physical B **275** 103 (2000),

[14] C. Leighton, M.R. Fitzsimmons, P. Yashar, A. Hoffmann, J. Nogues, J. Dura, C. F. Majkrzak, and Ivan K. Schuller, Phys. Rev. Lett. **86** 4394 (2001),

[15] X. Portier, A. K. Petford-Long, A. de Morais, N. W. Owen, H. Laidler, and K. O'Grady, J. Appl. Phys, **87** 6412 (2000),

[16] R. L. Stamps, J. Phys. D: Appl. Phys. **33** R247 (2000),

[17] S. O. Demokrikov, J. Phys. D: Appl. Phys. **31** 925 (1998),

[18] J. C. Slonczewski, J. Magn. Magn. Matter. **150** 13 (1995),

[19] P. Vavassori, M. Grimsditch, E. E. Fullerton, J. Magn. Magn. Matter. **223** 284 (2001),

[20] C. C. Yu, A. K. Petford-Long, J. Appl. Phys. **85** 5753 (1999),

[21] K Zhang, T. Kai, T. Zhao, H. Fujiwara, and G. J. Mankey, J. Appl. Phys. **89** 6814 (2001),

[22] C. Hou, J. Chen, M. T. Kief, Z. Gao, S. Mao and T. Pokhil, Appl. Phys. Lett. **78** 237 (2001),

[23] Th. G. S. M. Rijks, R. F. O. Roneerkens, R. Coehoorn, J. C. Kools, M. F. Gillies, J. N. Chapman, W. J. M. de Jonge, J. Appl. Phys. **82** 3442 (1997),

[24] A. Vedyayev, M. Chshiev, B. Dieny, J. Magn. Magn. Mater. **184** 145 (1998),

[25] B. Dieny, J. Magn. Magn. Mater. **136** 335 (1994),

[26] W. L. Lee, M. F. Toney, P. Tameerug, E. Allen, D. Mauri, J. Appl. Phys. **87** 6992 (2000),

[27] R. Linsay, J. N. Chapman, A. J. Craven, D. McBain, Ultramicroscopy **80** 41 (1999).

CHAPTER 4: EFFECT OF SYNTHETIC ANTIFERROMAGNET AND ANNEALING CONDITION ON FREE LAYER REVERSAL

Introduction

The free layer magnetisation reversal processes of various spin-valve structures have been discussed in chapter 3. It was found that the structure of the exchange bias layer, either AFM or SAF, did not have a significant effect on the free layer magnetisation reversal behaviour. However, there were changes in both the offset field and coercivity of the free layer. In this chapter, I will discuss further the effect of synthetic antiferromagnetic exchange bias structures [1-6] and annealing conditions [7] on the free layer reversal process.

Section 4.1 presents the work on optimising the SAF structure for optimum coupling strength between the pinned and reference layer by varying the thickness of the Ru, pinned and reference layers [3]. Reducing the layer thicknesses of SVs is crucial for high density storage systems as the recording bit size is shrinking rapidly [8]. The challenge is to reduce the thickness of a SV while maintaining its stability, both in terms of its electrical transport properties and magnetic properties. Thinning the SAF layer structure is also believed to improve the GMR performance of the SV sensor due to reduced current shunting in the SAF layers [9,10]. This may lead to an increase in the spin-dependent scattering probability at the free-layer/spacer/reference-layer (FL/Cu/RL) interfaces, which contribute to GMR. Therefore, a better GMR can be achieved. However, having a thinner SAF layer may affect the free layer magnetisation reversal. Thus, it is very important to investigate the free layer reversal of the thinner SAF SV films. TEM experiments on the free layer reversal of three BSV films with thinner SAF structures are presented in section 4.2.

The effect of different annealing fields on the free layer reversal process is described in section 4.3. Improved domain structures were observed for higher annealing fields. In order to understand the asymmetrical reversal process observed in the free layer, reversal mechanisms were studied as a function of field orientation and the results are presented in section 4.4. The modified Stoner-Wohlfarth model was used to analyse the reversal processes. The model provided a good description of the various reversal modes and there was reasonable agreement between predicted and observed fields at which key stages of the reversal took place, section 4.5.

4.1: Synthetic antiferromagnetic structure optimisation

A series of NiFe/CoFe BSV films with different SAF structures was deposited on thermally oxidised silicon substrates using a multi-target DC magnetron planetary deposition tool. A planetary deposition technique was used to produce high quality thin films. After the deposition, the films were annealed in a commercial annealing oven at 300° C in a field of 10 000 Oe for four hours. The change in resistance between parallel and antiparallel spin-valve states (dR) was measured for all films using a conventional four-point probe technique. A field varying from -2000 Oe to 2000 Oe was applied along the offset field direction of the spin-valve. The resulting dR/R vs *H* loop is called the hard axis loop. dR arises from spin dependent scattering as discussed in chapter 1. The purpose of the experiments was to determine how rapidly dR/R decreased from its maximum value in increasing positive fields.

Figures 4.1 and 4.2 show the dR/R vs *H* curve for varying Ru spacer layer thicknesses. The Ru thickness was changed from 6 Å to 10Å. The thicknesses of the pinned and reference layers (denoted as PL and RL) were fixed at 14Å and 18Å for figure 4.1; 12Å and 16Å for figure 4.2. dR/R depends on the orientation of the magnetisation in the free layer and the reference layer. It has a maximum value when they are antiparallel and a minimum value when they are parallel. As shown in figure 4.1 and 4.2, the maximum dR/R value was at low field when the magnetisation in the free layer switched at low external field and the magnetisation of the reference layer was lying in the opposite direction. The reference layer was antiferromagnetically coupled to the pinned layer through the oscillatory exchange coupling [11,12]. When the applied field was increased in the opposite direction to the magnetisation in the reference layer, the magnetisation in the reference layer begins to change towards the field direction. As the result of the large external field, the net magnetisation direction between the free and reference layer decreases. This leads to lower spin-asymmetry scattering between the free and reference layers, hence lower dR/R. Therefore, the stability of the SAF structure can be determined from the dR/R vs *H* loop.

Both figure 4.1 and figure 4.2 show that when the Ru thickness was 9 and 10Å, the dR/R loops have the smallest fall in dR/R at 2000 Oe. On the other hand, the Ru 7Å experiences the greatest fall in dR/R. This seems to imply a more stable SAF structure when the Ru thickness was 9 and 10Å. The fall in dR/R for Ru 7Å was not due to deteriorating film quality for lower Ru thicknesses, as the Ru 6Å film had a higher dR/R at 2000 Oe compared to Ru 7Å in both experiments. This suggests that film quality was not an issue for a thickness as small as 6Å. So, the fall in dR/R for Ru 7Å must be due

to the change in magnetisation in the reference and pinned layers. This suggests a comparatively weak SAF structure [4].

$$Stability = \frac{1}{dR/R_{maximum} - dR/R_{2000Oe}}$$

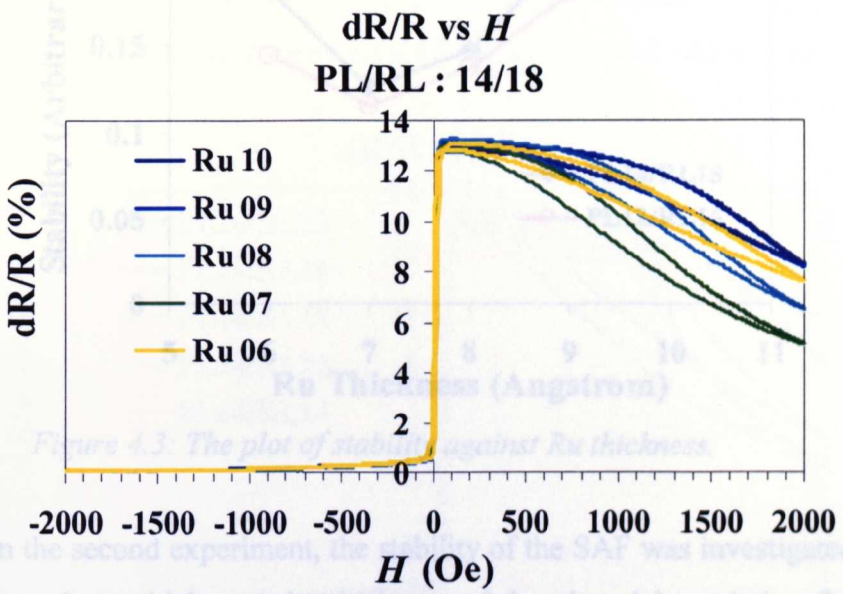

Figure 4.1: dR/R vs H curves for SAF structures with Ru thicknesses from 6 to 10Å. The pinned and reference layer thicknesses are 14 and 18Å respectively.

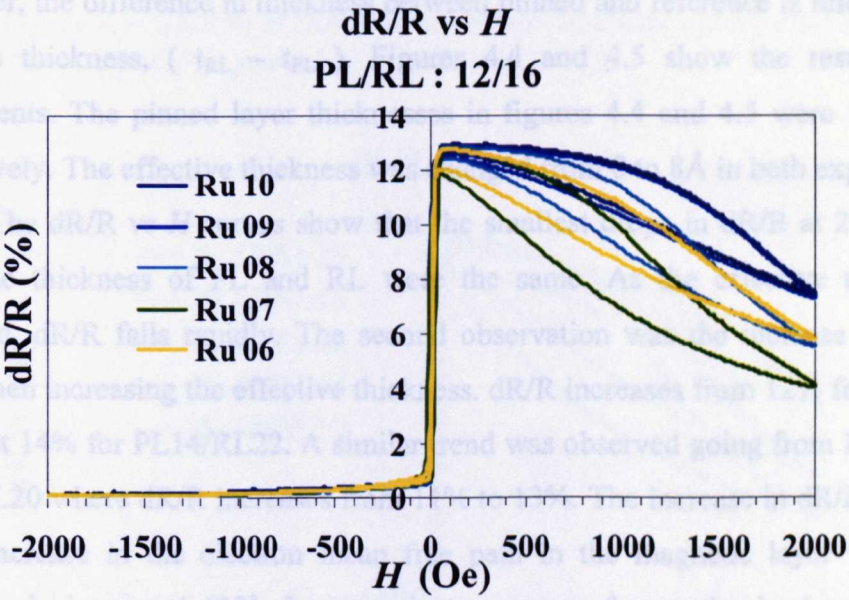

Figure 4.2: dR/R vs H curves for SAF structure with Ru thickness from 6 to 10Å. The pinned and reference layer thickness are 12 and 16Å respectively.

Figure 4.3 is a plot of the stability vs Ru thickness for both PL14:RL18 and PL12:PL16. The stability is defined here as the inverse of the drop in dR/R measured at 2000 Oe from the maximum value measured. Figure 4.3 shows that the stability is the highest for Ru 9, 10Å and the lowest for at Ru 7Å.

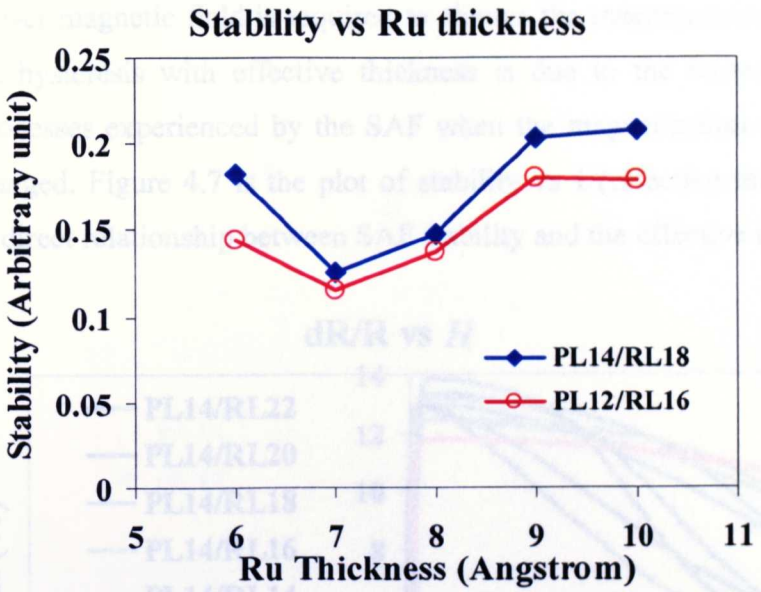

Figure 4.3: The plot of stability against Ru thickness.

In the second experiment, the stability of the SAF was investigated as a function of reference layer thickness, the thickness of the pinned layer being fixed. When the pinned and reference layers had the same thickness, we refer to a balanced structure. Moreover, the difference in thickness between pinned and reference is referred to as the effective thickness, ($t_{RL} - t_{PL}$). Figures 4.4 and 4.5 show the results from the experiments. The pinned layer thicknesses in figures 4.4 and 4.5 were 14Å and 12Å respectively. The effective thickness was changed from 0 to 8Å in both experiments.

The dR/R vs *H* curves show that the smallest drops in dR/R at 2000 Oe occur when the thickness of PL and RL were the same. As the effective thickness was increased, dR/R falls rapidly. The second observation was the increase in maximum dR/R when increasing the effective thickness. dR/R increases from 12% for PL14/RL14 to almost 14% for PL14/RL22. A similar trend was observed going from PL12/RL12 to PL12/RL20 where dR/R increases from 11% to 13%. The increase in dR/R might relate to the increase in the electron mean free path in the magnetic layer when the RL thickness is increased [13]. Longer electron mean free paths lead to lower sheet resistance R_s. As a result, dR/R is increased. The decreasing sheet resistance against RL thickness is shown in figure 4.6.

Apart from the increase of $dR/R_{maximum}$ and decrease of stability with effective thickness, the width of the loop was also affected by the effective thickness. In both PL14 and PL12 films, the width of the dR/R loops increased steadily with the effective thickness. When the reference layer was thicker than the pinned layer, there was a net

magnetic moment associated with the SAF. It increases with effective thickness and hence, a lower magnetic field is required to change the magnetisation in the SAF. The increase in hysteresis with effective thickness is due to the increase in irreversible reversal processes experienced by the SAF when the magnetisation distribution in the SAF is changed. Figure 4.7 is the plot of stability vs 1/(effective thickness). It shows clearly the direct relationship between SAF stability and the effective thickness.

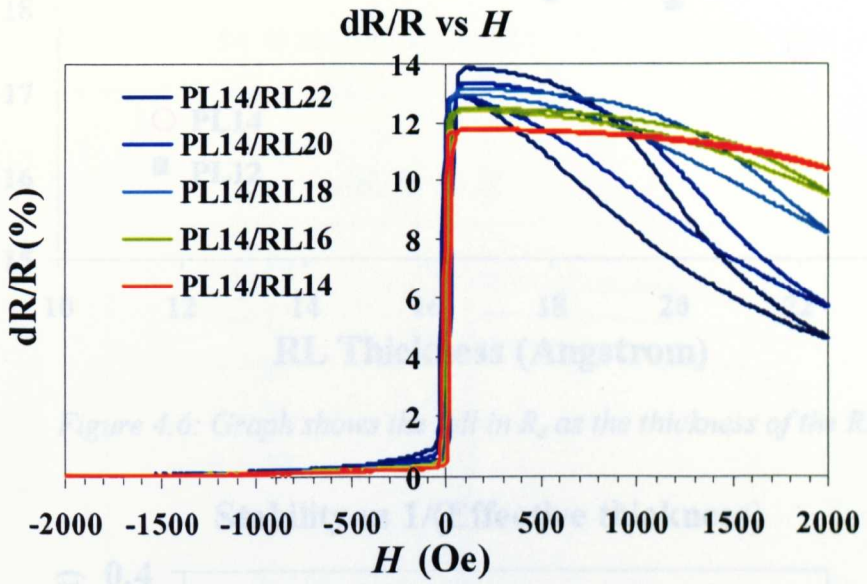

Figure 4.4: dR/R vs H curves for SAF structure with effective thickness from 0 to 8Å. The pinned layer thickness is 14Å.

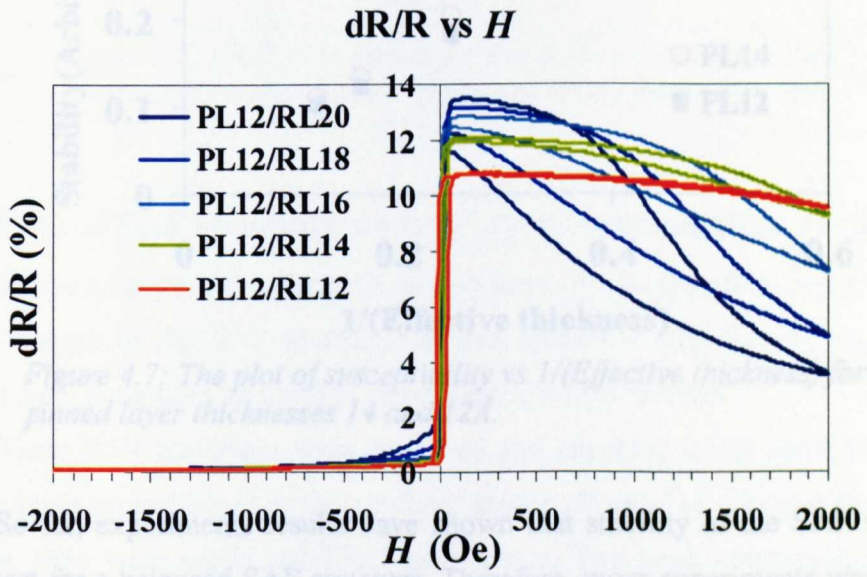

Figure 4.5: dR/R vs H curves for SAF structure with effective thickness thickness from 0 to 8Å. The pinned layer thickness is 12Å.

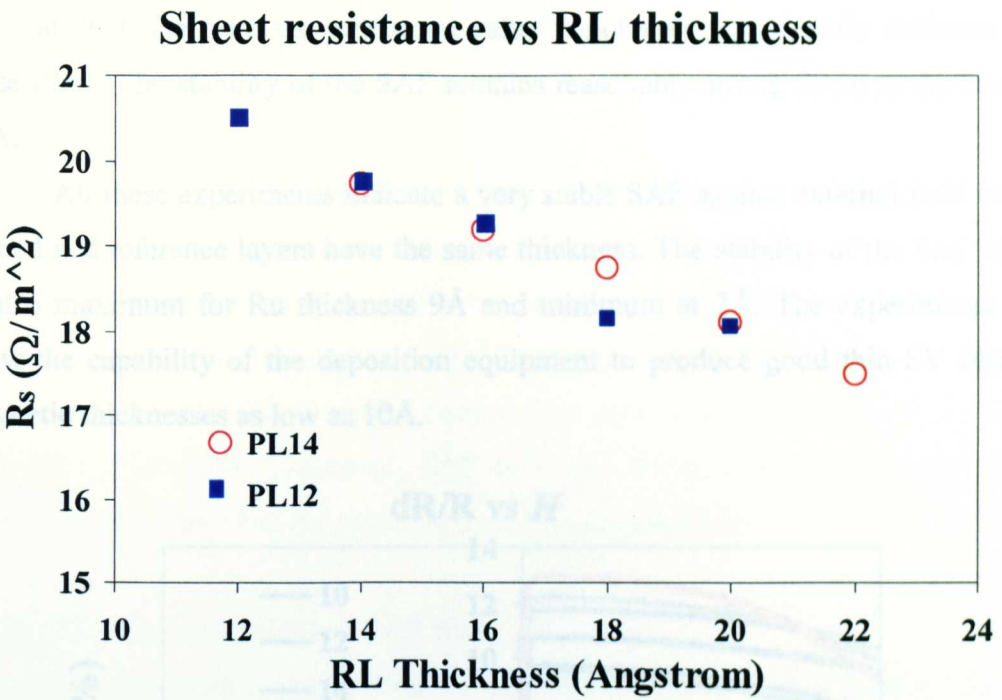

Figure 4.6: Graph shows the fall in R_s as the thickness of the RL.

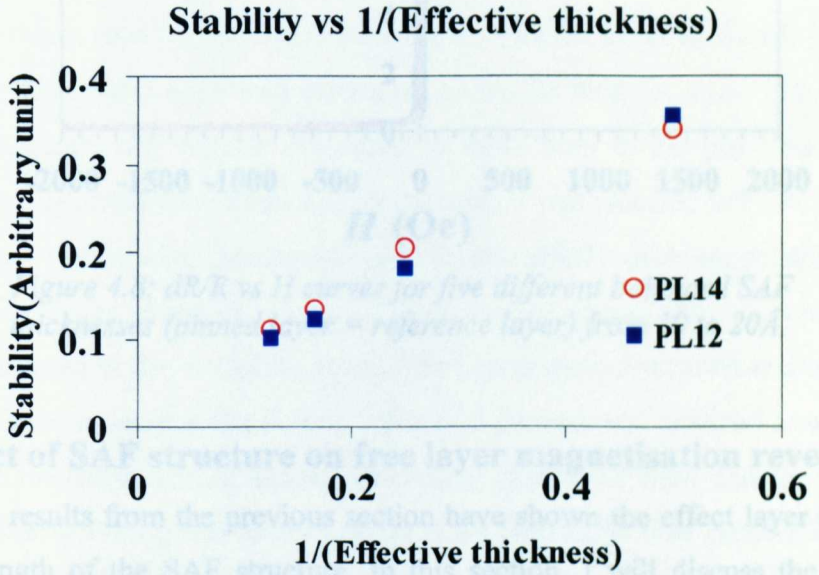

Figure 4.7: The plot of susceptibility vs 1/(Effective thickness) for both pinned layer thicknesses 14 and 12Å.

So far, experiments results have shown that stability of the SAF structure was the highest for a balanced SAF structure. Therefore, more experiments were carried out to investigate further the strength of the balanced SAF films. A series of balanced SAF bottom spin-valve films were deposited and annealed using the same method. The thickness of pinned (=reference) layer was varied from 10 to 20Å. The result is shown in figure 4.8. It is found that increasing the SAF thickness improves the dR/R. This is

due to the decrease in resistance in the magnetic layer as described earlier. The drop in dR/R at 2000 Oe from the maximum value is not very significantly different among these films. The stability of the SAF remains reasonably strong down to thicknesses of 10Å.

All these experiments indicate a very stable SAF against external field when the pinned and reference layers have the same thickness. The stability of the SAF structure is also maximum for Ru thickness 9Å and minimum at 7Å. The experiments further show the capability of the deposition equipment to produce good thin SV films with magnetic thicknesses as low as 10Å.

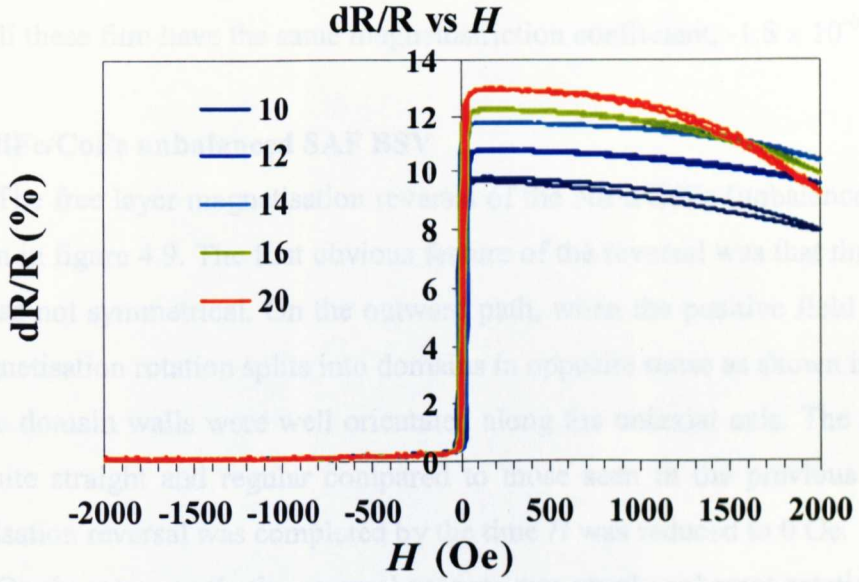

Figure 4.8: dR/R vs H curves for five different balanced SAF thicknesses (pinned layer = reference layer) from 10 to 20Å.

4.2: Effect of SAF structure on free layer magnetisation reversal

The results from the previous section have shown the effect layer thickness has on the strength of the SAF structure. In this section, I will discuss the influence of different SAF structures on the free layer magnetisation reversal.

Three BSV structures were deposited and annealed in the same equipment and with the same procedure as in the previous section. Instead of growing the films on the Si wafer, they were grown on TEM membranes. The stack compositions are shown below:

1: seed60/PtMn185/CoFe14/Ru9/CoFe18/Cu23/CoFe13/NiFe25/cap50

2: seed60/PtMn185/CoFe14/Ru9/CoFe14/Cu23/CoFe13/NiFe25/cap50

3: seed60/PtMn185/CoFe14/Ru7/CoFe18/Cu23/CoFe13/NiFe25/cap50

The SAF structure is highlighted in red. The first film had the unbalanced SAF. The second structure had Ru 9Å and balanced PL and RL thickness. The last film had Ru thickness 7Å and unbalanced PL and RL. Therefore, all three SV have different SAF structure stability.

The free layer magnetisation reversal mechanisms were studied using the Fresnel imaging mode. Any differences in the magnetisation reversal between these films should be attributed to the difference in SAF structure. This was because all these films were grown and annealed under the same conditions. The only difference in thicknesses was in the SAF layers. They will be referred to as NiFe/CoFe (unbalanced) SAF BSV, NiFe/CoFe (balanced) SAF BSV and NiFe/CoFe (unbalanced Ru7) SAF BSV. All these film have the same magnetostriction coefficient, -1.8×10^{-6}.

4.2.1: NiFe/CoFe unbalanced SAF BSV

The free layer magnetisation reversal of the NiFe/CoFe (unbalanced) SAF BSV is shown in figure 4.9. The first obvious feature of the reversal was that the magnetising cycle was not symmetrical. On the outward path, when the positive field was reduced, the magnetisation rotation splits into domains in opposite sense as shown in figure 4.9b-d. These domain walls were well orientated along the uniaxial axis. The domain walls were quite straight and regular compared to those seen in the previous chapter. The magnetisation reversal was completed by the time H was reduced to 0 Oe.

On the return path, the reversal process was purely coherent rotation. There was no presence of any domains. Figure 4.9g-k clearly shows the magnetisation ripple rotation. It rotated in the clockwise sense. The asymmetrical reversal was most probably due to specimen misalignment during the anneal process and uniaxial axes realignment due to heat treatment during anneal. Therefore, the offset field and the uniaxial axis were not exactly orthogonal to each other. This behaviour was successfully modelled using a modified Stoner-Wohlfarth model. Further discussion on analysis using the model is provided in section 4.5.

The ripple orientation in both figure 4.9c and h was almost 90° to the initial orientation. This means a zero magnetisation along the field direction. The field at these points was 15.6 Oe. Therefore, the offset field could be estimated roughly to be around 15.6 Oe. The hysteresis arising from this estimate will be no more than 1 Oe.

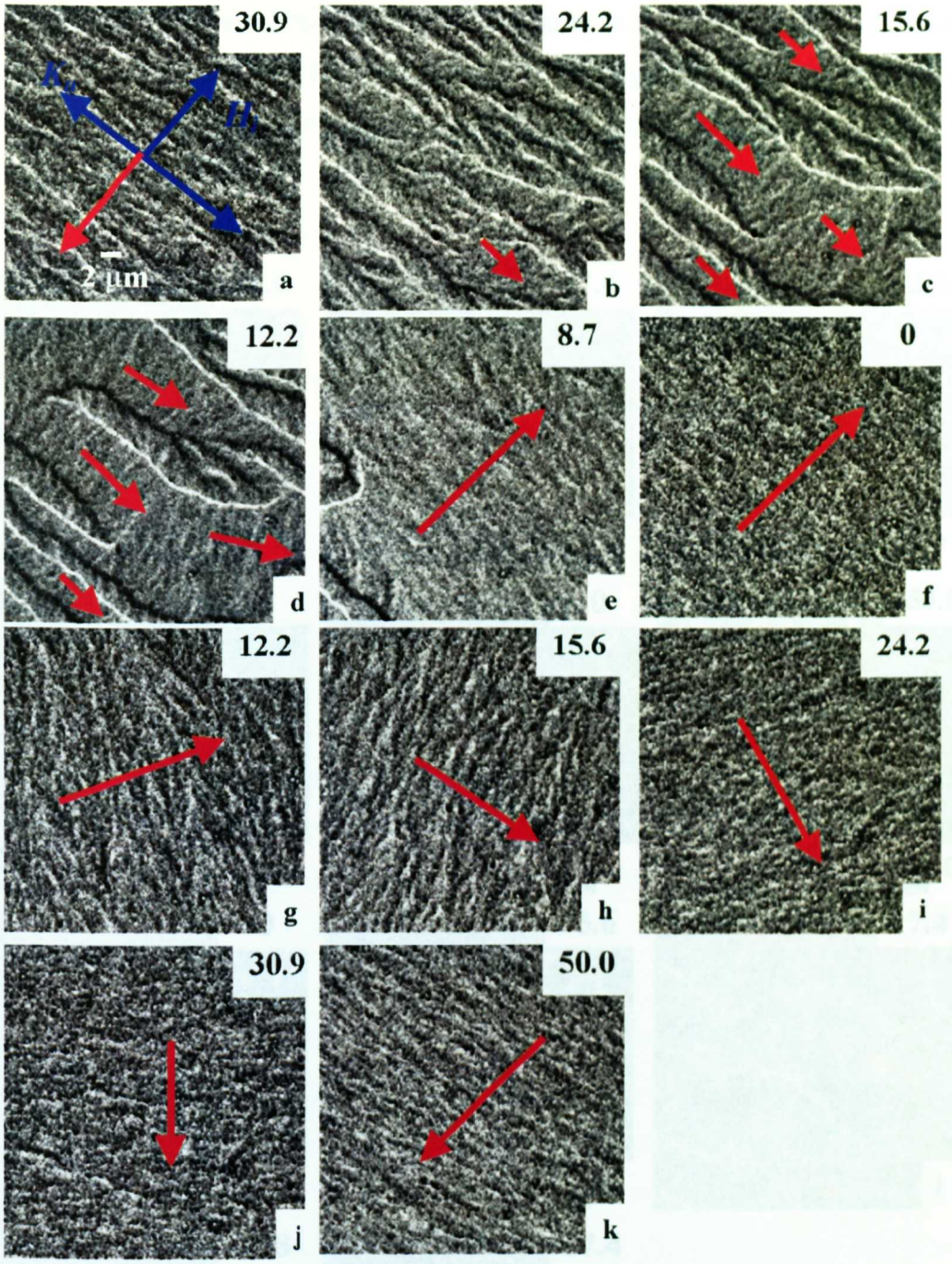

Figure 4.9: Fresnel image sequence for NiFe/CoFe unbalanced SAF BSV. Red arrows denote the direction of magnetisation as determined from the magnetisation ripple.

4.2.2: NiFe/CoFe balanced SAF BSV

The same in-situ TEM imaging experiment was carried out for the NiFe/CoFe (balanced) SAF BSV film. Figure 4.10 shows the complete reversal process recorded in Fresnel mode. The reversal process proceeded with domain formation on both the outward and return paths.

When the applied field was reduced from 57.4 Oe, the magnetisation splits into domains in opposite senses. This created the domain walls along the uniaxial axis. The domain walls were more irregular that those seen in the unbalanced BSV film in the

previous section. Figure 4.10b-d show the irregularity in the wall orientations. Some of these domains collapsed into 360° walls at H = 0 Oe, figure 4.10e. Applying a higher field in the negative direction gets rid some of the 360° walls. However, some still remained at H = -50.0 Oe.

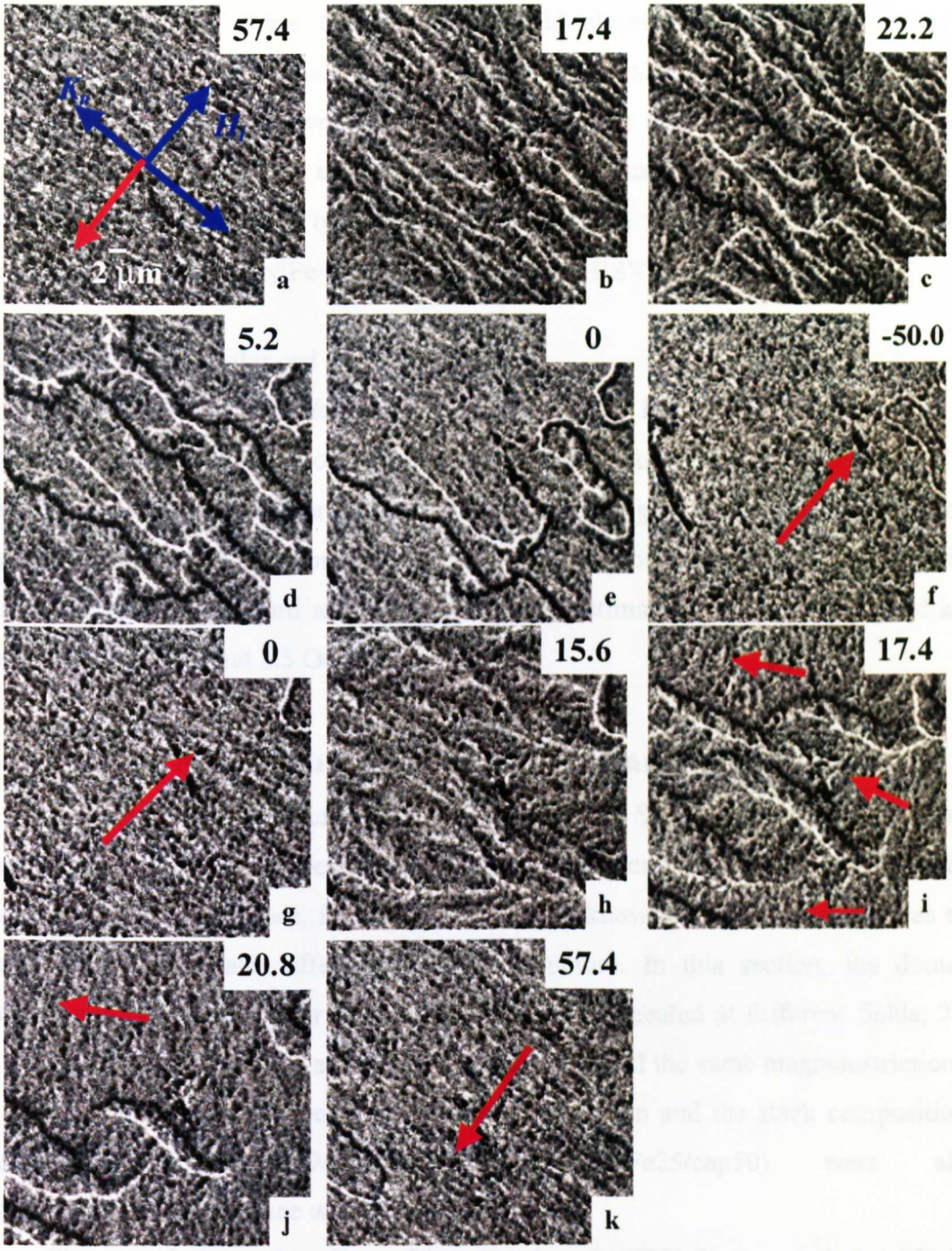

Figure 4.10: Fresnel image sequence for NiFe/CoFe balanced SAF BSV. Red arrows denote the direction of magnetisation as determined from the magnetisation ripple.

On the return path, no magnetisation ripple rotation was observed when the field was increased to 0 Oe. Further increase in positive applied field caused domains to

form, orientated along the uniaxial axis figure 4.10i. Some of the domains are bent. The bent domains were clearly visible in figure 4.10j; they were also highly persistent. These bent domains were not present on the outward path. For increasing applied field, the magnetisation outside these domains rotated in the anticlockwise sense, shown in figure 4.10i-k. The domains lasted until the reversal was completed.

The origin of these bent domains could simply due to the nature of a polycrystalline film, which always has some degree of localised anisotropy fluctuation.

If figure 4.10c and i were to be considered as the midpoint of the outward and return paths respectively, the offset field could be estimated to be around 20 Oe and coercivity of about 2.4 Oe. These values have increased from $\approx$ 15.6 Oe and $<$ 1 Oe respectively compared to NiFe/CoFe unbalanced SAF BSV.

4.2.3: NiFe/CoFe unbalanced Ru7 SAF BSV

The reversal process for NiFe/CoFe unbalanced Ru7 SAF BSV is shown in figure 4.11. Domains formed on both the outward and return paths. The orientation of these domain walls was rather symmetrical, shown in figure 4.11e and j. They were orientated almost along the uniaxial axis. The ripple rotation indicates a clockwise rotation on both the outward and return paths. The estimated value of offset field and coercivity are 8.5 Oe and 2.5 Oe respectively.

4.3: Improved domain structure for high field anneal BSV film

Various domain structures have been observed in SVs investigated so far. They were found to be closely related to the magnetostriction and magnetocrystalline anisotropy of the SV. Hence, it is also important to know if other factors such as the annealing conditions also affect the domain structure. In this section, the domain structure will be compared for NiFe/CoFe SAF BSV annealed at different fields, 250 Oe, 10 000 Oe and 20 000 Oe at 300°C. All these films had the same magnetostriction, -1.8 x 10^{-6}. They were deposited under the same condition and the stack compositions (seed60/PtMn185/CoFe20/Ru9/CoFe23/Cu23/CoFe13/NiFe25/cap50) were also identical. The only difference was the annealing field.

Figure 4.12 shows three Fresnel images taken for BSV films annealed at 250 Oe (figure 4.12a), 10 000 Oe (figure 4.12b) and 20 000 Oe (figure 4.12c). The images were taken at roughly the halfway point on the magnetising cycle where domain activity was a maximum. The BSV film annealed at 250 Oe and 10 000 Oe showed no significant differences in domain structure. The scale of the domains was quite small and irregular.

However, figure 4.12c shows a vast improvement in domain structure for the film annealed at 20 000 Oe. The size of the domains was larger and the walls were straighter.

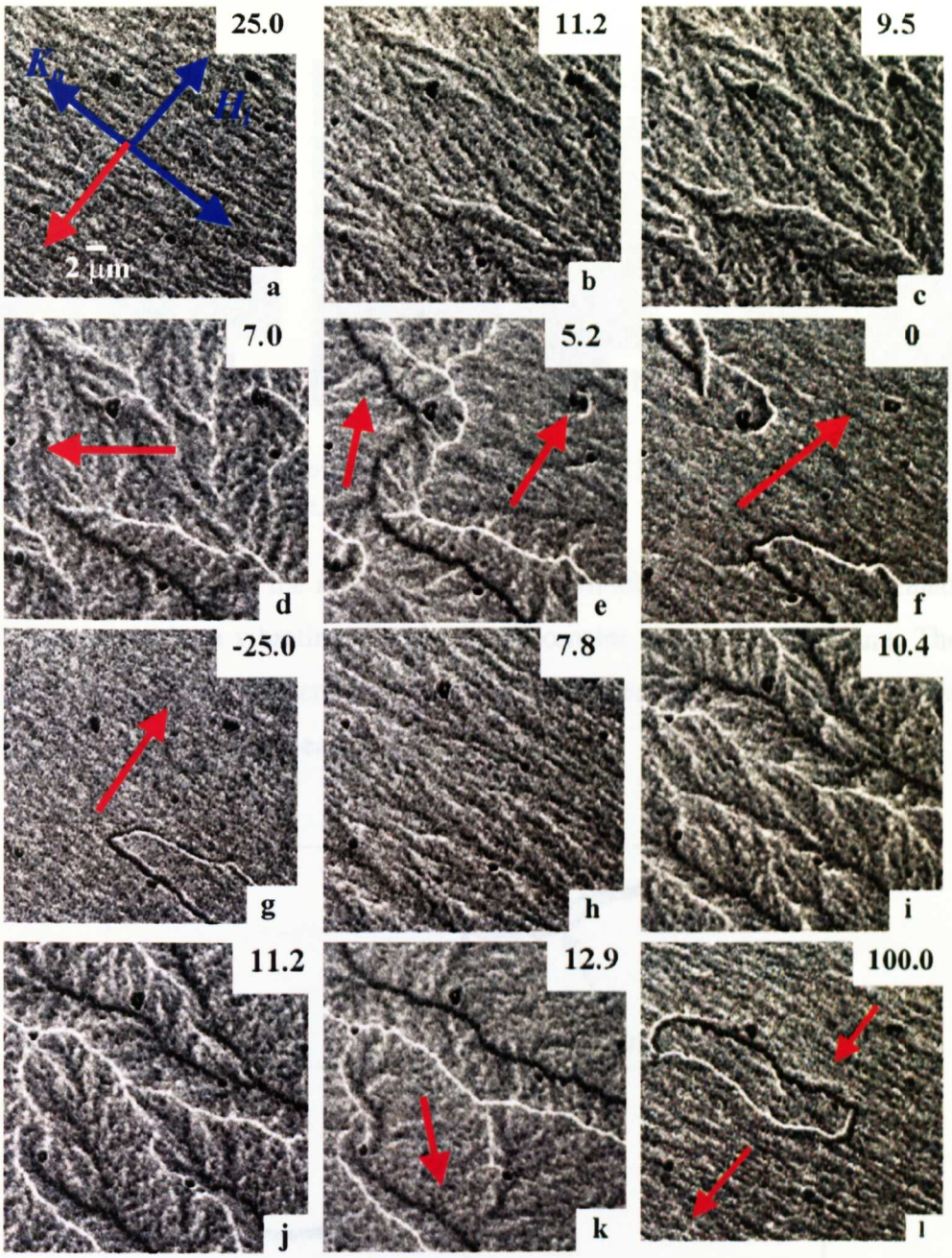

Figure 4.11: Fresnel image sequence for NiFe/CoFe (Ru7 unbalanced) SAF BSV. Red arrows denote the direction of magnetisation as determined from the magnetisation ripple.

The reason for improvement in domain structure could be that a high applied field during the annealing process will break the antiferromagnetic coupling between the PL and RL. When the SAF was heated to 300°C under a magnetic field, the exchange coupling between the AFM and PL ceased and the PL was no longer pinned. The antiparallel magnetisation of PL and RL will scissors towards the applied field

direction. They will reach saturation when the applied magnetic field was greater than the SAF saturation field of the SAF and they will align parallel to the field direction [14].

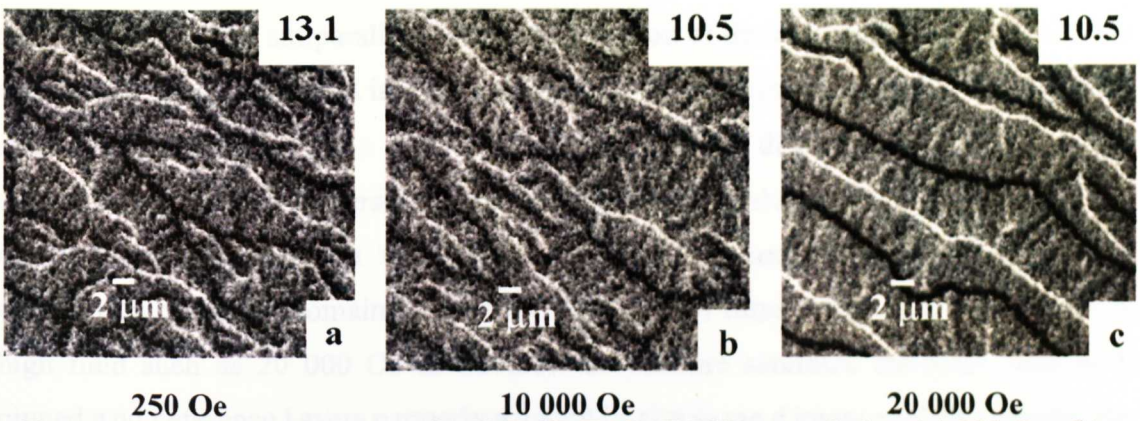

Figure 4.12: Domain structure for NiFe/CoFe SAF BSV annealed at (a) 250 Oe, (b) 10 000 Oe and (c) 20 000 Oe.

Figure 4.13 shows the *M* vs *H* loop of the NiFe/CoFe SAF BSV annealed at 20 000 Oe measured by a vibrating sample magnetometer at room temperature. The field applied during the measurement was 18 000 Oe. This was the maximum field available from the VSM used for the measurement.

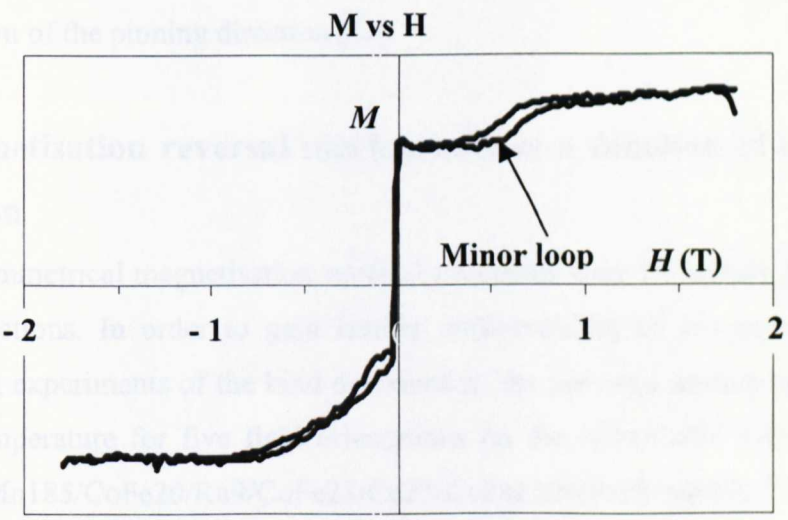

Figure 4.13: M vs H loop for NiFe/CoFe SAF BSV annealed at 2T. The loop was measured using a vibrating sample magnetometer.

The minor loop indicated by the arrow corresponds to a reversal in the magnetisation of the SAF structure. It shows that the saturation field of the SAF structure was above 10 000 Oe at room temperature. Therefore, an annealing field below 10 000 Oe may only partially break the indirect exchange coupling in the SAF. The magnetisation in the pinned and reference layers might break into domains or

become highly dispersed. Some of this dispersion could persist even after the field was removed. The reason being that when the film was cooled down under a magnetic field, the magnetisation of the PL was preserved due to the exchange bias coupling between the PL and AFM. Thus, when the field is removed, the RL magnetisation will rotate back and align itself antiparallel to the magnetisation of the PL. Since the magnetisation of the PL was not preserved in a saturation state, the magnetisation of the RL might not return to a uniform state. This might appear in the dispersion in the free layer magnetisation. Higher dispersion in the reference layer could lead to a greater interlayer coupling strength variation with the free layer. This could be the reason for the observation of greater domain noise in the free layer of films annealed at lower field. A high field such as 20 000 Oe at elevated temperature saturates the SAF, with both pinned and reference layers properly aligned in the same direction. This reduced the dispersion in the pinned and reference layers after annealing. As a result, a better defined unidirectional anisotropy could be produced. So, a well behaved magnetisation reversal process was observed in the free layer.

It was reported by Lu et al. that spin flop could occur during the magnetic annealing process. It happens because the annealing field was not strong enough to overcome the interlayer coupling between the PL and RL. Spin flop causes misalignment of the pinning direction [15].

4.4: Magnetisation reversal mechanisms as a function of applied field orientation

Asymmetrical magnetisation reversal processes were frequently observed in the previous sections. In order to gain further understanding of the asymmetry, in-situ magnetising experiments of the kind described in the previous section were carried out at room temperature for five field orientations on the NiFe/CoFe SAF BSV sample, (seed60/PtMn185/CoFe20/Ru9/CoFe23/Cu23/CoFe13/NiFe25/cap50). The orientations θ were all approximately antiparallel to the induced unidirectional anisotropy. It was difficult to set the angle of the applied field precisely with respect to the unidirectional induced anisotropy although subsequent changes in field orientation can be made with an accuracy of ±0.5°. Thus for now I denote the initial orientation (measured with respect to the unidirectional anisotropy) as θ_o in which case the remaining four field orientations were at $\theta_o + 4°$, $\theta_o + 6°$, $\theta_o + 8°$ and $\theta_o + 10°$. θ_o was chosen such that $\theta_o < 180° < \theta_o + 10°$. Extensive Fresnel image sequences were obtained in each case.

Figure 4.14 shows the free layer magnetisation reversal process when $\theta = \theta_o$. In a typical cycle the field in the plane of the specimen was varied from +86 Oe to -86 Oe and back again. Images shown here illustrate the most important stages of the reversal process. When the external field was reduced from a high positive value reversal proceeded essentially by coherent rotation in a clockwise sense, figures 4.14a-e. A few small domains can be seen in figure 4.14b but their presence was not significant and they vanished rapidly. That they formed at all is most likely due to the modest dispersion present in the film. By the time the field was reduced to 0 Oe, the magnetisation had rotated through almost 180°. However the ripple orientation in figures 4.14a and 4.14e are not parallel to each other and a negative field was required to effect the complete reversal. The return path was once again by coherent rotation and followed the outward path closely, figures 4.14f-h. Thus the magnetisation rotated in the anticlockwise sense for the return part of the cycle.

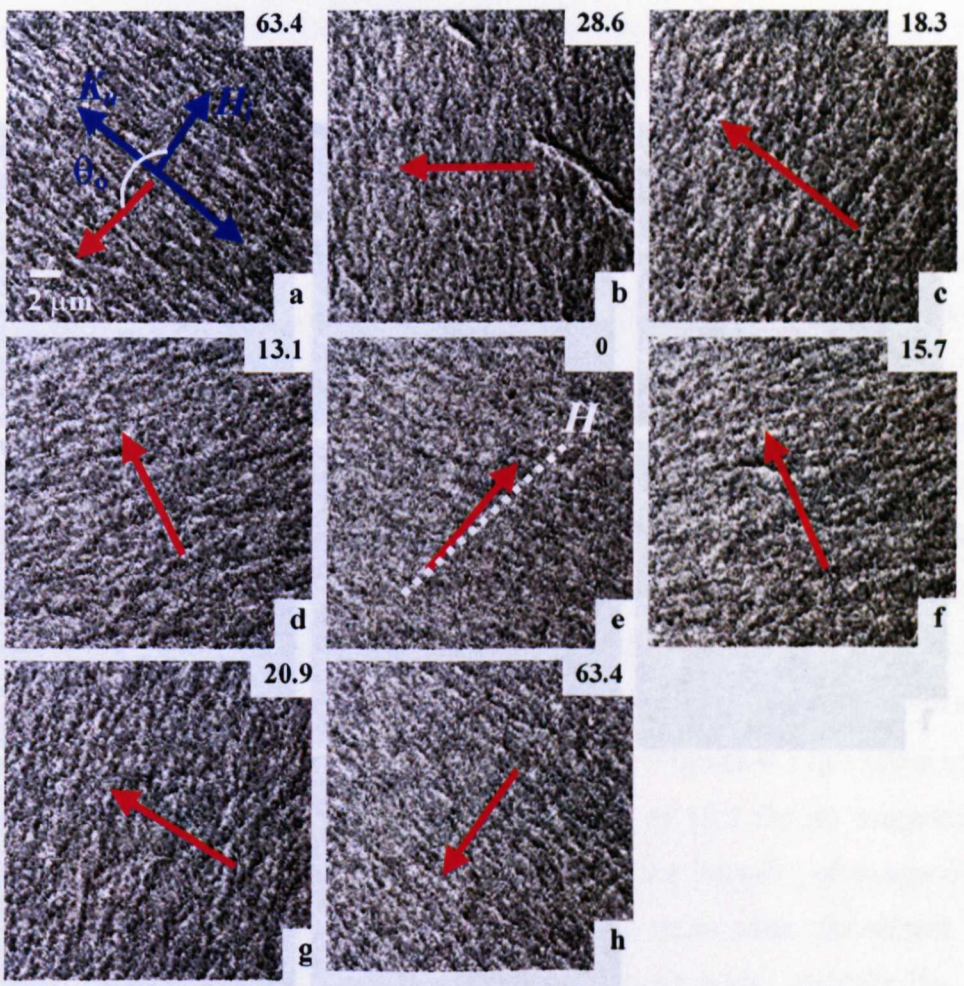

Figure 4.14: Fresnel image sequence showing the free layer magnetisation reversal process when $\theta = \theta_o$. Red arrows denote the direction of magnetisation as determined from the magnetisation ripple.

When the orientation of the applied field was changed to $\theta_o + 4°$, a significantly different reversal mechanism was observed as can be seen in figure 4.15. In this instance the field and the preferred orientation of the magnetisation in the free layer were more closely aligned. As the field was reduced from a high positive value, the film split into a multi-domain state, figure 4.15b. These domains were created by the magnetisation rotating in opposite senses in different local regions of the film. Thus, the orientation of the domain walls was parallel to the uniaxial anisotropy axis, and hence approximately orthogonal to the applied field direction. As such, the domain walls were highly immobile with magnetisation rotation taking place within each domain as the field was further reduced, figure 4.15c. As the field approached zero, a rapid collapse of domain walls ensued until the free layer was once again in a single domain state, this time with its magnetisation lying close to the unidirectional anisotropy direction, figure 4.15e. Such behaviour closely resembles a hard axis magnetisation process in a single layer film and has been observed previously in the free layer of spin-valves with crossed anisotropy.

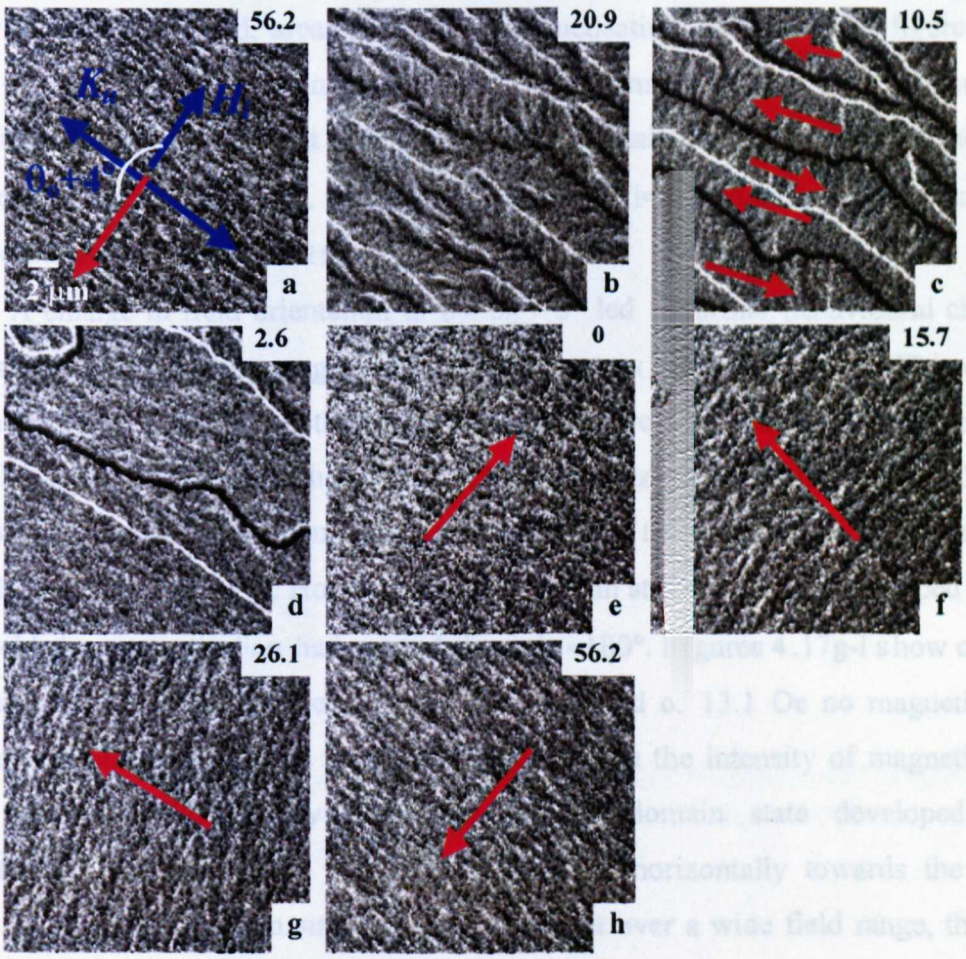

Figure 4.15: Fresnel image sequence showing the free layer magnetisation reversal process when $\theta = \theta_o + 4°$. Red arrows denote the direction of magnetisation as determined from the magnetisation ripple.

The magnetisation process on the return path was completely different. Here the magnetisation simply underwent a smooth coherent rotation in an anticlockwise sense as the field was increased, figures 4.15f-h. No multi-domain state was formed. Thus, for this field orientation, the cycle was asymmetrical with domain formation on the forward path and coherent rotation on the return paths.

Asymmetrical behaviour was again observed for the case $\theta = \theta_o + 6°$ as figure 4.16 shows. As the field was reduced, reversal began by magnetisation rotation in an anticlockwise sense, figures 4.16a-c. However, as was the case in figure 4.16b, a number of short-lived domains formed, but at a field of 15.7 Oe, the film was once again in a single domain state. The magnetisation was oriented approximately orthogonal to the original direction. A further reduction in field led to the formation of a much more complex domain structure, figure 4.16d. Although the structure is very irregular it is possible to identify domains in which the magnetisation is approximately vertically upwards whilst elsewhere it is virtually unchanged in direction from that in figure 4.16c. Thus the magnetisation in parts of the film had switched through angles >90° and, as such, had overshot the unidirectional anisotropy direction by ≈45°. As the field was further reduced, areas supporting magnetisation oriented as in figure 4.16c shrank and the magnetisation in the most part of the film rotated clockwise towards the field direction, figure 4.16f. At zero field a single domain state once again existed. As was the case when $\theta = \theta_o + 4°$, the return cycle simply involved coherent rotation in an anticlockwise sense, figures 4.16g-j.

A change in field orientation to $\theta = \theta_o + 8°$ led to further behavioural changes with asymmetrical processes again observed on outward and return paths. This can be seen in figure 4.17. The magnetisation in the free layer rotated coherently anticlockwise when the applied field was reduced from a high positive value, figures 4.17a-f. Ripple contrast (and hence dispersion) was strongest when the magnetisation had rotated through ≈135°, figure 4.17d. However, a multi-domain structure never developed and at zero field the magnetisation had rotated through ≈180°. Figures 4.17g-l show clearly that domains formed on the return path. Up to a field of 13.1 Oe no magnetisation rotation was observed and the principal change was in the intensity of magnetisation ripple, figure 4.17g. Shortly after this, a multi-domain state developed with magnetisation pointing either vertically upwards or horizontally towards the right, figures 4.17h,i. This domain structure did not persist over a wide field range, the film reverting to a near single domain state by a field of 18.3 Oe, figure 4.17j. Thereafter the

return path was completed by simple magnetisation rotation through ≈90° in an anticlockwise sense.

Increasing θ to θ_o+ 10° led to a return to magnetisation rotation on both parts of the magnetisation cycle. On the outward and return paths, rotation was in the anticlockwise and clockwise sense respectively.

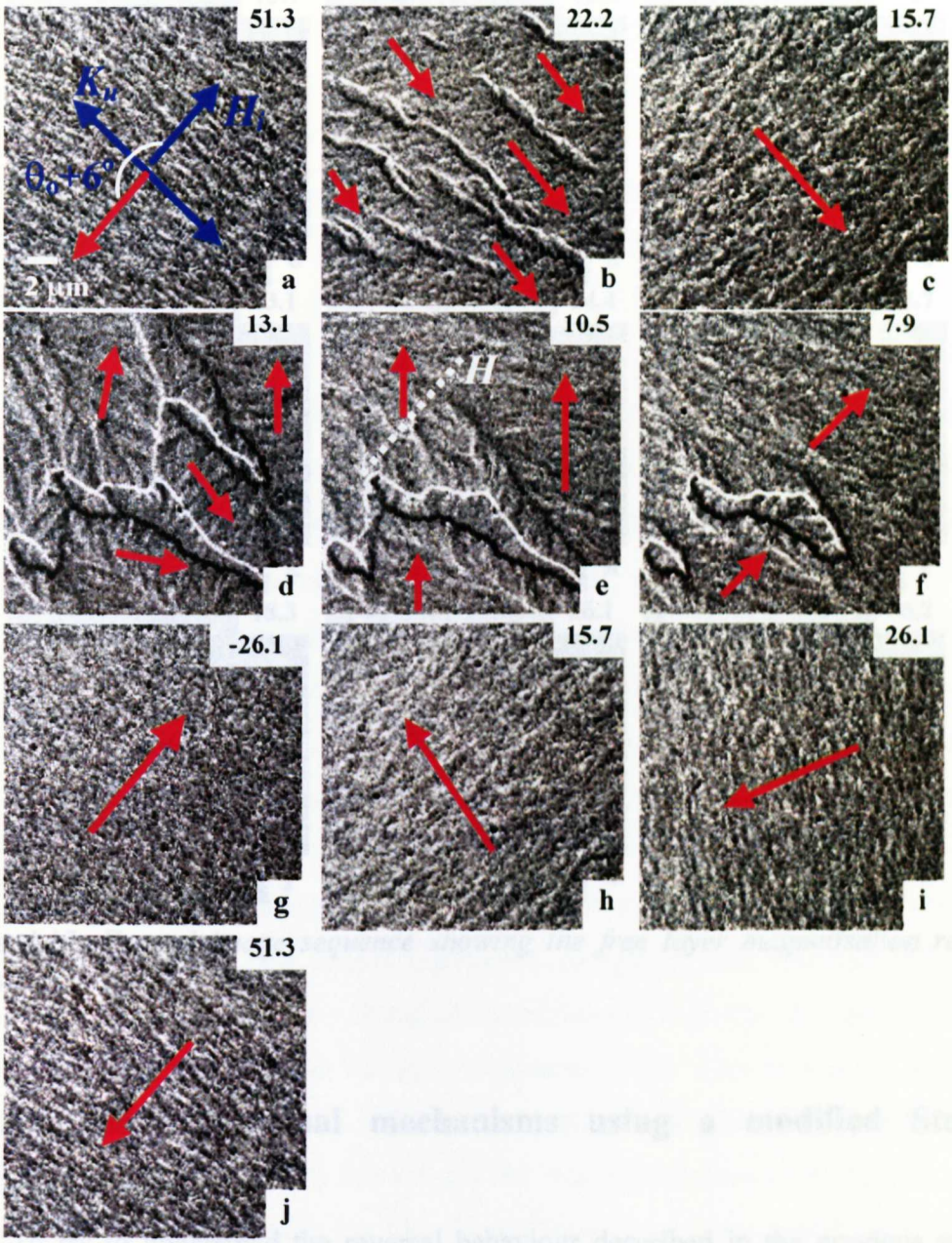

Figure 4.16: Fresnel image sequence showing the free layer magnetisation reversal process when $\theta = \theta_o + 6°$. Red arrows denote the direction of magnetisation as determined from the magnetisation ripple.

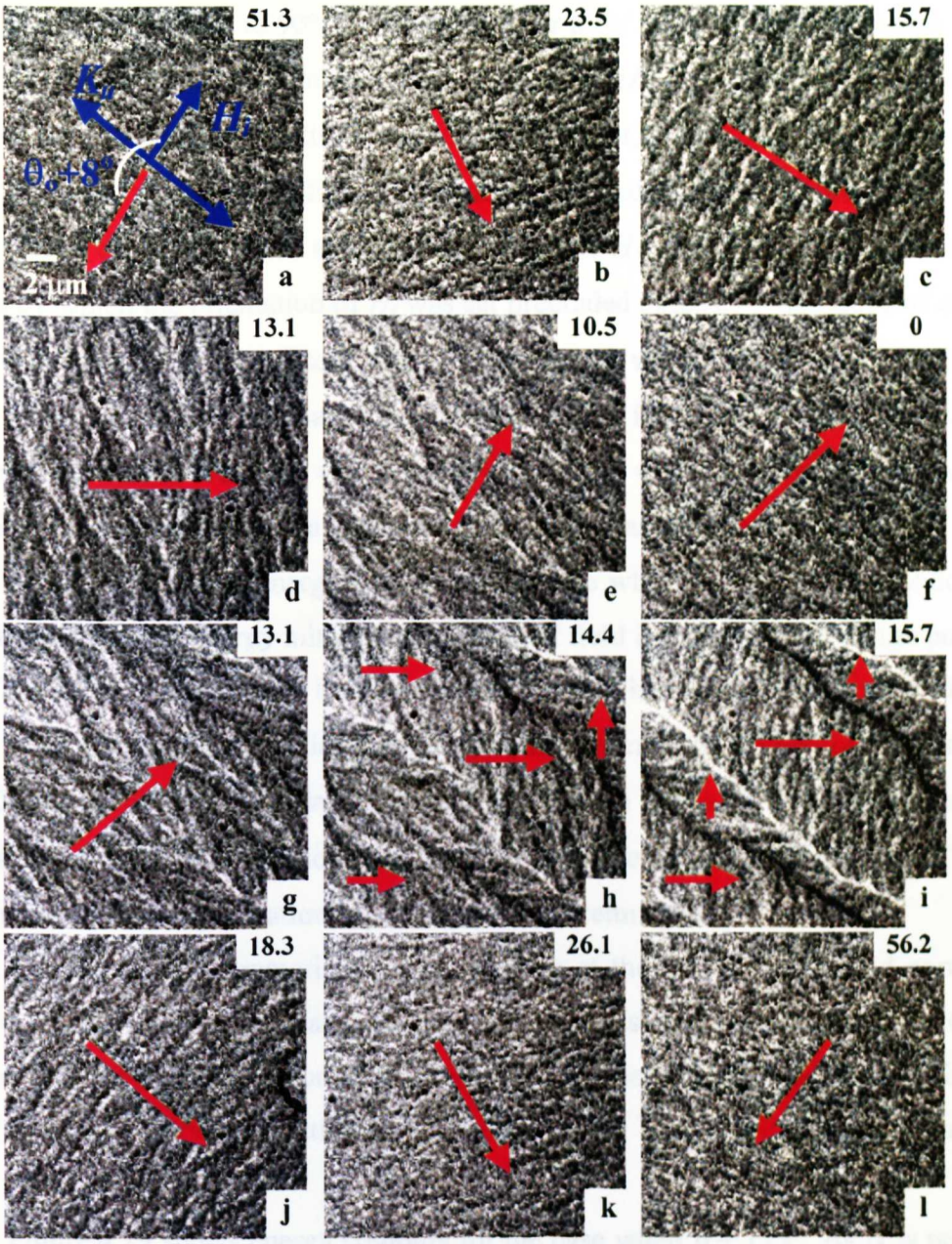

Figure 4.17: Fresnel image sequence showing the free layer magnetisation reversal process when $\theta = \theta_o + 8°$.

4.5. Analysis of reversal mechanisms using a modified Stoner-Wohlfarth model

To try to understand the reversal behaviour described in the previous section and, in particular the unexpected asymmetrical magnetisation processes, guidance was sought from the modified Stoner-Wohlfarth model. Note that the unidirectional anisotropy direction is used as the reference from which angles are measured, consistent with the practice of the previous section.

Initially ε was set to 90°, as appropriate for a SV with crossed anisotropy. With this condition imposed no combination of values for H_K and H_i could be found that predicted asymmetrical magnetisation reversal. However, allowing ε to depart modestly from 90° opened up the possibility of asymmetric reversal as described below.

Based on $MR(H)$ data, approximate values of H_K and H_i were known and the process by which the orientation of H_i was set precluded extensive variations of ε away from 90°. Variation of parameters about their expected values led to a set of preferred values that allowed the principal phenomena described in section 4.4 to be explained. The optimum values were H_K = 8 Oe, H_i = 12 Oe, ε = 87° and θ_o = 175°. All the families of energy curves shown in figures 4.18-21 are based on these values.

Figure 4.18 shows energy curves for the case where $\theta = \theta_o$ = 175°. Solid dots show the positions of energy minima as the applied field is reduced from a high positive value. The locus of the minima is shown on the figure. Thus as the field is reduced from 30 Oe to –2 Oe the magnetisation rotates smoothly from ≈180° to ≈0° on the outward path. On the return path the relevant energy minima are indicated by open circles and, for this value of θ, their locations are identical to those on the outward path. Thus a smooth rotation of magnetisation is predicted for the return path.

The results are summarised in the diagram at the bottom right-hand corner of figure 4.18. As noted, it indicates reversal by magnetisation rotation for each of the outward and return paths. Moreover, the model predicts clockwise rotation for the former and anticlockwise rotation on the return. This agrees with the experimental results shown in figure 4.14.

Figure 4.19 shows energy contours for the case when θ = 179°. As H is reduced from 22 Oe to 18 Oe, two almost equivalent energy minima develop. Thus two orientations of magnetisation are favoured approximately equally and, unsurprisingly, different local areas of film can be found supporting each. This is exactly what was observed in figure 4.15. There is no simple way to predict which orientation will be found in which area; presumably this reflects the local distribution of crystallites, which are responsible for dispersion in the film. Nonetheless we can see how a multi-domain state develops and why the orientation of magnetisation in successive domains rotates alternately clockwise and anticlockwise. As the field is reduced to 12 Oe, the positions of the energy minima in the model are approximately at 90° and –90° (270°). This agrees well with experiment where figure 4.15c shows the magnetisation in the domains to lie approximately orthogonal to the initial direction. At lower fields the energy

minima become increasingly asymmetric until at 4 Oe the barrier separating them disappears leaving a single global minimum.

The return path is indicated by the open circles. As the field is increased from 4 Oe to 8 Oe there is no incentive for different local areas of film to respond differently. For the 8 Oe case, although two minima have formed, the minimum at $\phi \approx 60^{\circ}$ is substantially lower than that at $\phi \approx -60^{\circ}$ with the result that the magnetisation throughout the film favours the former. Thus reversal on the return path is by coherent rotation in an anticlockwise sense. Again, the overall reversal mechanism is summarised in the diagram at the bottom right hand corner of figure 4.19 and is in good agreement with experiment.

With θ set to 181° the model provides an explanation for most, but not all, the experimental phenomena observed in the third reversal experiment, figure 4.16. The relevant energy contours are shown in figure 4.20. Upon reduction of H the magnetisation follows the global energy minimum leading to anticlockwise magnetisation rotation. However, at $H = 6$ Oe, the minimum in which the magnetisation lies becomes a local minimum separated from the global minimum, some 90° away by only a very shallow energy barrier which completely disappears when the field is further reduced. Thus a distinct jump in magnetisation direction would be expected. In practice a marked change in magnetisation direction took place over a small field range within which a multi-domain state existed. Moreover, both model and experiment showed the magnetisation after the jump to lie beyond the applied field direction so that as the field fell further the final stages of reversal involved coherent rotation in a clockwise sense.

The three stages of the reversal are shown schematically in the small inset diagram in figure 4.20. Whilst these generally give the correct picture, it should be noted that the field at which the jump is expected does not agree particularly well with the field range over which the complex domain structure was observed experimentally. On the return path, the model predicts anticlockwise rotation followed by a jump with a similar overshoot to that on the outward path, the process finishing again with rotation into the field direction. Experimentally, the predicted anticlockwise rotation was observed but no jump was seen nor did a multi-domain structure form at any stage. A discussion of possible sources for such discrepancies is described in the final section.

In the final case $\theta = 183°$ and appropriate energy contours are displayed in figure 4.21. On the outward path, the magnetisation follows the energy minima shown by the solid dots. This corresponds to an anticlockwise rotation in agreement with

experimental observation, figure 4.17. Rather flat energy contours for fields of 4 Oe and 6 Oe suggest that dispersion should be appreciable during the final 45° of the rotation. This is indeed what was observed in figure 4.17d but the fields involved were rather higher than those predicted by the model.

As the field is increased on the return path two alternative routes seem attractive. The shallow minima that develop for $H = 6$ Oe are of approximately equal depth so it is reasonable to expect that examples of each magnetisation orientation will be found in different local areas. A similar occurrence was discussed in connection with the outward path for the case where $\theta = 179°$. The resulting domain structure would be expected to persist until one of the minima disappears, and this occurs for a field ≈16 Oe. Thereafter the model predicts that the magnetisation rotates clockwise with increasing field back to its original orientation. Experiment shows that the domain structure disappears at a field ≈18 Oe and that the final part of the reversal is by clockwise rotation. Thus once again the principal features of the reversal are well accounted for though imperfect agreement exists between the predicted and observed fields at which prominent stages in the reversal occur.

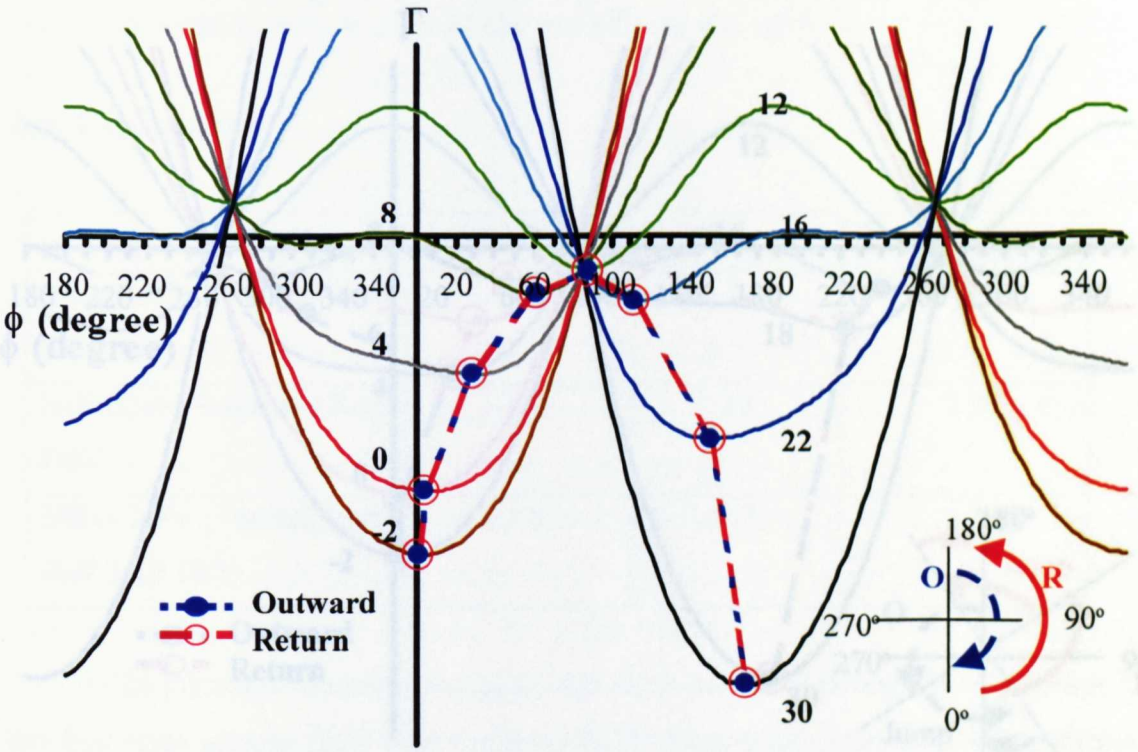

Figure 4.18: Energy contours deduced from the modified Stoner-Wohlfarth model with $H_K = 8$ Oe, $H_i = 12$ Oe, $\varepsilon = 87°$ and $\theta = 175°$.

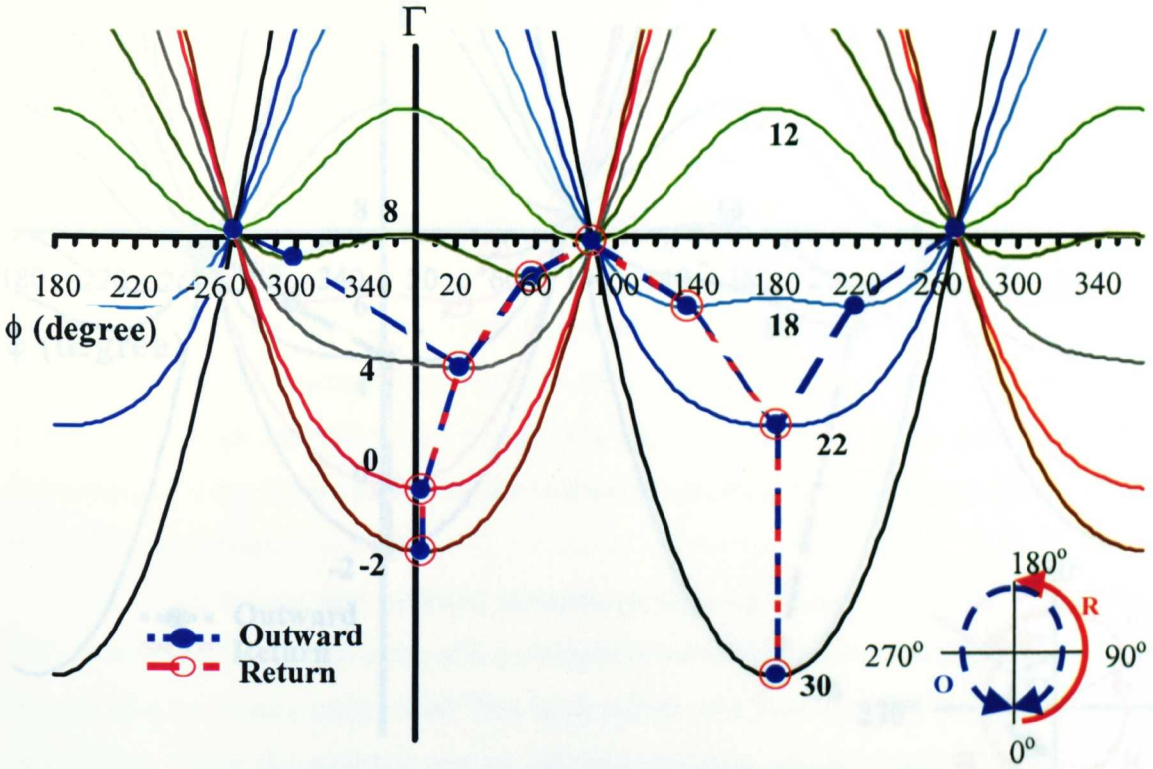

Figure 4.19: Energy contours deduced from the modified Stoner-Wohlfarth model with H_K = 8 Oe, H_i = 12 Oe, $\varepsilon = 87^o$ and $\theta = 179^o$.

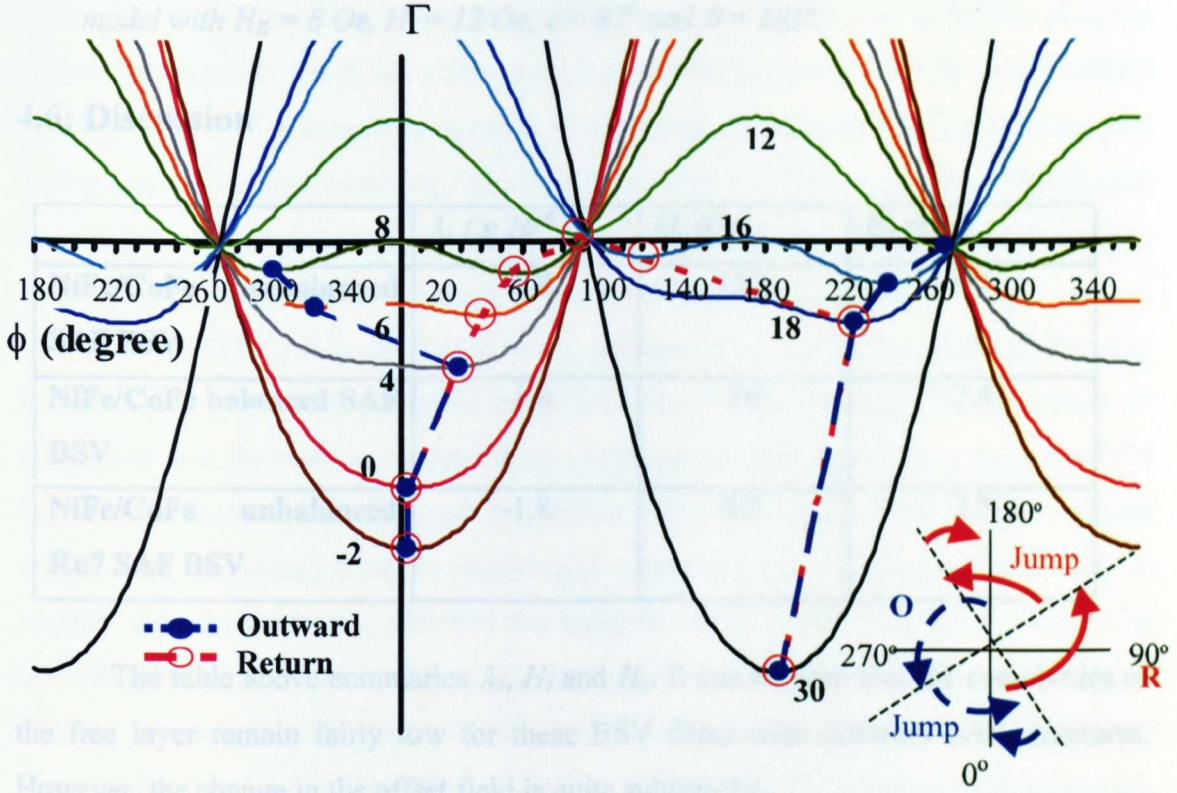

Figure 4.20: Energy contours deduced from the modified Stoner-Wohlfarth model with H_K = 8 Oe, H_i = 12 Oe, $\varepsilon = 87^o$ and $\theta = 181^o$.

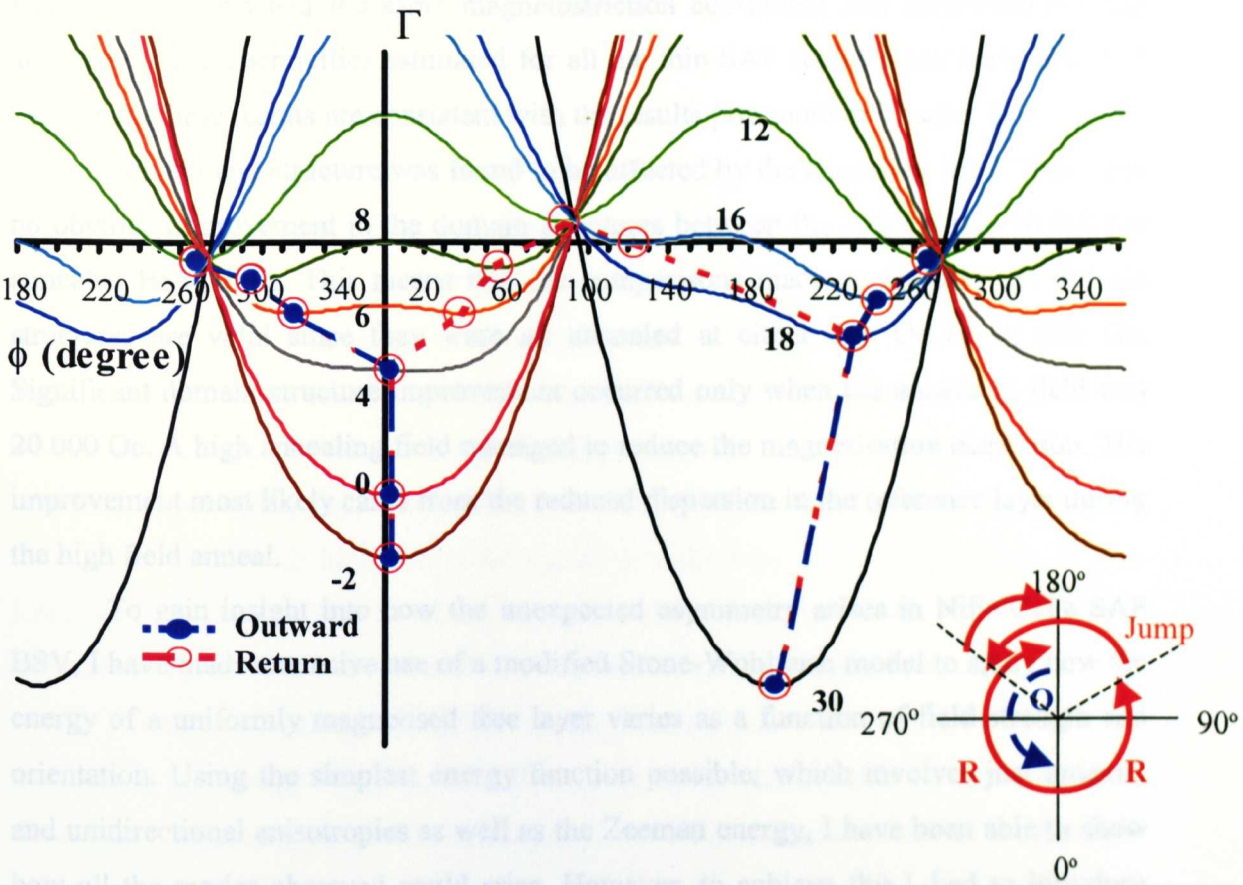

Figure 4.21: Energy contours deduced from the modified Stoner-Wohlfarth model with H_K = 8 Oe, H_i = 12 Oe, $\varepsilon = 87^o$ and $\theta = 183^o$.

4.6: Discussion

	λ_s (x 10^{-6})	H_i (Oe)	H_c (Oe)
NiFe/CoFe unbalanced SAF BSV	-1.8	15.6	< 1
NiFe/CoFe balanced SAF BSV	-1.8	20	2.4
NiFe/CoFe unbalanced Ru7 SAF BSV	-1.8	8.5	2.5

The table above summaries λ_s, H_i and H_c. It can be seen that the coercivities of the free layer remain fairly low for these BSV films with different SAF structures. However, the change in the offset field is quite substantial.

It was found in the experiments that there was no significant difference in the free layer reversal process for BSV films with various SAF structures. There was no great difference between the sizes of the domains either. This might be attributed to the

fact that the films had the same magnetostriction coefficient and magnetocrystalline anisotropy. The coercivities estimated for all the thin SAF samples are fairly low, < 3 Oe. Again, these results are consistent with the results presented in Chapter 3.

The domain structure was found to be affected by the annealing field. There was no obvious improvement in the domain structures between the 250 Oe and 10 000 Oe annealed BSV films. This means that the comparisons made so far between domain structures are valid since they were all annealed at either 250 Oe or 10 000 Oe. Significant domain structure improvement occurred only when the annealing field was 20 000 Oe. A high annealing field managed to reduce the magnetisation dispersion. The improvement most likely came from the reduced dispersion in the reference layer during the high field anneal.

To gain insight into how the unexpected asymmetry arises in NiFe/CoFe SAF BSV, I have made extensive use of a modified Stone-Wohlfarth model to study how the energy of a uniformly magnetised free layer varies as a function of field strength and orientation. Using the simplest energy function possible, which involves just uniaxial and unidirectional anisotropies as well as the Zeeman energy, I have been able to show how all the modes observed could arise. However, to achieve this I had to introduce modest symmetry breaking so that the unidirectional and uniaxial anisotropies were not exactly orthogonal. Such an offset could arise, for example, due to unintentional misalignment of the sample or modest realignment of the uniaxial anisotropies axis during post-deposition annealing [16,17]. It is reported in [18] that canting of the pinned and reference layers can occur in spin-valve films as well as the patterned spin-valves. Thermal-induced canting in the pinning field direction is also reported in [19].

Reversal by coherent rotation of the magnetisation and by mechanisms that may involve sharp irreversible jumps in magnetisation are both predicted by the model. In the former case the position of the energy minimum changes smoothly with field whilst in the latter the magnetisation gets trapped in a local minimum from which it cannot escape until the energy barrier separating it from the global minimum disappears. In practice domain processes, whereby the magnetic state of the film can no longer be described by a single parameter, frequently come into play to facilitate discontinuous changes in magnetisation direction. These frequently occur at fields lower than those required for the abrupt changes in orientation predicted by the single parameter model. Nonetheless the prediction of a discontinuous jump can be used as an indicator that domain processes might be observed in practice. Moreover the model gives an

indication of the uniformly magnetised states that exist before and after the jump takes place.

Not only did the model predict correctly the way in which the reversal took place in the majority of cases but there was often fair agreement between the predicted and observed fields at which key processes occurred. That the quantitative agreement was not better is hardly surprising given the simplicity of the model. Inevitably the model could not provide direct information on the formation of domains although, as we have shown, study of the energy contours allowed educated guesses to be made as to when and what type of domain structure might develop. Another omission that cannot be incorporated is dispersion in the film due to its polycrystalline nature.

For films with high magnetocrystalline anisotropy in the crystallites or with large magnetostriction this becomes increasingly problematic though for the soft free layer of the SV studied here the model proved sufficiently robust to be useful.

Another possible source of discrepancy is the fact that only three terms were included in the energy function. Effectively this means that there is no contribution to the energy variation from the pinned layer of the SV, an assumption that is only valid for a completely "rigid" pinned layer – that is one in which the magnetisation is completely unaffected by fields of the strength applied here. Such an assumption is probably reasonable for the SV investigated which was pinned by a SAF.

References:

[1] K. Ratzke, M. J. Hall, D. B. Jardine, W. C. Shih, R. E. Somekh, A. L. Greer, J. Magn. Magn. Mater. 204 61 (1999),

[2] K. Inomata, T. Nozaki, N. Tezuka, and S. Sugimoto, Appl. Phys. Lett. 81 310 (2002)

[3] D. V. Dimitrov, J. Van Ek, Y. F. Li, J. Q. Xiao, J. Magn. Magn. Mater. 218 273 (2000),

[4] Y. Huai, J. Zhang, G. W. Anderson, P. Rama, S. Funada, C. Y. Hung, M. Zhao, J. Appl. Phys. 85 5528 (1999),

[5] D. V. Dimitrov, J. Van Ek, Y. F. Li, J. Q. Xiao, J. Appl. Phys. 87 6427 (2000),

[6] A. de Morais and A. K. Petford-Long, J Appl. Phys. 87 6977 (2000),

[7] M. Saito, N. Hasegawa, F. Koike, H. Seki and T. Kuriyama, J. Appl. Phys. 85 4928 (1999),

[8] J. M. Daughton, J. Magn. Magn. Mater. 192 334 (1999),

[9] J. Hong, K. Noma, H. Kanai, J. Appl. Phys. 89 6940 (2001),

[10] S. Jo and M. Seigler, J. Appl. Phys. 91 7110 (2002),

[11] J. L. Leal, M. H. Kryder, IEEE Trans. Magn. 32 3434 (1996),

[12] S. S. P. Parkin, N. More, and K. P. Roche, Phys. Rev. Lett. 64 2304 (1990),

[13] B Dieny, J. Magn. Magn. Matter 136 335 (1994),

[14] H. C. Tong, C. Qian, L. Miloslavsky, S. Funada, X. Shi, F. Liu, and S. Dey, J. Appl. Phys. 87 5055 (2000),

[15] Z. Lu, G. Pan, A. Al-Jibouri and M. Hoban, J. Appl. Phys. 91 7116 (2002),

[16] L. Baril, D. Mauri, J. McCord, S. Gider, and T. Lin, J. Appl. Phys. 89 1320 (2001),

[17] S. Uchiyama, M. Takayasu, and T. Fujii, IEEE Trans. Magn. MAG-10 548 (1974),

[18] H. S. Cho, J. Chen, S. Cool, R. Michel, and N. Tabat, J. Appl. Phys. 87 4939 (2000),

[19] Y. Wu, G. Han, T. Chong, J. Appl. Phys. 89 7616 (2001).

CHAPTER 5: THERMAL EFFECTS ON THE FREE LAYER MAGNETISATION REVERSAL MECHANISM OF SPIN-VALVES

Introduction

The effect of temperature on the magnetisation reversal of the free layer of SVs is studied in this chapter. Understanding how SVs react to heat gives invaluable information for further SV development to improve their performance [1-8]. The thermal stability of a SV is one of the crucial factors determining the performance of the SV as a read back sensor. There are various heating sources of spin-valve sensor in a computer disk drive such as the dc interconnecting heating, dc write coil heating and write-to-read cross talk of interconnects [9]. The actual sensor device in a computer disk drive unit may be subjected to temperatures of 100-150°C [10]. Hence, understanding its response to heat is vital.

In-situ magnetising experiments were carried out for various temperatures and time durations. The effect of heat on the free layer reversal process is described in section 5.1 and section 5.2. An insight into why the reversal mode varied in the way it did was obtained using the modified Stoner-Wohlfarth model.

In-situ TEM annealing experiments were also carried out to study the behaviour of the SV film before and after the post-deposition anneal process. In section 5.3, the free layer reversal process is studied for an unannealed CoFe AFM TSV film. The film was annealed in the TEM to induce unidirectional anisotropy, and the reversal after annealing is discussed in section 5.4. Section 5.5 shows another in-situ TEM anneal experiment on the NiFe/CoFe SAF TSV. The experiment successfully reproduced the result observed in the film annealed using the conventional annealing oven.

5.1: Thermal effects on NiFe/CoFe SAF BSV

Thermal effects on the reversal mechanism on the conventional AFM SV films have been studied in [11,12]. It was also reported in [13] that the presence of a Ru layer in a SAF SV not only acts as a spacer inducing AF coupling but also behaves as a good diffusion barrier for Mn. Thermal degradation of SVs due to Mn diffusion is discussed in [14].

The NiFe/CoFe SAF BSV film was used in this experiment. The film composition is seed60/PtMn185/CoFe20/Ru9/CoFe23/Cu23/CoFe13/NiFe25/cap50. The film was annealed at 300°C in a field of 20 000 Oe for four hours. It is similar to

the film discussed in Chapter 4 section 4.4. The heating experiment was carried out using a commercial TEM heating holder where the temperature is monitored by a thermocouple on the specimen holder. The film was aligned so that the applied field was orientated along the offset field direction. Since the heating rod had no rotation mechanism, the film was re-aligned a few times until magnetic domains were observed during the magnetising cycle. This ensured that the applied and offset field direction were closely coincident. Given the difficulty in making the alignment, an element of luck was involved.

A Fresnel image sequence was recorded at room temperature (the ambient temperature within the TEM column). The temperature was then increased to 100°C at a rate of 10°C per minute. The film was left for one hour at 100°C before another Fresnel image sequence was recorded. Immediately after the magnetising sequence was recorded at 100°C, the temperature was increased to 200°C at the same rate. Three Fresnel image sequences were recorded at time intervals of one, two and three hours at a temperature of 200°C. The rod was left at 0° tilt at all times except when a magnetising experiment was carried out. The purpose was to avoid having any in-plane field on the film during the heating, which might affect the exchange bias layer. A total of five Fresnel image sequences were recorded.

5.1.1: Room temperature

The Fresnel image sequence recorded at room temperature is shown in figure 5.1. When the applied field was reduced, magnetisation in the free layer split into domains, figure 5.1a-c. The magnetisation in alternate domains rotated in opposite directions. Figure 5.1c shows where the magnetisation in the domain had rotated by about 90° from the initial direction. These domains vanished as the magnetisation increasingly aligned with the applied field direction. Almost all domains had collapsed when the field was reduced to zero. However, some domains turned into 360° loops as shown in figure 5.1e. The loop shown collapsed when the field was increased parallel to the offset field direction. The weak ripple contrast at saturation in figure 5.1f implies a weak localised dispersion.

On the return path, no ripple rotation was observed when the field was reduced to zero. This suggests that the applied field was aligned almost along the offset field direction. Magnetisation began to rotate in the clockwise sense when the field was increased antiparallel to the offset field direction. The reversal process was purely coherent rotation with no domain presence. Figure 5.1i shows the midway point on the

return path at 16.5 Oe. Comparing this to the midway point on the outward path allows the offset field and coercivity to be estimated at ≈17 Oe and ≈ 0.5 Oe.

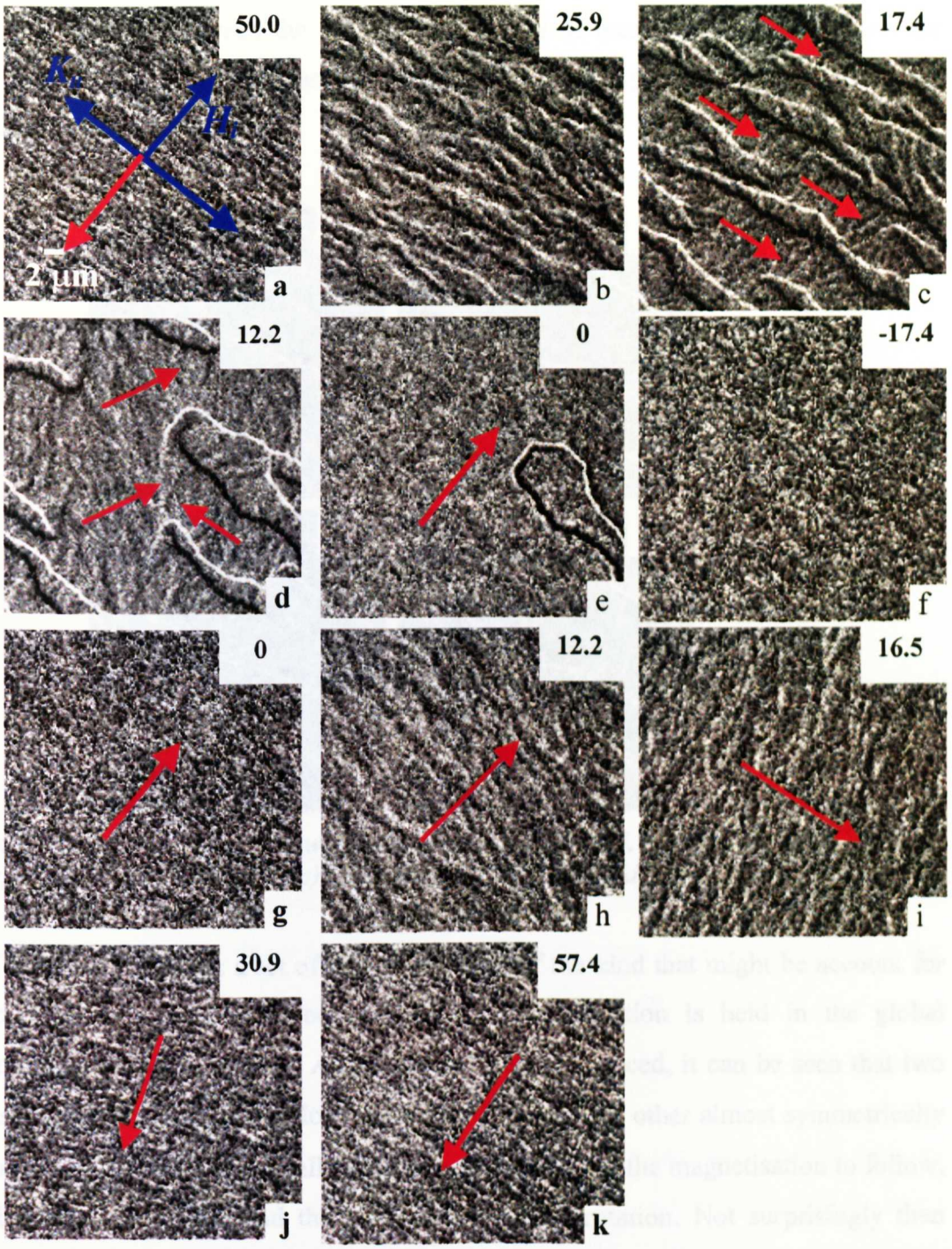

Figure 5.1: Fresnel image sequence for NiFe/CoFe SAF BSV at room temperature. It shows the symmetrical splitting rotation on the outward path and clockwise coherent rotation on the return path. Red arrows denote the direction of magnetisation as determined from the magnetisation ripple.

5.1.2: Domain structure at 100°C and 200°C

The free layer magnetisation reversal mechanisms recorded after the film was held at 100°C for one hour and at 200°C for one, two and three hours showed no

difference. All reversals were asymmetrical with domain formation on the outward path and coherent clockwise rotation on the return path. Figure 5.2 shows all the domain structures observed at 17.4 Oe at various temperature and time intervals. There is no obvious difference between the size and orientation of these domains. Therefore, the NiFe/CoFe SAF BSV is a thermally stable film for temperatures up to 200°C for durations of three hours.

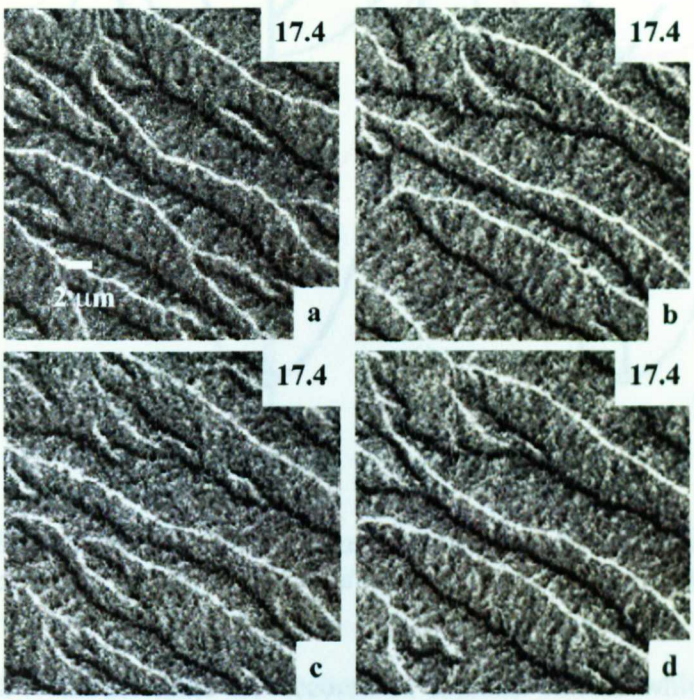

Figure 5.2: Fresnel images show the domain structure at 17.4 Oe for (a) 100°C for one hour, (b) 200°C for one hour, (c) 200°C for two hours and (d) 200°C for three hours.

Figure 5.3 shows a set of energy contours of the kind that might be account for the reversal behaviour observed. Initially the magnetisation is held in the global minimum at $\phi = 180°$, point P. As the reverse field is reduced, it can be seen that two almost equivalent minima develop, one at $\phi < 180°$ and the other almost symmetrically disposed at $\phi > 180°$. Thus equally attractive paths exist for the magnetisation to follow, one involving clockwise and the other anticlockwise rotation. Not surprisingly then different local areas of film begin to rotate in each direction with the result that domain walls form and these lie on average perpendicular to *H*. This is in accord with experimental observation. Once the reversal is complete the magnetisation lies at $\phi = 0°$.

Although two local minima also develop on the reverse path, it is apparent that in this instance one is more attractive than the other from the outset. Hence no multi-domain state forms and the return part of the cycle is accomplished by coherent rotation. Again this is in accord with observation for asymmetric reversal.

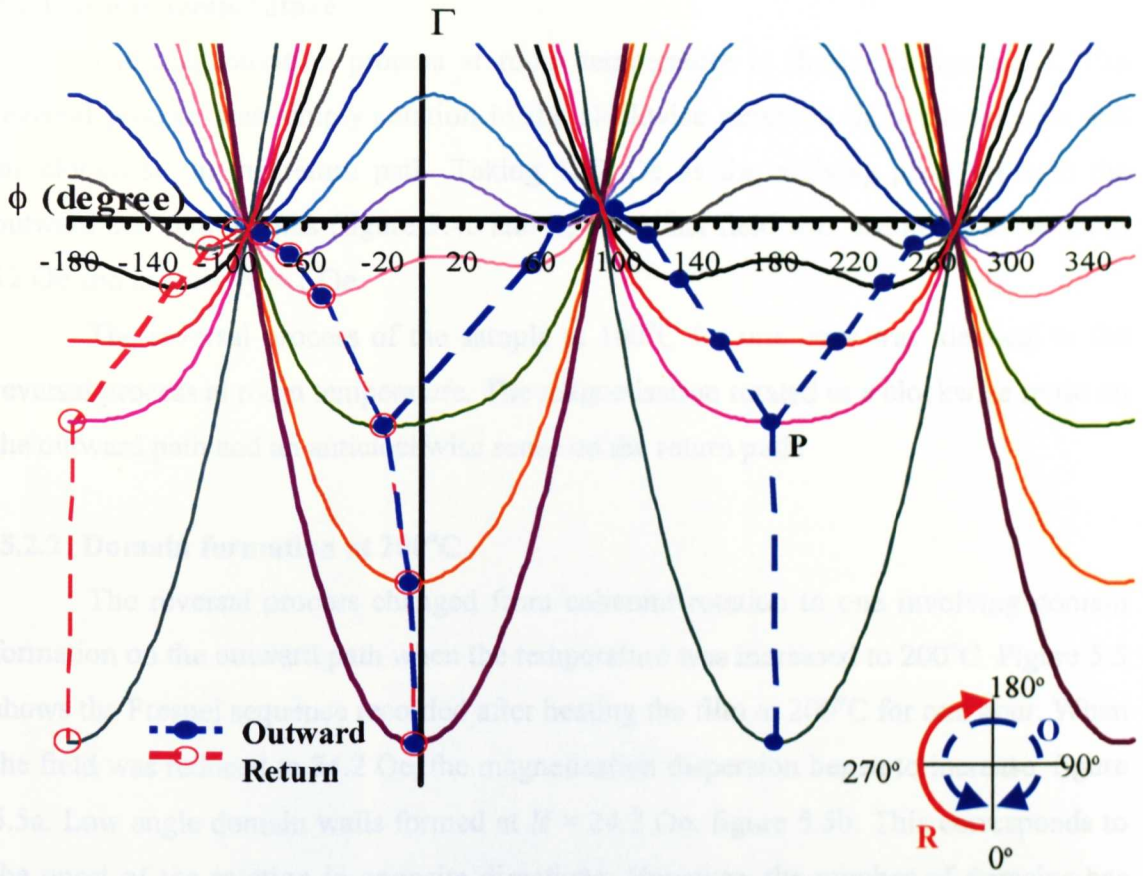

Figure 5.3: Energy contour deduced from the modified Stoner-Wohlfarth model. It shows a symmetrically split rotation on the outward and a coherent rotation on the return path.

The SW model takes no account of thermal effects which, if present, offer a source of energy to allow the magnetisation to jump small energy barriers and hence follow different reversal routes. Examination of the energy contours in figure 5.3 suggests that even if small energy barriers can be overcome there are no paths ϕ can follow that are comparably attractive to those already described.

5.2: Thermal effect on NiFe/CoFe Thin SAF BSV

The effect of heat on the free layer reversal mechanism was studied with the NiFe/CoFe SAF BSV with thinner SAF structure, the stack composition being seed60/PtMn185/CoFe14/Ru9/CoFe18/Cu23/CoFe13/NiFe25/cap50. The composition of the stack was identical to the stack studied in the previous section except for the pinned and reference layer thicknesses. The thinner stack will be referred to as NiFe/CoFe Thin SAF BSV. It received the same post-deposition anneal treatment as the NiFe/CoFe SAF BSV.

The same experimental procedure as in the previous section was used on this film. Five Fresnel sequences were recorded at room temperature, 100°C and 200°C.

5.2.1: Room temperature

The magnetisation process at room temperature is shown in figure 5.4. The reversal process was simply rotation in the clockwise sense on the outward path and anticlockwise on the return path. Taking 12.2 Oe as the midway point on both the outward and return paths (figure 5.4c and i), the offset field was estimated to be about 12 Oe and coercivity < 1 Oe.

The reversal process of the sample at 100°C for one hour was identical to the reversal process at room temperature. The magnetisation rotated in a clockwise sense on the outward path and an anticlockwise sense on the return path.

5.2.2: Domain formation at 200°C

The reversal process changed from coherent rotation to one involving domain formation on the outward path when the temperature was increased to 200°C. Figure 5.5 shows the Fresnel sequence recorded after heating the film at 200°C for one hour. When the field was reduced to 34.2 Oe, the magnetisation dispersion began to increase, figure 5.5a. Low angle domain walls formed at H = 24.2 Oe, figure 5.5b. This corresponds to the onset of the rotation in opposite directions. However, the number of domains has reduced and a small number of 180° domain walls still existed when the applied field was reduced to 15.6 Oe. At this point, the magnetisation in alternate domains was almost antiparallel. This created the high contrast 180° domain walls observed in figure 5.5d. The magnetisation in the domains continued to rotate in opposite senses when the positive field was further reduced and domains began to collapse at H = 13.9 Oe where the magnetisation was about 135° from the initial direction. The reversal process was complete at H = 0 Oe. Although domains were present in the outward path, the dominant mechanism was still rotation in the clockwise sense.

The reversal process on the return path was coherent rotation in the anticlockwise sense similar to those at room temperature and 100°C. Therefore, the reversal process had changed from symmetrical at room temperature to asymmetrical at 200°C. The offset field for this reversal process is estimated to be 17 Oe. This has increased from 12 Oe for the reversal process at room temperature. The coercivity remained fairly small at < 1 Oe. It is not clear at this point what causes the increase in the offset field at elevated temperature. The effect of temperature on coercivity and exchange bias for various AFM is reported by Mao et al. [14].

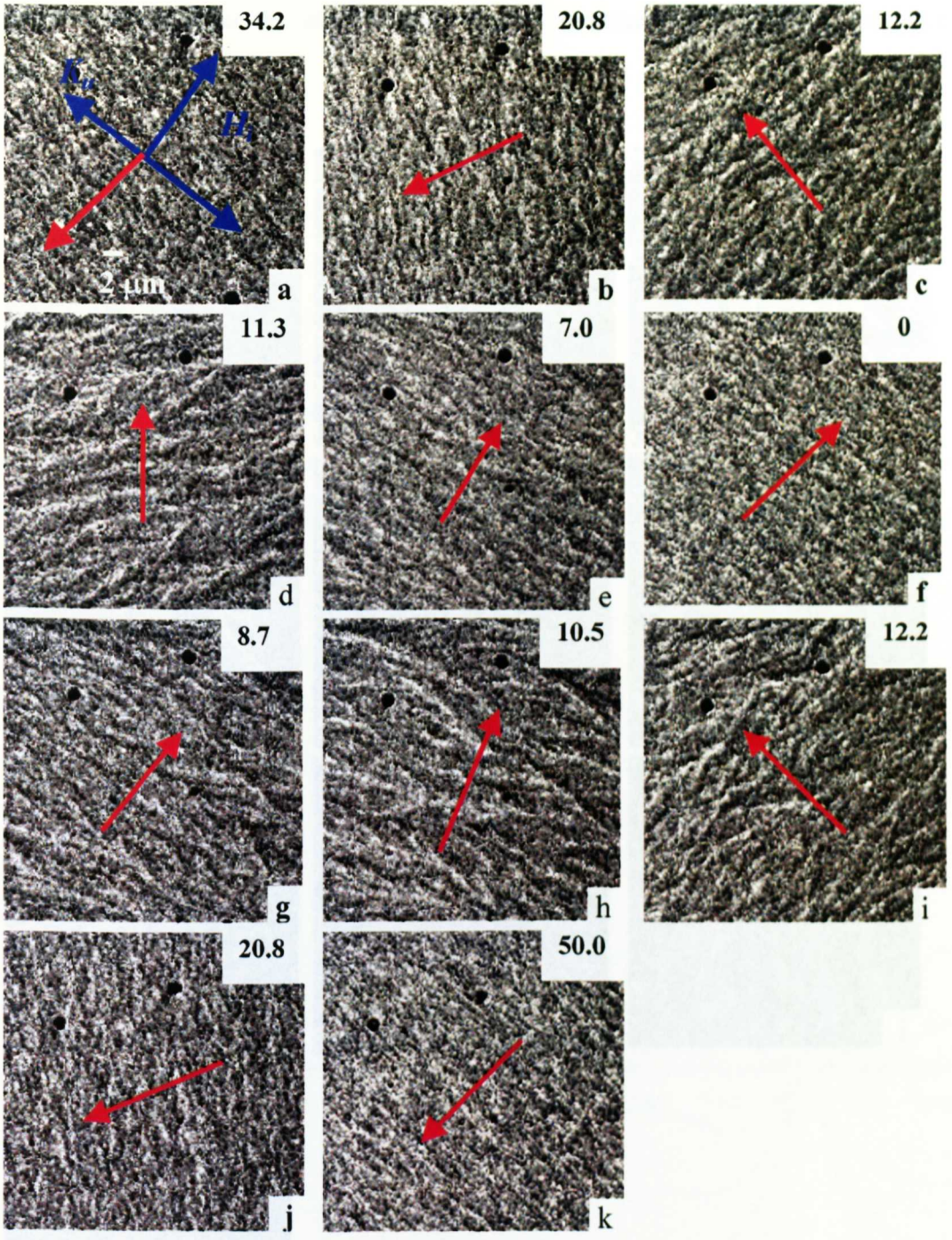

Figure 5.4: Fresnel image sequence for NiFe/CoFe ThinSAF BSV at room temperature. It shows the coherent magnetisation rotation on both the outward and return path. Red arrows denote the direction of magnetisation as determined from the magnetisation ripple.

There was no change in the reversal mechanism for the processes recorded at 200°C for one, two and three hours. Similar domain formation on the outward path and coherent rotation on the return path were observed. Hence, the reversal was temperature dependent but not time dependent for durations up to three hours.

However, when the temperature was reduced to room temperature, the reversal was restored to the initial coherent rotation on both outward and return paths. This

seems to indicate that the elevated temperature treatment did not alter the physical structure of the films.

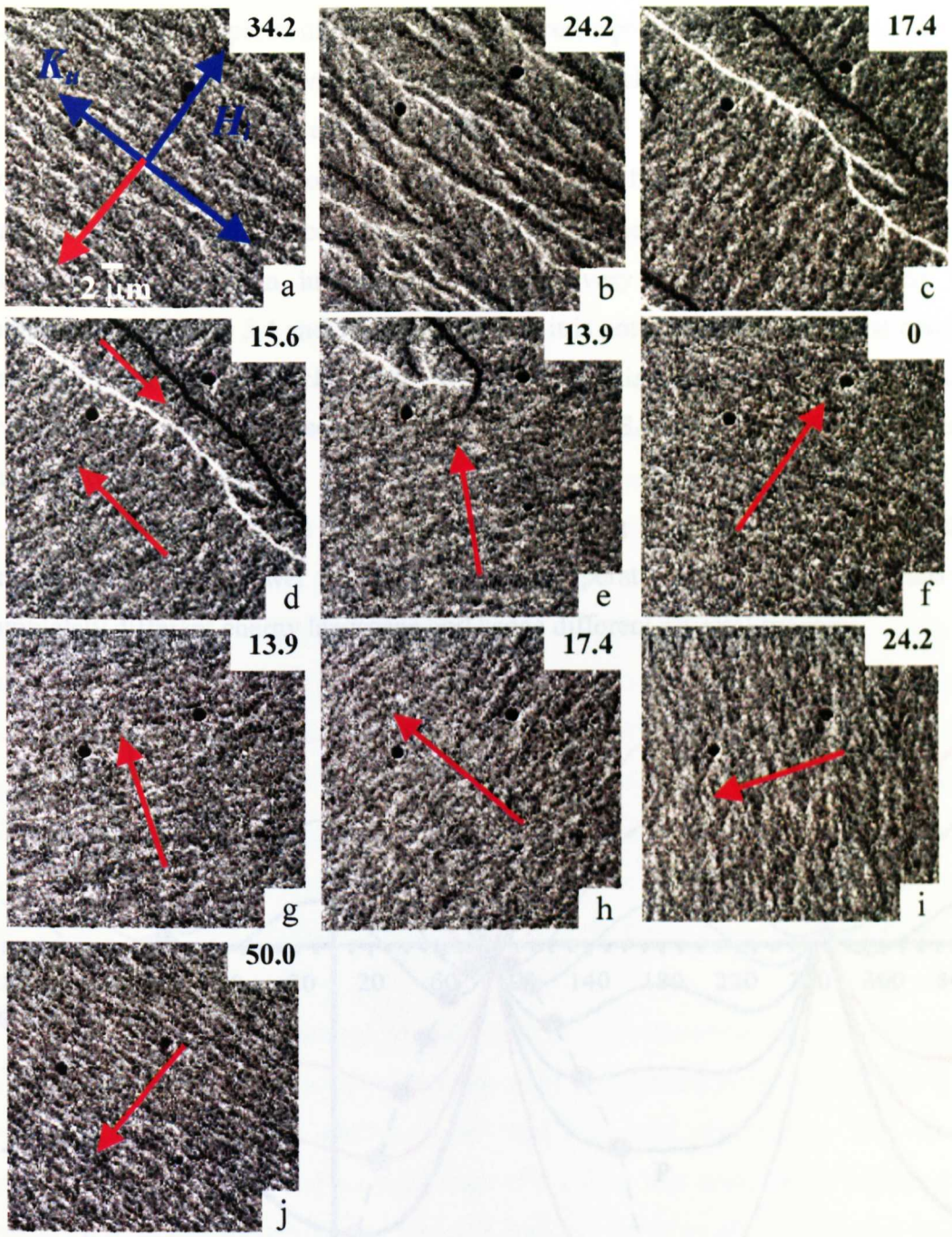

Figure 5.5: Fresnel image sequence for NiFe/CoFe ThinSAF BSV at 200°C for one hour. It shows domain formation on the outward path and anticlockwise coherent rotation on the return path. Red arrows denote the direction of magnetisation as determined from the magnetisation ripple.

To see what might be happening in the case of NiFe/CoFe ThinSAF BSV, the input parameters to the SW model used in figure 5.3 were modified slightly to produce the energy contours shown in figure 5.6. Here the difference between the two energy

minima available on the outward part of the cycle has increased slightly, though it remains less marked than that for the return path. Hence the most likely reversal mechanism involves following the path defined by the global minimum on both outward and return parts of the cycle. This corresponds to coherent rotation in a clockwise sense on the outward path and in an anticlockwise sense on the return. This was indeed what was observed for NiFe/CoFe ThinSAF BSV at the lower temperatures. Now in reality the energy contour marked P is almost flat over an appreciable angular range so that we might expect that as the thermal energy available to the system is increased the dispersion in the film becomes very large. This is exactly what comparison of figures 5.4 and 5.5 shows. Hence it is not surprising that as the reversing field is further reduced each of the two energy minima become populated and the reversal comes to closely resemble that of NiFe/CoFe SAF BSV with domains forming on the outward path.

Wu et al. reported that canting of pinning field direction can occur at temperature at much lower that the blocking temperature [16]. This may leads to a completely different energy landscape and hence different reversal process.

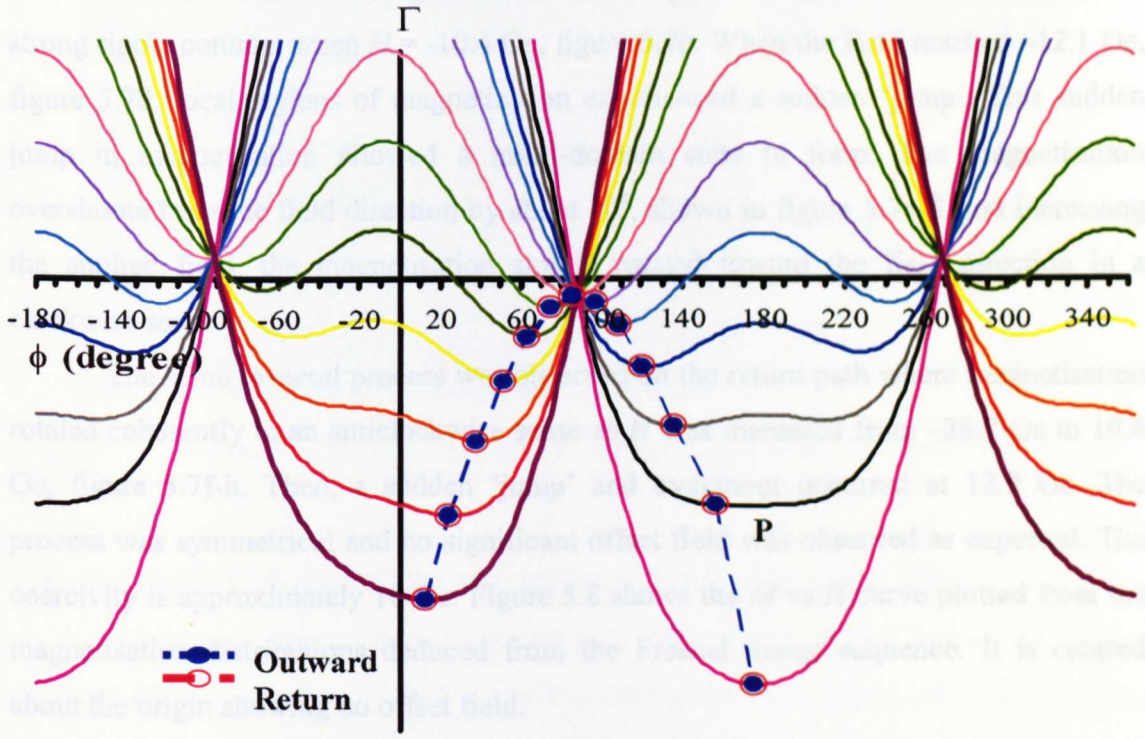

Figure 5.6: Energy contours deduced from the modified Stoner-Wohlfarth model. It shows the coherent magnetisation rotation reversal on both the outward and return path.

5.3: Magnetisation reversal of a pre-anneal CoFe AFM TSV

In this section, the free layer magnetisation reversal process of a pre-anneal CoFe AFM TSV (seed/CoFe30/Cu26/CoFe27/PtMn150/cap) is studied. The pre-anneal films have no exchange bias coupling between PtMn and CoFe because the PtMn was not in the antiferromagnetic state before annealing. Hence, the CoFe layer next to the PtMn layer was not pinned by the PtMn layer. This means that there should be only very weak or no offset field in the free layer. Since the difference in thickness between the two CoFe layers is only 3Å, they will reverse almost together when they are subjected to an external field. Without external field, the magnetisation in these layers is predominantly along the uniaxial anisotropy axis.

An external field was applied at approximately 90° to the uniaxial axis. The uniaxial axis was known due to the mark left by the tape on the specimen. The tape was used to hold the TEM membrane on the Si wafer during the deposition. Figure 5.7 shows the free layer reversal process of a pre-anneal CoFe AFM TSV. As the field was reduced from 25 Oe (figure 5.7a) to 0 Oe (figure 5.7b), magnetisation in the free layer underwent a coherent rotation to about 90° in the anticlockwise sense. Then, as the field was decreased further, the magnetisation showed greater dispersion, as shown by the strong ripple contrast when H = -10.4 Oe, figure 5.7c. When the field reached –12.1 Oe, figure 5.7d, local regions of magnetisation experienced a sudden 'jump'. This sudden jump in magnetisation allowed a multi-domain state to form. The magnetisation overshoots from the field direction by about 30°, shown in figure 5.7e. Upon increasing the applied field, the magnetisation slowly rotated toward the field direction in a clockwise sense.

The same reversal process was observed on the return path where magnetisation rotated coherently in an anticlockwise sense as H was increased from –28.7 Oe to 10.4 Oe, figure 5.7f-h. Then, a sudden 'jump' and overshoot occurred at 12.9 Oe. The process was symmetrical and no significant offset field was observed as expected. The coercivity is approximately 10 Oe. Figure 5.8 shows the M vs H curve plotted from the magnetisation distributions deduced from the Fresnel image sequence. It is centred about the origin showing no offset field.

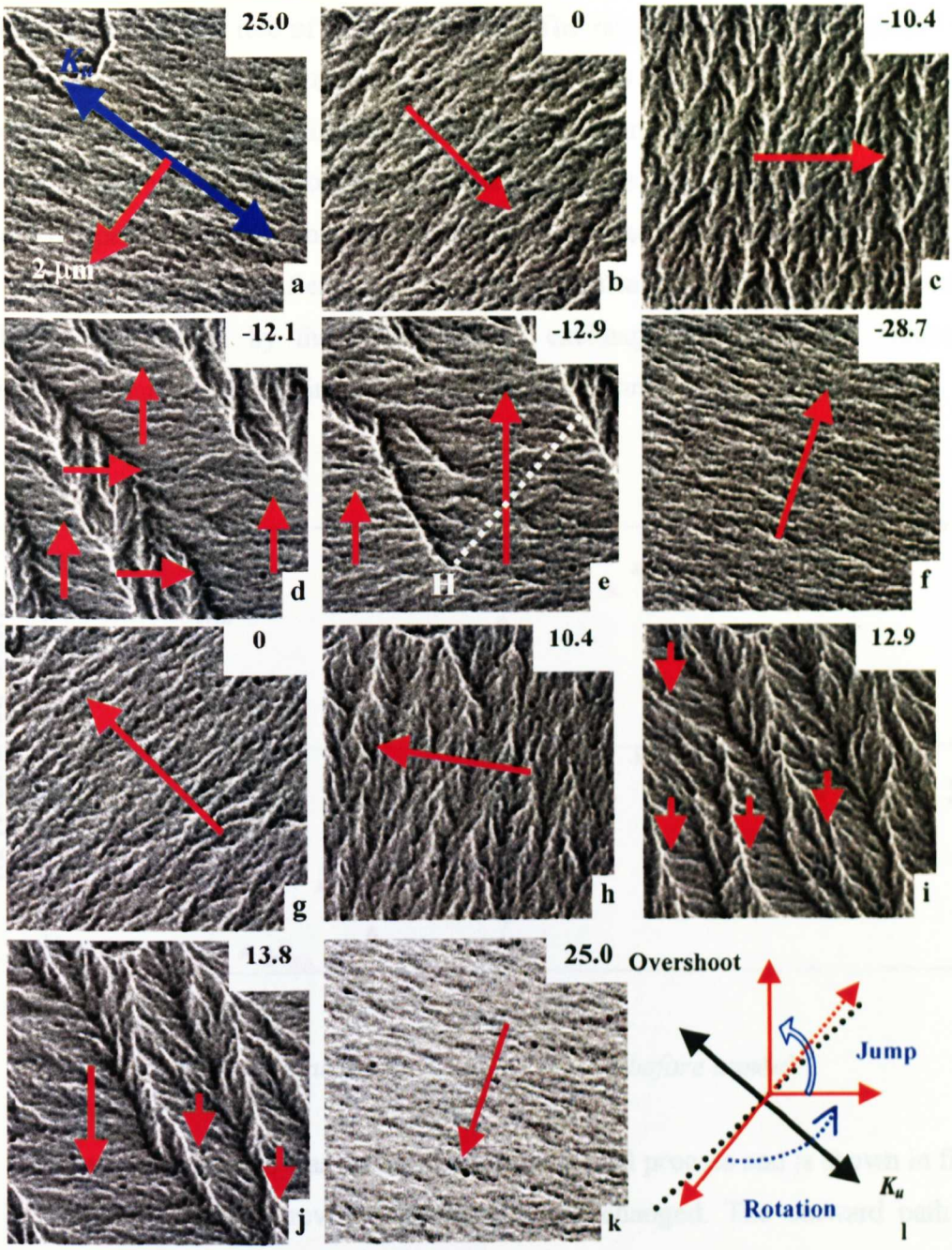

Figure 5.7: Fresnel image sequence of pre-anneal CoFe AFM TSV with H at 90 ° to K_u.

5.4: In-situ TEM annealing experiment for CoFe AFM TSV

After a reversal process was recorded for the pre-anneal film as described in the previous section, the in-situ TEM annealing experiment was carried out. The annealing process changes the phase of PtMn from FCC to FCT thus making it antiferromagnetic [17].

Keeping the specimen in the same heating rod and at the same orientation as in the previous section, it was tilted at 90° so that the plane of the film was parallel to the objective lens field in the TEM. The in-plane field was set to 250 Oe. The temperature

was then increased at a rate of 5 °C per minute. The rate was chosen to be close to the rate used in a commercial annealing oven, which was about 4 °C per minute. The temperature was increased until 300°C was reached. Then, the specimen was left at this temperature and vacuum for four hours. After four hours, the temperature was reduced to room temperature at the same rate. The specimen orientation was unchanged all the time when this was done. After annealing, the magnetisation of the CoFe layer next to the PtMn was pinned by the PtMn through exchange bias coupling. Hence, an unidirectional anisotropy was induced in the configuration.

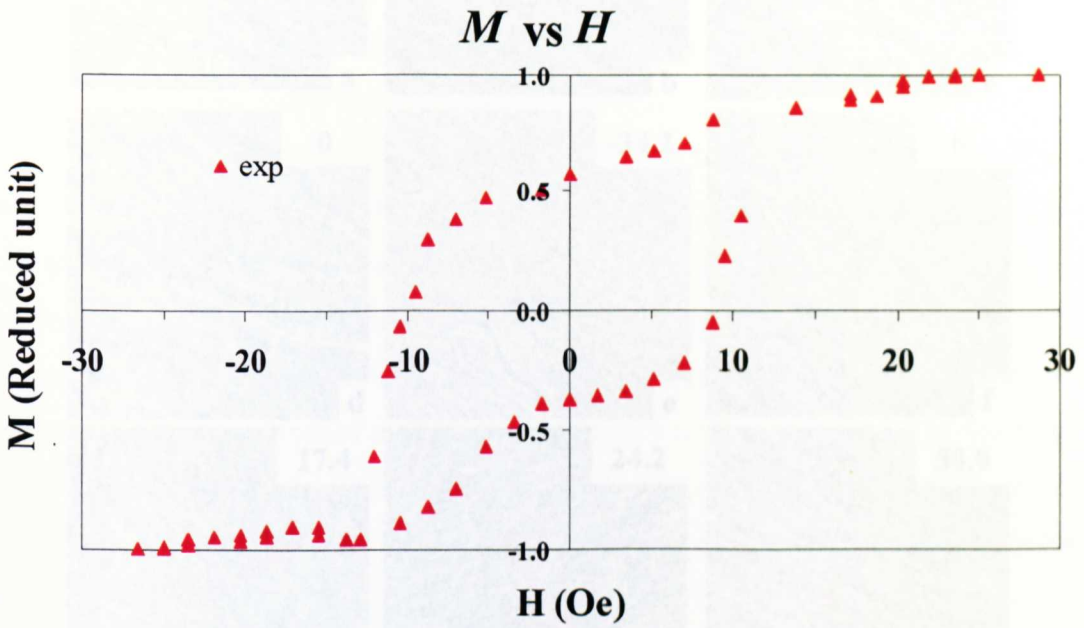

Figure 5.8: M vs H curves for CoFe AFM TSV before anneal.

A reversal sequence was recorded after the anneal process and is shown in figure 5.9. It is obvious that the reversal mechanism has changed. The outward path was dominated by domains arising where magnetisation split locally. Domains of some kind persisted over a long range of field, 360° loops still being present at -34.2 Oe, figure 5.9e. On the return path, reversal proceeded by rotation in the clockwise sense. The 360° loop formed during the outward path grew slightly in size and it turned into a small local domain. Taking 10.5 Oe and 24.2 Oe (figure 5.9c and h) as the midway points on the outward and return paths respectively, the offset field induced after the anneal was about 17 Oe and coercivity has reduced from 10 Oe (before anneal) to about 7 Oe. These values are reasonably close to the values estimated for the film annealed using a commercial annealing oven, which are 20 Oe of offset field and 6 Oe of coercivity. Please refer to the discussion in Chapter 3 section 3.2 on these values.

The change in reversal mechanism before and after the anneal was most likely due to the induced offset field in the free layer. The asymmetrical reversal process after anneal was caused by the slight misalignment of the offset field from orthogonal to the uniaxial axis. Similar to those discussed previously.

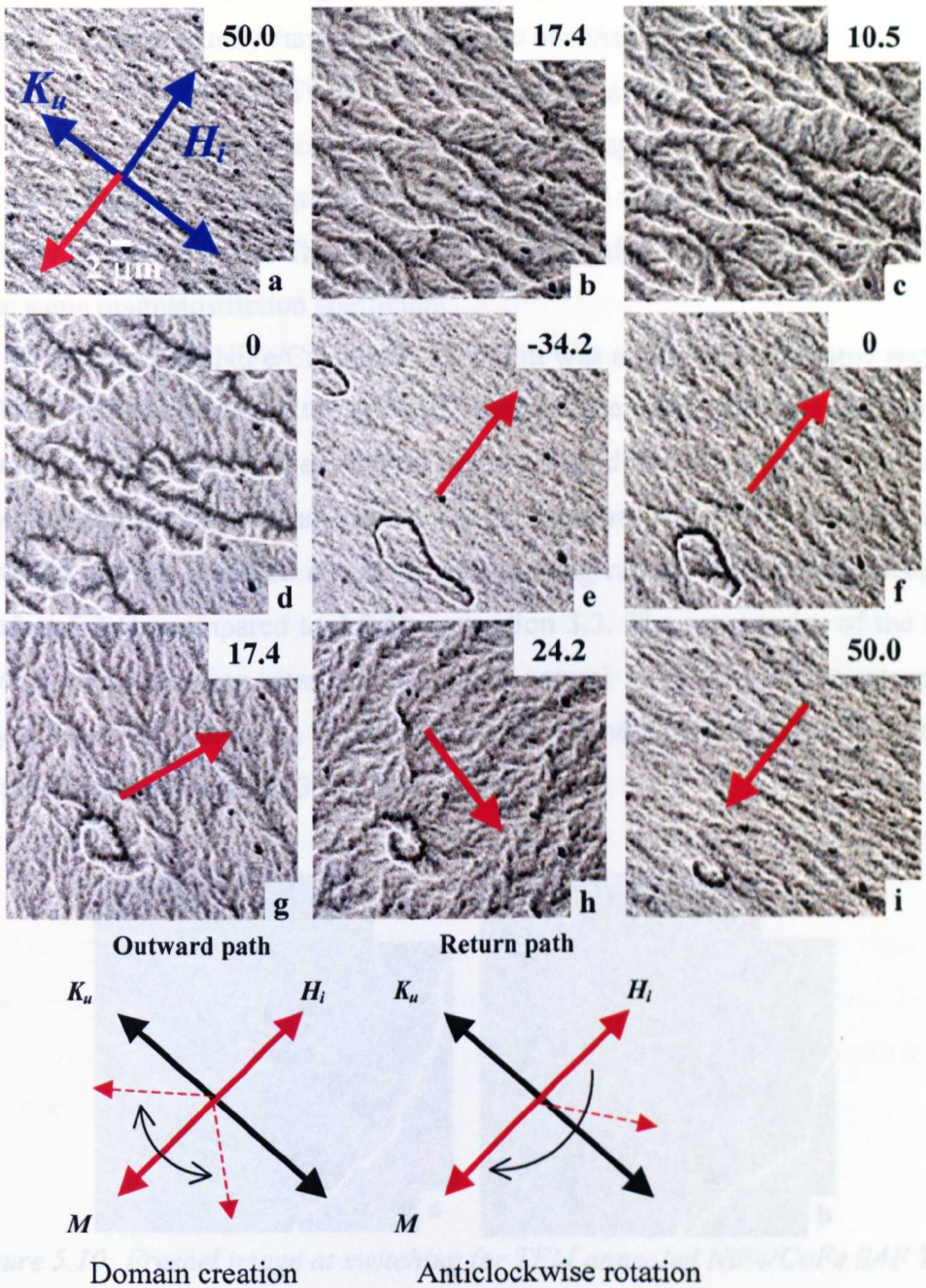

Figure 5.9: Fresnel image sequence of annealed CoFe AFM TSV with H at θ° from orthogonal to K_u.

5.5: In-situ TEM annealing experiment of NiFe/CoFe SAF TSV

The NiFe/CoFe SAF TSV discussed in section 3.3 has a very simple free layer magnetisation reversal process. In order to investigate this further and to check its reproducibility, a TEM in-situ annealing experiment was carried out. The experiment was done to imitate the post-deposition annealing process to induce the unidirectional anisotropy, which is usually carried out using the commercial annealing oven.

A NiFe/CoFe SAF TSV film was deposited at the same time as the film in section 3.3. The uniaxial anisotropy was induced by applying a small magnetic field during the deposition. The film discussed in section 3.3 was annealed in a conventional commercial annealing oven. The pre-anneal and annealed NiFe/CoFe SAF TSV films have the same magnetostriction coefficient.

The unannealed NiFe/CoFe SAF TSV film was annealed in the same way as the CoFe AFM TSV discussed in the previous section. The result is shown in figure 5.10. Both images were taken at the same field but at a time difference of a few seconds. The free layer magnetisation reversal process was the same as the film studied in section 3.5. The reversal process involved a domain wall moving rapidly through the specimen. It occurred at 5.2 Oe compared to 4.8 Oe in section 3.3. The irregularity of the domain wall was due to pinning sites cause by the natural variability in anisotropy in a polycrystalline film. Hence the TEM annealing experiment had successfully reproduced the reversal process in section 3.3.

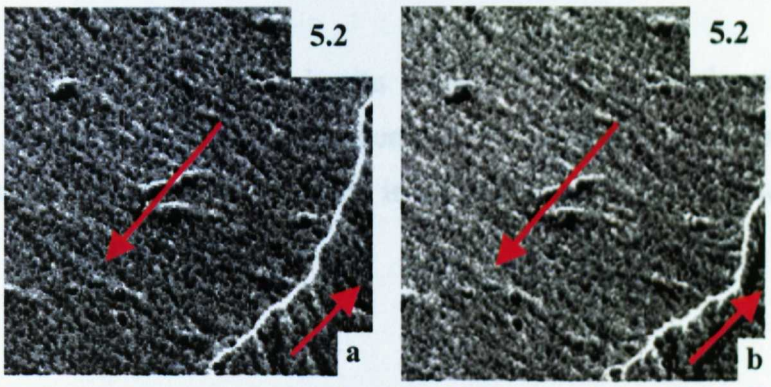

Figure 5.10: Fresnel image at switching for TEM annealed NiFe/CoFe SAF TSV.

5.6: Discussion

The influence of thermal effects on the free layer magnetisation reversal for two different types of synthetic antiferromagnetic BSV was discussed in this chapter. The experimental results have shown that the domain structure during the reversal process was not significantly affected by temperature rise for the NiFe/CoFe SAF BSV sample. There was no observable change in either the domain size or wall orientation during and after the heating experiment. However, the effect of temperature was more substantial in the reversal in the NiFe/CoFe Thin SAF BSV.

The change in magnetisation reversal was attributed to the increase in magnetisation dispersion due to thermal effects. The increase in dispersion created local regions with slightly different energy landscape. Hence, local regions find different reversal paths are energetically favoured. As a result, a different reversal process was observed at elevated temperature.

In general, both SV films were fairly stable for temperature up to 100°C.

The reversal process before and after annealing for the CoFe AFM TSV was different. An offset field was successfully introduced after the annealing process. Reasonable agreement was found between the offset field and coercivity for films annealed in-situ in the TEM and in a commercial annealing oven. The reversal process also changed from a symmetrical to an asymmetrical process after annealing. The reason was most probably that the alignment of the applied field during anneal was not exactly orthogonal to the uniaxial axis. This is similar to the reversal process discussed in section 4.4.

The NiFe/CoFe SAF TSV in-situ TEM annealing experiment successfully produced the same free layer reversal process as that of the film discussed in section 3.3. This illustrates the capability of using in-situ TEM annealing techniques to induce unidirectional anisotropy in a SV film.

References:

[1] K. Ratzke, M. J. Hall, D. B. Jardine, W. C. Shih, R.E. Somekh and A. L. Greer, J Magn. Magn. Mater **204** 61 (1999),

[2] J. L. Leal, and M. H. Kryder, J. Appl. Phys. **83** 3720 (1998),

[3] G. W. Anderson, Y. Huai, and M. Pakala, J. Appl. Phys. **87** 5726 (2000),

[4] D. Han, Z. Gao, S. Mao, and J. Ding, J. Appl. Phys. **87** 6424 (2000),

[5] J. P. Nozleres, S. Jaren, Y. B. Zhang, A. Zeltser, K. Pentek and V. S. Speriosu, J. Appl. Phys. **87** 3920 (2000),

[6] D. V. Dimitrov, J. van Ek, Y. F. Li and J. Q. Xiao, J. Appl. Phys. **87** 6427 (2000),

[7] M. J. Carey, N. Smith, B. A. Gurney, J. R. Childress, and T. Lin, J. Appl. Phys. **89** 6579 (2001),

[8] R. H. Taylor, R. O'Barr, and Y. Yamamoto, J. Appl. Phys. **85** 5036 (1999),

[9] E. Jang, G. Wang, K. Y. Cho, and H. Lee, J. Appl. Phys. **91** 8769 (2002),

[10] D. V. Dimitrov, J. Van Ek, Y. F. Li, J. Q. Xiao, J. Magn. Magn. Mater. **218** 273 (2000),

[10] X. Portier, A. K. Petford-Long, T. C. Anthony, and J. A. Brug, Appl. Phys. Lett. **75** 1290 (1999),

[11] S. J. T. Murdoch, J. N. Chapman, T. G. Pokhil, S. Mao, and E. S. Murdock, J. Appl. Phys. **87** 4945 (2000),

[12] R. T. Huang, F. R. Chen, and J. J. Kai, J. Appl. Phys. **89** 7625 (2001),

[13] M. Takiguchi, S. Ishii, E. Makino, and A. Okabe, J. Appl. Phys. **87** 2469 (2000),

[14] S. Mao, N. Amin, and E. Murdock, J. Appl. Phys. **83** 6807 (1998),

[15] Y. Wu, G. Han, T. Chong, J. Appl. Phys. **89** 7616 (2001),

[16] A. Maesaka, S. Ishii and A. Okabe, J. Appl. Phys. **88** 3982 (2000),

CHAPTER 6: CHARACTERISATION OF BI-FILAMENT IN-SITU MAGNETISING ROD FOR TRANSMISSION ELECTRON MICROSCOPE

Introduction

In this chapter, I am going to present some of the characterisation work I have done on a new in-situ magnetising rod. The rod was designed and constructed by Dr. G. Yi, Dr. W. A. P. Nicholson, Dr. S. McVitie and Prof. J. N. Chapman. The rod is built as a new way of performing in-situ magnetising experiments. Prior to this, there were two methods in use to carry out in-situ magnetising experiments. The first method is the tilting of the specimen in a vertical field, as described in section 2.2.3. This was used to perform all the magnetising experiments presented in chapter 3, 4, and 5. The second method uses a set of coils built into the TEM sample holder, which generates a horizontal field in the sample plane. The drawback of this method is that the horizontal field deflects the electron beam well away from the optic axis. Hence constant realignment of the beam is required to restore the electron beam to the optic axis.

This problem is overcome by the design of the new magnetising rod. The rod is designed such that deflection of the beam is theoretically zero. However, in practice a small deflection is observed due to departures from perfect symmetry. The rod is also capable of generating short current pulses. The design and construction of the rod is described in detail in section 6.1. My work involved mainly the characterisation of the rod including determination of the temperature and magnetic field generated as a function of electrical current through the wire. This is discussed in section 6.2. Experiments were also done on patterned magnetic elements using the new rod. The purpose of the experiments was to study the angular dependence of switching field as a function of element orientation [1,2]. The results and analysis are presented in section 6.3 and 6.4 respectively. Finally, a discussion is given in section 6.5.

6.1: Rod design and specification

The stage consists of two current carrying gold wires each 100 μm in diameter. A schematic is shown in figure 6.1. These wires are called the bi-filament. 1 A of current input from a power supply to the rod gives 0.5 A of current through each gold wire. Gold is used because of its high electrical conductivity. The gold wires are pressed into two grooves cut in two insulated copper bars, 100 μm apart, figure 6.1 and

6.2(a)(b). These copper bars also act as heat sinks and current leads. On top of the wires is a layer of insulator; pieces of Mylar were used. Two similar rods were built, one for the Philips CM20 TEM and the other for the JEOL 2000 TEM.

There are two power supplies which can be used in conjunction with either rod. The first is a 0 to 12 A, 30 V DC supply which can be used to power the rod directly up to a maximum of about 6 A, limited by the temperature rise. The calibration of temperature rise as a function of DC voltage is shown in the next section. Figure 6.3 shows the circuit diagram of the experimental set-up. The second power supply is powered from the 12 A supply and can provide pulses of up to 30 A with a repetition rate of 1 s through a pulse generator. It has an output to an oscilloscope so that the voltage developed across a 0.1 Ω measuring resistor can be used to measure the current. Magnetic elements fabricated on a 2 mm^2 TEM membrane will be placed face down onto the stage as shown in figure 6.1. The trick is to centre the specimen so that the 100 μm^2 silicon nitride window is in the centre of the 100 μm gap between the wires. It is also very important to align the specimen so that the applied field direction lies as close as possible to the desired direction relative to the specimen. This can be done with an accuracy of $\pm 2^{\circ}$.

The closest separation from the centre of the gold wires to the specimen is 50 μm, shown in figure 6.4. However, adding more layers of Mylar can increase this separation. Each Mylar layer has a thickness of 25 μm. A circular hole of 1.5 mm diameter is cut on the Mylar layer so that the 100 μm^2 window does not come into direct contact with the Mylar layer which may damage the fragile Si_3N_4 window. The hole is also small enough to keep the 2 mm^2 TEM substrate from falling through, figure 6.2(c).

The specimen is clamped into position by a copper plate at the top of the stage, figure 6.2(d). The clamping plate is built with holes in it so that re-alignment of the specimen is possible by moving the specimen using a pair of tweezers through the holes.

As shown in figure 6.4, the vertical field components generated by the individual gold wires cancel each other out in between the gap. Therefore, the specimen only experiences the horizontal field. Moreover, there is an equal and opposite horizontal field below the wires. Hence, the net deflection experienced by the electron beam is zero. However, this assumes the two wires are perfectly symmetrical.

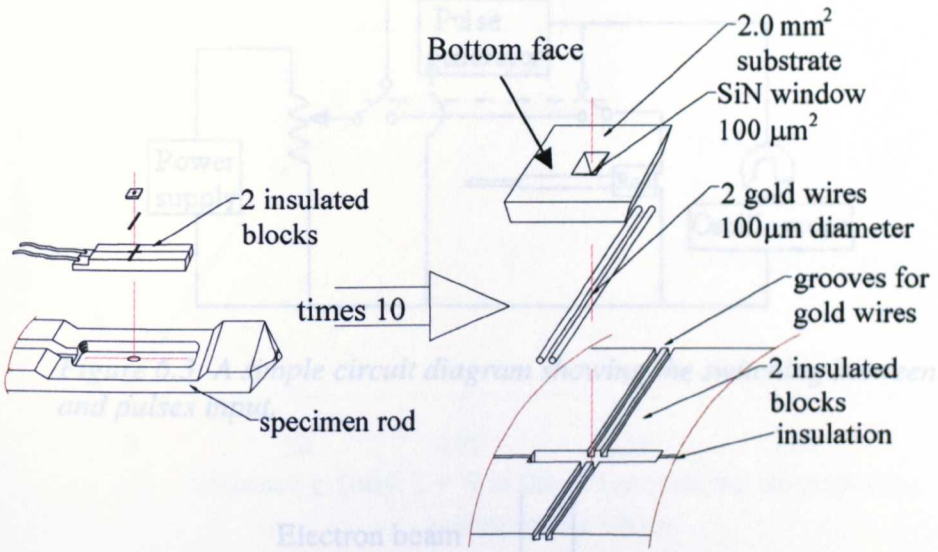

Figure 6.1: Schematic showing the construction of the bi-filament rod.

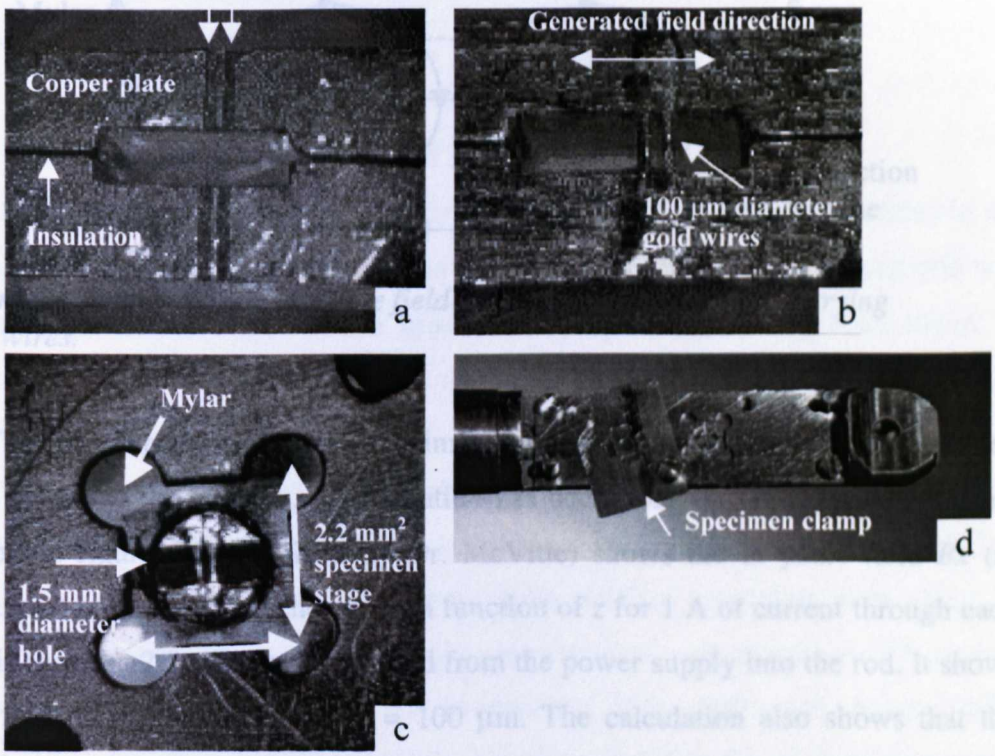

Figure 6.2: Optical images taken from the actual bi-filament rod showing (a) grooves on the copper plates, (b) the gold wires in the grooves, (c) the Mylar layers with a 1.5 mm diameter hole and specimen stage and (d) the specimen clamp at the top.

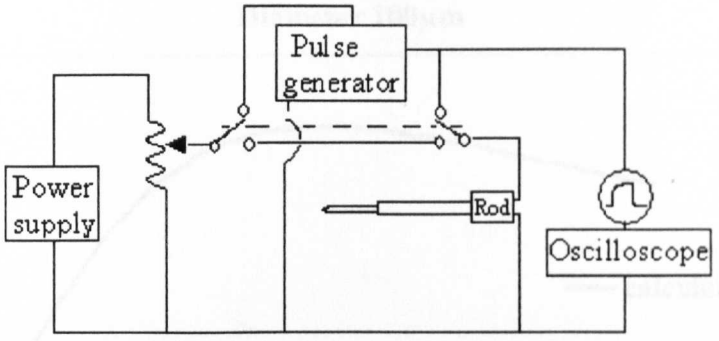

Figure 6.3: A simple circuit diagram showing the switching between DC and pulses input.

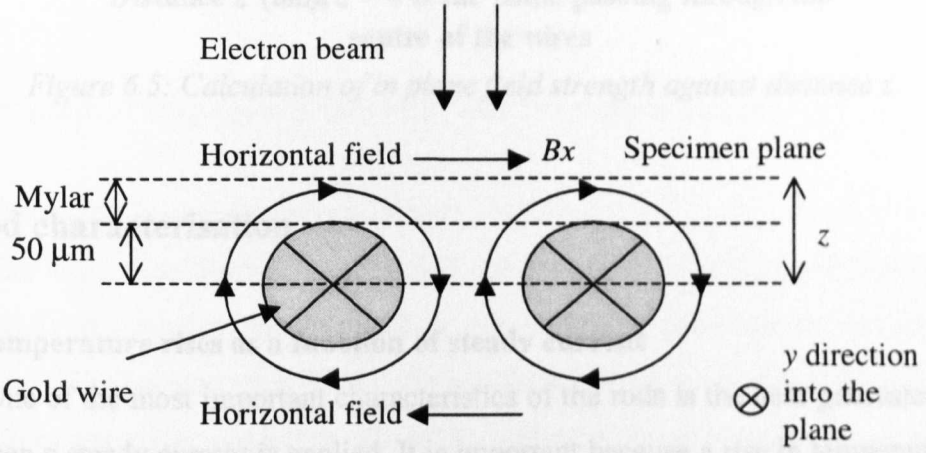

Figure 6.4: Schematic showing the field generated by the current carrying gold wires.

The field experienced by the specimen depends on the distance of the specimen from the centre of the wires, z. A calculation has been done by Dr. Stephen McVitie. The graph in figure 6.5 (provided by Dr. McVitie) shows the in plane field Bx (in Oersted units) at the centre of the gap as a function of z for 1 A of current through each wire. This means a 2 A current is supplied from the power supply into the rod. It shows that the field is maximum around z = 100 μm. The calculation also shows that the variation in field strength along the x direction is not significant. Hence, it is reasonable to assume a uniform field in the x-y plane.

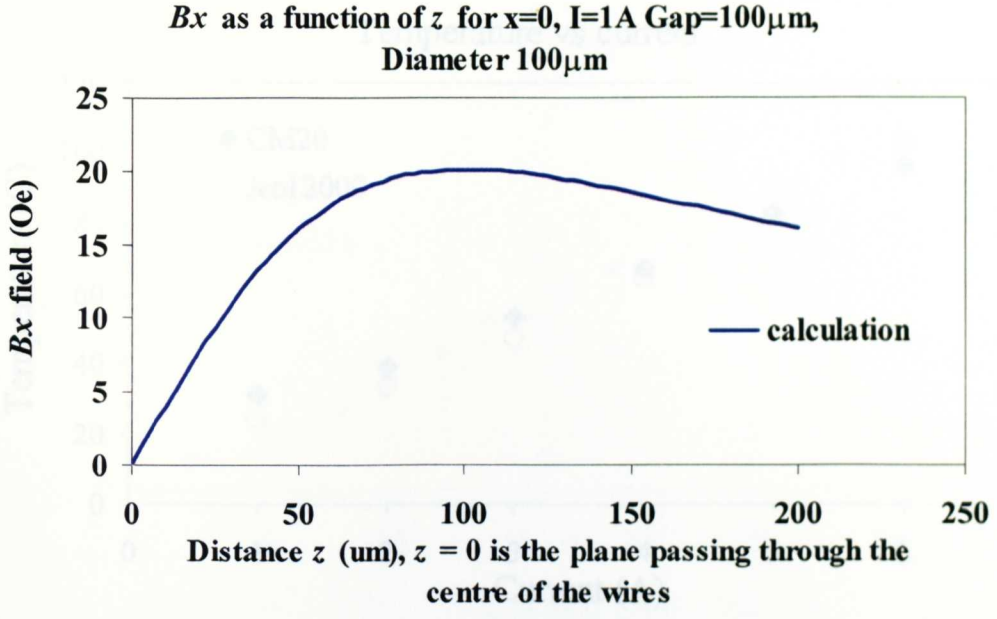

Figure 6.5: Calculation of in plane field strength against distance z.

6.2: Rod characterisation

6.2.1: Temperature rises as a function of steady current

One of the most important characteristics of the rods is the heat generated in the wires when a steady current is applied. It is important because a rise in temperature will affect the magnetic behaviour of the specimen during a magnetising experiment. A thermocouple is built into the stage of the rod. This allows the temperature of the stage to be monitored during the experiment.

Figure 6.6 shows the rise in temperature as a function of steady current applied. The electrical current was increased with a step interval of 1 A. This is equal to 0.5 A through each wire. At every step, the temperature reading was taken after about 15 minutes, time enough for it to settle. The temperature was measured for current amplitude up to 6 A. At this current, the temperature of the stage was almost 100°C. Both rods show a very similar characteristic, as shown in figure 6.6. The graph shows a linear increase in temperature at a rate of about 16.8 °C/A for the CM20 rod and 16.6 °C/A for the Jeol 2000 rod.

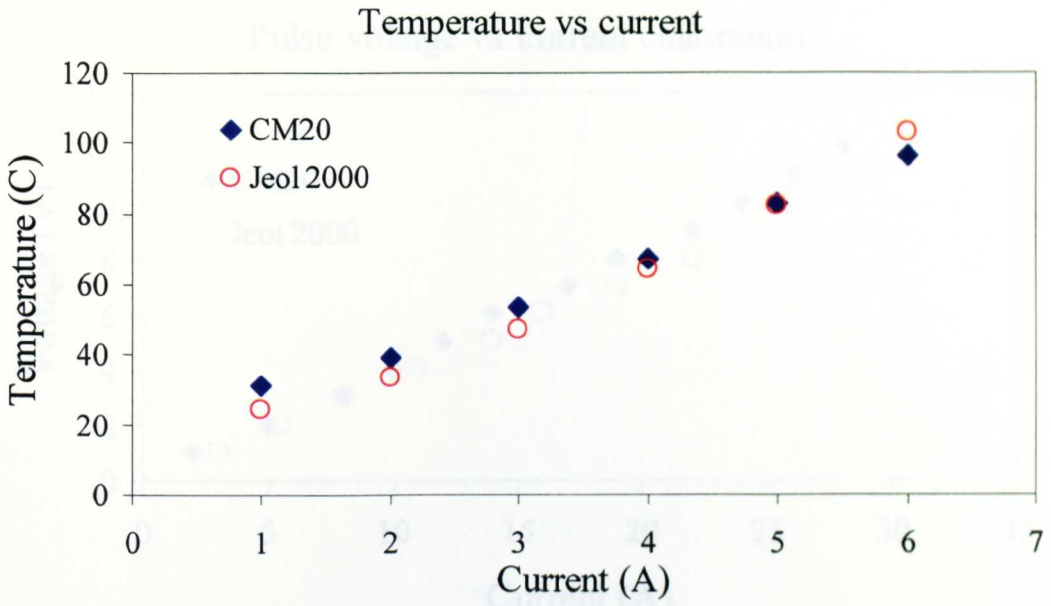

Figure 6.6: Temperature rises as a function of steady current.

6.2.2: Input voltage against pulse current

The second calibration was carried out for the input voltage supplied by the power supply to the pulse generator and the corresponding pulse current delivered. The duration of the pulse was about 20 μs. An oscilloscope was used to measure the output voltage from the pulse generator. Since this output voltage was developed across a known resistance of 0.1 Ω, the corresponding output current per volt can be determined. The pulse voltage was calibrated for currents up to 30 A, which was the maximum supported by the pulse generator. The calibration result is shown in figure 6.7. The amplitude of current generated per volt is about 2.4 A for the CM 20 rod and 2.7 A for the Jeol 2000. Due to the short pulse length, the temperature rise at large currents is negligible.

6.2.3: Magnetic field calibration

The third calibration of the rods was the magnetic field calibration. Two different methods were use to calibrate the field generated per unit current applied. Both calibrations were carried out using steady current. It is shown in figure 6.5 that the in plane field *Bx* on the specimen varies as a function of *z*. Hence, it is necessary to calibrate the field strength at various height *z*.

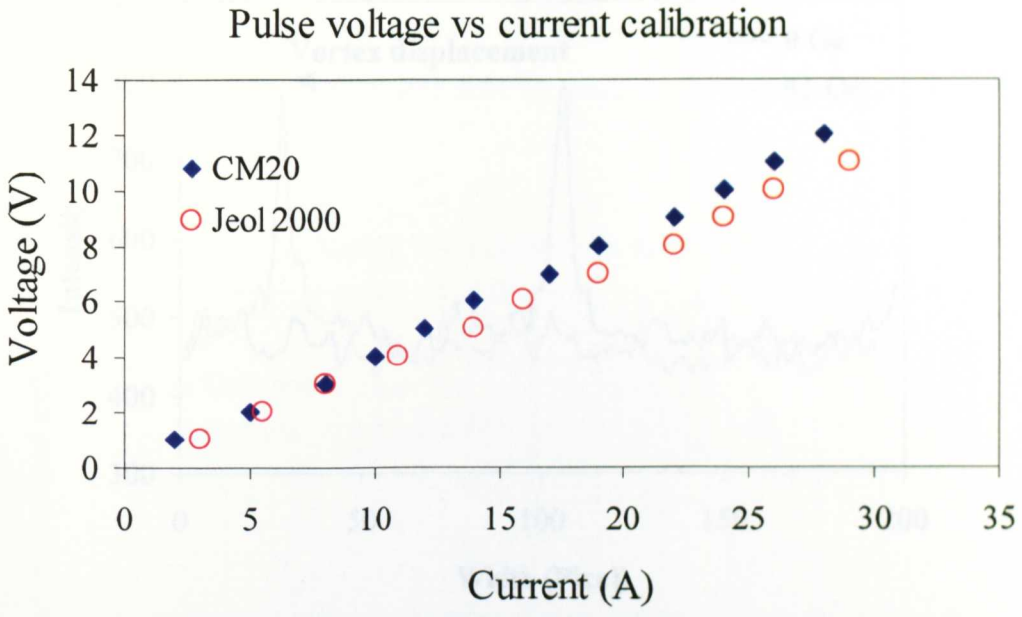

Figure 6.7: Current calibration for various pulse voltages applied.

The first method used was to measure the displacement of the vortex in a square magnetic element [3]. The vortex of a magnetic element reacted to the magnetic field and its displacement from the field free position can be measured accurately. Figure 6.8 shows the shift in vortex position at 0 and 45 Oe respectively. The central vortex moved vertically from the bottom side of the element to the top but remains more or less at the horizontal midpoint. The element used for the calibration was a 4 x 4 μm^2 square $Ni_{80}Fe_{20}$ element with thickness of 30 nm. The element was fabricated on the TEM window using electron beam lithography and the lift-off process.

The displacement of the vortex was measured using the intensity profile of the image, as illustrated in figure 6.9. By measuring the displacement of the intensity peak from the zero field position for various applied fields, a chart of vortex displacement as a function of field can be plotted.

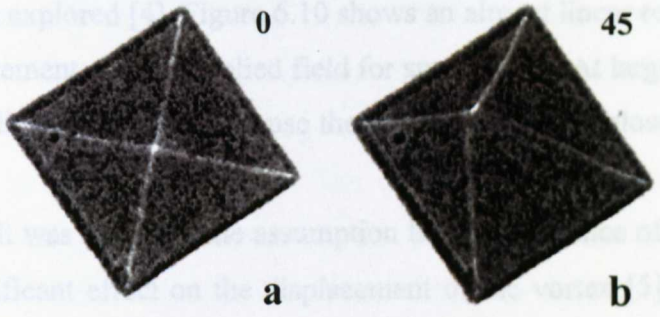

Figure 6.8: Fresnel images showing the displacement of a square NiFe element at (a) 0 Oe and (b) 45 Oe.

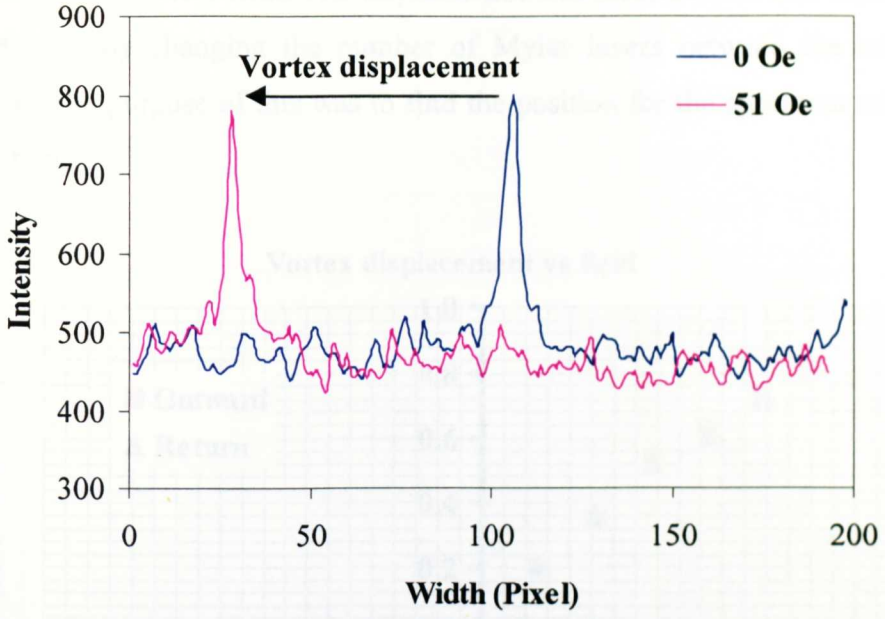

Figure 6.9: An illustration of the vortex displacement measurement by determining the shift in the intensity peak at (a) 0 Oe and (b) 51 Oe.

The first vortex displacement series was measured using the standard magnetising method used throughout this thesis, which involved tilting the specimen in a constant vertical field. The temperature inside the TEM column was about 27°C during the experiment. The result is shown in figure 6.10. The vortex displacement was measured as a fraction of shift from the position when no field was applied.

$$vortex\ \ displacement = \frac{vortex\ \ position\ \ at(H) - vortex\ \ position\ \ at(H=0)}{vortex\ \ position\ \ at(H=0)}$$

The displacement was measured for both positive and negative field directions. In other words, the vortex was brought through a hysteresis cycle but without driving the vortex too close to the edge of the element. Only the reversible part of the vortex displacement was explored [4]. Figure 6.10 shows an almost linear relationship between the vortex displacement and the applied field for small fields. At larger fields (> 40 Oe), the shift was not linear. This was because the vortex has moved close to the edge of the element.

This result was based on the assumption that the presence of a constant vertical field has no significant effect on the displacement of the vortex [5]. Results in a later section shows that this assumption was valid.

The vortex displacement of the same square $Ni_{80}Fe_{20}$ element was measured in the bi-filament rod as a function of steady current. No vertical field was present

throughout this measurement. The displacement was measured for two separations z, 75 and 100 μm, by changing the number of Mylar layers between the wires and the specimen. The purpose of this was to find the position for the specimen when the field is maximum.

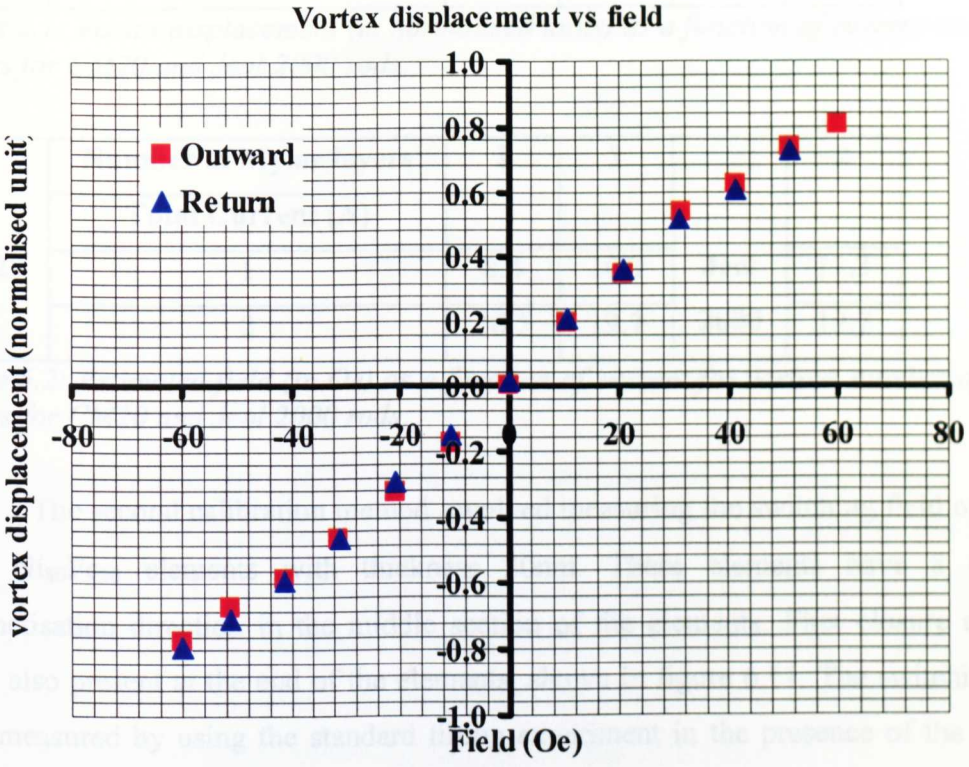

Figure 6.10: The graph showing the vortex displacement as a function of field by tilting the specimen in a constant vertical field.

The displacements of the vortex at two current values were measured in the same way as described earlier. Only two current values, 1 and 2 A were used for the calibration to keep the temperature of the stage as low as possible. According to figure 6.6, the temperature of the stage at 2 A was no more than 40°C. Calibrations were done for both rods separately in the Philips CM20 TEM and Jeol 2000. The results are shown in table 6.1. The magnetic field generated at each current was also estimated by comparing the vortex displacement using the bi-filament rods and the result shown in figure 6.10. This is shown in table 6.2. The estimation using vortex displacement is reasonable since the field generated by the rod was quite low. Therefore, the displacement of the vortex was relatively linear within the field range in consideration. Results in table 6.1 and 6.2 show that both the CM20 and Jeol 2000 rods behave consistently, as anticipated.

	Number of Mylar layers	1	2		2
	Total Current (A)				
CM20	1	0.13	0.17	Jeol	0.18
	2	0.26	0.32	2000	0.32

Table 6.1: Vortex displacement (in normalised units) as a function of current and Mylar layers for CM20 and Jeol 2000 rods.

	Number of Mylar layers	1	2		2
	Total Current (A)				
CM20	1	8.4	10.9	Jeol	11.3
	2	16.3	19.7	2000	19.7

Table 6.2: Estimated field (in Oe) as a function of current for various number of Mylar layers for CM20 and Jeol 2000 rods.

The second calibration method involved measuring the switching field of 2 x 12 μm^2 $Ni_{80}Fe_{20}$ elements with thickness 30nm. These elements have a uniform magnetisation direction in the middle section of the elements. Flux closure domains were also present at the end of the elements, shown in figure 6.11. The switching field was measured by using the standard tilting experiment in the presence of the vertical field. Figure 6.11 shows the switching of the elements at 22 Oe. This can be seen from the shift in the vortex position at the end of the elements.

These elements were used to determine the values of steady current required to switch them in the bi-filament rod. Experiments were carried for the CM20 rods for various numbers of Mylar layers. For the case of the Jeol 2000 rod, only one calibration was done for two layers of Mylar. The result is shown in table 6.3.

Numbers of Mylar	1	2
CM20	2.4 A	2 A
Jeol 2000		2 A

Table 6.3: Switching current value (in A) for the 2 x 12 μm^2 $Ni_{80}Fe_{20}$ elements. These current values are the total input current into the rod.

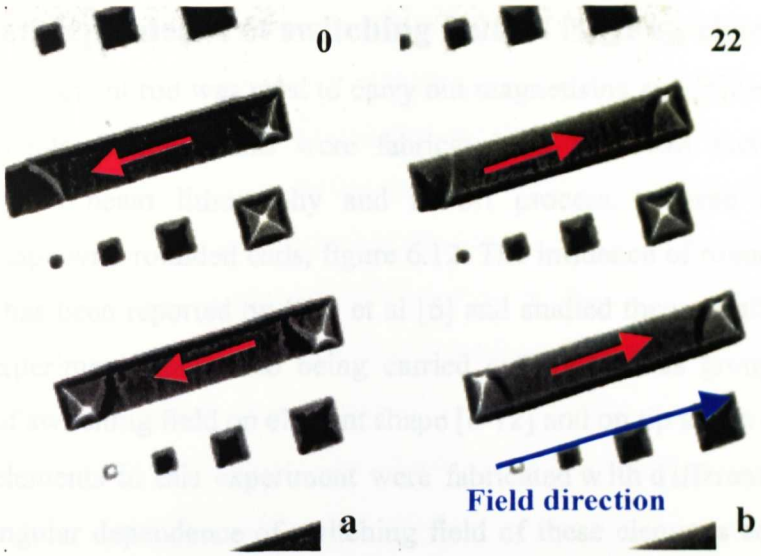

Figure 6.11: Fresnel images showing the switching of the 2 x 12 μm^2 NiFe elements at 22 Oe.

Experiments were also carried out to measure the switching current of these elements in the CM20 bi-filament rod in the presence of the vertical field. The aim was to find out if the vertical field has any observable effect on the switching current of the elements. The experimental results with and without the vertical field on were the same. This justifies the assumption made earlier that the presence of a small vertical field has no significant effect on the switching field of the magnetic elements.

Table 6.4 summarises the field calibration result for both the CM20 and Jeol 2000 rods. It shows the field for 1 A of total current input. The results show that when there was two layers of Mylar in between the wires and the specimen, the field was the highest. This corresponds to z = 100 μm. This value is consistent with the calculation value shown in figure 6.5.

Number of Mylar layers	**1 (z = 75 μm)**	**2 (z = 100 μm)**
CM20	8 +/- 1 Oe	10 +/- 1 Oe
Jeol 2000		10+/- 1 Oe

Table 6.4: A summary of field calibration for both the CM20 and Jeol 2000 bi-filaments rods. The fields shown correspond to 1 A of total current input.

6.3: Angular dependence of switching field of $Ni_{80}Fe_{20}$ elements

The bi-filament rod was used to carry out magnetising experiments on patterned $Ni_{80}Fe_{20}$ elements. The elements were fabricated on the TEM membrane using a standard electron beam lithography and lift-off process. These elements are a rectangular shape with rounded ends, figure 6.12. The influence of rounding the ends of Co elements has been reported by Kirk et al [6] and studied theoretically by Rave et al [7]. Many experiments have also being carried out by various groups to study the dependence of switching field on element shape [8-12] and on tip shape [3,13-15].

The elements in this experiment were fabricated with different orientations θ. Hence, the angular dependence of switching field of these elements could be studied. Moreover, there were elements with five different dimensions but with the same shape and thickness, which was 12 nm. This allows the switching field to be investigated as a function of element size as well as orientation. Table 6.5 shows the dimensions of all the elements. There were twelve elements for each dimension and orientation.

Dimension, a x b (μm x μm)	Aspect ratio
4.2 x 0.7	6 : 1
2.4 x 0.4	6 : 1
2.1 x 0.3	7 : 1
1.75 x 0.25	7 : 1
1.0 x 0.16	6.25 : 1

Note that the aspect ratio of these elements was almost constant. Element length and aspect ratio was found to have little effect on switching field [16].

The sample was aligned in such a way that the shape anisotropy axis of the reference element was along the applied field direction, $\theta = 0°$. Various types of end domain states were observed in the remanent state; an example is shown in figure 6.12. The end domains reduce the magnetostatic energy. The minimisation of magnetostatic energy by creating domains has been discussed in Chapter 1, section 1.1.1f. End domain type (I) in figure 6.12a was the most common structure observed for this sample. The Landau-Lifshitz-Gilbert (LLG) simulation program was used to simulate the remanent state of the element. The end domain type obtained from the LLG simulation, shown in figure 6.12b,c was similar to that of type (I) in figure 6.12a. Both experiment and

simulation show that the magnetisation rotates away from the shape anisotropy axis at the end, hence creating end domains and reducing magnetostatic energy [3, 13].

Before a pulse field was applied to the sample, the sample was saturated in high field to set a consistent initial state for the elements. This was done by tilting the sample to the vertical position, and then increasing the objective lens current to the maximum. This corresponds to a field of about 6000 Oe acting on the sample. This was sufficient to saturate the elements for this sample. The objective current was then reduced to zero and the sample was returned to a horizontal position. After high field saturation, all elements have end domain type (I). The experiment was carried out in the absence of the vertical field.

Setting all the elements in the same remanent state is critical in this experiment since different edge domain configuration can result in different switching fields [17].

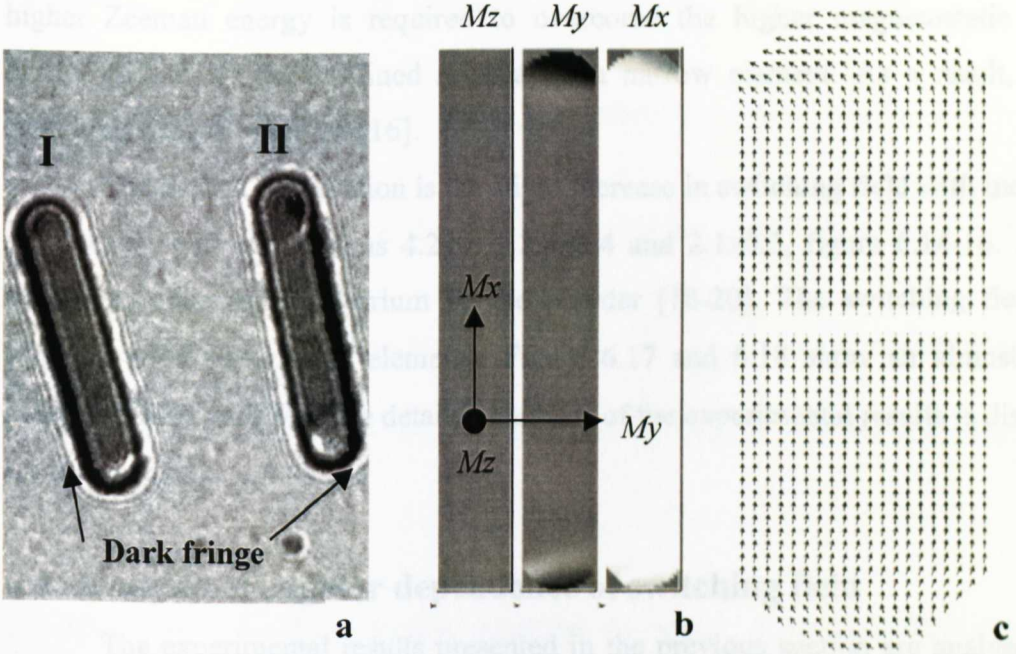

Figure 6.12: (a) Fresnel image showing two different type of end domains observed for the largest NiFe element at remanent state, (b) An LLG simulation image showing end domain type (I) and (c) the rotation of magnetisation away from the shape anisotropy axis at the end.

Pulsed voltages with 0.5 V intervals were applied to the sample using the pulse generator described in the previous section. The number of elements switching at each interval was recorded. The switching can be seen from the dark fringe along the edge of the element, figure 6.12a. When the magnetisation of the element switches from one direction to the opposite direction, the dark fringe also changes from one side of the element to the other side.

All the elements were saturated in high field before each increment of voltage to ensure a consistent initial remanent state. This was done in every case. For an array of elements, each element has a slightly different switching field due to the difference in nucleation fields for switching the magnetisation into the opposite direction.

Since the experiments were carried out using the bi-filament rod with two layers of Mylar, the corresponding field at each interval was calculated from the calibration results shown in the previous section.

The switching field as a function of element orientation for all the element dimensions are shown in figure 6.14-18. The results show a regular increase in switching field as the dimensions of the element decrease, as anticipated. The interplay between exchange, Zeeman and shape anisotropy energies determines the magnetisation reversal process. With decreasing element size, the demagnetising field arising from the magnetic charges formed at the element edges becomes increasingly important. Hence, higher Zeeman energy is required to overcome the higher magnetostatic potential barrier caused by the confined reversal in a narrow element. As a result, a higher switching field is observed [16].

The second observation is the slight increase in switching field with increasing θ for element with dimensions 4.2x0.7, 2.4x0.4 and 2.1x0.3, figure 6.14-16. A similar trend was observed in Barrium Ferrite powder [18-20]. The switching field is less sensitive to θ for smaller elements. Figure 6.17 and 6.18 show an almost constant switching field with θ. More detailed analysis of the experimental results is discussed in the next section.

6.4: Analysis of angular dependence of switching field

The experimental results presented in the previous section are analysed in this section using two models, the Stoner-Wohlfarth model [21] and the Kondorsky function [18-20, 22]. The magnetisation reversal in magnetic elements can take place by either coherent rotation or domain nucleation, similar to those observed in the SV films. The former mechanism more associated to Stoner-Wohlfarth type behaviour. The latter gives rise to the Kondorsky type behaviour, which is discussed in section 6.4.2.

Reversal involving domain wall displacement takes place at lower fields than processes involving magnetisation rotation. The reason is that domain wall displacement requires less energy than magnetisation rotation [23,24]. Hence, magnetisation is usually reversed by the displacement of domain walls before

magnetisation rotation occurs. Therefore, the Stoner-Wohlfarth model gives an upper bound to the switching field.

6.4.1: Switching field calculation using the Stoner-Wohlfarth model

By assuming a single domain magnetic element with shape anisotropy K under an applied field H, the energy E of this system can be expressed as

$E = K \sin^2(\phi - \theta) - \mu_o M_s H \cos(\phi)$

where the angle θ is the applied field orientation with respect to the easy axis of the elements and the angle ϕ is the angle of the magnetisation vector from the applied field direction, shown in figure 6.13. μ_o and M_s are the permeability of free space and the saturation magnetisation respectively. Equilibrium occurs when $\frac{\partial E}{\partial \phi} = 0$. However, the equilibrium can be stable or unstable. Stable equilibrium requires $\frac{\partial^2 E}{\partial \phi^2} > 0$, while $\frac{\partial^2 E}{\partial \phi^2} < 0$ gives an unstable equilibrium. Therefore, the critical condition ($H = H_o$) must be that $\frac{\partial^2 E}{\partial \phi^2} = 0$. This critical field also indicates the switching field, $H_s = H_o$. Hence, by solving the energy function for $\frac{\partial E}{\partial \phi} = 0$ and $\frac{\partial^2 E}{\partial \phi^2} = 0$, the relationship between the applied field orientation θ and the switching field H_s can be established, and is shown in the equation,

$\sin 2\theta = \frac{1}{p^2}\left(\frac{4 - p^2}{3}\right)^{\frac{3}{2}}$ (Please refers to Appendix A for the derivation of this relationship.) where $p = -\frac{2H_s}{H_d}$. H_d is the demagnetising field.

$H_d = -N M_s$

where N is the demagnetising factor.

To a good approximation, $N = \frac{t}{w}$, where t and w are the thickness and width of the element respectively [25].

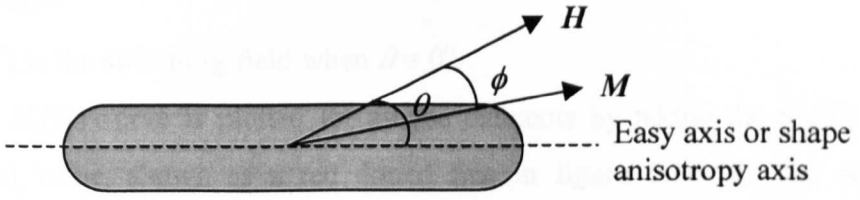

Figure 6.13: Schematic showing the angular relationship.

By using M_s = 10 000 Oe for the $Ni_{80}Fe_{20}$ elements, the angular dependence of the switching field for each elements is shown in figure 6.14-18. The Stoner-Wohlfarth curves show a rapid decrease in switching field with the applied field orientation. This contradicts the experimental result which shows a slight increase. The fields calculated using the Stoner-Wohlfarth model are also much higher than the experimental values at all orientations. This is due to the fact that the elements switch at lower fields by domain wall displacement instead of magnetisation rotation [24].

However, the discrepancy between the theoretical and experimental switching field values is smaller at larger applied field orientation. The reason may be that at larger applied field orientation, the switching is more likely to occur with magnetisation rotation than domain nucleation. Therefore, the reversal behaviour more closely resembles Stoner-Wohlfarth type behaviour.

6.4.2: Switching field calculation using the Kondorsky function

Analysis in the previous section indicates that the experimental angular dependence of switching field for the $Ni_{80}Fe_{20}$ elements did not follow Stoner-Wohlfarth behaviour. Hence, the Kondorsky function, which is based on domain wall displacement, is used to analyse the experimental results. The Kondorsky function assumes that the domain wall pinning field is proportional to the variation of the domain wall surface energy density with respect to the wall displacement [18-20, 22].

Therefore, the Kondorsky function is only applicable for reversal processes without magnetisation rotation. This usually occurs when the field is applied close to the easy axis of the elements. This also means that the Kondorsky function is only applicable if the switching field is much lower than the shape anisotropy field of the element.

The angular dependence of switching field in the Kondorsky function is expressed by

$$H_s(\theta) = \frac{H_s(0^\circ)}{\cos(\theta)}$$

where $H_s(0^\circ)$ is the switching field when $\theta = 0^\circ$.

The $H_s(\theta)$ curve is plotted for all the elements by taking the $H_s(0^\circ)$ from the experimental value, shown as a red dotted line in figure 6.14-18. The comparison between the experimental data and the Kondorsky function shows remarkable agreement. The angular dependence of switching field in all elements shows very good Kondorsky-type behaviour. For large elements, agreement is found for θ up to 45°.

Discrepancies occur for smaller elements at large value of θ. Figure 6.19 shows the switching field as a function of element width for various orientations. It shows that the Kondorsky function fits better for larger element widths and smaller value of θ. This is not very surprising since domain activity is much lower in smaller elements. Hence, the Kondorsky assumption for a domain wall displacement dominated reversal process does not apply well here. The discrepancy between the Kondorsky switching field and the experiments at larger orientation was also reported in [19,20] for Barrium Ferrite powder.

The analysis using the Stoner-Wohlfarth model and the Kondorsky function has shown that domain wall displacement has played a very important role in the switching field of the rounded end $Ni_{80}Fe_{20}$ elements. For $\theta = 0^\circ$, the switching field deduced from the Stoner-Wohlfarth model can be as much as four or five time higher than the experimental value. This difference is reduced for larger θ. The opposite is true for the Kondorsky analysis where the disagreement between the theoretical and experimental values increases with θ.

Element defects such as edge roughness also reduce the switching field by creating vortices, which will move though the width of the element [26]. Hence, this favours the Kondorsky reversal behaviour. Systematic studies of edge effects were reported by Hermann et al [27].

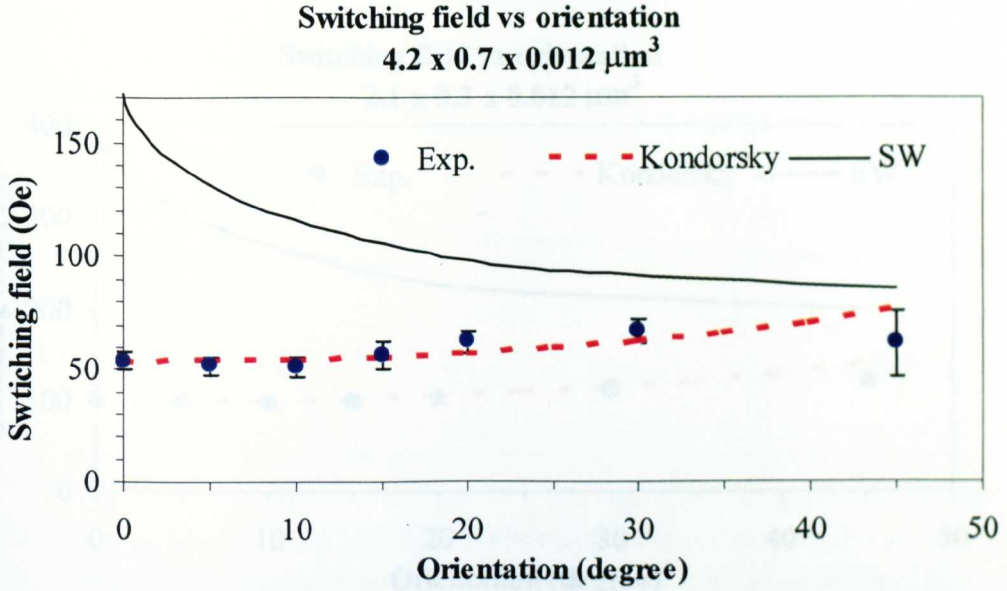

Figure 6.14: Comparison of the angular dependence of switching field determined experimentally with Stoner-Wohlfarth and Kondorsky models for the 4.2 x 0.7 x 0.012 μm³ $Ni_{80}Fe_{20}$ element. Aspect ratio 6:1.

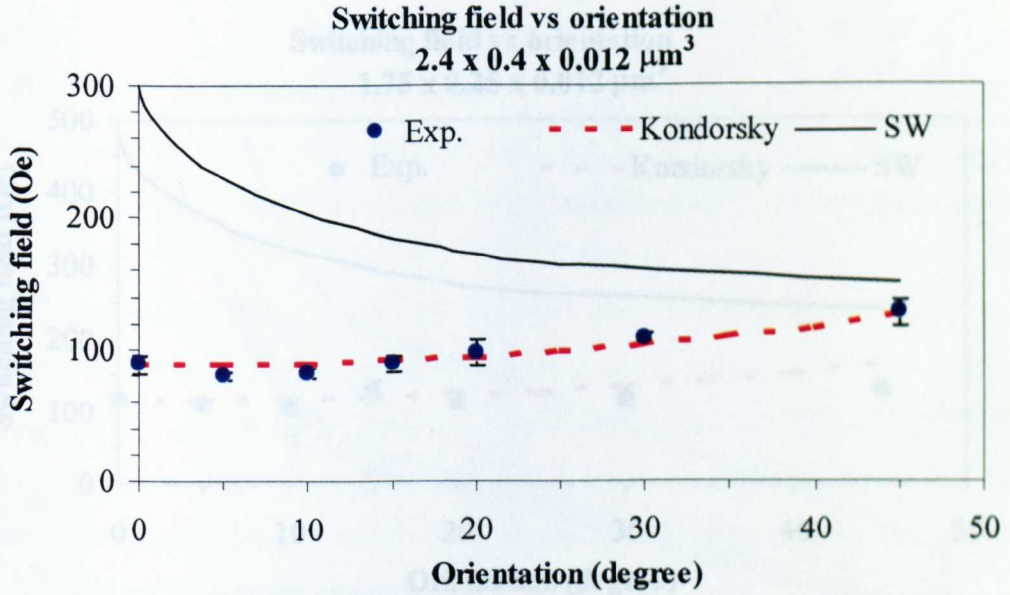

Figure 6.15: Comparison of the angular dependence of switching field determined experimentally with Stoner-Wohlfarth and Kondorsky models for the 2.4 x 0.4 x 0.012 μm³ $Ni_{80}Fe_{20}$ element. Aspect ratio 6:1.

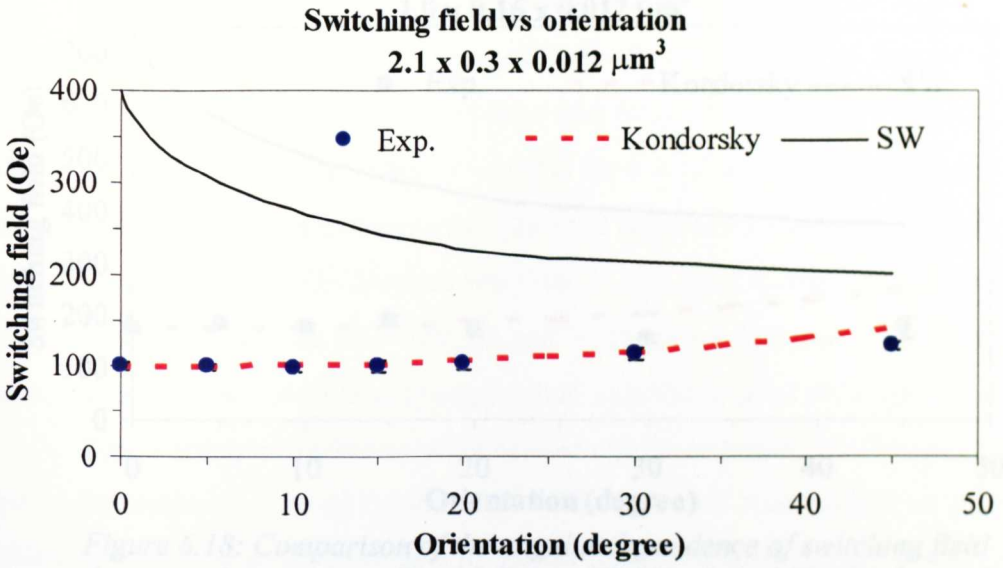

Figure 6.16: Comparison of the angular dependence of switching field determined experimentally with Stoner-Wohlfarth and Kondorsky models for the 2.1 x 0.3 x 0.012 μm³ $Ni_{80}Fe_{20}$ element. Aspect ratio 7:1.

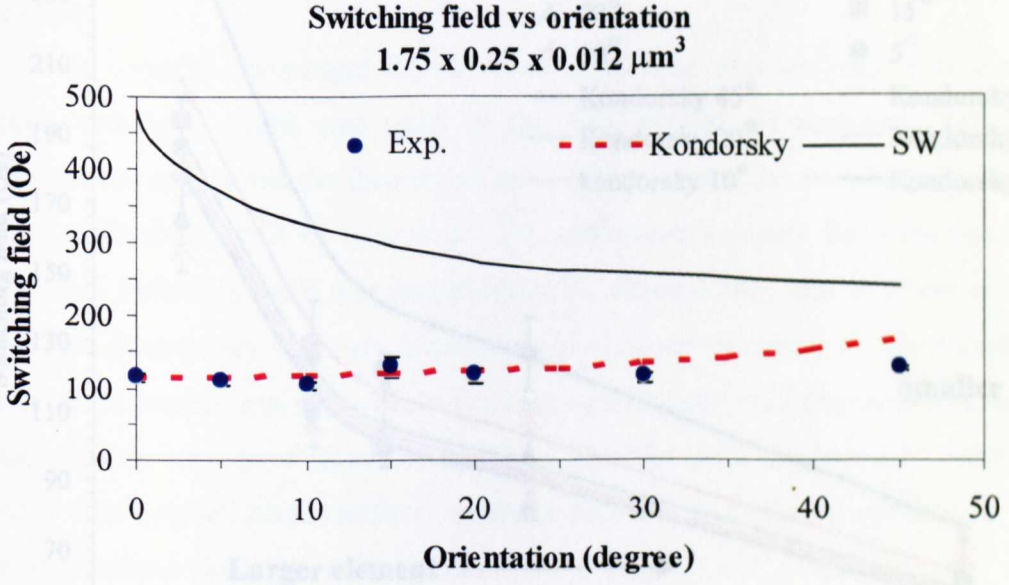

Figure 6.17: Comparison of the angular dependence of switching field determined experimentally with Stoner-Wohlfarth and Kondorsky models for the 1.75 x 0.25 x 0.012 μm³ $Ni_{80}Fe_{20}$ element. Aspect ratio 7:1.

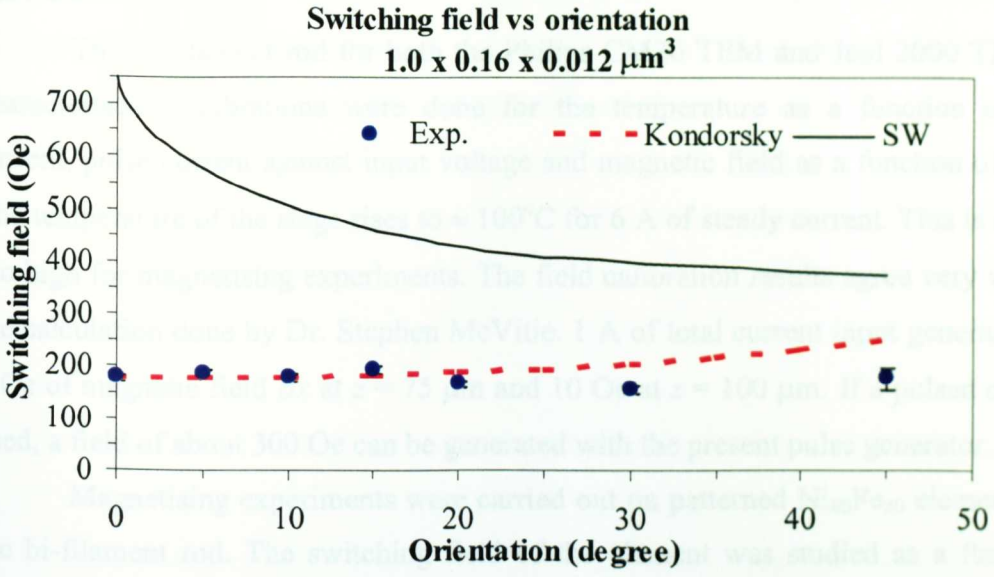

Figure 6.18: Comparison of the angular dependence of switching field determined experimentally with Stoner-Wohlfarth and Kondorsky models for the 1.0 x 0.16 x 0.012 μm³ $Ni_{80}Fe_{20}$ element. Aspect 6.25:1.

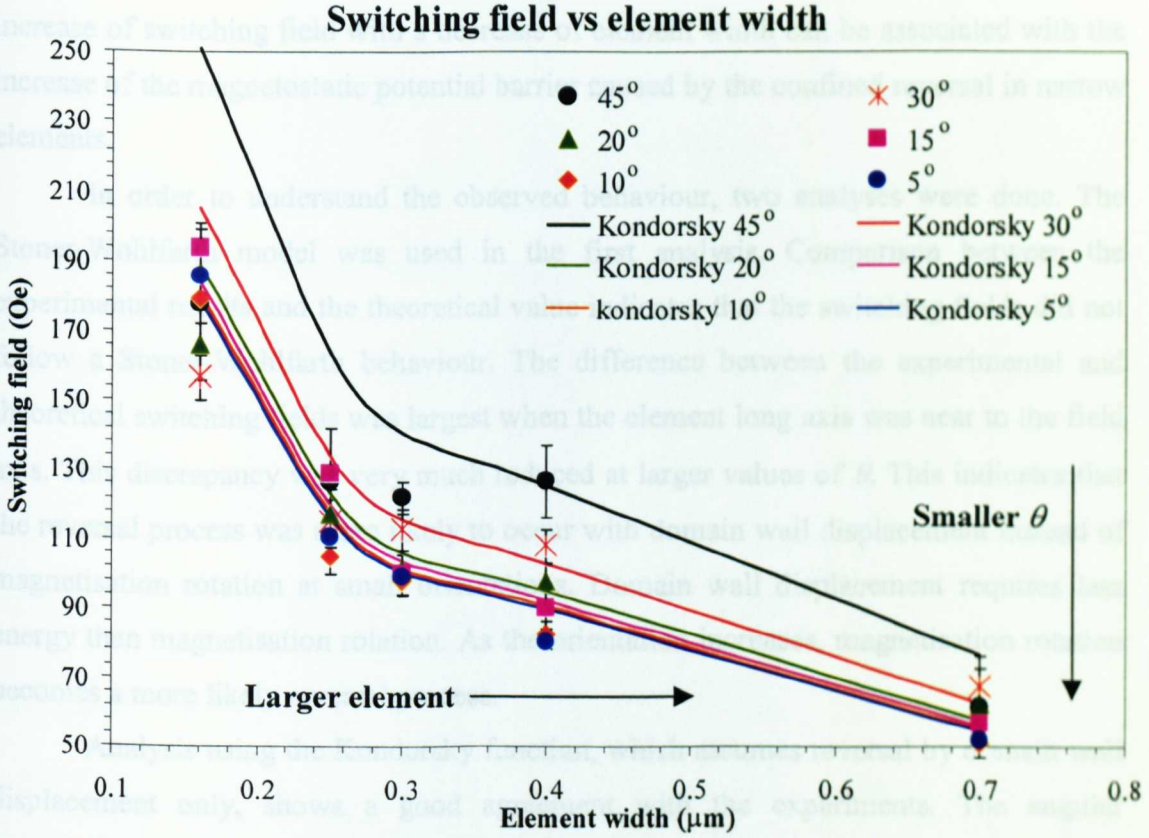

Figure 6.19: Chart showing the switching field as a function of element width for orientation 45°, 30°, 20°, 15°, 10° and 5°.

6.5: Discussion

The bi-filament rod for both the Philips CM20 TEM and Jeol 2000 TEM were characterised. Calibrations were done for the temperature as a function of steady current, pulse current against input voltage and magnetic field as a function of current. The temperature of the stage rises to $\approx 100^{o}C$ for 6 A of steady current. This is normally too high for magnetising experiments. The field calibration results agree very well with the calculation done by Dr. Stephen McVitie. 1 A of total current input generates about 8 Oe of magnetic field Bx at $z = 75$ μm and 10 Oe at $z = 100$ μm. If a pulsed current is used, a field of about 300 Oe can be generated with the present pulse generator.

Magnetising experiments were carried out on patterned $Ni_{80}Fe_{20}$ elements using the bi-filament rod. The switching field of the element was studied as a function of orientation relative to the easy axis of the element. A slight increase in switching field with θ was observed for most of the elements. The exception was for the smaller dimension elements where the switching field was less sensitive to the orientation. The increase of switching field with a decrease of element width can be associated with the increase of the magnetostatic potential barrier caused by the confined reversal in narrow elements.

In order to understand the observed behaviour, two analyses were done. The Stoner-Wohlfarth model was used in the first analysis. Comparison between the experimental results and the theoretical value indicates that the switching fields did not follow a Stoner-Wohlfarth behaviour. The difference between the experimental and theoretical switching fields was largest when the element long axis was near to the field axis. This discrepancy was very much reduced at larger values of θ. This indicates that the reversal process was more likely to occur with domain wall displacement instead of magnetisation rotation at small orientations. Domain wall displacement requires less energy than magnetisation rotation. As the orientation increases, magnetisation rotation becomes a more likely reversal process.

Analysis using the Kondorsky function, which assumes reversal by domain wall displacement only, shows a good agreement with the experiments. The angular dependence of the switching field generally follows the Kondorsky characteristic. However, discrepancies were found for smaller elements with larger values of θ. The reason can simply be that domain activity is lesser in the smaller elements. Hence, the Kondorsky assumption is not applicable.

In summary, the angular dependence of switching field for rounded end $Ni_{80}Fe_{20}$ elements shows a Kondorsky-type behaviour at small θ and seems to tend toward Stoner-Wohlfarth-type behaviour at large values of θ.

Appendix A: Angular switching field calculation using the Stoner-Wohlfarth model

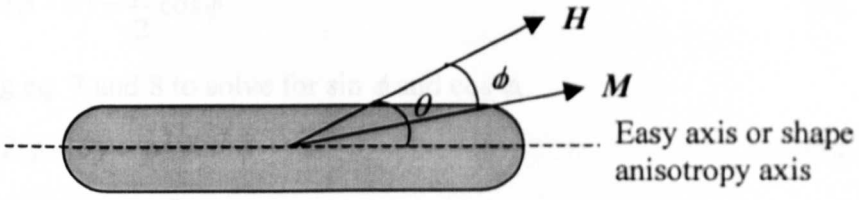

Figure A1: Angular relationship between ϕ and θ relative to the easy axis.

The Stoner-Wohlfarth energy function of the system can be written as

$$E = K \sin^2(\phi - \theta) - \mu_o M_s H \cos(\theta) \qquad \text{(eq. 1)}$$

The definition of angle ϕ and θ are shown in figure A1. M_s and μ_o is the saturation magnetisation and the permeability of free space respectively. H is the applied magnetic field and K is the shape anisotropy.

The energy function (eq 1) can be re-written in a reduced form,

$$\varepsilon = H_d \sin^2(\phi - \theta) - 2H\cos(\phi) \qquad \text{(eq. 2)}$$

where H_d is the demagnetising field. $H_d = -N M_s$.

Critical condition occurs when $\frac{\partial \varepsilon}{\partial \phi} = 0$ and $\frac{\partial^2 \varepsilon}{\partial \phi^2} = 0$. When these conditions are satisfied, magnetisation switching occur and the applied field H is equal to the switching field H_s.

Therefore, at $H = H_s$

$$\frac{\partial \varepsilon}{\partial \phi} = H_d \sin 2(\phi - \theta) + 2H_s \sin\phi = 0 \qquad \text{(eq. 3)}$$

$$\frac{\partial^2 \varepsilon}{\partial \phi^2} = 2H_d \cos 2(\phi - \theta) + 2H_s \cos\phi = 0 \qquad \text{(eq. 4)}$$

Solving eq. 3 and 4 give

$$\sin 2(\phi - \theta) = -\frac{2H_s}{H_d}\sin\phi \qquad \text{(eq. 5)}$$

$$\cos 2(\phi - \theta) = -\frac{H_s}{H_d}\cos\phi \qquad \text{(eq. 6)}$$

Substituting $p = -\frac{2H_s}{H_d}$ into eq. 5 and 6,

$$\sin 2(\phi - \theta) = p \sin \phi \qquad \text{(eq. 7)}$$

$$\cos 2(\phi - \theta) = \frac{p}{2} \cos \phi \qquad \text{(eq. 8)}$$

Using eq. 7 and 8 to solve for $\sin \phi$ and $\cos \phi$,

$$\sin^2 2(\phi - \theta) = p^2 \sin^2 \phi \qquad \text{(eq. 9)}$$

$$\cos^2 2(\phi - \theta) = \frac{p^2}{4} \cos^2 \phi \qquad \text{(eq. 10)}$$

eq. 9 + eq. 10 gives

$$p^2 \sin^2 \phi + \frac{p^2}{4} \cos^2 \phi = 1 \qquad \text{(eq. 11)}$$

From eq. 11,

$$\sin \phi = \sqrt{\frac{4 - p^2}{3p^2}} \text{ and } \cos \phi = \sqrt{\frac{4(p^2 - 1)}{3p^2}}$$

Substitute these into eq.7 and 8 and solve for $\sin 2\theta$,

$$\sin 2\theta = \frac{1}{p^2} \left(\frac{4 - p^2}{3}\right)^{\frac{3}{2}}$$

References:

[1] K. Ramstock, J. J. M. Ruigrok and J. C. Lodder, Sensors and Actuators **81** 359 (2000),

[2] J. Yu, U. Rudiger, A. D. Kent, L. Thomas and S. S. Parkin, Phys. Rev. B **60** 7352 (1999),

[3] R. D. Gomez, T. V. Luu, A. O. Pak, K. J. Kirk and J. N. Chapman, J. Appl. Phys. **85** 6163 (1999),

[4] R. D. Gomez, T. V. Luu, A. O. Pak, I. D. Mayergoyz, K. J. Kirk and J. N. Chapman, J. Appl. Phys. **85** 4598 (1999),

[5] K. J. Kirk, M. R. Scheinfein, J. N. Chapman, S. McVitie, M. F. Gillies, B. R. Ward and J. G. Tennant, J. Phys. D: Appl. Phys. **34** 160 (2001),

[6] K. J. Kirk, J. N. Chapman and C. D. W. Wilkinson, J. Appl. Phys. **85**, 5237 (1999),

[7] W. Rave, K. Ramstock and A. Hubert, J. Magn. Magn. Mater. **183** 329 (1998),

[8] C. Vieu, J. Gierak, H. Launois, T. Aign, P. Meyer, J. P. Jamet, J. Ferre, C. Chappert, V. Mathet, H. Bernas, Microelectron. Eng. **53** 191 (2000),

[9] T. Devolder, C. Chappert, Y. Chen, E. Cambril, H. Launois, H. Bernas, J. Ferre, J. P. Jamet, J. Vac. Sci. Technol. B **17** 3177 (1999),

[10] C. A. Ross, H. I. Smith, T. Savas, M. Schattenburg, M. Hwang, M. Walsh, M. C. Abraham, R. J. ram, J. Vac. Sci. Technol. B **17** 3168 (1999),

[11] J. N. Chapman, P. R. Aitchison, K. J. Kirk, S. McVitie, J. C. S. Kools, M. F. Gillies, J. Appl. Phys. **83** 5321 (1998),

[12] R. P. Cowburn, D. K. Koltsov, A. O. Adeyeye, M. E. Welland, D. M. Tricker, Phys. Rev. Lett. **83** 1024 (1999),

[13] K. J. Kirk, J. N. Chapman, C. D. W. Wilkinson, Appl. Phys. Lett. **71** 539 (1997),

[14] J. Fidler and T. Schrefl, J. Magn. Magn. Mater. **203** 28 (1999),

[15] N. Dao, S. R. Homer and S. L. Whittenburg, J. Appl. Phys. **86** 3262 (1999),

[16] K. J. Kirk, J. N. Chapman, S. McVitie, P. R. Aitchison, C. D. W. Wilkinson, Appl. Lett. Phys. **75** 3683 (1999),

[17] Y. Zheng and J. G. Zhu, J. Appl. Phys. **81** 5471 (1997),

[18] F. Schumacher, J. Appl. Phys. **69** 2465 (1991),

[19] F. Schumacher, J. Appl. Phys. **70** 3184 (1991),

[20] H. J. Richter, J. Appl. Phys. 65 3597 (1989),

[21] E. C. Stoner and E. P. Wohlfarth, Trans. R. Soc. (London) Ser. A **240** 599 (1948),

[22] E. Kondorsky, J. Phys. (Moscow) II, 161 (1940),

[23] J. Shi, S. Tehrani, T. Zhu, Y. F. Zheng and J. G. Zhu, Appl. Phys. Lett. **74** 2525 (1999),

[24] R. D. McMichael, J. Eicke, M. J. Donahue and D. G. Porter, J. Appl. Phys. **87** 7058 (2000),

[25] A. Hubert and R. Schafer, Magnetic Domains: The Analysis of Magnetic Microstructures, Springer, pg. 120-121 (1998),

[26] T. Schrefl, J. Fidler, D. Suss and W. Scholz, J. Phys. B **275** 55 (2000),

[27] M. Hermann, S. McVitie and J. N. Chapman, J. Appl. Phys. **87** 2994 (2000),

CHAPTER 7: MICRO-ELECTROMAGNET FABRICATION

Introduction

Patterned arrays of discrete single domain nanoparticles have the potential to store 1 Tbit/in^2 (1000Gbit/in^2) [1-3]. This makes patterned magnetic elements an interesting field to explore. Up to now, studies involving the imaging of patterned elements have relied on the application of a global field to an entire array of elements [4]. For example the field applied in the TEM discussed in this thesis so far, either by using the objective field or the bi-filament rod is homogeneous over an area much larger than the field of view [5-7].

The motivation to make a micro-electromagnet is that it can be used to magnetise a small element in the TEM or the MFM. It will allow the fields to be varied and magnetising cycles to be repeated easily, and therefore facilitate studies of the reproducibility of film and element properties, similar to the bi-filament rod discussed in the previous chapter. Moreover, the smaller versions of the electromagnet will also allow magnetising of elements locally, which is not possible for the bi-filament rod, and hence lead to useful information on interactions between elements within an array.

Presented in this chapter is all the work that was carried out to develop a fabrication technique for a micro-electromagnet. The search and test for a suitable insulation material is discussed in section 7.1 and followed by the complete fabrication technique developed in section 7.2. Problems and difficulties encountered in fabricating a functional device are included in section 7.3. In order to find solution to the difficulties, the FLUX3D micromagnetic simulation software was used to simulate a modified design. This is presented in section 7.4. The new and improved structure was successfully fabricated and discussed in section 7.5.

7.1: Insulation materials testing

A micro-electromagnet consists of a magnetic core with current carrying coils wound around it. The first challenge in making the electromagnet device has been to find a suitable material to insulate the magnetic core layer from the current carrying coil (gold) layer. The thickness of the insulating layer must be low enough (preferably < 200 nm) so that the interaction between the flux generated by the current carrying coils and the magnetic core is maximum. But this insulating layer must also be thick enough to prevent the flow of electrons.

A number of dielectric materials were tested, such as Polyimide [8-10] and the negative photoresist SU8 [11-13]. Polyimide is a dielectric which is widely used in industry as an insulator. However, test results showed that it was very difficult to get the thickness of the Polyimide under 1 μm using spin-coating even if it was spun at 8000rpm for 60s. Please refer to Chapter 2, section 2.5.2 for resist coating.

SU8 is a new negative photoresist, epoxy-type, based on EPON SU8 resin (from Shell Chemical). It is a very thick resist (>50 μm) developed for microelectromechanical structure (MEMS) application. This is far too thick for the micro-electromagnet. Hence, the resist was diluted with a solvent known as PGMEA. There are two crucial factors in determining the thickness of the spun resist. They are the concentration of the resist and the spin speed. In general, the thickness t of the resist is directly proportional to $C^2/\sqrt{v}$, where C is the concentration of the resist and v is the speed of spinning. Hence, diluting the resist is a more efficient way to produce a thinner layer of resist. A thickness of <300 nm was achieved for the diluted SU8 resist. However, processing a very thin layer of SU8 was very tricky. Air bubble and cracks often appeared in the preliminary tests as shown in figure 7.1(a).

The next attempt was to use a conventional positive photoresist, Shipley Microposit S1805 as an insulation layer. Tests of this photoresist spun at 5000 rpm for 60 s and baked at 200°C for 60 minutes showed good surface flatness, good metal adhesion and thickness ≈300 nm, figure 7.1(b). The purpose of high temperature baking at 200°C was to harden the resist so that it became a permanent structure. However, since this photoresist only worked with photolithography, it created another problem. Photolithography using the UV mask aligner for very small structures was very difficult. In general, it is reckoned that state-of-the-art photolithography can reach ~100 nm, but only with a very expensive mask aligner.

To proceed, either the micro-electromagnet had to be modified or another insulating material needed to be sought. Finally, a photoresist that can be used for both the e-beam and photolithography, known as UVIII was tested. Test results showed that if this resist was spun at 6000 rpm for 60 s, it produced a thickness of about 150 nm, a layer is shown in figure 7.1(c). However, UVIII can easily be washed away by other solvents such as acetone. In order to make it a permanent structure, it was baked at a high temperature of 200°C for 60 minutes. This process is called hard baking. Due to the ease of fabrication, the thin layer depth, wide accessibility and use for e-beam lithography, UVIII resist was chosen as the insulation layer material for micro-electromagnet fabrication.

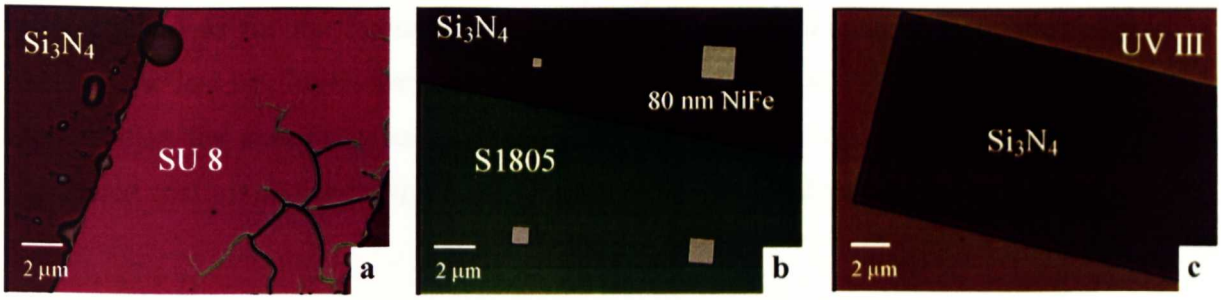

Figure 7.1: Insulation material testing. (a) SU8 photoresist, (b) Shipley Microposit S1805 photoresist and (c) UVIII photoresist.

7.2: Designs and fabrication technique

The micro-electromagnet was fabricated using e-beam lithography. The basics of e-beam lithography have been presented in Chapter 2, section 2.5.

The first fabrication layer was the bottom coil layer, figure 7.2. It was made by spinning two layers of e-beam resist PMMA with the bottom layer having a lower molecular weight than the top layer. This is very important as it creates a good overhang, which improves the edge profile of the pattern. Firstly, ELV 2010 12% resist was spun on the substrate at 5000 rpm for 60 sec, followed by baking in the oven at a temperature of 180°C for 30 minutes. Then, another layer of resist (higher molecular weight) ELV 2041 4% was spun at the same the rate and baked at the same temperature for 60 min. The sample was then exposed to the e-beam at a dose of 400 $\mu C/cm^2$. Post exposure development was carried out using the mixed developer MIBK:IPA at 1:1 ratio at 21°C for 60 sec. Evaporation of Ti(33nm)/Au(160nm) was done using the Plassys MEB 450 evaporator at a pressure of $<2x10^{-6}$Pa followed by lift-off in acetone at 45°C. Gold was chosen as the conducting layer due to the excellent electrical conductivity and titanium was used to provide good adhesion of the metal to the substrate.

The next layer was the bottom insulation layer, figure 7.2. The photoresist UVIII was spun on the sample at 6000 rpm for 60 sec, followed by baking on a hot plate at a temperature of 134°C for 60 sec. The e-beam exposure dose used for UVIII was 27 $\mu C/cm^2$. The UVIII required a post exposure bake at 134°C on the hot plate for 60 sec before developing. The solvent used to develop the UVIII was MF-CD 26 (Tetra Methyl Ammonium Hydroxide) with a developing time of 60 sec. After the UVIII was developed, it was put into an oven to hard bake at 200°C for 60 min. This ensured that the UVIII layer would stay permanently on the substrate.

After this, the magnetic core layer was patterned using the same bilayer PMMA resist method as for the bottom coil layer. 100 nm of NiFe was evaporated on the sample. The last two layers were the top insulation and the top coil layers. These were fabricated in the same way as the bottom coil and the bottom insulation layer. The completed result is shown in figure 7.2 with the cross-sectional views.

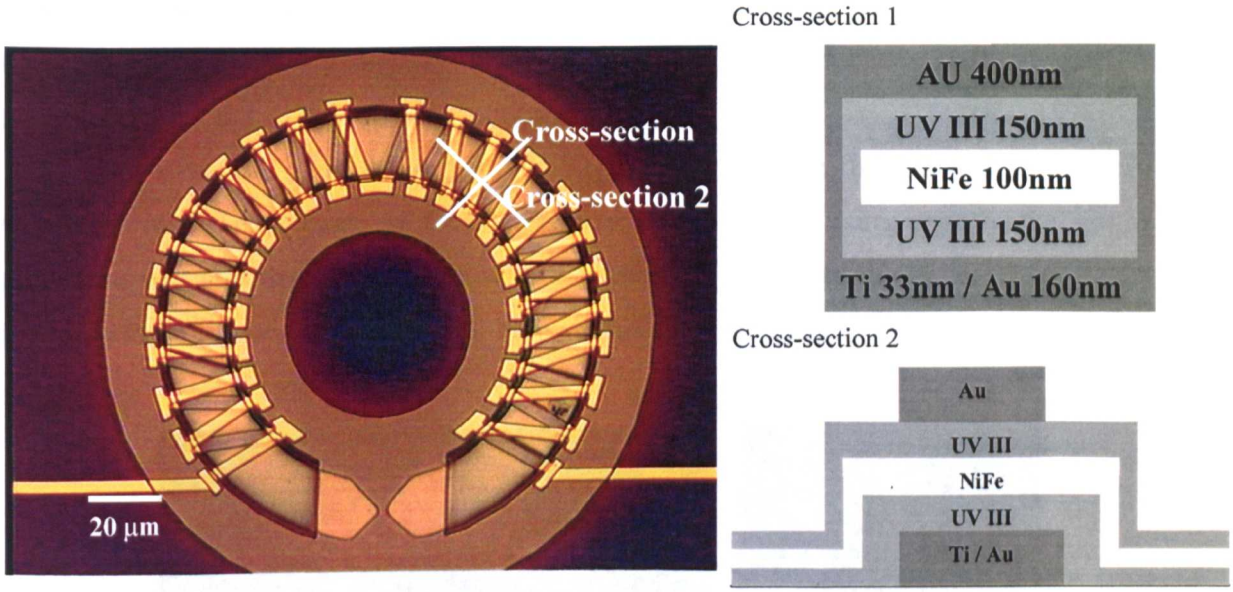

Figure 7.2: A complete micro-electromagnet structure fabricated using multilayer e-beam lithography.

7.3: Difficulties and problems

A complete micro-electromagnet structure was fabricated. However, it was not a functional device. The problem was due to the bad contact between the bottom and top conducting coils. The step height of ≈ 700 nm from the bottom to the top coil layer caused cracks to develop along the edges when depositing the top coil layer, show in figure 7.3. This meant that the device did not conduct any electrical current.

Various methods were tried to overcome this problem including electroplating a thick gold layer on the top coil layer to cover up the cracks. However, the electroplating process was not suitable for the micro-electromagnet. This was because the sulphuric acid used during the electroplating process destroyed both the insulation (UVIII photoresist) and magnetic core (NiFe) layers.

Other tests included evaporating 200 nm of gold layer at different angles to the sample in order to cover the step. This method also failed to produce a continuous coil layer. Eventually, the problem was partly solved by reducing the number of coils surrounding the magnetic core, hence reducing the possibility of cracks, shown in figure

7.4. This combined with evaporating a very thick layer of gold ≈ 400 nm on the top coil layer could avoid cracks at the edges. The working device has an electrical resistivity in the range of kΩ. Figure 7.5 shows the magnetic force microscopy scans of the device. It shows that the rectangular shape 30 nm thick NiFe elements 1 x 1.5 μm^2 were partially magnetised after a 20 mA current was applied to the device. The field generated by the device was only enough to influence the magnetisation of the elements nearest to the pole piece. For the elements further away from the pole piece, magnetic flux closure domains were observed in figure 7.5. The magnetic domain structures in the magnetic pole piece were also clearly visible in figure 7.5.

However, the yield and reproducibility of fabricating a functional device were extremely low. The chance of fabricating a working device using exactly the same procedure was less than 10%. Even with the simplest design as shown in figure 7.4b, the reproducibility was not improved. Hence, further modification was necessary.

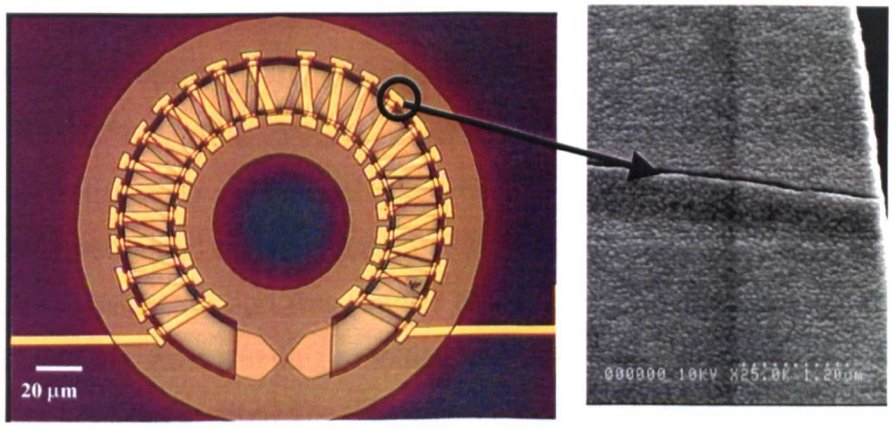

Figure 7.3: Scanning electron microscopy image showing a crack developed on the top coil layer.

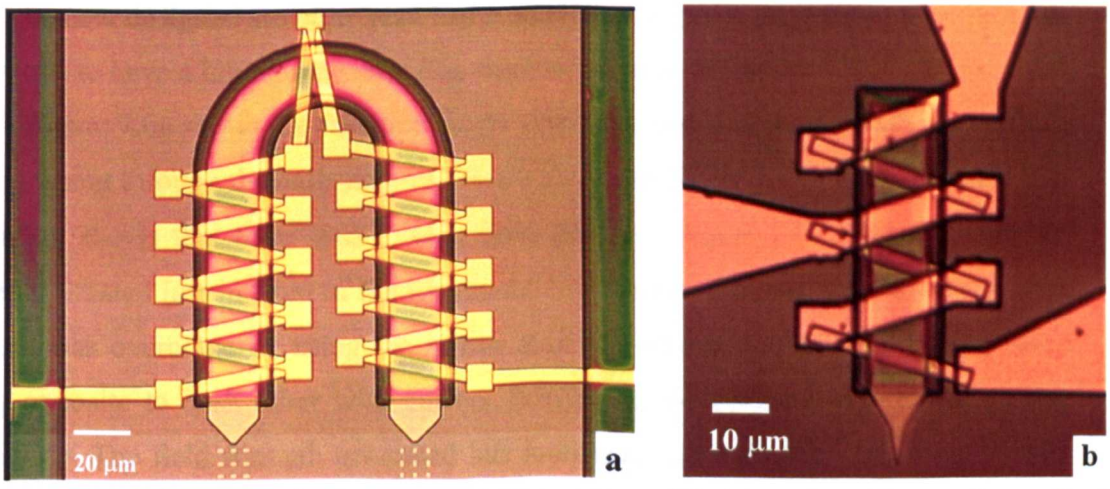

Figure 7.4: The micro-electromagnet design was modified to reduce the numbers of coil. (a) A U-shape micro-electromagnet and (b) A pencil-shape micro-electromagnet.

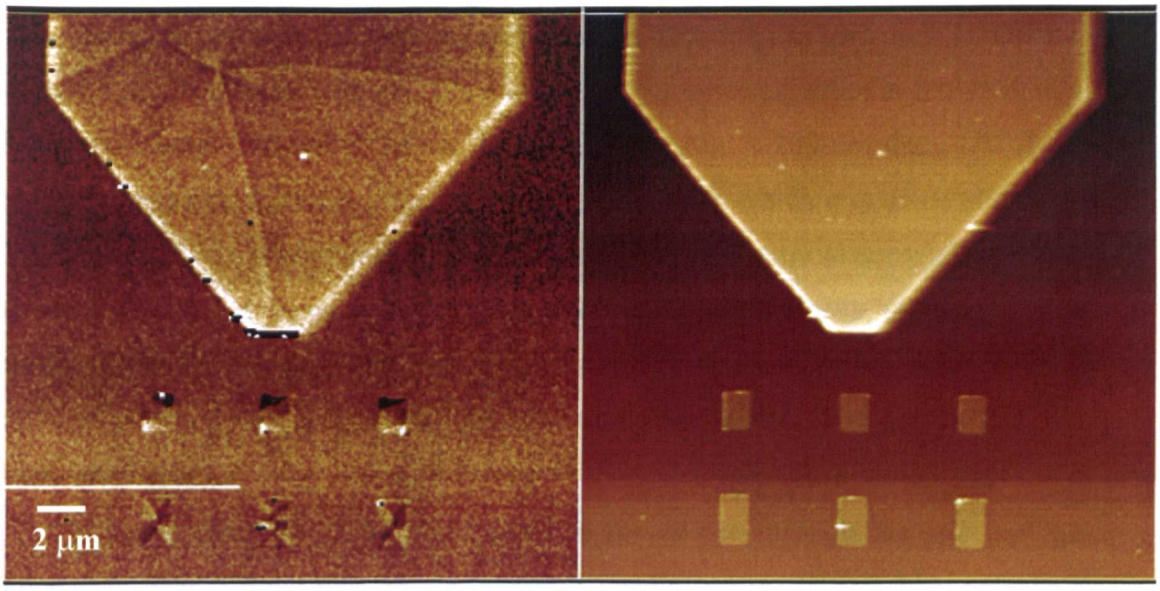

Figure 7.5: A magnetic force microscopy scan shows the partially magnetised magnetic elements (left image) and the corresponding topography scan on the right.

7.4: FLUX3D micromagnetic simulation

The FLUX3D are finite element programs developed by CEDRAT [14] for the analysis of electromagnetic and thermal phenomena. The program was used to simulate a new micro-electromagnet structure and possible field output, shown in figure 7.6. The new micro-electromagnet design was simpler and since all the conducting layers were on the same layer (no more stepping problem), this may solve the cracking problem as discussed in the previous section. The fabrication procedure for the new design was also simplified due to reduced number of layers, one insulating and one coil layer instead of two as in the old structure. This allowed the new structure to be fabricated in a shorter time. The new designed structure also had a smaller pole piece dimension. The purpose of this was to have a higher magnetic flux concentration at the pole.

Figure 7.6a shows the case of a single core. The field output was calculated for 5 mA of current through the coils and results are shown in figure 7.7a in unit of A/m. The simulation shows that there was a large field gradient, figure 7.7a. Hence, magnetic elements situated just in front of the tip should experience differing field strengths. The problem was overcome by using the mirror structure where two magnetic cores were facing opposite to each other with current flowing in the opposite directions, shown figure 7.6b. The field strength generated has increased and a constant field region was created in between the gap of 1 μm^2. The field strength was more than 15000 A/m (188 Oe) for 5 mA of current, as shown in figure 7.7b.

7.5: Double pole piece structure

By using the same fabrication procedure as described in section 7.2, the newly designed micro-electromagnet was fabricated. The complete structure is shown in figure 7.8. The coil layer consists of 33 nm Ti and 160 nm Au. A 200 nm thick UVIII layer was used to separate the coils from the top magnetic layer, which was made of 30 nm of NiFe. The coils were designed in such a way that when an electrical current is applied, it flows in opposite directions comparing top and bottom poles. Hence, the magnetic flux generated from the top and bottom coils interact to create a uniform in-plane field. The fabricated device had a bigger gap than the modelled device. The gap in the actual device was 2 μm^2.

A bias voltage of 15 V was applied to the device through the 160 μm^2 gold contact pad. The voltage was applied using a needle probe. At this bias voltage, an electrical current of amplitude 30 mA was measured. This gave about 0.5 kΩ of resistance. The resistance was reduced by almost half from the U-shaped structure shown in figure 7.4(a). The yield was also improved significantly. A yield of more than 90% was easily achievable with extremely good reproducibility.

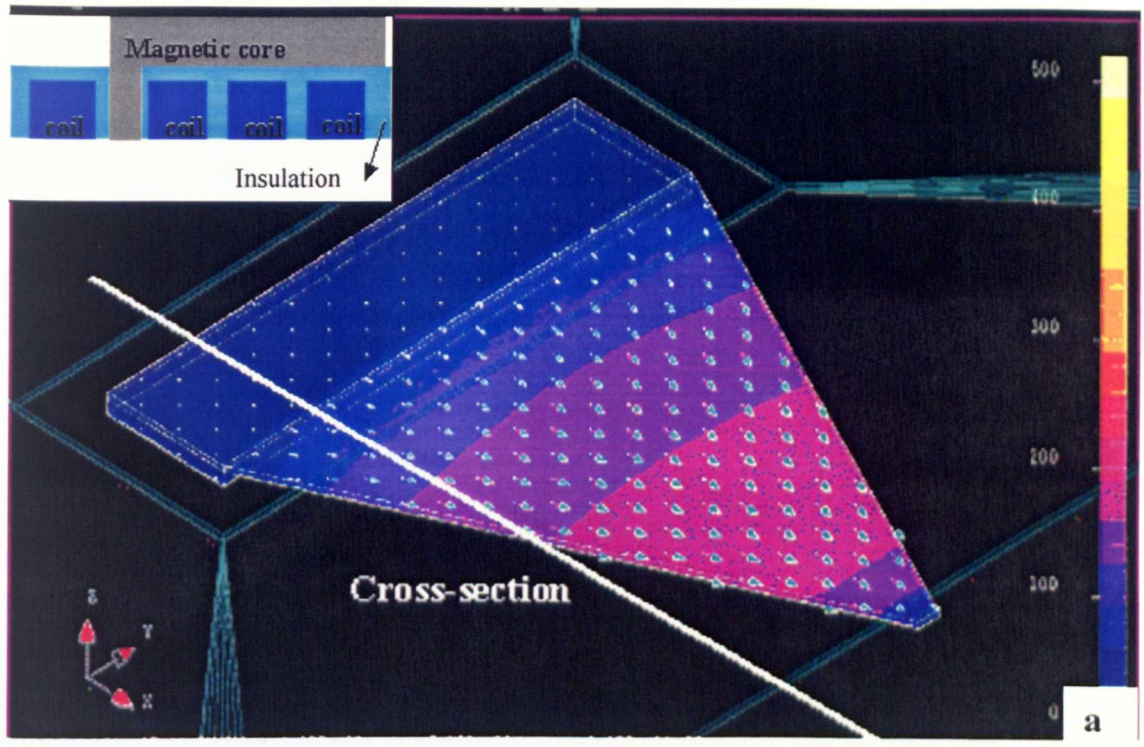

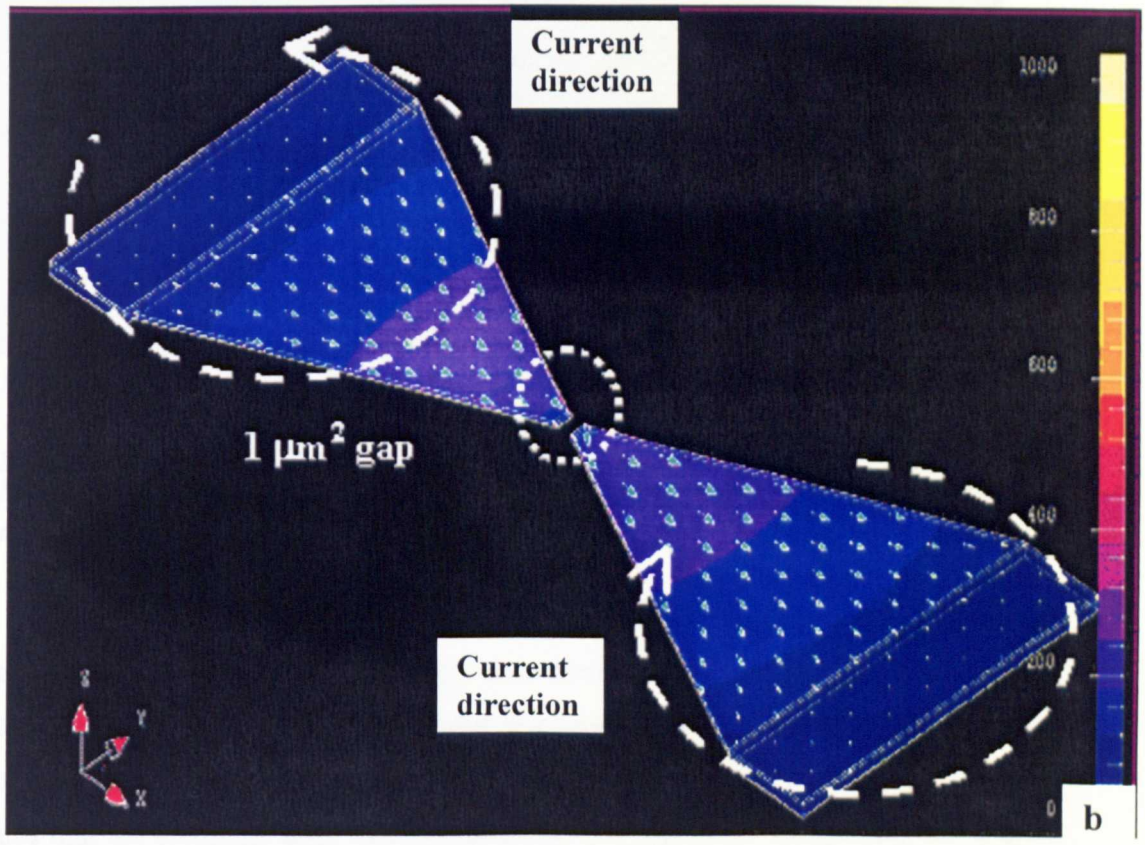

Figure 7.6: Flux 3D micromagnetic simulation of (a) a single pole piece micro-electromagnet and (b) a double pole piece micro-electromagnet with current flowing in the opposite direction. The diagram on the top right corner of image (a) shows the cross section of the structure.

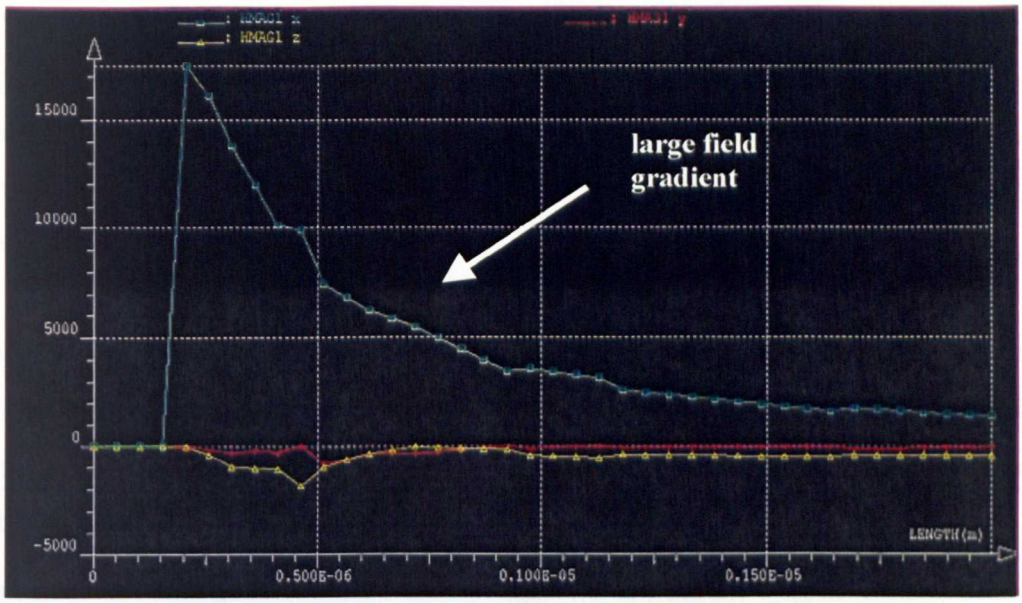

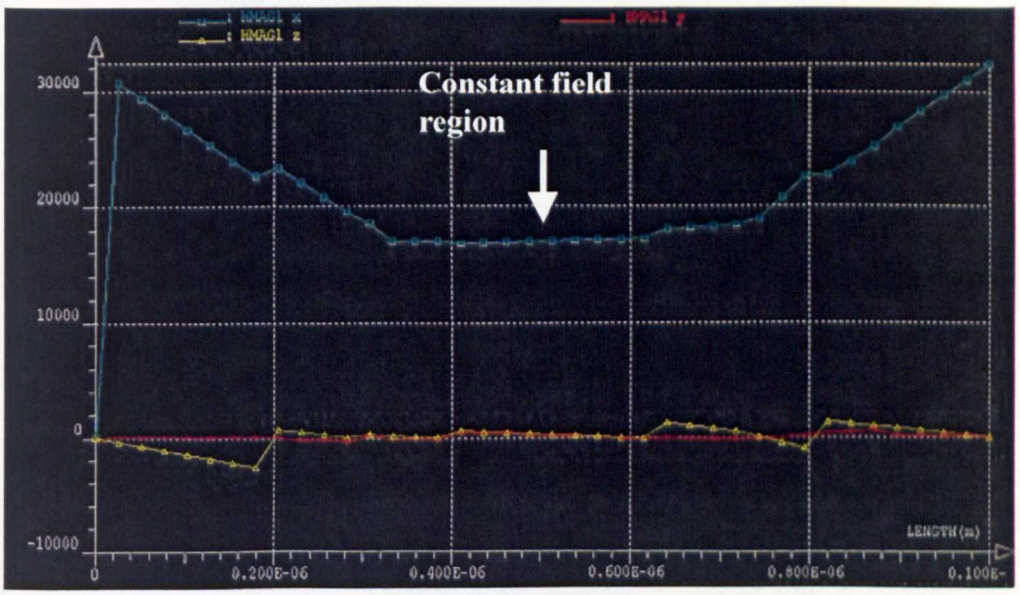

Figure 7.7: Calculation of generated field strength for 10 mA of current as a function of distance from the pole tip, shown by the blue curve. (a) A huge field gradient for the single pole piece structure and (b) A constant field region in between the gap for the double pole piece structure. y-axis is magnetic field in units A/m, and x-axis is distance in units μm.

Magnetic force microscopy was used to image the magnetic structure on the pole piece. Scanning was carried out every time after positive and negative bias voltages were applied to the device. Figure 7.9 shows the small change in the magnetic remanent state of the magnetic elements in between the pole piece after the applied voltages. This indicates that the elements were exposed to some external field. These were 1.5 x 0.5 x 0.2 μm^3 NiFe elements. However, these elements are not suitable for calibrating the field strength of the device because they did not show a uniform magnetisation state. More devices have to be made with magnetic elements with larger aspect ratio, elements similar to those used in the previous chapter, to calibrate the bi-filament rod. Finally,

MFM images in figure 7.10 show the domain structure of the magnetic pole. The topography images on the left column show the step in the device due to the coils underneath the magnetic pole. But, the magnetic images on the right column show a continuous film in the magnetic structure and this structure changed after it was subjected to opposite voltages.

The new design had solved the problems described in section 7.3. The yield and reproducibility have improved significantly. The structure also has a better electrical conductivity with resistance around 0.5 kΩ. A large current up to 40 mA can be applied to the device without damaging the device. The new design has also a reduced number of fabrication layers, hence it can be fabricated fairly quickly.

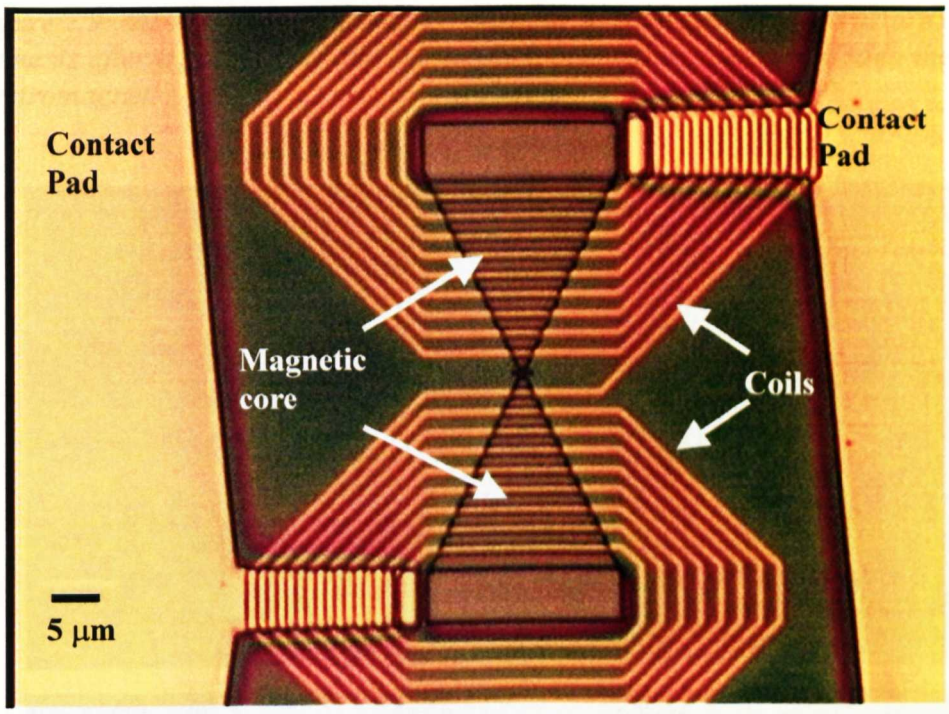

Figure 7.8: A complete fabricated micro-electromagnet structure based on the new design.

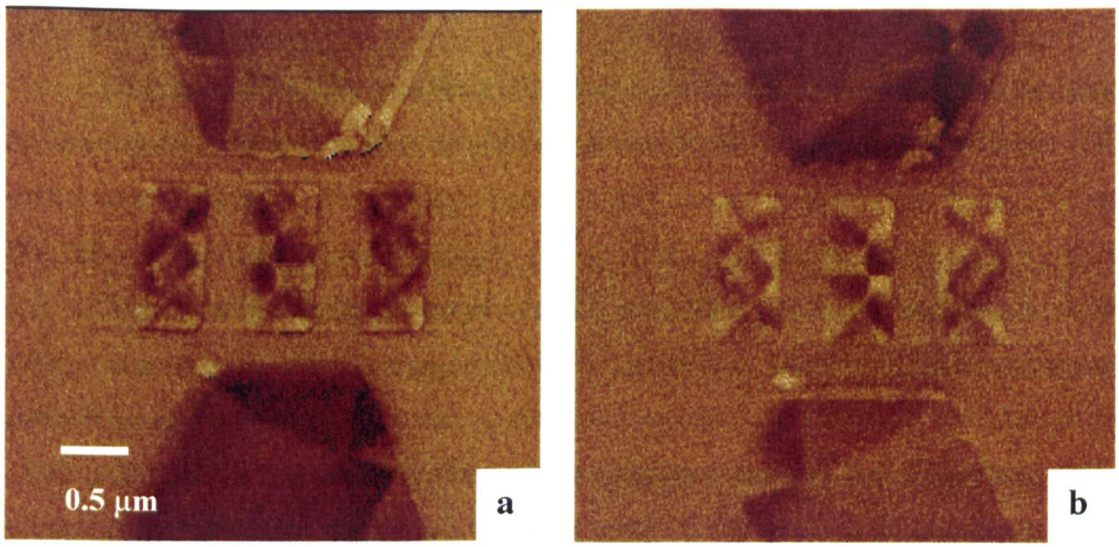

Figure 7.9: MFM images showing the changes in the flux closure structure of the NiFe elements after a positive (a) and (b) negative bias voltage was applied to the micro-electromagnet.

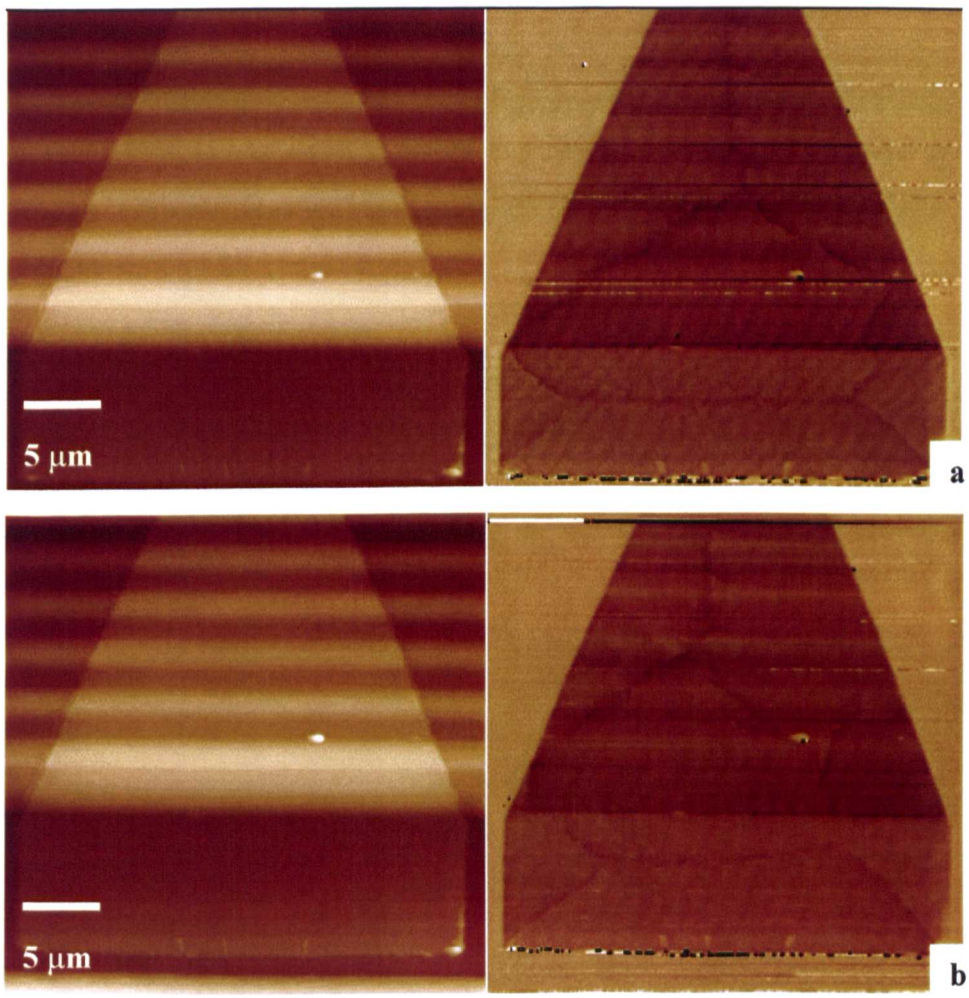

Figure 7.10: For the pole, changes in the magnetic domain structure at remanent state before the applied voltage in (a) and after the applied voltage (b). Topography images on the left and magnetic images on the right.

7.6: Discussion

Numerous tests and modifications have been carried out to fabricate the micro-electromagnet device. The best insulating material suitable for the device is the UVIII photoresist. This resist is very easy to process and is readily accessible. It allows a very thin layer of insulation to be created.

Modifications to the device design and fabrication procedure were made in order to improve the yield and the reproducibility of the device. The FLUX3D micromagnetic simulation software was also used to find a more efficient structure. The double pole piece structure has been found to be able to overcome some of the difficulties, such as cracks in the coil layer. Since, all the coils were on the same layer, the stepping and crack problems could be avoided. The new structure was also relatively easy to fabricate. The reliability of the fabrication procedure for making the double pole piece electromagnet device has also vastly improved. The device has been shown to be able to generate a magnetic field. However, the strength of the field has yet to be calibrated.

References

[1] C. A. Ross, H. I. Smith, T. Savas, M. Schattenburg, M. Farhoud, M. Hwang, M. Walsh, M. C. Abraham and R. J. Ram, J. Vac. Sci. Technol. **B 17** 3168 (1999),

[2] G. F. Hughes, 2002 IEEE International Magnetic Conference, GA06,

[3] K. Nielsch, R. Hertel, R. B. Wehrspohn, J. Barthel, J. Kirscher, U. Gosele, S. F. Fisher, H. Kronmuller, T. Schweinbock and D. Weiss, 2002 IEEE International Magnetic Conference, GB02,

[4] Martha Pardavi-Horvath, J. Magn. Magn. Mater **177-181** 213 (1998).

[5] K. J. Kirk, J. N. Chapman, C. D. W. Wilkinson, J. Appl. Phys. Lett. **71** 539 (1997),

[6] K. J. Kirk, J. N. Chapman, S. McVitie, P. R. Aitchison, and C. D. W. Wilkinson, J. Appl. Phys. **87**, 5105 (2000),

[7] K. J. Kirk, J. N. Chapman, and C. D. W. Wilkinson, J. Appl. Phys. **85**, 5237 (1999),

[8] G. Samuelson, Polymer Materials for Electronic Applications, Chapter 8, p. 93 American Chemical Society (1982),

[9] Y. K. Lee and J. D. Craig, Polymer Materials for Electronic Applications, Chapter 9, p. 107 American Chemical Society (1982),

[10] A. Saiki, K. Mukai, S. Harada and Y. Miyadera, Polymer Materials for Electronic Applications, Chapter 10, p. 123 American Chemical Society (1982),

[11] K. Y. Lee, N. LaBianca, S. Rishton, S. Zolgharnain, J. D. Gelorme, J. Shaw, and T. H. P. Chang, J. Vac. Sci. Technol. B **13** 3012 (1995),

[12] H. Lorentz, M. Despont, N. Fahrni, N. LaBianca, P. Renaud and P. Vettiger, J. Micromech. Microeng. **7** 121 (1997),

[13] H. Lorentz, M. Despont, N. Fahrni, J. Brugger, P. Vettiger and P. Renaud, Sensors and Actuators A **64** 33 (1998),

[14] http://www.cedrat.com/,

CHAPTER 8: CONCLUSIONS AND FUTURE WORK

Introduction

Lorentz transmission electron microscopy has been used extensively throughout my research to study the magnetisation reversal behaviour of various magnetic films. Free layer magnetisation reversal mechanisms of crossed anisotropy spin-valves structure were studied extensively. A variety of reversal modes were observed including coherent rotation, domain formation and discontinuous 'jumps' in magnetisation. Asymmetrical reversal processes were also observed in some of the spin-valve films where coherent rotation occurred on one side of the hysteresis loop and domain formation on the other. The modified Stoner-Wohlfarth model was used to analyse the reversal processes. Despite the simplicity of the model, good agreement between the model and experimental results were found in many cases.

Studies on magnetisation reversal were extended to patterned magnetic elements. My work also involved developing a new magnetising stage for the TEM. The new bi-filament rod was characterised and used to carry out experiments on patterned NiFe elements. An advance was also made in the fabrication of a micro-electromagnet to allow the generation of localised magnetic fields. This is important for studying the interaction between magnetic elements in arrays.

8.1: Conclusion

Free layer magnetisation reversal processes for various spin-valve structures were described in chapter 3. These spin-valves have different magnetostriction coefficients, magnetocrystalline anisotropies and coercivities. Some were TSVs and some were BSVs. They also had different exchange bias structures, which were simple AFM and SAF. The experimental results showed that a simple reversal process was often associated with those films with low magnetostriction coefficient and magnetocrystalline anisotropy. The reason could be that the magnetisation dispersion was lower in films with low magnetostriction coefficient and magnetocrystalline anisotropy. This led to an overall simpler magnetisation reversal process with coherent rotation when an external field was applied near to the offset field direction. Lower localised anisotropy fluctuations also resulted in higher domain wall mobility. Conversely, strong localised anisotropy fluctuations, inevitable in polycrystalline films with high anisotropy in the grains, led to complex domains and hence, higher coercivity.

Varying the applied field orientation relative to the offset field direction also simplified the free layer reversal process for most films. For these films, breaking the symmetry by applying a field slightly away from the offset field direction created a favourable sense in which all the local moments could rotate. However, this was not true for films with high dispersion.

Asymmetrical domain processes were observed in some of the films. Structural tests were carried out to study the texture of the films. No apparent correlation was found between the film texture quality and asymmetrical complex domain formation.

The effect on the free layer reversal process of using a synthetic antiferromagnet in spin-valves was studied in chapter 4. Experiments performed on a series of BSV films with the same magnetostriction coefficient and magnetocrystalline anisotropy but different SAF structures showed no significant difference in the reversal process of the free layer. This seems to suggest that magnetostriction and magnetocrystalline anisotropy play a more dominant role in affecting the free layer reversal process, as found in chapter 3.

Domain structures were studied for a series of BSV films with the same SAF structure but annealed in different magnetic fields. These films were grown at the same time and had identical composition. Therefore they had the same magnetostriction coefficient and magnetocrystalline anisotropy. They were annealed in vacuum separately in 250 Oe, 10 000 Oe and 20 000 Oe at 300°C for 4 hours. Magnetic imaging results showed a significant improvement in films annealed at 20 000 Oe. No difference in magnetic domain structure for films annealed in 250 Oe and 10 000 Oe was evident. Domain structures for films annealed at 20 000 Oe were comparatively larger and the walls straighter.

The hysteresis loop measured from the films annealed at 20 000 Oe showed that the saturation field for the SAF was more than 10 000 Oe. Hence, when SVs were annealed in lower fields the antiferromagnetic coupling between the PL and RL was never entirely overcome. Thus, local variations in magnetisation direction are expected. However, in higher fields such variations will be substantially suppressed simply because the magnetisation in both layers was essentially parallel to the field direction. Hence, it seems likely that when the SV was cooled and the coupling between the PL and PtMn was established, whatever local variation in orientation existed was frozen into the structure. Moreover, it persisted after the field was removed due to the strong antiferromagnetic coupling between the PL and RL. Since, the free layer is coupled

weakly to the underlayers, it seems reasonable to expect local variations in the properties of the free layer.

Magnetisation reversal processes were also studied as a function of applied field orientation in chapter 4 for a BSV film. Various reversal modes were observed ranging from simple coherent rotation to modes involving a mixture of rotation and complex domain processes as the field orientation changed by only a few degrees. In particular, asymmetric magnetisation reversals, whereby the modes on the outward and return paths of a magnetisation cycle differed were seen on occasion.

To gain insight into how the unexpected asymmetry might arise, a modified Stone-Wohlfarth model was used extensively to study how the energy of a uniformly magnetised free layer varies as a function of field strength and orientation. Using the simplest energy function possible, which just involves uniaxial and unidirectional anisotropies as well as Zeeman energy, it is possible to show how all the modes observed could arise. However, a modest symmetry breaking had to be introduced in order to achieve this. Symmetry breaking means that the unidirectional and uniaxial anisotropies were not exactly orthogonal. Such an offset could arise, for example, due to unintentional misalignment of the sample during post-deposition annealing or modest realignment of the uniaxial anisotropy axis during post-deposition annealing.

Not only did the model predict correctly the way in which the reversal took place in the majority of cases but there was often fair agreement between the predicted and observed fields at which key processes occurred. That the quantitative agreement was not better is hardly surprising given the simplicity of the model. Inevitably the model could not provide direct information on the formation of domains, although study of the energy contours allowed educated guesses to be made as to when and what type of domain structure might develop.

Another omission that cannot be incorporated is dispersion in the film due to its polycrystalline nature. For films with high magnetocrystalline anisotropy in the crystallites or with large magnetostriction this becomes increasingly problematic though for the soft free layer of the SV studied here the model proved sufficiently robust to be useful. Another possible source of discrepancy is the fact that only three terms were included in the energy function. Effectively this means that there is no contribution to the energy variation from the pinned layer of the SV, an assumption that is only valid for a completely "rigid" pinned layer – that is one in which the magnetisation is completely unaffected by fields of the strength applied here. Such an assumption is probably reasonable for the SV investigated which was pinned by a SAF.

Finally, representing the interaction between the free layer and the other magnetic layers by an effective field is itself an approximation and in reality the coupling can be rather more complex. For example, biquadratic coupling has been shown to be significant in many studies of magnetic multilayer films and this would give rise to an additional term in the energy expression. Indeed, the inclusion of further terms and relaxation of the requirement for a completely rigid pinned layer might provide an alternative way of accounting for the asymmetric behaviour. However, in the absence of firm knowledge of the magnitude of the omitted effects their inclusion would simply be a matter of increasing the number of fitting parameters.

The effect of temperature on free layer reversal process was studied in chapter 5. Thermal stability of two different types of SAF BSVs was investigated, one having a thicker SAF layer than the other.

It was found that the SV with the thinner SAF layer was more susceptible to temperature rise. A change in reversal process was observed between room temperature and 200°C. The process changed from a simple coherent rotation to an asymmetrical reversal process with domain formation on the outward path and simple rotation on the return path. No such changes were observed in the SV with thicker SAF layers.

The change in magnetisation reversal was attributed to the increase in magnetisation dispersion due to thermal effects. Again, insight on what might be the cause of the changes was sought using the modified Stoner-Wohlfarth model. Despite the fact that the Stoner-Wohlfarth model takes no account of thermal effects which, if present, offer a source of energy to allow the magnetisation to jump small energy barriers and hence follow different reversal routes, it still provides insight into how the experimental observation arises.

In-situ TEM annealing experiments were also carried out. The annealing experiments were able to induce unidirectional anisotropy. The reversal process for films annealed in a commercial annealing oven was successfully reproduced using the in-situ TEM annealing.

The studies of magnetisation reversal for magnetic thin films were extended to patterned magnetic elements. In chapter 6, the design and construction of a bi-filament rod was described.

The switching field of a $Ni_{80}Fe_{20}$ element was studied as a function of field orientation relative to the easy axis of the element using the bi-filament rod. The experimental results showed a slight increase in switching field with field orientation measured relative to the long axis for most of the elements. The exception was for the

smaller dimension elements where the switching field was less sensitive to field orientation.

A comparison between the experimental results and the theoretical values from the Stoner-Wohlfarth model indicate that the switching did not behave like a Stoner-Wohlfarth reversal. The difference between the experimental and theoretical switching field was largest when the element orientation was near to the field axis. This discrepancy was very much reduced at larger field angle. This suggests that the reversal process was more likely to occur with domain wall displacement instead of magnetisation rotation.

Analysis using the Kondorsky function, which assumes reversal by domain wall displacement only, showed good agreement with the experiments. The angular dependence of the switching field showed a good Kondorsky characteristic. However, a discrepancy was found for smaller elements at larger field angles. The reason could simply be that domain activity is lesser in the smaller elements. Hence, the Kondorsky assumption is not applicable.

Overall, the angular dependence of switching field shows a Kondorsky-type behaviour at small field angles tending toward Stoner-Wohlfarth-type behaviour at large field angles.

Work on designing and fabricating a micro-electromagnet was presented in chapter 7. The micro-electromagnet serves as an alternative magnetising method to study patterned magnetic elements. The micro-electromagnet also acts as a source of local field, which allows magnetising of a few elements in an array. This facilitates the study of interaction within an array.

A fabrication technique was developed and the device has been shown to be able to generate magnetic field. Modifications to the device design and fabrication procedure were made in order to improve the yield and the reproducibility of the device. The double pole piece structure has been found to be able to overcome some of the difficulties, such as cracks on the coil layer. The new structure was also relatively easy to fabricate. The reliability of the fabrication procedure for making the double pole piece electromagnet device has also vastly improved. However, the strength of the field generated has yet to be calibrated.

8.2: Future work

In this section, I discuss briefly further work that may be done in the future for both continuous films and patterned elements. Most of the work described here is an extension of what I achieved during my research.

8.2.1: Continuous films

It was found during my research that magnetocrystalline anisotropy and magnetostriction play an important role in the free layer reversal process. Various reversal modes were also observed at different applied field orientations θ. The effect of having $\varepsilon < 90^{\circ}$ has given rise to an asymmetrical reversal process. Hence, the parameters θ and ε have been explored to some extend in this thesis. The next parameter of interest may be the value H_i. The offset field value may also play an important role in the free layer reversal process.

An artificial offset field can be created by using the new bi-filament rod. A schematic is shown in figure 8.1. A constant current through the wires will generate a constant field on the film. The most important thing is that the amplitude of the current and hence the strength of the offset field, can be controlled accurately. According to the calibration shown in chapter 6, a current amplitude of 2 A generates a field of about 20 Oe. This is sufficient since the offset field in most of SV films is below 20 Oe. A low current of 2 A will also keep the temperature of the stage from getting too high and affecting the magnetic behaviour of the film. The magnetising experiments can then be carried out in this configuration using the "tilting in a vertical field" method.

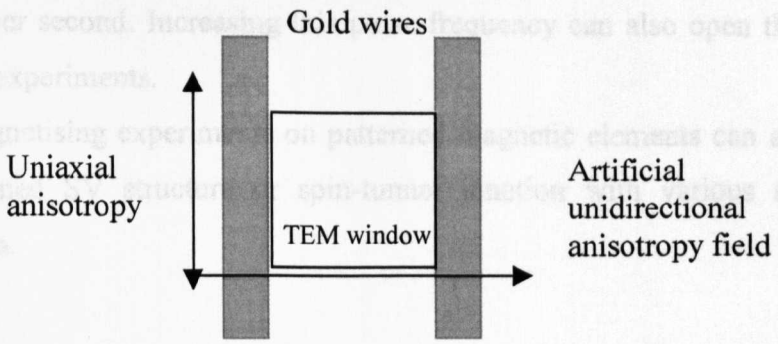

Figure 8.1: Schematic showing the use of the bi-filament rod to create an artificial unidirectional anisotropy field.

8.2.2: Patterned magnetic elements

The micro-electromagnet fabrication technique described in chapter 7 may require more refining in order to increase the field strength generated. The thickness of the magnetic core layer may have to be increased. The simulation discussed in chapter 7 was based on a 100nm thick core magnetic layer.

At this moment, the only way available to test the generated field is by applying a steady current through the device using a probe to make contact with the contact pad. The field generated by the device was determined by the remanent state of the magnetic elements after the current was applied. The problem of this is that the maximum current that can be applied using the probe system is limited.

In future, a stage may be built so that a steady current can be applied to the device while MFM scanning can be done at the same time. This will allow in-situ magnetising experiments to be carried out in the MFM.

The micro-electromagnet device could also be fabricated on the TEM window. This will require a rod that is capable of making contact with the device and allow current to be passed though the device. Hence, a new rod may have to be designed and built. The localised field generated will enable interactions between magnetic elements to be studied more thoroughly.

The pulse generator used to carry out experiments in chapter 6 may also be modified so that pulses with different length become possible. Preferably pulse lengths in the nanosecond regime for which there is immense commercial interest, are required. High current transistors can also be used to increase the current limit of the pulse generator. Hence, larger fields can be applied. At present, only one pulse can be generated per second. Increasing this pulse frequency can also open the door to other interesting experiments.

Magnetising experiments on patterned magnetic elements can also be extended to a patterned SV structure or spin-tunnel junction with various size, shape and composition.